

Heat and Mass Transfer Aspects of Coaxial Laser Cladding and its Application to Nickel-Tungsten Carbide Alloys

by

Gentry Wood

A thesis submitted in partial fulfillment of the requirements for the degree of

Doctor of Philosophy

in

Materials Engineering

Department of Chemical and Materials Engineering
University of Alberta

©Gentry Wood, 2017

Abstract

Simple engineering expressions capable of predicting the cross sectional geometry of weld beads deposited using laser cladding technologies are presented. The formulae can determine the width and maximum height of a single clad bead directly from fundamental engineering principles. These parameters have practical implications in targeting specific clad thickness and predicting the overlap between beads to create continuous protective surface layers. This work has been developed to address the problems associated with implementing state of the art numerical simulations that are often too difficult, costly, and time consuming for practitioners to use and empirical expressions that cannot be applied outside a rigid set of parameters or for a particular material system. The approach in this work decouples the heat and mass transfer aspects of the cladding process considering first the heat transfer in the substrate to estimate the molten pool boundaries and secondly, the interactions of the powder cloud with the molten pool to predict the mass transfer and resulting clad build up.

For the thermal analysis, scaling principles and asymptotic considerations are applied to Rosenthal's point heat source. Expressions are presented for the maximum width of any isotherm directly, which, applied in the context of the melting temperature, output the maximum width of the molten pool. This characteristic value of the molten pool is the width of cross section of the solidified clad. Point heat source estimates are shown to be consistently within 70% for a wide range of laser powers, powder feed rates, and travel speeds in coaxial laser cladding of nickel-tungsten carbide alloys (Ni-WC). To improve the prediction, a numerical solution was developed to Eagar's dimensionless representation of isotherm geometry for a Gaussian heat source. For the same set of experiments, the numerical approach predicts the cross section within $\pm 10\%$ of actual measurements for clad width and height. The role of convection in the heat transfer of the molten clad pool

is evaluated using an existing framework for welding systems. This analysis is applied to the Ni-WC composite system, which indicates that conduction is more significant than convection under typical process conditions for this high solid fraction weld overlay. This result supports the use of a conduction based model to predict isotherm geometry in the proximity of the heat source and melt zone.

Considering the mass transfer of the process, the bead profile is shown to be accurately represented by a parabola for the circular geometry of the laser beam and experimental conditions in this work. A new model for catchment efficiency (mass transfer efficiency) is proposed relating the area ratio of the projected powder cloud and molten pool to this efficiency. An expression for the height of the bead is proposed by combining the curvature of the bead surface, the catchment efficiency, and an overall mass balance of the cross section. Predictions for catchment efficiency for the Ni-WC experiments in this work were shown to be within $\pm 10\%$ for all but the low laser power tests. For these same tests, estimates for the calculated height were shown to consistently over predict the bead height by 20%.

The final result is a series of simple equations for width and maximum height of a single clad bead that can be solved easily based upon parameters known prior to cladding. The results of this work are based upon fundamental engineering principles and therefore can be generally applied outside of a particular material system and in some cases are even applicable to other cladding and welding processes.

Preface

The material presented in this thesis comprises the author’s research project under supervision of Dr. Patricio Mendez. This work has been funded by Natural Sciences and Engineering Research Council (NSERC) of Canada (CRD Grant ID 240897616) in partnership with industrial sponsor Apollo-Clad Laser Cladding, a division of Apollo Machine and Welding Ltd.

Chapter 1, the introduction of this work, is based on two sources written by the author of this thesis. The first is a section of the review paper published as Mendez, P.F., Barnes, N., Bell, K., Borle, S., Gajapathi, S., Guest, S.D., Izadi, H., Kamyabi, A., Wood, G., 2013. “Weld Processes for Wear Resistant Overlays”, *Journal of Manufacturing Processes*. Dr. Patricio Mendez was the supervisory author. The section on laser cladding processes was co-written by Wood, G. and Bell, K. The second document is the NSERC grant CRD application described above for which Wood, G. was the primary author. This application was reviewed prior to submission by Dr. Mendez.

Chapter 2 of this work is published as Wood, G., Mendez, P.F., 2015 “Disaggregated Metal and Carbide Catchment Efficiencies in Laser Cladding of Nickel-Tungsten Carbide”, *Welding Journal*. Dr. Patricio Mendez was the supervisory author.

Chapter 3 of this work is published as Wood, G., Al Islam, S., Mendez, P.F., 2014 “Calibrated Expressions for Welding and their Application to Isotherm Width in a Thick Plate”, *Soldagem & Inspeção*. Shahrukh Al Islam’s role was to generate correction curves as part of the mathematical analysis. He is a co-author of the paper for his contributions. Dr. Patricio Mendez was the supervisory author. Notation from the published version has been altered slightly in this thesis to be consistent with subsequent analyses. An addendum to the paper has been added to relate the general formulae presented for welding in the published work to the laser cladding experiments in Chapter (2). This

addendum outlines a fundamental intermediate step in the development of the proposed formulae for maximum isotherm width in this thesis.

Chapter 4 of this work is accepted for publication as Wood, G., Mendez, P.F., 2015 “First Order Prediction of Bead Width and Height in Coaxial Laser Cladding”, *Proceedings of Numerical Analysis of Weldability*, IIW Commission IX Mathematical Modelling of Weld Phenomena, Graz, Austria. Accepted. Dr. Patricio Mendez was the supervisory author.

Chapter 5 of this work is submitted to *Welding in the World* as Wood, G., Mendez, P.F., 2016 “The Role of Thermocapillary Flows in Heat Transfer of Laser Cladding of Nickel-Tungsten Carbide”. Dr. Patricio Mendez was the supervisory author.

As the supervisory author on all the papers presented in this thesis, Dr. Patricio Mendez provided advice for conducting all experiments and for the resulting analysis and interpretation. Dr. Patricio Mendez also revised all publications prior to submission. The format of this thesis is paper-based and there is repetition, specifically in the “Experimental” sections of chapters that rely on different analysis of the same set of experiments.

To Hannah and Jackson, for your love, support, and patience in my constant pursuit of knowledge and self-improvement. You are my reason for being. We have accomplished this work together and for that I am forever grateful.

“It’s the questions we can’t answer that teach us the most. They teach us how to think. If you give a man an answer, all he gains is a little fact. But give him a question and he’ll look for his own answer.”

- Patrick Rothfuss

Acknowledgements

There are so many people worthy of thanks for their personal and professional contributions to my success in graduate school. I feel incredibly humbled in this moment as my studies come to end, and I will do my best to name everyone that I can knowing full well that it is an impossible task.

First and foremost I have to thank my family for their unyielding love and support through this journey we embarked on together. Thank you Hannah and Jackson for allowing me to take time to learn about something that I love, which has been no small sacrifice for our young family. Mom, thank you for the meals, for your confidence in me, and for your unconditional love. Dad, thank you for your example of dedication and discipline, for your support of my pursuing engineering, and for your love. I could not be more proud to be a second generation engineer. Daniel, Wesley, and Lori, you are my family forever, and I am grateful to have such wonderful siblings.

This experience would not have been possible if not for the patience and foresight of my supervisor and friend Dr. Patricio Mendez. I cannot believe that I have spent over 6 years together, and it is remarkable for me to look back at the engineer I was compared to where I stand now. Again another humbling experience. We will forever joke that “progress is made through pain and suffering”. We have spent so much time together working under pressure that I am sometimes surprised we have made it this far. My secret is that I enjoyed those moments. The proposals, papers, presentations, reports, and lab activities that made us work so hard have been one of my greatest sources of accomplishment in my time at university. It has forever changed me. Thank you for patiently reviewing endless drafts of sometimes mediocre work and having the kindness to understand my short comings as an engineer. I am looking forward to a long and meaningful friendship after my time at the CCWJ, and all I ask in return is a copy of

your bible on scaling of welding problems at some point in my life. I had no idea I was going to join a religion again after an offer to do a PhD three weeks after we first met, but now that I'm a member I need the literature!

I'd like to take a moment to thank my friends who are with me now in the lab and those who were apart of mentoring me in the beginning. It was so much more enjoyable to spend most days working with someone who shared my sense of humour. I'd never admit it again but thanks Nairn for being a great friend and motivator to get me out of bed and go to the gym, but let's face it: you will never bench as much as me so stop trying. Thanks Jordan, Cory, Vivek, Mitch, Rebecca, and Dima for the time we have spent together working towards making the lab a better place. I have shared your pride, and I consider myself lucky to have worked with so many top-notch engineers. I'd be remiss to not thank Stuart and Steve who where the dynamic duo leading the lab before I got there. I learned so much from your examples and leadership - plus there are no better drinking buddies for an evening at Hudsons or Ratt. Thanks Goetz for your role behind the scenes in the lab. I have always appreciated your enthusiasm for cool new projects, and the answer to coffee is always firmly YES! To sum it all up, thanks to everyone in the CCWJ, who are too many to name, whom I have taught, toured, mentored, been mentored by, and had the pleasure of interacting with. My time has been enriched by the high calibre of motivated, friendly, and talented persons here in our lab. The future of welding is bright and I have no doubt who the leaders will be!

This opportunity would not have been possible if not for the support of my industrial sponsor Apollo Clad Laser Cladding. I'd like to thank three people in particular for their role in making this happen. Thank you Kurtis for mentoring me as a cocky third year engineer, not just because it was your job, but because you cared about my work and development. You gave me the training to be the best damn polishing monkey the lab has ever had, and I'll never forget it. Your quick wit made my days so much easier to

get through, and I will always look up to you. Thanks my friend. Thank you Doug for seeing the potential in such a metallurgical greenie and pushing the whole thing through. It meant a lot to have someone at my back to make this happen. I have a lot to learn, and I am confident that you will help me learn how to protect myself from forces of I digress. And finally thank you Laurie Willis, CEO of Apollo, with whom I have interacted little, but who was willing to take a chance on me. I'm biased but I think it was a pretty good bet!

My thesis has direct contributions from so many people, and I'd like to take a small moment here to thank those who worked with me on this project. Special thanks to Ying and Louie who have slugged it out with the differential equations and scaling techniques. You guys are the real scaling masters, and I am so happy that we had the chance to work together on this. You have taught me so much, and I am grateful to you on so many levels. Thank you Shahrukh, Francois, Lukas, Alvia, Tooba, Yixuan and Zifan for all your work on my project. I'm sorry I was always so slow and protective of my work, and thanks for your patience as I learned how to delegate responsibility. Working with all of you has made me a better engineer. Your contributions are scattered throughout this thesis, which I think is pretty cool and shows the quality of what you all accomplished.

Special thanks to my lifelong friends Nick and Kelsey, Scott, Dan Valdes, Becky, Joel, Zach, Nathan, the rest of the Brain clan, and Matt and the boys. You have always helped me put things in perspective, provided support, friendship, and love that has made it possible to get through the tough times and enjoy those moments at the top. I'm a MAT E, but I'm not too proud to say thanks and I love you guys.

I think a classy way to end this long list of thank you's would be to thank the welding community that has supported me over the last four years with scholarships, hands-on training, and friendship. Thanks to the members of the CWA, AWS, and IIW communities who have supported me financially and welcomed me into such an exciting

field. I plan to stay active and involved. Who knew that welding (even a PhD in welding) would be my path. I'm just glad that I have a great community to be apart of personally and professionally.

My time at the UofA has been one of the most exciting times of my life. I have been very fortunate and privileged for having had this opportunity. I hope that this work, and those to come in the future, will show that this was an opportunity well used.

Table of Contents

1	Introduction	1
1.1	Introduction	1
1.2	Objectives	6
1.3	Thesis Outline	7
1.4	References	8
	8
2	Dissagregated Metal and Carbide Catchment Efficiencies in Laser Cladding of Nickel-Tungsten Carbide	11
2.1	Introduction	11
2.2	List of Symbols	14
2.3	Experimental Setup	15
2.3.1	Laser Cladding Equipment	15
2.3.2	Powder Feed	15
2.3.3	Sample Preparation and Analysis	16
2.3.4	Cladding Procedure	17
2.3.5	Experimental Matrix	19
2.4	Determination of Catchment Efficiency	20
2.4.1	Carbide Powder Efficiency	20
2.4.2	Metal Powder Efficiency	22
2.4.3	Overall Powder Efficiency	23
2.5	Results	24
2.6	Discussion	29
2.7	Conclusions	32
2.8	Acknowledgements	32
2.9	Appendix 2.1 Tungsten Carbide Density	33
2.10	References	36
	36
3	Calibrated Expressions for Welding and their Application to Isotherm Width in a Thick Plate	38
3.1	Introduction	38

3.2	List of Symbols	40
3.3	Engineering Design Rules: Minimal Representation and Calibration Approach	41
3.4	Applying the MRC Approach to a Welding Problem	42
3.4.1	Step 1: List All Physics Considered Relevant	46
3.4.2	Step 2: Identify All Dominant Factors	46
3.4.3	Step 3: Solve Approximate Problem using Dominant Factors	47
3.4.4	Step 4: Check for Self-Consistency	53
3.4.5	Step 5: Compare Predictions to Reality	53
3.4.6	Step 6: Calibrate Predictions	55
3.5	Discussion	62
3.6	Conclusions	63
3.7	Acknowledgements	64
3.8	Appendix 3.1 Application of the MRC Approach to Laser Cladding of Ni-WC	65
3.9	References	73
	73
4	First Order Prediction of Bead Width and Height in Coaxial Laser Cladding	75
4.1	Introduction	75
4.2	List of Symbols	80
4.3	Experimental Setup	81
4.3.1	Laser Cladding Equipment	81
4.3.2	Powder Feed	82
4.3.3	Experimental Matrix	82
4.3.4	Cladding Procedure	83
4.3.5	Test Coupon Preparation and Analysis	87
4.4	Thermal Analysis for Bead Width	88
4.4.1	Calculation of Isotherm Width and Depth	92
4.4.2	Effect of the Bead on Heat Transfer	95
4.4.3	Estimation of the Beam Distribution Parameter σ	97
4.5	Estimation of Catchment Efficiency η_m	99
4.6	Prediction of Bead Height h_m	102
4.7	Comparison with Experiments	103
4.8	Discussion	110
4.9	Conclusions	113
4.10	Acknowledgements	114
4.11	Appendix 4.1 Bead Area Approximation	114
4.12	Appendix 4.2 Material Properties as a Function of Temperature	116
4.13	References	119
	119

5	Role of Thermocapillary Flows in the Laser Cladding of Nickel-Tungsten Carbide Alloys	123
5.1	Introduction	123
5.2	Methodology	129
5.2.1	Problem Formulation	130
5.2.2	Regimes and Dimensionless Groups for Characterizing Low-Prandtl-Number Thermocapillary Flows	132
5.2.3	Characteristic Values of Regime III	134
5.3	Target System	136
5.3.1	Experiments and Cross Section Measurements	136
5.3.2	Heat Source Characterization	138
5.3.3	Reference Temperature for Regime III	140
5.3.4	Clad Pool Constituents	142
5.4	Ni-WC Clad Pool Material Properties	143
5.4.1	Effective Viscosity μ_{eff}	144
5.4.2	Effective Values Summary	147
5.5	Results	147
5.6	Discussion	150
5.7	Conclusions	151
5.8	Acknowledgements	152
5.9	Appendix 5.1 CO ₂ Laser Beam Characterization	152
5.10	Appendix 5.2 Material Properties for the Composite Clad Pool	153
5.10.1	Effective Heat Capacity $c_{p_{eff}}$	154
5.10.2	Effective Viscosity μ_{eff}	158
5.10.3	Effective Thermal Conductivity k_{eff}	162
5.10.4	Effective Surface Tension Coefficient $\sigma_{T_{eff}}$	165
5.10.5	Density ρ_{eff}	168
5.11	References	173
	173
6	Conclusions and Future Work	178
6.1	Conclusions	178
6.2	Future Work	181
6.3	References	182
	182
	Bibliography	183
	Appendix A. Thermophysical Properties of 4145-MOD Steel	194
7.1	Introduction	194
7.2	List of Symbols	196
7.3	Chemistry, Heat Treatment, and Applications of 4145-MOD Steel	197
7.3.1	Chemistry	197

7.3.2	Heat Treatment	197
7.3.3	Applications	198
7.4	4145-MOD Transformation Temperatures	198
7.5	4145-MOD Thermal Conductivity	199
7.6	4145-MOD Heat Capacity	203
7.7	4145-MOD Density	209
7.7.1	ThermoCalc TM Density	209
7.7.2	Calculation of Density from Dilatometry Data	211
7.7.3	4145-MOD Dilatometry Experiments	212
7.7.4	Determination of ρ_{eff} for 4145-MOD	216
7.8	4145-MOD Thermal Diffusivity	218
7.9	Conclusions	221
7.10	Appendix A.1 Materials Testing Report for 4145-MOD Steel	222
7.11	Appendix A.2 Literature Alloy Chemistries	225
7.12	Appendix A.3 Derivation for Compound Molar Mass	225
7.13	References	227
	227
Appendix B. Uncertainty Analysis		230
8.1	Introduction	230
8.2	Uncertainty Analysis for Process Parameters	232
8.2.1	Laser Power Uncertainty	232
8.2.2	Powder Feed Rate Uncertainty	233
8.2.3	Travel Speed Uncertainty	235
8.3	Uncertainty Analysis for Measured Parameters	237
8.3.1	Powder Feed Mass Fraction Uncertainty	237
8.3.2	Cross Section Area Measurement Uncertainties	239
8.3.3	Cross Section Measured Width and Height Uncertainty	243
8.3.4	Stereo Photograph Measurement Uncertainty	246
8.4	Uncertainty Analysis for Material Properties	249
8.5	Uncertainty Analysis for Calculated Values	251
8.5.1	Uncertainty Analysis for Calculated Bead Width	252
8.5.2	Catchment Efficiency Calculation Uncertainty	256
8.5.3	Height Model Prediction Uncertainty	263
8.5.4	Bead Reinforcement Area Uncertainty	265
8.5.5	Parabolic Reinforcement Area Uncertainty	265
8.5.6	Circular Reinforcement Area Uncertainty	267
8.6	References	269
	269

Appendix C. MATLAB Code for Chapter 4	270
9.1 Step 1a. Determining the \hat{y}^* Solution Set for the Heat Affected Zone . . .	270
9.2 Step 1b. Determining the \hat{z}^* Solution Set for the Heat Affected Zone . . .	272
9.3 Step 2a. Determination of Maximum $-\hat{y}^*$	273
9.4 Step 2b. Determination of Maximum $-\hat{z}^*$	274
9.5 Step 3. Optimization for $\hat{\sigma}$ and \hat{T}_{HAZ}	275
9.6 Output All Values of Interest to Excel	277

List of Tables

2.1	Properties of powders used in the experiments	16
2.2	Experimental matrix for cladding of Ni-WC onto a 4145-MOD substrate for all beads. Target preheat was 260 °C (500 °F)	20
2.3	Bead area and carbide volume fraction measurements for experimental test beads	25
2.4	Carbide, metal powder, and overall catchment efficiency for the experimental clad beads	26
3.1	Values of optimized calibration constants for $f_{y_{m_0}}$ and $f_{y_{m_\infty}}$	59
3.2	Parameters to predict the maximum width of the melting isotherm for experimental cladding trials of Ni-WC on 4145-MOD steel	66
3.3	Comparison of measured Ni-WC bead width to predictions produced from the MRC approach applied to a Rosenthal isotherm	67
3.4	Total uncertainty for the measured bead width, calculated bead width, and experimental process variables	68
4.1	Properties of powders used in the experiments	82
4.2	Experimental matrix for cladding of Ni-WC onto a 4145-MOD substrate for all beads. Target preheat was 260 °C (500 °F)	83
4.3	Effective thermophysical properties of 4145-MOD steel	92
4.4	Bead area and carbide volume fraction measurements for the experimental test beads	105
4.5	Measured HAZ dimensions, clad dimensions, and catchment efficiency for the experimental clad beads	105
4.6	Calculated dimensions and catchment efficiency for the experimental clad beads	106
4.7	Total uncertainty for measured and calculated parameters for bead width, catchment efficiency, and height	107
4.8	Total uncertainty for measured and calculated reinforcement area	116
5.1	Regime classification for low Pr thermocapillary flows [1]	134
5.2	Bead cross sectional measurements used in calculations of characteristic values of thermocapillary flows in this work	138

5.3	Parameters characterizing the heat source and power absorption during laser cladding	140
5.4	Values for the effective heat capacity analysis of a Ni-WC composite clad pool. T_0 is 1692 K for all solid fractions analyzed here.	141
5.5	Chemistry data for the components of the Ni-WC powders used in this analysis	142
5.6	Values for the effective viscosity analysis of a Ni-WC composite clad pool	146
5.7	Effective thermophysical properties for the composite Ni-WC pool used in this analysis of thermocapillary flows	147
5.8	Summary of the dimensionless quantities to characterize thermocapillary flows for typical laser cladding conditions of Ni-WC	147
5.9	Summary of the characteristic values for laser cladding of Ni-WC presented in Section 2.3	150
5.10	Literature surface tension values for nickel and nickel based alloys	166
7.1	Composition of 4145-MOD steel used in preliminary experiments	197
7.2	Transformation temperatures of 4145-MOD	199
7.3	Geometry, mass, and density of 4145 MOD dilatometry samples	213
7.4	Heating rate test values for 4145-MOD dilatometry trials	214
7.5	Composition of steel chemistries from literature used as comparison for 4145-MOD thermophysical properties	225
8.6	Uncertainty analysis for measured laser power	232
8.7	Uncertainty analysis summary for measured laser power	233
8.8	Uncertainty analysis summary for the parameters of Equation (8.22)	234
8.9	Uncertainty analysis summary for Equation (8.22)	235
8.10	Measured 4145-MOD Steel Substrate Diameter D	236
8.11	Uncertainty analysis summary for the parameters of Equation (8.26)	236
8.12	Uncertainty analysis summary for Equation (8.22)	237
8.13	Uncertainty analysis summary for the parameters of Equation (8.30)	238
8.14	Uncertainty analysis summary for Equation (8.30)	239
8.15	Uncertainty analysis summary for the parameters of Equation (8.34)	240
8.16	Uncertainty analysis summary for Equation (8.34)	241
8.17	Uncertainty analysis summary for the parameters of Equation (8.39)	242
8.18	Uncertainty analysis summary for Equation (8.39)	243
8.19	Uncertainty analysis summary for the parameters of Equation (8.43)	244
8.20	Uncertainty analysis summary for Equation (8.43)	246
8.21	Uncertainty analysis summary for the parameters of Equation (8.48)	247
8.22	Uncertainty analysis summary for Equation (8.49)	249
8.23	Uncertainty analysis summary for 4145-MOD thermophysical properties	250
8.24	Uncertainty analysis summary for Equation (8.54)	251
8.25	Preheat measurement summary for the experimental cladding of Ni-WC on 4145-MOD steel	253

8.26	Uncertainty analysis summary for the parameters of Equation (8.59) . . .	254
8.27	Uncertainty analysis summary for Equation (8.59)	256
8.28	Uncertainty analysis summary for the parameters of Equation (2.4) . . .	257
8.29	Uncertainty analysis summary for Equation (2.4)	259
8.30	Uncertainty analysis summary for Equation (2.8)	261
8.31	Uncertainty analysis summary for Equation (2.8)	263
8.32	Uncertainty analysis summary for Equation (4.19)	265
8.33	Uncertainty analysis summary for Equation (4.17)	267
8.34	Uncertainty analysis summary for Equation (4.21)	269

List of Figures

1.1	Left: Large mining component being manipulated with a CNC system relative to a robotic laser assembly. Right: Schematic of a typical coaxial laser system.	2
2.1	Schematic of a cross section of a deposited clad bead from the experiments.	16
2.2	Laser cladding during Bead 3 run.	18
2.3	Cross section of Bead 3 etched with 3% Nital for 5 seconds.	24
2.4	Python script output showing carbide area for Bead 3.	25
2.5	Effect of power on catchment efficiency.	27
2.6	Effect of powder feed rate on catchment efficiency.	28
2.7	Effect of travel speed on catchment efficiency.	29
2.8	Cubic B1-type "rock salt" structure of the WC_{1-x} phase.	33
2.9	Density of WC_{1-x} as a function of C stoichiometry.	35
3.1	Isotherms and temperature profiles for point heat source in a thick plate.	44
3.2	Exact correction factors for y_m as a function of T^* . $f_{y_{m_0,e}}$ is the correction factor for the low T^* regime and $f_{y_{m_0,\infty}}$ for the high T^* regime.	55
3.3	Comparison of the exact correction factors to the calibrated correction factors. The maximum error is below 0.8%.	57
3.4	Error as a function of T^* for $f_{y_{m_0}}$ and $C_3 = 0.865$	58
3.5	Identification of C_3 to minimize the maximum absolute error of $f_{y_{m_0}}$	59
3.6	Effect of laser power on the measured bead width of Ni-WC deposited on a 4145-MOD steel substrate. Powder feed rate and travel speed were held constant at 49.20 g/min and 25.45 mm/s respectively.	69
3.7	Effect of powder feed rate on the measured bead width of Ni-WC deposited on a 4145-MOD steel substrate. Laser power and travel speed were held constant at 3.99 kW and 25.45 mm/s respectively.	69
3.8	Effect of travel speed on the measured bead width of Ni-WC deposited on a 4145-MOD steel substrate. Laser power and powder feed rate were held constant at 3.99 kW and 49.20 g/min respectively.	70
3.9	Comparison of cross section measured bead width to the calculation based on a Rosenthal heat source.	71
3.10	Comparison of stereo photo measured bead width to the calculation based on a Rosenthal heat source.	71

4.1	Photo of the powder cloud showing the powder jet focus at the nozzle working distance for the experimental trials.	84
4.2	Procedural timeline for the cladding experiments.	86
4.3	Laser cladding during the Bead 9 run.	86
4.4	Schematic of a cross section of a deposited clad bead from the experiments.	88
4.5	Schematic of the laser cladding process without powder.	89
4.6	Left: Dimensionless surface isotherm showing the location of maximum width for Bead 3. Right: Dimensionless centreline isotherm showing the maximum depth location for Bead 3. Both figures use the Bead 3 parameters from Table 4.2.	95
4.7	Schematic of heat conduction through the bead reinforcement during laser cladding.	95
4.8	Comparison of the calculated σ to burn marks made on an acrylic substrate. The working distance was 19 mm matching the experimental trials.	98
4.9	Left: Overlap of the powder cloud with the beam spot approximation for the melting isotherm. Right: Overlap of the powder cloud with the experimental matrix centre point melting isotherm (Bead 3) calculated from this work. The dimensions are to scale with $\hat{\sigma} = 1.62$ mm, $\widehat{y}_{m,b} = 1.69$ mm, and $\widehat{r}_p = 1.77$ mm.	99
4.10	Proposed elliptical approximation of the catchment area compared with a Rosenthal isotherm overlapping the projected powder cloud area.	101
4.11	Stereomicrograph of the Bead 3 surface finish of the clad used to calculate an average width over the visible length of the bead.	103
4.12	Cross section of Bead 3 etched with 3% Nital for 5 seconds.	104
4.13	Python script output showing carbide area for Bead 3.	104
4.14	Comparison of measured bead width to the calculation based on a Gaussian heat source.	108
4.15	Comparison of measured catchment efficiency to the calculated catchment efficiency predicted by Equation (4.16).	109
4.16	Comparison of measured height to the calculated height from Equation (4.19).	110
4.17	Comparison of the measured bead reinforcement area to parabola and circle area approximations.	115
4.18	Temperature dependence of 4145-MOD steel thermal conductivity (top left), density (top right), heat capacity (bottom left), and thermal diffusivity (bottom right) showing effective values for the HAZ and clad melt isotherms.	118
4.19	Left: Temperature dependence of Ni thermal conductivity. Right: WC thermal conductivity as a function of temperature. Both graphs show effective properties for the calculated HAZ (1228 K) and melting isotherm.	119

5.1	Left: Rivas system coordinates and problem configuration [1]. Right: Laser cladding pool showing the largely above surface pool geometry of the process.	131
5.2	Cross section of the solidified Ni-WC clad from this work etched with 3% Nital for 5 seconds.	137
5.3	Python script output showing carbide area for the Ni-WC laser clad in this analysis.	138
5.4	Global caustic of the CO ₂ laser beam in this work. Spatial units are in mm, and the relative power intensity (vertical axis) corresponds to a total laser power of 4 kW laser power.	139
5.5	The effect of carbide volume fraction on the effective viscosity of the molten pool.	146
5.6	Process map for thermocapillary flows. The dashed lines indicate a boundaries of the Rivas' regimes defined by the conditions in Table (5.1). The shaded area in the plot corresponds to the A=0.4, which applies to all the cases considered here. The dot labelled " $f_{v_{cb}} = 0$ " corresponds to the conditions Pr = 0.03 and Re _σ = 125405. The dot labelled " $f_{v_{cb}} = 0.386$ " corresponds to the conditions Pr = 0.15 and Re _σ = 6779. The dot labelled " $f_{v_{cb}} = 0.5$ " corresponds to the conditions Pr = 0.47 and Re _σ = 799. . .	149
5.7	Second moment of the beam profile results for the CO ₂ laser in this work. Units are in mm, and the y to x scale is 5:1 to emphasize the divergence angle ϕ	153
5.8	Molar enthalpy of the Ni-Cr-B-Si matrix used in this work as a function of temperature from ThermoCalc TM	155
5.9	Specific heat capacity of Ni-Cr-B-Si matrix used in this work as a function of temperature showing the effective value used in this work.	156
5.10	Specific heat capacity of WC as a function of temperature showing the effective value used in this work.	157
5.11	Heat capacity of WC as a function of temperature for different stoichiometries of the compound.	158
5.12	Experimental data for viscosity of pure nickel as a function of temperature summarized by Iida and Guthrie (Figure 6.27) [34].	159
5.13	Viscosity of pure nickel as a function of temperature showing the effective value used in this work.	162
5.14	Thermal conductivity as a function of temperature showing the effective value for the Ni-Cr-B-Si powders used in this work.	164
5.15	Thermal conductivity as a function of temperature showing the effective value for the tungsten carbide powders used in this work.	165
5.16	Surface tension coefficient of Ni-Si binary alloys [36]. Orginal work by Shergin <i>et al.</i>	167
5.17	Density of liquid nickel as a function temperature showing the effective value for ρ_m used in this work.	170

5.18	Thermal expansion of WC as a function temperature for the a-axis of the crystal.	171
5.19	Density of WC as a function temperature showing the effective value for ρ_c used in this work.	172
7.1	Mills model prediction for 4145-MOD thermal conductivity.	201
7.2	Comparison of k_{eff} , Mills model, and literature values of 4145-MOD thermal conductivity.	202
7.3	Molar enthalpy of 4145-MOD as a function of temperature from ThermoCalc TM	203
7.4	Specific heat capacity of 414- MOD calculated from Equation (7.4).	205
7.5	Zoomed view of specific heat capacity of 4145-MOD as a function of temperature calculated from Equation (7.4).	206
7.6	Effective specific heat capacity of 4145-MOD determined from ThermoCalc TM	207
7.7	Specific heat capacity of 4145-MOD compared to similar steel heat capacities found in literature.	208
7.8	Molar volume of 4145-MOD as a function of temperature modelled in ThermoCalc TM	210
7.9	Density of 4145-MOD as a function of temperature modelled in ThermoCalc TM	211
7.10	Heating rate effects on the mean linear coefficient of thermal expansions of 4145-MOD as a function of temperature.	215
7.11	4145-MOD density temperature dependence calculated using Equation (7.10).	216
7.12	Comparison of 4145-MOD densities to similar chemistries in literature.	217
7.13	Thermal diffusivity of 4145-MOD calculated using Equation (7.11).	219
7.14	Comparison of α_{eff} to thermal diffusivity of alloys having similar chemistries to 4145-MOD.	220

Chapter 1

Introduction

1.1 Introduction

Lasers for industrial welding and coating applications have become increasingly important in early 21st century as an alternative to traditional plasma arcs [1–3]. The application of weld coatings for the purposes of modify surface characteristics or dimensional build-ups and repair is termed “cladding”. Laser cladding is an overlay deposition technology where metallic or composite based coatings are metallurgically bonded to a substrate in near-net shape geometry using a laser heat source. These value added coatings, commonly referred to as “clads” or “overlays”, are applied for surface modification for improved wear or corrosion resistance or for dimensional repairs of high value components. Typical clads are on the order of 4 to 5 millimetres in width and one millimetre in height, and by overlapping clad beads it is possible to create protective material coatings encompassing entire surfaces. Laser cladding relies on a highly localized laser heat source to melt a substrate creating a liquid melt pool similar to traditional arc welding processes. A powder substrate is supplied to the pool from a lateral (from the side) or coaxial (along the beam axis) feed system using a carrier gas. The solid powder interacts with the beam and melts as it penetrates the molten surface of the clad pool. The substrate is manipulated using computer numeric controlled (CNC) or robotic systems, and as the

stationary beam traverses across the moving surface, the molten pool solidifies creating the clad. An overview of a coaxial robotic laser assembly (the focus of this analysis) and a schematic of the process are shown in Figure (1.1).



Figure 1.1: Left: Large mining component being manipulated with a CNC system relative to a robotic laser assembly. Right: Schematic of a typical coaxial laser system.

Laser cladding offers a unique combination of low heat input, fast solidification rates, small thermal distortions, and high welding speeds [4, 5]. Particularly attractive to clad coatings is the small fusion zone of the process, which can yield micron sized heat affected zones with a minimum dilution of the substrate. The lack of mixing between different layers helps maintain the integrity and performance of the clad, which is often of dissimilar metal composition. For wear applications, composite clad materials consisting of a matrix phase interspersed with a secondary ceramic phase have become the leading material systems for abrasion based wear applications [1]. These material systems can be split into two groups: non melting secondary phase systems and precipitating secondary phase systems. The non-melting secondary phase group relies on the low heat input of the laser process to minimize dissolution to the secondary reinforcing particles that are present in their final form in the feed powder. A key example of this is the nickel-tungsten carbide (Ni-WC), which contains hard, ceramic WC particles embedded in the nickel-

based matrix. This system is the focus of the experimental work in this thesis. The precipitating secondary phase group takes advantage of the fast cooling characteristics of the process to promote fine dispersion and uniform distribution of the reinforcing phase that forms in-situ during solidification. An example of this solidification mechanism is found in chromium carbide overlays with the primary M_7C_3 carbides nucleating during solidification. Common material systems for hardfacing and component refurbishment are nickel based super alloys such as alloy 625 and 718, cobalt based super alloys, and martensitic stainless overlays in addition to the Ni-WC and chromium based overlays discussed prior.

The geometry of the deposited laser clad bead is a key factor determining important parts of the process such as the number of overlapping beads required to coat entire surfaces and the number of layer-on-layer passes to target a specific thickness. In the case of excessive deposited thickness, post-clad grinding operations are required, which are time consuming and costly particularly for wear resistant material systems. Predictive tools for the bead geometry exist in literature with authors taking a variety of numerical [3, 5–14], analytical [4, 15–18], regression/experimental [15, 19–21], neural network [22], and combined approaches [23]. Despite the enormous promise of bead geometry models for process optimization, the industry at large has not yet benefited greatly from a scientific approach to laser materials processing.

The primary challenge in the modelling of clad geometry is obtaining a balance between complexity and application in practice. Analytical and experimental models can be more easily applied by practitioners and engineers in the field but are often oversimplified to the point where they fail to make predictions outside of the conditions from which they are generated. Typically, this approach reduces the mathematical difficulty by neglecting complex interactions between the laser beam, powder particles, and substrate. The most common assumptions are neglecting latent heat of phase transformations, mod-

elling Gaussian beam shape and power distribution, ignoring powder preheat due to beam attenuation, instantaneous pool mixing, and zero powder mass loss. While these simplifications can provide practical solutions, they quickly break down at industrially relevant conditions as the aforementioned assumptions are no longer valid.

Increased modelling complexity comes from consideration of the simplifying assumptions of analytical models of the past. This complexity has necessitated finite element and fluid flow models to account for material thermophysical properties as a function of temperature, latent heats, solid-liquid interactions in the molten pool, particle preheats, and complex laser power density, and thermocapillary flows. This approach requires considerations of coupled energy, mass, and momentum equations, but these models remain computationally challenging and complex. Such numerical approaches require experts in the fields of heat transfer, mass transfer, fluid flow, and computer simulation. Current state of the art numerical models are typically validated in a particular range and for a particular material system; however, rarely does this range correspond to relevant levels of industrial cladding processes. One of the greatest shortfalls of modern modelling is the inability to make generalizations outside a single material system. The validation step of most models is limited to a single material case. The narrow scope of this validation does not lend itself to widespread applicability, and conclusions drawn from each study must be considered on a case to case basis.

The current state of laser clad modelling is stuck between simplistic analytical models and overly complex numerical simulations. No intermediate solution exists that is simultaneously easy to use, meaningful, and general simultaneously. As a result, the industry continues to use a primarily trial and error approach to cladding procedure development. Limited to no use of predictive tools for bead geometry are implemented; instead, operators rely on experience to make in-process manipulations based on the appearance of the molten bead and measurement of deposited material. The operator of a laser system

controls critical parameters such as laser power, powder feed rate, and travel speed within prescribed limits until they obtain a product that meets dimensional and quality control requirements. The variability and uncertainty in clad geometry is largely the result of a lack of understanding of individual parameter effects on the process, where often even the direction of necessary adjustments is unknown. This complexity is the result of the interdependence of the multiple process parameters on the physical mechanisms governing clad geometry simultaneously. For example, beam power and powder flow rate are often increased simultaneously to maximize the rate of coating deposition. Greater particle presence in the beam increases scattering caused by absorption and reflection of the incident beam prior to reaching the substrate. Beam power is increased to balance this effect, which also increases the energy absorption of the powder cloud as the powders are preheated prior to reaching the clad pool. It has been observed that there is a limit to powder flow rate until increases in beam power cannot compensate and create a stable pool. This sudden change in behaviour of the cladding process highlights the complexity and coupling of the phenomena involved. Many such interdependencies exist in laser cladding making direct isolated parameter-output relations difficult from theory.

The new understanding of this work comes from both the implementation of scaling principles to the field of laser clad modelling and the application of fundamental engineering principles to develop meaningful, general process models. For the scaling analysis, dimensionless groups representing the dominant phenomena under industrially relevant conditions are identified. Dimensional analysis helps reduce the problem complexity from a large number of process variables down to the meaningful groups of parameters on which the problem truly depends. Scaling approaches such as those by Rivas [24], Roy [25], Fuerschbach [26], and Mendez [27–29] have addressed the shortcomings of simpler and practical approaches by considering multiple phenomena through dimensionless groups. These authors have shown that this approach is capable of making meaningful predic-

tions boundary layers, peak pool temperatures, and regimes of dominant physics during welding processes. This approach is implemented in this work to reduce the complexity of the cladding process into a set of useful and reliable heuristics obtained from knowledge of the physical principles involved, not just casual observation. The result is new insight into the fundamental heat transfer, mass transfer, and fluid flow mechanisms in laser cladding processes. The practical implications are the reduction of qualification times for new material systems, lessened post-clad machining times, and the identification of scientifically determined process windows. Substantial benefits in the form of improved productivity and reduced costs in the production of laser clad overlays can be realized.

1.2 Objectives

The main objective of this research project is to illustrate that the cross sectional geometry of a laser clad weld bead can be predicted in a general, simple, and accurate way. In order to achieve this goal, the following objectives have been established:

- Establish a mathematical framework to identify the laser clad bead width from fundamental heat transfer equations.
- Propose an expression for the maximum height of a laser clad bead using mass conservation principles.
- Apply the developed models to experimental tests to illustrate its applicability for a range of laser processing conditions.
- Evaluate the role of fluid flow in the heat transfer of a laser clad pool for typical cladding conditions.

These objectives have been evaluated for the composite Ni-WC system in this thesis, but can be extended in theory to any alloy system using the expressions developed in this work.

1.3 Thesis Outline

This thesis consists of 5 chapters (not including the introduction) focusing on achieving the above objectives. An brief outline of each chapter is included below.

- Chapter (2) presents a new definition for mass capture efficiency (colloquially “catchment efficiency”) of composite weld overlays. The proposed equations are capable of distinguishing between the catchment of each constituent in a two component powder feed. The results are then used to calculate catchment efficiency of Ni-WC laser clad overlays deposited under a variety of process conditions.
- Chapter (3) outlines a new methodology that proposes direct predictions of maximum isotherm width from Rosenthal’s thick plate solution. The results of this theoretical heat transfer analysis are then applied to the laser cladding experiments performed in Chapter (2) to predict bead width from the melting isotherm.
- Chapter (4) presents the keystone publication of the thesis, which presents the prediction of bead width from a numerical solution to the dimensionless Gaussian heat source equation proposed by Eagar [30]. This section also presents a new model for catchment efficiency, which can be predicted from knowledge of the powder cloud geometry and isotherm width, along with a prediction of maximum bead height from fundamental engineering principles. The models and procedures developed

here are then applied to the experiments of Chapter (2).

- Chapter (5) characterizes the role of convection in the heat transfer of Ni-WC alloys deposited using laser cladding processes. The methodology employed here is based on an existing framework presented by Rivas and Ostrach for molten metals, which applies to the Ni-WC system in this work [24].
- Chapter 6 summarizes the major findings of the thesis and presents concrete conclusions. A future work section is also included to address remaining issues and areas of potential future development to build on the results of this work.

1.4 References

- [1] P.F. Mendez, N. Barnes, K. Bell, S. D. Borle, S. S. Gajapathi, S. D. Guest, H. Izadi, A. Kamyabi Gol, and G. Wood. Welding Processes for Wear Resistant Overlays. *Journal of Manufacturing Processes*, 16:4–25, 2013.
- [2] E. Toyserkani, A. Khajepour, and S. Corbin. *Laser Cladding*. CRC Press LLC, 2005.
- [3] A.F.A. Hoadley and M. Rappaz. A Thermal Model of Laser Cladding by Powder Injection. *Metallurgical Transactions B*, 23B(12):631–642, 1992.
- [4] R. Colaço, L. Costa, R. Guerra, and R. Vilar. A Simple Correlation Between the Geometry of Laser Cladding Tracks and the Process Parameters. In *Laser Processing: Surface Treatment and Film Deposition*, pages 421–429. Kluwer Academic Publishers, Netherlands, 1996.
- [5] V.M. Weerasinghe and W.M. Steen. Laser Cladding of Blown Powder. *Metal Construction*, 19:1344–1351, 1987.
- [6] A.J. Pinkerton and L. Lin. Modelling the Geometry of a Moving Laser Melt Pool and Deposition Track via Energy and Mass Balances. *Journal of Physics D: Applied Physics*, 27:1885–1895, 2004.
- [7] E.H. Amara, F. Hamadi, L. Achab, and O. Boumia. Numerical Modelling of the Laser Cladding Process using a Dynamic Mesh Approach. *Journal of Achievements in Materials and Manufacturing Engineering*, 15:100–106, 2006.

- [8] P. Farahmand and R. Kovacevic. An Experimental-Numerical Investigation of Heat Distribution and Stress Field in Single- and Multi-Track Laser Cladding by a High-Power Direct Diode Laser. *Optics and Laser Technology*, 62:154–168, 2014.
- [9] A. Fathi, E. Toyserkani, A. Khajepour, and M. Durali. Prediction of Melt Pool Depth and Dilution in Laser Powder Deposition. *Journal of Applied Physics D: Applied Physics*, 39:2613–2623, 2006.
- [10] E. Toyserkani, A. Khajepour, and S. Corbin. Three-Dimensional Finite Element Modeling of Laser Cladding by Powder Injection: Effects of Powder Feedrate and Travel Speed on the Process. *Journal of Laser Applications*, 15(153):1306–1318, 2003.
- [11] L. Han, F.W. Liou, and K.M. Phatak. Modelling of Laser Cladding with Powder Injection. *Metallurgical and Materials Transactions B*, 35B:1139–1150, 2004.
- [12] Y.S. Lee, M. Nordin, S.S. Babu, and D.F. Farson. Influence of Fluid Convection on Weld Pool Formation in Laser Cladding. *Welding Journal*, 93:292–300, 2014.
- [13] M. Picasso, C. F. Marsden, J. D. Wagnière, A. Frenk, and M. Rappaz. A Simple but Realistic Model for Laser Cladding. *Metallurgical and Materials Transactions B*, 25B:281–291, 1994.
- [14] I. Tabernerero, A. Lamikiz, S. Martinez, E. Ukar, and L.N. López de Lacalle. Geometric Modelling of Added Layers by Coaxial Laser Cladding. *Physics Procedia*, 39:913–920, 2012.
- [15] H. E. Cheikh, B. Courant, J.-Y. Hascoët, and R. Guillén. Prediction and Analytical Description of the Single Laser Track Geometry in Direct Laser Fabrication from Process Parameters and Energy Balance Reasoning. *Journal of Materials Processing Technology*, 212:1832–1839, 2012.
- [16] C. Lalas, K. Tsirbas, K. Salonitis, and G. Chryssolouris. An Analytical Model of the Laser Clad Geometry. *International Journal of Advanced Manufacturing Technology*, 32:34–41, 2007.
- [17] F. Lemoine, D. Grevey, and A. Vannes. Cross-Section Modeling Laser Cladding. pages 203–212. Proceedings of SPIE - The International Society for Optical Engineering, December 1993.
- [18] F. Lemoine, D. Grevey, and A. Vannes. Cross-Section Modeling of Pulsed Nd:YAG Laser Cladding. In *Laser Materials Processing and Machining*, volume 2246, pages 37–44. Proceedings of SPIE - The International Society for Optical Engineering, November 1994.

- [19] J.P. Davim, C. Oliveira, and A. Cardoso. Predicting the Geometric Form of Clad in Laser Cladding by Powder Using Multiple Regression Analysis (MRA). *Materials and Design*, 29:554–557, 2008.
- [20] O. Nenadl, V. Ocelík, A. Palavra, and J.Th.M De Hosson. The Prediction of Coating Geometry from Main Processing Parameter in Laser Cladding. *Physics Procedia*, 56:220–227, 2014.
- [21] U. de Oliveira, V. Ocelík, and J. Th. M. De Hosson. Analysis of Coaxial Laser Cladding Processing Conditions. *Surface and Coatings Technology*, 197:127–136, 2005.
- [22] D. Ding, Z. Pan, D. Cuiuri, H. Li, S. van Duin, and N. Larkin. Bead Modelling and Implementation of Adaptive MAT Path in Wire and Arc Additive Manufacturing. *Robotics and Computer-Integrated Manufacturing*, 39:32–42, 2016.
- [23] P. Peyre, P. Aubry, R. Fabbro, R. Neveu, and A. Longeut. Analytical and Numerical Modelling of the Direct Metal Deposition Laser Process. *Journal of Applied Physics D: Applied Physics*, 41:1–10, 2008.
- [24] D. Rivas and S. Ostrach. Scaling of Low-Prandtl-Number Thermocapillary Flows. *International Journal of Heat and Mass Transfer*, 35(6):1469–1479, 1992.
- [25] G. G. Roy, R. Nandan, and T. Debroy. Dimensionless Correlation to Estimate Peak Temperature During Friction Stir Welding. *Science and Technology of Welding and Joining*, 11(5):606–608, 2006.
- [26] P. W. Fuerschbach and G. R. Eisler. Determination of Material Properties for Welding Models by Means of Arc Weld Experiments. Number 5, pages 15–19. Trends in Welding Research, Proceedings of the 6th International Conference, 2002.
- [27] P. F. Mendez. Synthesis and Generalization of Welding Fundamentals to Design New Welding Technologies: Status, Challenges and a Promising Approach. *Science and Technology of Welding and Joining*, 16:348–356, 2011.
- [28] Karem E. Tello, Satya S. Gajapathi, and P. F. Mendez. Generalization and Communication of Welding Simulations and Experiments using Scaling Analysis. pages 249–258. Trends in Welding Research, Proceedings of the 9th International Conference, ASM International, 2012.
- [29] P.F. Mendez and T.W. Eagar. Order of Magnitude Scaling: A Systematic Approach to Approximation and Asymptotic Scaling of Equations in Engineering. *Journal of Applied Mechanics*, 80(1):1–9, 2012.
- [30] T.W. Eagar and N.S. Tsai. Temperature Fields Produced by Traveling Distributed Heat Sources. *Welding Journal*, 62(12):346–355, 1983.

Chapter 2

Dissaggregated Metal and Carbide Catchment Efficiencies in Laser Cladding of Nickel-Tungsten Carbide

2.1 Introduction

Powder based welding processes such as laser cladding or plasma transfer arc welding (PTAW) are the industry standard for depositing tungsten-carbide based wear resistant coatings [1]. The dimensions, performance, and cost of the final coating or “clad” are directly dependent on the amount of free flight powder that adheres to the molten surface of the clad pool contributing to the clad build up [1–3]. Not all of the powders that exit the cladding head end up as part of the clad bead; the fraction of powders that do is termed the “catchment efficiency” by practitioners.

The focus of this analysis is the efficiency in laser deposition of nickel tungsten carbide (Ni-WC) overlays. The Ni-WC powder blend contains two parts: a primarily Ni powder (referred to hereafter as metal powder), which solidifies to create the matrix and ceramic tungsten carbide particles, which serve as the wear resistant phase in the overlay. The carbides must remain unmelted during the cladding process, contrary to most other wear

protection alloys such as chromium carbide where the reinforcing phase forms in-situ during solidification. Although the microstructural aspects of the Ni-WC are not a focus of this analysis, it is important to note that the WC symbol in Ni-WC does not directly refer to the stoichiometric 1:1 form of the carbide only and is used interchangeably with WC, W_2C and the non-stoichiometric WC_{1-x} . The carbide form used in this analysis is the non-stoichiometric WC_{1-x} .

There have been various contributions to the understanding of catchment efficiency in literature, which can be grouped into two categories: models of catchment efficiency and experimental exploration of laser parameter to optimize efficiency.

Among models of efficiency, Picasso *et al.* developed a numerical algorithm to compute powder efficiency accounting for the angular dependence of laser power absorption and melt pool shape based on a Gaussian heat distribution [4]. Lin and Steen presented a model of efficiency based on the geometry of the powder stream at the nozzle focus point, molten pool, and the degree of overlap between the powder stream and molten pool [5]. Frenk *et al.* proposed a model of efficiency for off-axis laser cladding with a theoretical maximum mass efficiency of 69% that was experimentally validated [6]. Partes studied the effects of melt pool geometry and nozzle alignment on catchment efficiency taking into account particle time of flight and surface melting under the beam [7].

Researchers that have studied parameter optimization for laser cladding of homogeneous alloys include Oliviera *et al.* who analyzed the effect of laser power, powder feed rate, and substrate travel speed on powder efficiency and proposed experimentally determined correlations to fit 316 L stainless steel cladding trials [8]. Gremaud *et al.* determined the optimal efficiency for thin walled structures made of single stacked laser clad beads. This work explored the effect of travel speed and powder feed rate on efficiency for a variety of alloys [9]. A select few researchers have also studied the efficiency of laser cladding of Ni-WC.

Powder efficiency in Ni-WC laser cladding is relatively unexplored. Zhou *et al.* studied the effect of laser spot dimensions with laser induction hybrid cladding on efficiency of Ni-WC coatings, but did not directly report values for efficiency. Increases in bead width and height were qualitatively correlated to increased capture efficiency [10]. Angelastro *et al.* optimized the process parameters of power, powder feed rate, and travel speed for a multilayer clad of Ni-WC with Co and Cr additions reporting only an overall value for deposition efficiency [11].

Of the researchers who have measured and modelled efficiency most have used homogeneous single component powder feeds, and for those who have directly worked with Ni-WC none have discriminated between components. This work presents for the first time a detailed analysis of individual component efficiencies for a mixed powder feed, linking the mass capture of two types of immiscible powders to measurable quantities of the process and the cross section of the deposited clad. In this work, laser power, powder feed rate, and travel speed are varied to study the effects on carbide and metal powder catchment efficiency independently.

2.2 List of Symbols

Symbol	Unit	Description
a_{B1}	m	Lattice parameter of the cubic WC_{1-x} unit cell
A_{bD}	m^2	Dilution area of the clad bead
A_{bR}	m^2	Reinforcement area of the clad bead
A_{bT}	m^2	Total clad area
η_m	1	Combined catchment efficiency of both powders
η_{m_c}	1	Catchment efficiency of the carbide only
η_{m_m}	1	Catchment efficiency of the metal powders only
ϵ	1	Total uncertainty
$f_{m_{c_p}}$	1	Weight fraction of carbide in the powder feed
$f_{m_{m_p}}$	1	Weight fraction of metal powders in the powder feed
$f_{v_{c_b}}$	1	Volume fraction of carbide in the clad bead
m_c	kg	Mass of WC_{1-x} unit cell
m'_{c_b}	$kg\ m^{-1}$	Linear mass density of carbide in the clad bead
m_{c_p}	kg	Mass of carbide in the powder feed
m'_{c_p}	$kg\ m^{-1}$	Linear mass density of carbide in the powder feed
m_{m_p}	kg	Mass density of metal powder in the powder feed
m'_{m_p}	$kg\ m^{-1}$	Linear mass density of metal powder in the powder feed
\dot{m}_p	$kg\ s^{-1}$	Total mass transfer rate of the powder feed
m_p	kg	Total mass of the powder feed
M_C	$kg\ mol^{-1}$	Molar mass of carbon
M_W	$kg\ mol^{-1}$	Molar mass of tungsten
N_A	$atoms\ mol^{-1}$	Avegado's number
N_C	atoms	Number of carbon atoms in the WC_{1-x} unit cell
N_W	atoms	Number of tungsten atoms in the WC_{1-x} unit cell
q	W	Laser power
ρ_c	$kg\ m^{-3}$	Density of the carbide
ρ_m	$kg\ m^{-3}$	Density of the metal powders
t_p	s	Time for the powder collection test
U	$m\ s^{-1}$	Substrate travel speed
V_c	m^3	Volume of the WC_{1-x} unit cell
W_f	1	Weight fraction
$1 - X$	1	Stoichiometry of carbon phase in the WC_{1-x} phase

2.3 Experimental Setup

2.3.1 Laser Cladding Equipment

For the experimental trials performed here, the power source was a Rofin Sinar HF860 6.0 kW CO₂ laser assembly with water cooled copper mirror optics. The focal distance of the final beam focusing mirror was 345 mm (13.595”), and cladding was performed 19 mm (0.75”) out of focus beyond the focal point conforming to typical industrial practices. A GTV GmbH & Co. Twin 2/2 disk powder feeder was used to meter powder to the cladding nozzle with a set Ar carrier gas flow rate of 6.5 L/min. The cladding nozzle was a coaxial Fraunhofer Coax-8 production nozzle capable of feed rates up to 150 g/min through a series of 50 equally spaced ports between two concentric conical guides. Ar shield gas flow rate was set at 45 cfh. The substrate positioning system is a CNC controlled x-y lathe bed with a mounted four jaw chuck headstock and tailstock spindle support. Surface rotation speeds were programmed into the CNC system for a given diameter substrate. For the precision equipment used, it was considered that the actual rotation speed matched its set point.

2.3.2 Powder Feed

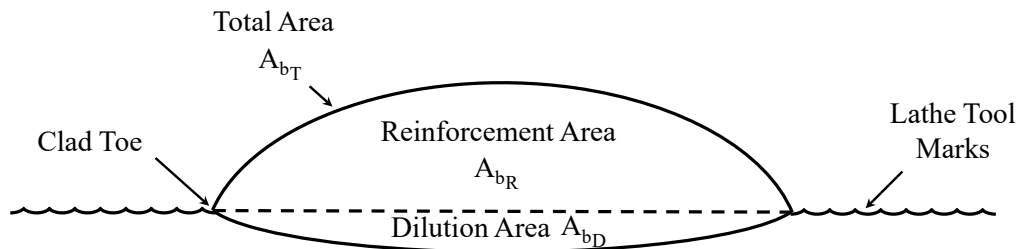
The powder feed used in this analysis was a mixture of cast spherical fused tungsten carbide and a Ni-Cr-B-Si blend of metals, which comprise the metal matrix in the deposited overlay. The carbide chemistry reported by the powder supplier was 3.8 wt% C and the balance W, which corresponds to a stoichiometry of WC_{0.6}. The two component powders were mixed together by the sponsor in 60%-40% weight fractions of carbide to metal powder respectively. Size range, reported manufacturer hardness range, weight fractions, and densities are listed in Table 2.1. Density of the carbide is analyzed in Appendix 2.1.

Table 2.1: Properties of powders used in the experiments

Component	Size Range (μm)	Expected Hardness Range After Deposition (HV)	Weight Fraction W_f (%)	Density ρ (kg/m^3)
Carbide Powder	45-106	2700-3500	62.60	16,896
Metal Powder	53-150	425	37.40	8100

2.3.3 Sample Preparation and Analysis

Individual beads were sectioned using a wet saw, mounted, polished to a $0.04 \mu\text{m}$ finish, and etched for 5 seconds with 3% Nital to reveal the HAZ. Photomicrographs of the sample cross sections were stitched together to create panoramas of the total bead area and HAZ using Adobe PhotoshopTM. The reinforcement area A_{bR} , dilution area A_{bD} and total area A_{bT} were measured by analysing pixels of the selected region and converting pixel measurements to an actual area using the image scale bar calibrated to a known

**Figure 2.1:** Schematic of a cross section of a deposited clad bead from the experiments.

The area fraction of the carbide was measured using an internally developed PythonTM script that identified the carbides based on colour contrast with the matrix. The clad

area was isolated from the picture and the contrast was adjusted using PhotoshopTM to improve the distinction between the two phases.

2.3.4 Cladding Procedure

The test clads were performed on a 254 mm long, 20.3 mm thick, 165 mm outer diameter 4145-MOD cylindrical steel substrate. The loaded sample was rotationally centered to within 25 μm (0.001") using an alignment dial indicator. The surface of the bearing was prepared with an initial acetone wash to remove any oil or grease followed by manual grinding between passes to remove any remaining debris. Conforming to the sponsor's existing direct carbide application procedures, a preheat of 533 K was applied to the rotating substrate using a propane torch. The temperature was checked before each pass using a touch thermocouple at the 0°, 90°, 180°, and 270° positions on the cylinder along the rotation direction. These temperature measurements were performed along the centreline of the upcoming bead. Some variation in preheat temperatures was observed across the four measured points, but values within 25°C of each other and the target preheat temperature were taken as acceptable.

The laser power, powder feed, and substrate rotation were programmed to begin simultaneously with the shutter closed to momentarily delay the start of cladding and allow the parameters time to ramp up to test levels. After a 5 second waiting period, the shutter was opened and the cladding began. A 360° bead was deposited with no pitch followed immediately by a 2 mm pitch and 180° overlapping bead without interruption. The overlapping beads were included to provide bead-on-bead samples for future analysis and are not included as part of this study. Beads were placed 51 mm (2") away from the edges of the coupon to prevent heat accumulation effects. A 12.5 mm (0.5") gap between bead centres was left to allow adequate room for sectioning. Once the half circumference

overlapping bead was finished, the shutter was closed effectively stopping the clad process while the laser power and powder feed rate ramped down. The travel speed was set to shift rapidly to the maximum value of $25^\circ/\text{s}$ to complete the second full rotation and place the starting point directly beneath the nozzle. Figure (2.2) shows an example of the in-process Ni-WC clad deposit.

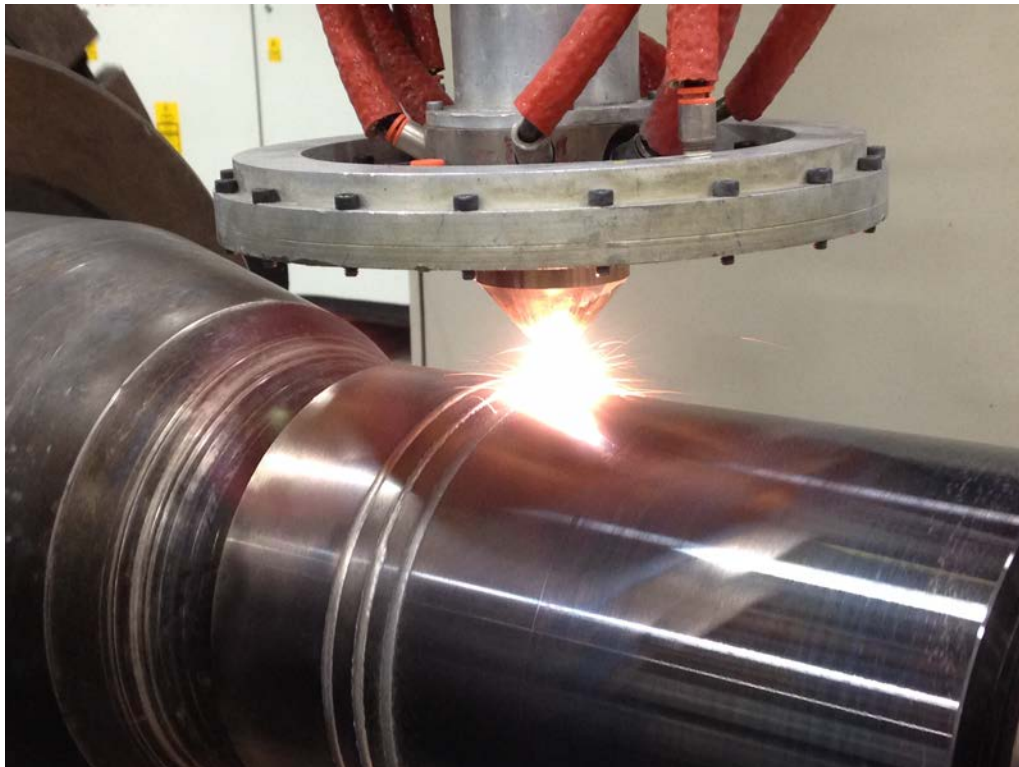


Figure 2.2: Laser cladding during Bead 3 run.

The laser power and powder feed rates were calibrated at the beginning of the experiment and before trials with a parameter change to confirm levels at the substrate. Laser power was measured using a 10 kW Comet 10K-HD power probe, which acts as a copper calorimeter for 1 second laser exposures. Feed rate was measured by manually capturing the powder flow for $t_p = 2$ min, measuring the accumulated mass, and reporting a per minute average rate. This calibration is necessary to link the rotation speed of the disk

feeder to actual mass flow rates. Travel speed was confirmed by extracting the calibrated positional data output by the CNC for each trial at the end of testing.

2.3.5 Experimental Matrix

The parameters tested were laser power, powder feed rate, and travel speed. These parameters were chosen because there is direct control over them, and they are known to have a large influence on the laser cladding operation. These are the main parameters used to design cladding procedures and maintain quality during the cladding operation.

A modified fractional factorial design was used with the three aforementioned process variables. The test matrix centre point (Bead 3) was selected to represent the industrial levels. Each factor was given 5 levels totalling 13 experiments having the common centre point. Interaction effects between parameters cannot be assessed with the experimental matrix used, but these interactions do not affect the conclusions obtained. Additional testing to analyze combined effects and repetition at each parameter level was not possible due to the nature of using industrial production equipment for testing and allotted experiment time limited to a single day. The experimental design test run order was randomized to eliminate procedural bias. This was done by assigning each trial a randomly generated number and arbitrarily sorting low to high. Recorded test measurements of each parameter are shown in Table 2.2.

Table 2.2: Experimental matrix for cladding of Ni-WC onto a 4145-MOD substrate for all beads. Target preheat was 260 °C (500 °F)

Bead Number	Laser Power q (kW)		Powder Feed Rate \dot{m}_p (g/min)		Target Travel Speed U (mm/s)		Average Temperature (°C)
	Target	Measured	Target	Measured	Target	Measured	Measured
Bead 1*†	5.0	4.98	50	49.20	25.40	25.45	257
Bead 2*	3.0	3.09	50	49.20	25.40	25.45	257
Bead 3*	4.0	3.99	50	49.20	25.40	25.45	261
Bead 4	4.0	3.99	50	49.20	19.05	19.09	258
Bead 5†	4.0	3.99	30	28.80	25.40	25.45	268
Bead 6†	4.0	3.99	50	49.20	31.75	71.81	264
Bead 7*	4.5	4.54	50	49.20	25.40	25.45	263
Bead 8*	3.5	3.53	50	49.20	25.40	25.45	264
Bead 9*	4.0	3.98	50	49.20	12.70	12.73	263
Bead 10†	4.0	3.98	60	62.95	25.40	25.45	264
Bead 11†	4.0	3.98	40	42.25	25.40	25.45	264
Bead 12	4.0	3.98	50	49.20	38.10	38.18	267
Bead 13†	4.0	3.98	70	68.30	25.40	25.45	263

* Laser power measurement performed immediately before test.

† Powder feed rate measurement performed immediately before test.

2.4 Determination of Catchment Efficiency

The derivations for carbide, metal powder, and total catchment efficiency are presented as functions of the powder densities, compositions, process feed rates and velocities, and area fractions in the solidified clad bead.

2.4.1 Carbide Powder Efficiency

Carbide efficiency is the ratio of mass of carbide in the bead to mass of carbide in the powder feed:

$$\eta_{m_c} = \frac{m'_{cb}}{m'_{cp}} \quad (2.1)$$

where η_{m_c} is the carbide catchment efficiency (1), m'_{c_b} is the linear mass density of carbide in the clad bead (kg/m), and m'_{c_p} is the linear mass density of carbide in the powder feed (kg/m). The linear mass density of carbide in the bead is given by:

$$m'_{c_b} = f_{v_{c_b}} A_{b_T} \rho_c \quad (2.2)$$

where $f_{v_{c_b}}$ is the volume fraction of carbide in the bead (1), A_{b_T} is the total cross sectional area of the bead (m²), and ρ_c is the density of the carbide (kg/m³). $f_{v_{c_b}}$ and A_{b_T} are measured from the image cross section, and ρ_c is calculated from crystallographic analysis of the unit cell shown in Appendix 2.1 . Equation (2.2) is valid when the distribution of carbides is isotropic, and the volume fraction of carbides is the same as the area fraction of any cross section. The total cross sectional area of the bead A_{b_T} is subdivided into the reinforcement area A_{b_R} above the surface level as a result of mass addition from the process, and the dilution area A_{b_D} due to mixing of the steel substrate and molten metal powders to create a metallurgical bond. These areas are shown in Figure (2.1). A_{b_T} appears in Equation (2.2) to account for carbides that can settle below the surface during solidification. In laser cladding processes, A_{b_D} is small compared to A_{b_R} , typically less than 5% of the total area and has been reported to be as low 1-2% [12]. The mass of carbide in the powder is given by:

$$m'_{c_p} = \frac{f_{m_{c_p}} \dot{m}_p}{U} \quad (2.3)$$

where $f_{m_{c_p}}$ is the weight fraction of carbide in the powder feed (kg/m), which is measured directly while weighing each component during blending of the carbide and metal powders. \dot{m}_p is the total mass transfer rate of the powder feed (kg/s), which is determined after a two minute particle collection test and weight measurement, and U is the sub-

strate travel speed (m/s), which is taken from electronic position record of the CNC as an rpm measurement of the chuck and converted to a travel speed considering the measured outer diameter of the cylindrical substrate. Substituting Equations (2.2) and (2.3) into Equation (2.1), the carbide efficiency can be calculated from measured quantities as:

$$\eta_{m_c} = \frac{U A_{b_T} \rho_c f_{v_{c_b}}}{\dot{m}_p f_{m_{c_p}}} \quad (2.4)$$

2.4.2 Metal Powder Efficiency

Metal powder efficiency is the ratio of mass of metal powder in the bead to mass of metal powder in the powder feed.

$$\eta_{m_m} = \frac{m'_{m_b}}{m'_{m_p}} \quad (2.5)$$

where η_{m_m} is the metal powder catchment efficiency (1), m'_{m_b} is the linear mass density of metal powder in the clad bead (kg/s), and m'_{m_p} is the linear mass density of metal powder in the powder feed (kg/m). The mass of metal powder in the bead is given by:

$$m'_{m_b} = (1 - f_{v_{c_b}}) A_{b_R} \rho_m \quad (2.6)$$

where ρ_m is the density of the metal powder reported from the powder manufacturer (kg/m³). In Equation (2.6), A_{b_R} appears instead of A_{b_T} to account for only the addition of mass from the process. This distinction excludes the bead area contribution from dilution that was existing mass prior to cladding; however, with A_{b_D} on the order of 1-2%, A_{b_R} can be considered the same as A_{b_T} for controlled cladding processes. The mass

of metal powder in the total powder/carbide mix is given by:

$$m'_{m_p} = \frac{f_{m_{m_p}} \dot{m}_p}{U} \quad (2.7)$$

where $f_{m_{m_p}}$ is the is weight fraction of metal powders in the powder feed (1), which is measured directly while weighing each component during blending of the carbide and metal powders. Substituting Equations (2.6) and (2.7) into Equation (2.5), the metal powder efficiency can be calculated from measured quantities as:

$$\eta_{m_m} = \frac{U A_{b_R} \rho_m (1 - f_{v_{c_b}})}{\dot{m}_p f_{m_{m_p}}} \quad (2.8)$$

2.4.3 Overall Powder Efficiency

Overall efficiency is the ratio of the carbide and metal powders in the bead to the total amount of powders exiting the cladding head:

$$\eta_m = \frac{m'_{c_b} + m'_{m_b}}{\dot{m}_p / U} \quad (2.9)$$

where η_m is the overall powder efficiency (1). Substituting Equations (2.4) and (2.6) into Equation (2.9), the overall powder efficiency can be calculated from measured quantities as:

$$\eta_m = \frac{U}{\dot{m}_p} [A_{b_T} f_{v_{c_b}} \rho_c + A_{b_R} (1 - f_{v_{c_b}}) \rho_m] \quad (2.10)$$

2.5 Results

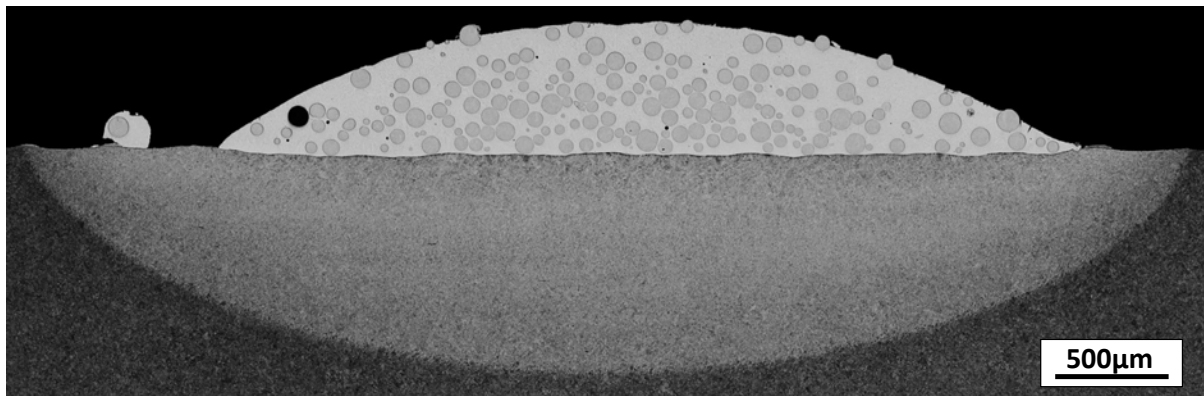


Figure 2.3: Cross section of Bead 3 etched with 3% Nital for 5 seconds.

Occasionally small sintered particles outside of the main bead were observed, such as the one shown on the left side of the bead in Figure (2.3). These sintered powders do not contribute to the build up of the main bead and are not considered as part of this analysis of efficiency for single beads. Voids in clad bead were also occasionally observed and were typically accounted for as matrix material in the calculations. This is a reasonable approximation for beads with low porosity such as those in these experiments. Figure (2.3) shows a void on the left side of the bead likely caused by a carbide being pulled out during the sample preparation process based on its size and edge roughness at high magnification. Figure (2.4) shows the output of the PythonTM script highlighting the carbide area. The colours are randomly generated by the program.

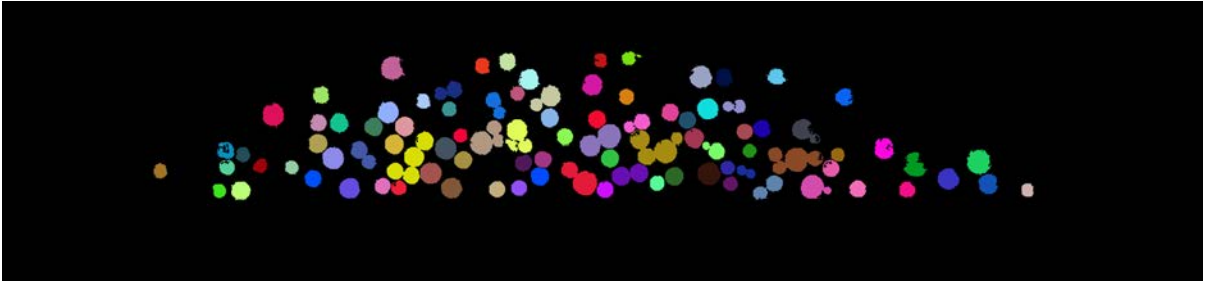


Figure 2.4: Python script output showing carbide area for Bead 3.

Table 2.3 summarizes the area and carbide fraction measurements from all experimental clads. Using the data from Tables 2.2 and 2.3 and Equations (2.4), (2.8), and (2.10), the carbide, metal powder, and overall efficiency were determined for all experiments. These efficiencies are summarized in Table 2.4. The uncertainty in the values of catchment efficiency was quantified for Equations (2.4), (2.8), and (2.10) using standard techniques described by Beckwith *et al.* [13]. This analysis is outlined in detail in Appendix B of this thesis.

Table 2.3: Bead area and carbide volume fraction measurements for experimental test beads

Bead Number	Total Area A_{b_T} (mm ²)	Reinforcement Area A_{b_R} (mm ²)	Carbide Volume Fraction $f_{v_{cb}}$ (%)
Bead 1	1.89	1.65	33.64
Bead 2	0.72	0.68	30.05
Bead 3	1.52	1.40	28.48
Bead 4	2.27	2.11	29.30
Bead 5	1.19	0.85	20.27
Bead 6	1.02	0.95	34.42
Bead 7	1.46	1.38	34.29
Bead 8	1.19	1.12	38.04
Bead 9	3.59	3.42	34.71
Bead 10	1.90	1.79	36.39
Bead 11	1.37	1.16	36.26
Bead 12	0.67	0.65	37.48
Bead 13	1.96	1.88	38.56

Table 2.4: Carbide, metal powder, and overall catchment efficiency for the experimental clad beads

Bead Number	Carbide Efficiency η_{m_c} (%)	Uncertainty $\pm\epsilon_{\eta_{m_c}}$ (%)	Metal Powder Efficiency η_{m_m} (%)	Uncertainty $\pm\epsilon_{\eta_{m_m}}$ (%)	Overall Efficiency η_m (%)	Uncertainty $\pm\epsilon_{\eta_m}$ (%)
Bead 1	53.33	6.38	73.53	8.18	60.89	4.79
Bead 2	18.19	2.18	32.18	3.55	23.42	1.82
Bead 3	36.21	4.33	67.20	7.40	47.80	3.72
Bead 4	41.80	5.00	75.06	8.27	54.24	4.22
Bead 5	34.45	4.12	77.81	8.48	50.67	3.99
Bead 6	36.88	4.41	52.58	5.86	42.75	3.35
Bead 7	41.81	5.00	60.93	6.79	48.96	3.83
Bead 8	37.83	4.53	46.79	5.27	41.18	3.26
Bead 9	52.12	6.24	75.08	8.37	60.71	4.75
Bead 10	45.25	5.42	59.77	6.70	50.68	3.99
Bead 11	48.43	5.80	58.09	6.51	52.04	4.14
Bead 12	31.52	3.77	40.81	4.59	35.00	2.75
Bead 13	45.65	5.46	55.82	6.30	49.45	3.91

The trends in efficiency for carbide, metal powder, and the overall were analyzed by separating the tests into the three test blocks for power, powder feed rate, and substrate travel speed. Figures (2.5), (2.6), and (2.7) show the effects of power, powder feed rate, and travel speed on catchment efficiency. Error analysis for \dot{m}_p and U in Figures (2.6) and (2.7) is present, but the resulting error bars are smaller than the thickness of each data point in the respective figures.

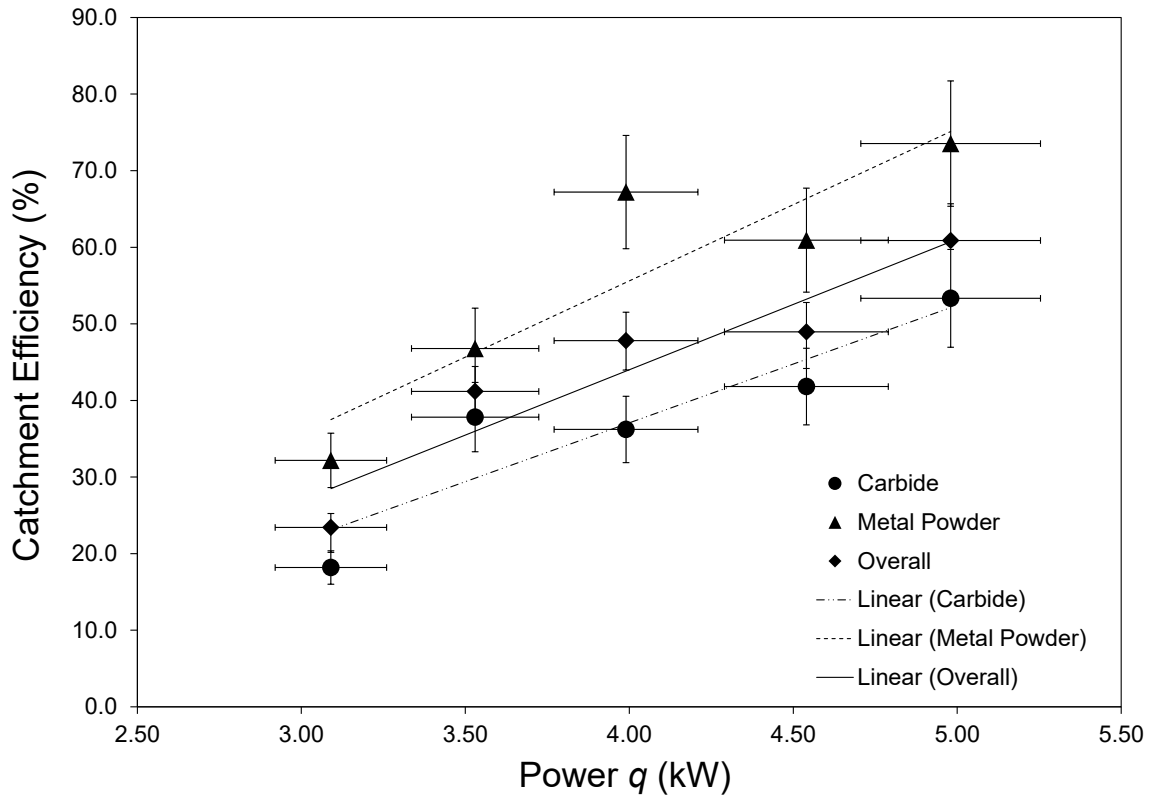


Figure 2.5: Effect of power on catchment efficiency.

Figure (2.5) shows increasing laser power increases both the carbide and metal efficiency. The linear trend lines in the graph aim at capturing the overall behaviour of catchment; these lines are not models or an attempt to represent a particular physical phenomenon. The trend lines indicate that the overall catchment efficiency increases approximately 17%/kW for the conditions tested.

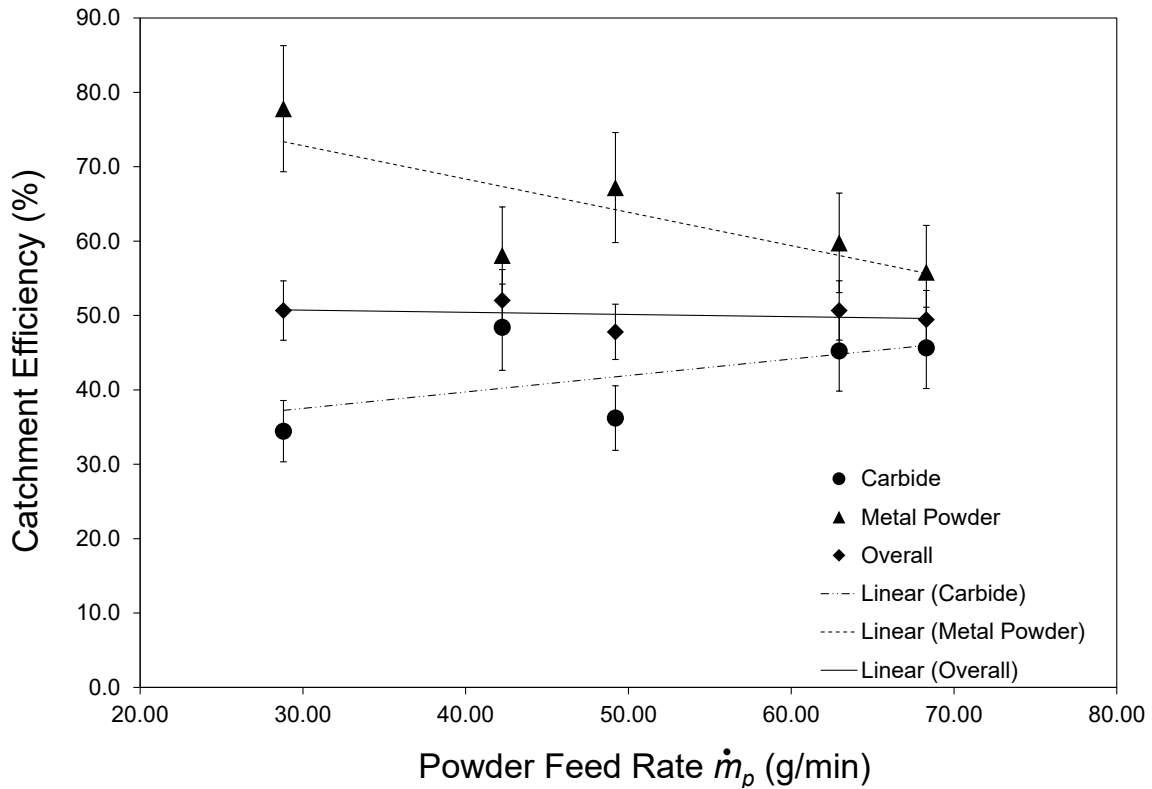


Figure 2.6: Effect of powder feed rate on catchment efficiency.

Figure (2.6) shows that metal powder efficiency decreases with powder feed rate ($\sim 0.45\%/g/min$), while carbide efficiency increases ($\sim 0.22\%/g/min$). The smaller effect on carbide efficiency was on the order of the confidence interval and further work is needed to confirm this trend. For the values measured, the overall catchment efficiency was nearly insensitive to powder feed rate. It is important to highlight that while overall efficiency was approximately constant, carbide fraction varied in a measurable way (carbide fraction increased with powder feed rate). This carbide fraction is of high importance for the quality and performance of the clad.

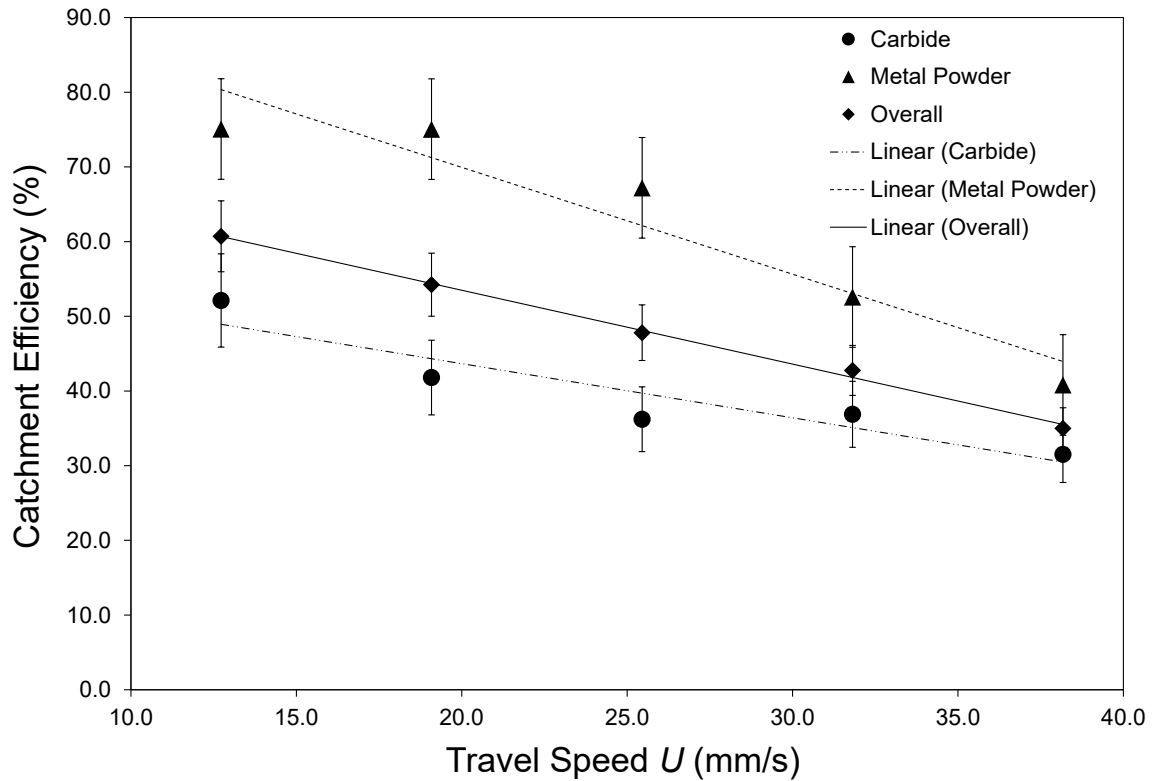


Figure 2.7: Effect of travel speed on catchment efficiency.

Figure (2.7) shows that increasing travel speed decreases the carbide, metal powder, and overall efficiencies. The overall efficiency shows a decreasing trend of 1%/mm/s with a total $\sim 25\%$ decrease in efficiency for the conditions tested.

2.6 Discussion

Increasing laser power demonstrated a rise in carbide, metal powder, and total efficiency, which is most likely due to increased molten pool size with higher power density. There is also likely an increase in particle preheat, which contributes to increased efficiency as observed by Kumar and Roy [14]. In practice, there is a limit to the effectiveness of the carbide efficiency increase at high power levels, as the heat sensitive carbides dissolve

and reprecipitate brittle phases on their surfaces, which degrades wear performance [1].

For the powder feed rate test block, the decreased trend in metal powder efficiency and increased trend in carbide efficiency with increased feed rate can be exploited to manipulate the carbide fraction in the deposited clad. Despite the negligible change in overall efficiency on a percentage basis, this behaviour would be limited in practice by the likelihood of disbonding the clad from the substrate with excessive powder in the cloud and shadowing of the laser beam creating an unstable clad pool.

The observed decrease in carbide, metal powder, and overall efficiency with increased travel speed was consistent with the linearly decreasing approximation by Colaço *et al.* [15]. This trend is likely due to the decreased interaction time between the laser beam and the substrate, which decreases the molten pool size. This explanation is supported by the decrease in width and height of beads with increasing travel speed shown by several sources [8, 15, 16].

For all experiments, the metal powder efficiency was higher than the carbide, which is consistent with favourable wetting of the primarily nickel powder to the molten nickel pool. This explanation is supported by the findings of Guest *et al.* who observed carbides ricocheting off the surface of a molten nickel weld pool during gas metal arc welding of Ni-WC [17]. It will be important in future analyses to confirm the variation in component efficiencies is not related to biasing by the powder feeders at different parameter levels.

Mathematically, Equations (2.4), (2.8), and (2.10) are valid on the interval $0 \leq f_{v_{c_b}} \leq 1$, however in practice the value of $f_{v_{c_b}}$ will not typically exceed 50%. This value represents a physical limit of not enough metal powder matrix material to create a fully dense clad. The observed result of excessive carbide fraction is voids in the interparticle regions between carbide particles, which dramatically affect performance and are industrially unacceptable. A value of 1, representing 100% WC in the deposited clad is not physically possible using the laser cladding process.

Some important assumptions were made in this work that are addressed here. It was assumed that the area fractions of a single cross section was representative of the bead volume. This assumption is typically made because of the long preparation time required for each individual sample. In measuring the carbide efficiency, pores or voids were occasionally observed in the cross section, which were included in the calculations as matrix area. These voids were not regularly observed and can be reasonably assumed to have a negligible effect on the reported trends in this work. The PythonTM program occasionally missed tracking carbides, and the carbide fractions measured are a lower bound. Because very few carbides are omitted, the measurements are taken as representative of the actual carbide fraction. Finally, the dilution of carbides in the matrix was neglected; this is reasonable because reprecipitated carbides were not observed in any sample.

The accuracy of the PythonTM measurements could possibly be improved by discriminating porosity due to gas or shrinkage from that of pulled-out carbides during sample preparation. Shrinkage porosity has a rough and irregular shape, while gas porosity and pulled-out carbides have round shapes. Gas porosity and pulled-out carbides can be further discriminated due to the presence of a smooth diffuse reflections in voids related to gas porosity.

While the developed equations for component efficiency were demonstrated using the Ni-WC system, this method could be extended to any two component powder feed system with the same distinct components in the powder feed and deposited bead. The same equations would also be valid using off-axis powder feeding as typically done for inner diameter applications and are not exclusive to coaxial cladding.

2.7 Conclusions

This work has evaluated for the first time the individual efficiencies for a dual component powder feed made of tungsten carbide and metal powders. Preliminary experimental data for single beads of the Ni-WC powder mixture deposited using a 6 kW CO₂ laser indicated that:

- Increasing laser power increased carbide, metal powder, and overall efficiency.
- Powder feed rate had a minimal effect on overall efficiency, but demonstrated a simultaneous decrease in metal powder efficiency with an increase in carbide efficiency. This is relevant to controlling the carbide fraction in the deposited clad.
- Increasing travel speed showed strong decreases in carbide, metal powder, and overall efficiency.
- In all cases the metal powder efficiency was observed to be higher than the carbide.

2.8 Acknowledgements

The authors wish to acknowledge the helpful comments and suggestions from Doug Hamre, head of research and development at Apollo-Clad Laser Cladding, a division of Apollo Machine and Welding Ltd. Apollo, who is the industrial sponsor for this work, was instrumental in sharing their knowledge, equipment, and powder blends. The authors also acknowledge NSERC for providing project funding for this research. Student scholarships from the American Welding Society and Canadian Welding Association were gratefully received.

2.9 Appendix 2.1 Tungsten Carbide Density

The density of the carbide ρ_c was calculated using the mass and volume of the unit cell ($\rho_c = m_c/V_c$). The crystallography of WC_{1-x} is the cubic “rock salt” B1-type [18]. For this type of carbide (MC_{1-x} where M stands for metal), the variation in stoichiometry arises from structural vacancies in the non-metallic sites [19], namely C for WC_{1-x} . Figure (2.8) shows the WC_{1-x} unit cell involving 4 tungsten and 4 carbon in its interior. The mass of the unit cell is calculated in Equation (2.7).

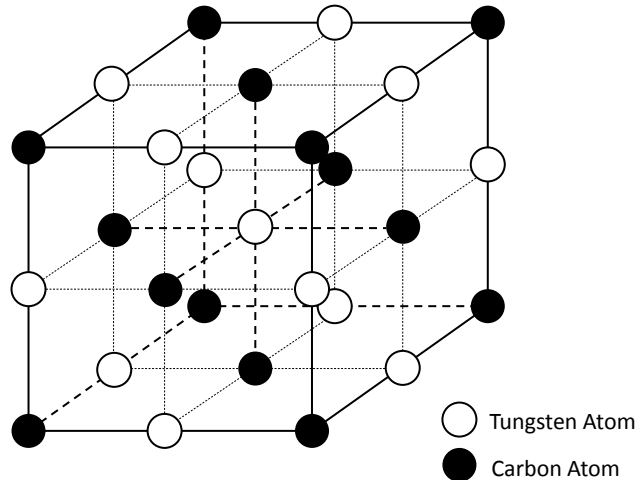


Figure 2.8: Cubic B1-type “rock salt” structure of the WC_{1-x} phase.

$$m_c = \frac{N_W M_W + N_C M_C (1 - X)}{N_A} \quad (2.11)$$

where m_c is the mass of the WC_{1-x} unit cell (kg), $N_W = 4$ is the number of W atoms in the unit cell (atoms), M_W is the molar mass of W (kg/mol), $N_C = 4$ is the number of C atoms in the unit cell (atoms), M_C is the molar mass of C (kg/mol), $(1 - X)$ is the stoichiometry of C in the WC_{1-x} phase (1), and N_A is Avogadro’s number (atoms/mol).

The volume of the unit cell is given by $V_c = a_{B1}^3$ where V_c is the volume of the WC_{1-x} unit cell, and a_{B1} is the lattice parameter of the same unit cell. Kurlov and Gusev have investigated the unit cell lattice parameters reported in literature and developed a best fit quadratic to represent the change in lattice parameter as a function of carbon content in the WC_{1-x} structure [20].

$$a_{B1} = 0.4015 + 0.0481(1 - X) - 0.0236(1 - X)^2 \quad (2.12)$$

The final form of the theoretical density of WC_{1-x} is then:

$$\rho_c = \frac{N_W M_W + N_C M_C (1 - X)}{N_A \left[0.4015 + 0.0481(1 - X) - 0.0236(1 - X)^2 \right]^3} \quad (2.13)$$

WC_{1-x} has a homogeneity region between $(1-X) = 0.59$ and $(1-X) = 1.00$ [21]. Using Equation (2.13), the density of WC_{1-x} was determined for the entire homogeneity region shown in Figure (2.9). For the carbides involved in this work, $(1-X) = 0.604$ corresponding to a density of 16,896 kg/m³.

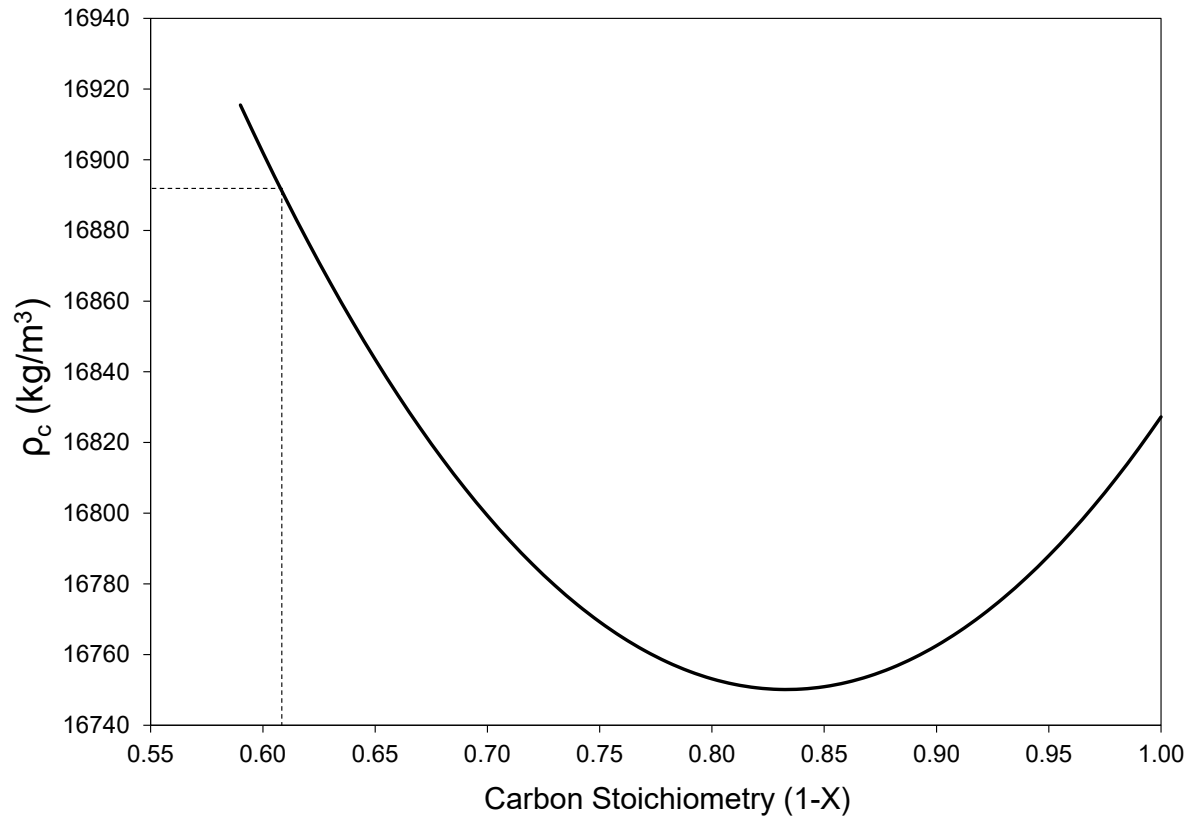


Figure 2.9: Density of WC_{1-x} as a function of C stoichiometry.

2.10 References

- [1] P.F. Mendez, N. Barnes, K. Bell, S. D. Borle, S. S. Gajapathi, S. D. Guest, H. Izadi, A. Kamyabi Gol, and G. Wood. Welding Processes for Wear Resistant Overlays. *Journal of Manufacturing Processes*, 16:4–25, 2013.
- [2] S.D. Guest. *Depositing Ni-WC Wear Resistant Overlays with Hot-Wire Assist Technology*. PhD thesis, University of Alberta, 2014.
- [3] J. Lin. A Simple Model of Powder Catchment in Coaxial Laser Cladding. *Optics & Laser Technology*, 31:233–238, 1999.
- [4] M. Picasso, C. F. Marsden, J. D. Wagnière, A. Frenk, and M. Rappaz. A Simple but Realistic Model for Laser Cladding. *Metallurgical and Materials Transactions B*, 25B:281–291, 1994.
- [5] J. Lin and W. M. Steen. Powder Flow and Catchment during Coaxial Laser Cladding. In *Lasers in Materials Processing*, volume 3097, pages 517–524. The International Society for Optical Engineering, 1997.
- [6] A. Frenk, M. Vandyoussefi, J. D. Wagnière, A. Zryd, and W. Kurz. Analysis of the Laser-Cladding Process for Stellite on Steel. *Metallurgical and Materials Transactions B*, 28B:501–508, 1997.
- [7] K. Partes. Analytical Model of the Catchment Efficiency in High Speed Laser Cladding. *Surface & Coatings Technology*, 204:366–371, 2009.
- [8] U. de Oliveira, V. Ocelik, and J. Th. M. De Hosson. Analysis of Coaxial Laser Cladding Processing Conditions. *Surface and Coatings Technology*, 197:127–136, 2005.
- [9] M. Gremaud, J. D. Wagnière, A. Zryd, and W. Kurz. Laser Metal Forming: Process Fundamentals. *Surface Engineering*, 12(3):251–259, 1996.
- [10] S. Zhou, Y. Huang, and X. Zeng. A Study of Ni-Based WC Composite Coatings by Laser Induction Hybrid Rapid Cladding with Elliptical Spot. *Applied Surface Sciences*, 254:3110–3119, 2008.
- [11] A. Angelastro, S. L. Campanelli, G. Casalino, and A. D. Ludovico. Optimization of Ni-Based WC/Co/Cr Composite Coatings Produced by Multilayer Laser Cladding. *Advances in Materials Science and Engineering*, pages 1–7, 2013.
- [12] L. St-Georges. Development and Characterization of Composite Ni-Cr + WC Laser Cladding. *Wear*, 263:562–566, 2007.

- [13] T.G. Beckwith, R.D. Marangoni, and J.H. Leinhard V. *Mechanical Measurements*. Pearson Prentice Hall, 6 edition, 2007.
- [14] S. Kumar and S. Roy. Development of Theoretical Process Maps to Study the Role of Powder Preheating in Laser Cladding. *Computational Materials Science*, 37:425–433, 2006.
- [15] R. Colaço, L. Costa, R. Guerra, and R. Vilar. A Simple Correlation Between the Geometry of Laser Cladding Tracks and the Process Parameters. In *Laser Processing: Surface Treatment and Film Deposition*, pages 421–429. Kluwer Academic Publishers, Netherlands, 1996.
- [16] H. E. Cheikh, B. Courant, J.-Y. Hascoët, and R. Guillén. Prediction and Analytical Description of the Single Laser Track Geometry in Direct Laser Fabrication from Process Parameters and Energy Balance Reasoning. *Journal of Materials Processing Technology*, 212:1832–1839, 2012.
- [17] S. D. Guest, J. Chapuis, G. Wood, and P.F. Mendez. Non-Wetting Behaviour of Tungsten Carbide Powders in Nickel Weld Pool: New Loss Mechanism in GMAW Overlays. *Science and Technology of Welding and Joining*, 19(2):133–141, 2014.
- [18] A.S. Kurlov and A.I. Gusev. Phases and Equilibria in the W–C and W–Co–C Systems. In *Tungsten Carbides: Structure, Properties and Application in Hardmetals*, pages 5–56. Springer International Publishing, Switzerland, 2013.
- [19] A.A. Rempel. Atomic and Vacancy Ordering in Nonstoichiometric Carbides. *Physics - Uspekhi*, 39(1):31–56, 1996.
- [20] A. S. Kurlov and A. I. Gusev. Phase Equilibria in the W-C System and Tungsten Carbides. *Russian Chemical Reviews*, 75(7):617–636, 2010.
- [21] R. V. Sara. Phase Equilibria in the System Tungsten-Carbon. *Journal of The American Ceramic Society*, 5:251–257, 1965.

Chapter 3

Calibrated Expressions for Welding and their Application to Isotherm Width in a Thick Plate

3.1 Introduction

Recent advances in technology have made it possible to consider welding a scientific endeavour rather than an art form [1]. These advancements mean that welders can now make use of plasma arcs, lasers, electron beams, explosives and mechanical devices to join metals at the atomic level [2]. Despite the enormous progress in the last 30 years, there is a distinct lack of insightful, quantitative, physically relevant guidelines for welding problems [2]. For the most part, an empirical trial and error approach has been used in industry to solve complex welding problems. This approach has only been capable of providing answers in a limited range of real life scenarios, and as a result these answers have not enhanced intuition, creativity, or engineering judgement. At the academic level, numerical simulations have been developed to make meaningful predictions about welding processes. However, due to their complexity and lack of wide scale applicability, they have seen limited acceptance and use by practitioners in industry [3].

The absence of general solutions to welding problems is a result of the complex, multi-

coupled physics of the process. Typically welding involves many of the issues of thermofluids in addition to electromagnetic body forces, chemical reactions, phase transformations, and complex free surface conditions [3]. The large number of coupled phenomena leads to welding technologies being notoriously difficult to study, be it experimentally or through numerical simulation. This paper presents a promising approach to address the limitations of empirical experiments and numerical simulations of the past. Complex problems in welding can be tackled using asymptotic expressions and appropriate correction factors. In essence, a complex welding problem can be reduced and solved by inputting parameters into inexpensive and common spreadsheet software. This approach provides an alternative to existing procedure development techniques, which bridges the gap between the complexity of numerical simulations and the exhaustive, costly nature of trial and error qualifications.

The proposed methodology for this asymptotic analysis is a six-step procedure called the Minimal Representation and Calibration (MRC) approach. The results of the MRC approach can be calibrated against experiments, numerical models, or exact solutions. In this study, the MRC methodology is introduced and applied to Rosenthal's thick plate equation for isotherm temperature for point heat sources [4]. The relationship between weld parameters and substrate temperature profile has also been explored [5–9]. The maximum width of a given temperature isotherm is determined using asymptotic equations (also known as scaling laws), which capture the change in maximum width in a generalized way. Correction factors are then derived to match the exact solution of Rosenthal's equation to the derived expressions. An example has also been included to demonstrate the application of the results of the MRC procedure to a real world welding scenario.

3.2 List of Symbols

Symbol	Unit	Description
A	m^2	Area
α	m s^{-2}	Thermal diffusivity
B	Variable	Bias uncertainty
C_1, C_2, C_3	1	Constants used to calibrate correction factor estimates
e	1	Error
ϵ	Variable	Total uncertainty
η	1	Process thermal efficiency
f	1	Correction factor
k	$\text{W m}^{-1} \text{K}^{-1}$	Thermal conductivity
l	m	Length
n	1	Number of samples
P	Variable	Precision uncertainty
Q	W	Nominal heat input
r	m	Magnitude of the distance from the origin
s_T	Variable	Standard deviation
T	K	Temperature
T_0	K	Preheat
U	1	Travel velocity [m/s]
x	m	x-coordinate position
y	m	y-coordinate position

Symbol	Description
Superscripts	
-	Average value
*	Dimensionless value
^	Calculated estimate
+	Calibrated value
Subscripts	
b	Bead
e	Exact value
HAZ	Heat affected zone
∞	For fast heat sources ($T^* \ll 1$)
m	Maximum
$meas$	Measured
0	For slow heat sources ($T^* \gg 1$), with the exception of T_0 (preheat)
sc	Actual scale calibration
sc	Measured scale calibration
y	y-coordinate

3.3 Engineering Design Rules: Minimal Representation and Calibration Approach

For a wide range of engineering disciplines, design rules are an essential part of practice. They almost always have the form shown in Equation (3.1) [10].

$$(\textit{Simple Formula}) \times (\textit{Correction Factor}) \quad (3.1)$$

The success and generality of Equation (3.1) can be extended to a variety of engineering problems outside of welding [10]. Examples of such an approach can be found in stress concentration analysis in solid mechanics [11], fluid dynamic drag [12], bearing life calculation [13], and stress in gear teeth [14].

The MRC approach is based on the most idealized conception that is still able to capture the dominant phenomena. Correction factors are then applied to the formula to take into account the most important departures from the ideal case, which can then be calibrated to minimize the deviation between the scaled and exact solutions. Some special features of the MRC approach, which are described in [10], are:

- Predictions made by the MRC approach are made only for characteristic values (such as maximum value of a field), not for whole fields. The dependence that is being studied is not based on the independent variables, but rather on the problem parameters. In a typical welding problem, a characteristic value could be the width of an isotherm, which is demonstrated in subsequent sections, and not the exact magnitude of temperature at any position in space. Characteristic values are studied in further detail in [15].
- Once the correction factors are obtained, they are easy to calculate based on in-

formation that is known beforehand. The formula proposed in this paper has the form of a power law, with the correction factors that can be well tabulated. For example, in a welding problem, process efficiency, thermal diffusivity, travel velocity, nominal heat input, thermal conductivity and preheat are known quantities prior to welding. Parameters should not include magnitudes such as molten metal velocity, which can only be determined after simulation or experimentation.

- The correction factors take into account secondary phenomena which are originally discarded during the initial stages of the MRC approach. As such, the correction factors have a physical, real world meaning and applicability.
- The correction factors can be used to determine a limit to the validity of the idealized cases.
- Minimal expressions that are properly calibrated generally reproduce existing experimental data with accuracy comparable to experiments.
- As real world problems approach the idealized case, the correction factors tend to 1 or a constant value of magnitude equal to 1. Thus the model and reality correspond to a consistent value of the order of 1 to one another in the asymptotic limit.

3.4 Applying the MRC Approach to a Welding Problem

The MRC approach is able to capture the multicoupled, multiphysics nature of welding. It has the ability to account for a range of phenomena, rather than the case by case experimental expressions often used in industry. This ability ensures generality is achieved. MRC consists of the following steps, which were first proposed by Karem *et al.* [10]:

1. List all physics considered relevant

2. Identify dominant factors
3. Solve approximate problem considering only dominant factors
4. Check for self-consistency
5. Compare predictions to “reality”
6. Calibrate predictions

To illustrate these steps, the width of an isotherm in a thick substrate using Rosenthal’s solution for point heat sources is considered, which is shown in Equations (3.2) and (3.3) [4]. Thick plate substrate in this case is defined as a semi-infinite plate where the heat flow is three-dimensional.

$$T = T_0 + \frac{\eta Q}{2\pi k r} \exp \left[-\frac{U}{2\alpha}(r + x) \right] \quad (3.2)$$

$$r = \sqrt{x^2 + y^2} \quad (3.3)$$

where T is the temperature of interest (K), T_0 is the preheat temperature (K), η is the thermal efficiency of the heat source (1), Q is the power of the heat source (W), k is the thermal conductivity of the substrate (W/mK), x, y are the x,y coordinates respectively (m), r is the radial distance (m) (Equation 3.3), U is the travel speed (m/s), and α is the thermal diffusivity (m^2/s). A graphic representation of Equation (3.2) is shown in Figure (3.1). The x-axis is fixed to the centerline of the moving heat source, and positive x is denoted to be the direction of motion with the frame of reference attached to the heat source.

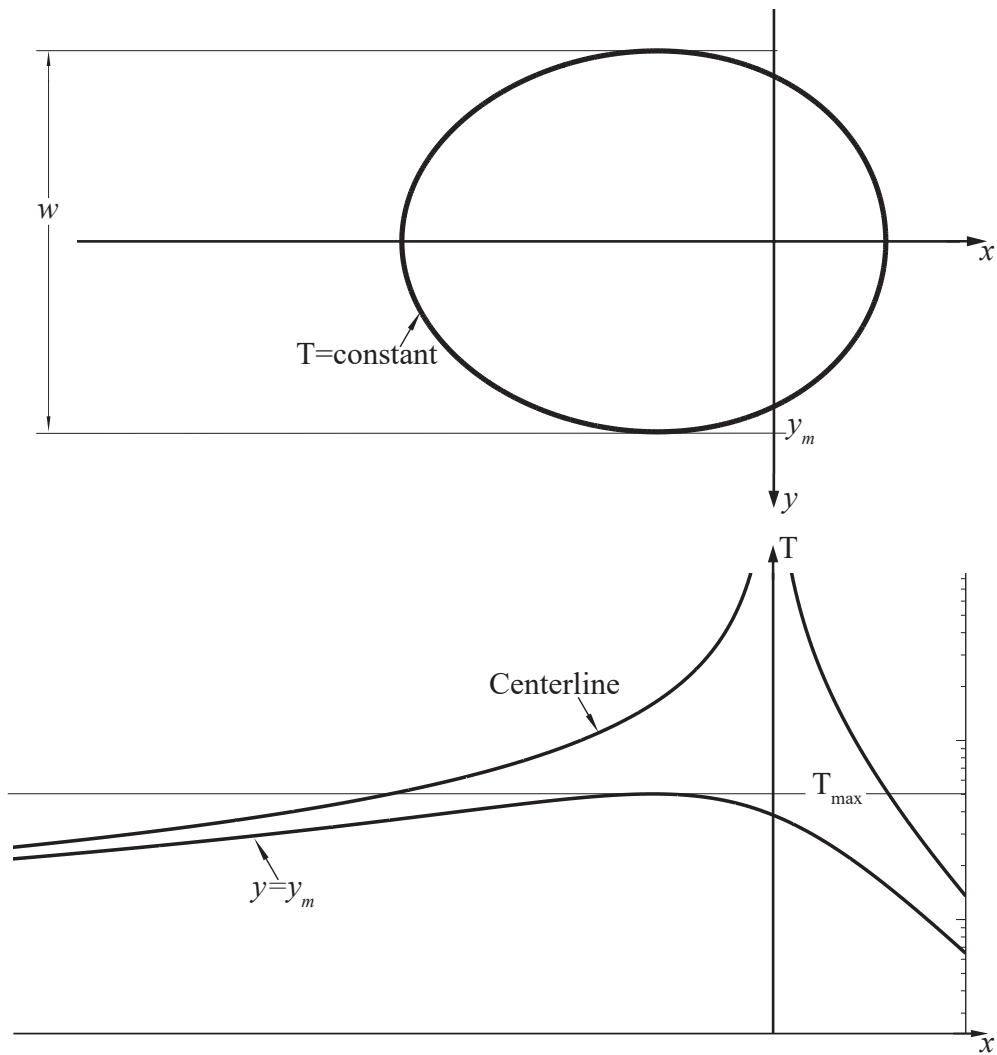


Figure 3.1: Isotherms and temperature profiles for point heat source in a thick plate.

The independent variables ($\{X\}$), dependent variables ($\{U\}$), and parameters ($\{P\}$) for Rosenthal's thick plate solution are shown in Equations (3.4)-(3.6).

$$\{X\} = \{x, y\} \quad (3.4)$$

$$\{U\} = \{T\} \quad (3.5)$$

$$\{P\} = \{Q, k, U, \alpha\} \quad (3.6)$$

Equation (3.2) can be normalized as follows:

$$T^* = \frac{1}{r^{**}} \exp(-r^* - x^*) \quad (3.7)$$

$$r^* = \sqrt{(x^*)^2 + (y^*)^2} \quad (3.8)$$

where T^* is the dimensionless temperature (1), r^* is the dimensionless radial coordinate defined in Equation (3.8) (1), x^* is the dimensionless x-coordinate, and y^* is the dimensionless y-coordinate. The dimensionless x^* , y^* , and T^* values are defined as follows:

$$x^* = \frac{U}{2\alpha} x \quad (3.9)$$

$$y^* = \frac{U}{2\alpha} y \quad (3.10)$$

$$T^* = (T - T_0) \frac{4\pi k \alpha}{\eta Q U} \quad (3.11)$$

The dimensionless groups in Equations (3.9)-(3.11) reduce the problem from a total of seven variables down to three variable groups. Note that Equation (3.8) is not truly independent and is a function of Equations (3.9) and (3.10). The MRC approach is now applied to illustrate how very general power laws can be combined with correction factors to produce the original solution with high accuracy.

3.4.1 Step 1: List All Physics Considered Relevant

This list must include dominant phenomena, and may include various secondary phenomena. The following is a list of phenomena that is considered especially relevant in welding problems:

- Conduction: Heat transported by molecular mechanisms in the solid substrate.
- Advection: Heat transported due to the relative motion of torch and plate.
- Radiation: Heat lost by the hot surface of the substrate.
- Convection: Heat transported in the weld pool due to the motion of molten metal.
- Phase transformations: Absorption or release of heat due to the transformation from solid to liquid or between different solid-state phases.
- Electromagnetic effects: Flow of current in electric welding creates body forces affecting the motion of molten metal.

3.4.2 Step 2: Identify All Dominant Factors

The minimal representation of a system is based only on the dominant factors, with the secondary factors being accounted for by the correction factors. Identification of dominant factors is critical, and can be formal, intuitive, or a combination of both [10]. An

inspection of the normalized Rosenthal solution shows that there are two dimensionless independent variables, one dimensionless dependent variable, and no dimensionless parameters. Rosenthal intuitively determined that the following approximations had only secondary effects:

- No fluid flow in the molten pool
- Constant material properties with temperature
- Infinite plate size
- Point heat source
- No convective or radiative heat loss occurs from the surface
- No phase transformations

Rosenthal analysis considers only two mechanisms of heat transfer: conduction and advection, establishing two asymptotic regimes depending on which mechanism dominates. These two regimes are consistent with the solution of Equation (3.7), where, for a characteristic value such as isotherm width, there is a relationship between two dimensionless groups only. The two regimes in Rosenthal's solution can then be captured by the value of T^* . For high values of T^* ($T^* \gg 1$) conduction is dominant, while for low values of T^* ($T^* \ll 1$) advection is dominant. These two regimes also correspond to what are often called “slow” and “fast” heat sources respectively.

3.4.3 Step 3: Solve Approximate Problem using Dominant Factors

The problem is simplified when only dominant factors are considered, and the solutions can be numerical, exact or approximate. For the example considered here, there are two regimes each characterized by a different dominant phenomena. At $T^* \gg 1$ conduction

governs isotherm size, while at $T^* \ll 1$ advection is dominant. A good estimate for the maximum isotherm width has the following general form applicable to both regimes:

$$y_m = \widehat{y}_m f_{y_{m,e}}(T^*) \quad (3.12)$$

where y_m is the true value of the maximum isotherm width (m), \widehat{y}_m is an asymptotic estimate solution to the problem (m), and $f_{y_{m,e}}$ is a correction factor that would result in the exact value (1), which is a function of T^* . The estimate \widehat{y}_m is derived separately for the low and high T^* regimes. The key difference for the estimates is the characteristic shape of the isotherm in the asymptotes of the T^* domain. For low T^* values the isotherms become increasingly elongated due to the dominant effect of advection, and at high T^* values the isotherms become circular as conduction dominates and the heat is dissipated equally in the $(xy)^*$ plane.

Low T^* Regime

Equation (3.1) can be rewritten using the following notation for low T^* values:

$$y_m = \widehat{y}_{m_0} f_{y_{m_0,e}}(T^*) \quad (3.13)$$

where \widehat{y}_{m_0} is the estimate for the asymptotic regime when T^* approaches 0 (advection dominant) (m) and $f_{y_{m_0,e}}$ is the correction factor that results in an exact solution for $T^* \leq 1$ (1). For the fast moving heat source, the elongated isotherms have a much larger length to width ratio and satisfy the condition $y^*/x^* \ll 1$. Equation (3.3) can be rearranged in terms of y^*/x^* by factoring $(x^*)^2$ from underneath the square root. Only the negative solution of $|x^*|$ is considered for this analysis because the maximum width

will always occur at a negative x^* position. For $x^* < 0$ Equation (3.3) becomes:

$$r^* = -x^* \sqrt{1 + \left(\frac{y^*}{x^*}\right)^2} \quad (3.14)$$

Using the first two terms of an expansion of the square root around 1, Equation (3.14) can be transformed to the following form:

$$r^* \approx -x^* \left[1 + \frac{1}{2} \left(\frac{y^*}{x^*}\right)^2 \right] \quad (3.15)$$

By multiplying the equation by -1 and subtracting x^* from both sides, the left side of the equation represents the argument of the exponential of Equation (3.7).

$$-r^* - x^* \approx x^* \left[1 + \frac{1}{2} \left(\frac{y^*}{x^*}\right)^2 \right] - x^* \quad (3.16)$$

Multiplying the x^* term through and simplifying the results, we arrive at the following form of the approximation:

$$-r^* - x^* \approx -\frac{1}{2} \frac{(y^*)^2}{x^*} \quad (3.17)$$

Substituting Equation (3.17) into Equation (3.7) yields an expression for low T^* values in terms of both x^* and y^* :

$$T^* \approx \frac{1}{x^*} \exp \left[-\frac{1}{2} \frac{(y^*)^2}{x^*} \right] \quad (3.18)$$

Differentiation of Equation (3.18) with respect to x^* , leads to the resulting expression:

$$\frac{\partial T^*}{\partial x^*} \approx \frac{\exp \left[\frac{(y^*)^2}{x^*} \right] [2x^* - (y^*)^2]}{2(x^*)^3} \quad (3.19)$$

where $\partial T^*/\partial x^*$ is the change in dimensionless temperature with respect to the dimensionless x-coordinate. By setting $\partial T^*/\partial x^* = 0$, the location of the dimensionless estimate of maximum y^* at low T^* values can be determined, which after simplification leads to a direct relationship between $\widehat{y}_{m_0}^*$ in terms of the dimensionless x coordinate at the maximum $x_{m_0}^*$.

$$x_{m_0}^* = \frac{(\widehat{y}_{m_0}^*)^2}{2} \quad (3.20)$$

where $\widehat{y}_{m_0}^*$ is the dimensionless estimate of the maximum y-coordinate for fast heat sources (1), and $x_{m_0}^*$ is the dimensionless x-coordinate at the location of maximum isotherm width (1). By substituting Equation (3.20) into Equation (3.18), a relationship of $\widehat{y}_{m_0}^*$ as a function of only T^* can be established. The significance of this relationship is that isotherm width can now be expressed exclusively by a single dimensionless parameter.

$$\widehat{y}_{m_0}^* = \sqrt{\frac{2}{eT^*}} \quad (3.21)$$

By inputting the parameters of T^* from Equation (3.11) into Equation (3.21), the following expression is obtained, which equates the estimate of dimensionless isotherm width exclusively in terms of welding parameters.

$$\widehat{y}_{m_0}^* = \sqrt{\frac{e^{-1}\eta QU}{2\pi k\alpha(T - T_0)}} \quad (3.22)$$

By substituting Equation (3.10) into Equation (3.22), we can develop an expression for the dimensional estimate \widehat{y}_{m_0} for low T^* values.

$$\widehat{y}_{m_0} = \sqrt{\frac{2e^{-1}\alpha\eta Q}{\pi kU(T - T_0)}} \quad (3.23)$$

Inserting the above result into Equation (3.13) gives us an expression for the exact solution y_{m_0} in terms of the derived approximation multiplied by a correction factor for low T^* values.

$$y_{m_0} = \sqrt{\frac{2e^{-1}\alpha\eta Q}{\pi kU(T - T_0)}} f_{y_{m_0,e}} \quad (3.24)$$

High T^* Regime

Similar to low T^* , the general formula for y_m can be expressed using notation for high T^* values:

$$y_m = \widehat{y}_{m_\infty} f_{y_{m_\infty,e}}(T^*) \quad (3.25)$$

where \widehat{y}_{m_∞} is the estimate for the asymptotic regime when T^* approaches infinity (conduction dominant) (m) and $f_{y_{m_0,\infty}}$ is the correction factor that results in an exact solution for $T^* > 1$ (1). At high T^* values, Rosenthal's solution predicts that the isotherm takes the shape of a circle centred at the heat source. Equation (3.7) therefore reduces to the approximate form below:

$$T^* \approx \frac{1}{r^*} \quad (3.26)$$

At the maximum point of the isotherm for high T^* values, $x^* = x_{m_\infty}^* = 0$, leaving only the y^* component of r^* , which is denoted $\widehat{y}_{m_\infty}^*$. This leads to the following expression

for $\widehat{y_{m_\infty}}^*$ in terms of only T^* .

$$\widehat{y_{m_\infty}}^* = \frac{1}{T^*} \quad (3.27)$$

where $\widehat{y_{m_\infty}}^*$ is the dimensionless estimate for the maximum isotherm width for slow heat sources ($T^* \ll 1$). Substituting the values from Equation (3.11) in Equation (3.27), an expression for $\widehat{y_{m_\infty}}^*$ is obtained in terms of welding process variables for a given temperature.

$$\widehat{y_{m_\infty}}^* = \frac{\eta Q U}{4\pi k \alpha (T - T_0)} \quad (3.28)$$

The above equation can be rearranged to dimensional form by substituting Equation (3.10) as follows:

$$\widehat{y_{m_\infty}} = \frac{\eta Q}{2\pi k (T - T_0)} \quad (3.29)$$

Inserting the results of Equation (3.29) into the general expression for y_m for high T^* values, we obtain an expression for the exact solution of y_{m_∞} as a function of the derived estimate multiplied by the correction factor for high T^* values.

$$y_{m_\infty} = \frac{\eta Q}{2\pi k (T - T_0)} f_{y_{m_\infty, e}} \quad (3.30)$$

where y_{m_∞} is the true value for the maximum isotherm width for slow heat sources (conduction dominant) (m).

3.4.4 Step 4: Check for Self-Consistency

In this simple uncoupled example, self-consistency is not a problem. The consideration of only two relevant phenomena guarantees that when one phenomenon is neglected the other will govern system behaviour. For more complex scenarios involving three or more coupled phenomena, it is necessary to confirm that the secondary factors are of secondary importance and magnitude. By computing the value of terms in the governing equation using the estimate of the characteristic value, the significance of neglected phenomena can be evaluated. The simple case applies to maximum isotherm width using Rosenthal's equation, where advection and conduction are the only two relevant phenomena under consideration.

3.4.5 Step 5: Compare Predictions to Reality

It is important that scaling laws are validated through comparisons with reality. Reality for this example is considered to be Rosenthal's exact solution. The exact correction factors for high and low T^* regimes can be derived from the ratio of the exact to estimate solutions for maximum isotherm width, which is described in detail in this section.

Low T^* Regime

The exact correction factor for $T^* < 1$, $f_{y_{m_0,e}}$, can be mathematically described by the ratio of the exact solution to the estimate solution. Taking advantage of this definition, the exact correction factor can also be represented by the ratio of the dimensionless exact solution and dimensionless estimate as both are multiplied by the same normalizing factor.

$$f_{y_{m_0,e}}(T^*) = \frac{y_{m_0}^*}{\overline{y_{m_0}^*}} \quad (3.31)$$

Substituting the relationship established in Equation (3.21) into Equation (3.31), we arrive at the following expression for $f_{y_{m_0,e}}$, which depends only on T^* :

$$f_{y_{m_0,e}}(T^*) = \sqrt{\frac{e}{2} y_{m_0}^* \sqrt{T^*}} \quad (3.32)$$

High T^* Regime

Similar to the low T^* regime, the exact correction factor for high T^* values, $f_{y_{m_\infty,e}}$ is defined as the following ratio of the dimensionless exact solution to dimensionless estimate:

$$f_{y_{m_\infty,e}}(T^*) = \frac{y_{m_\infty}^*}{\widehat{y_{m_\infty}^*}} \quad (3.33)$$

Inserting the relationship from Equation (3.27) into Equation (3.33), the following expression for $f_{y_{m_\infty,e}}$ as a function of only T^* is established:

$$f_{y_{m_\infty,e}}(T^*) = y_{m_\infty}^* T^* \quad (3.34)$$

As $f_{y_{m_0,e}}$ approaches $T^* \ll 1$ and $f_{y_{m_\infty,e}}$ approaches $T^* \gg 1$, the exact correction factors tend to 1, which indicates the estimates are good in the asymptotes of each regime. This behaviour is shown in Figure (3.2).

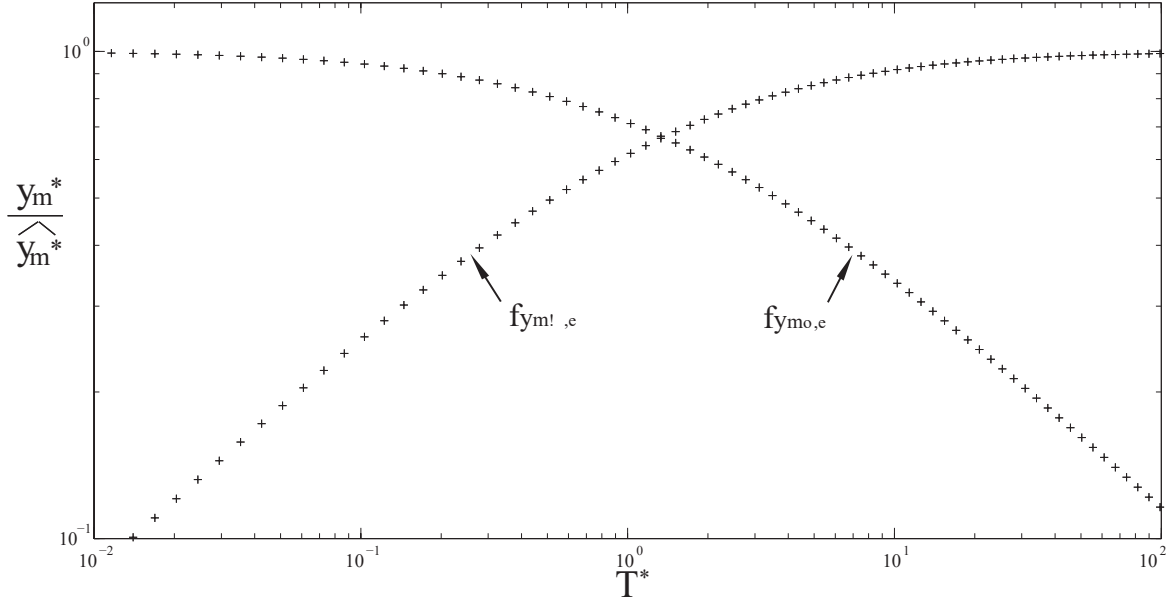


Figure 3.2: Exact correction factors for y_m as a function of T^* . $f_{y_{m_0},e}$ is the correction factor for the low T^* regime and $f_{y_{m_\infty},e}$ for the high T^* regime.

3.4.6 Step 6: Calibrate Predictions

The exact correction factors can be approximated with an appropriate function resulting in a high quality estimate based only on parameters known beforehand, which has the following general form:

$$\widehat{y}_m^+ = \widehat{y}_m f_{y_m} \tag{3.35}$$

where \widehat{y}_m^+ is the calibrated asymptotic estimate (m) and f_{y_m} is the approximate correction factor (1). The exact correction factors, $f_{y_{m_0},e}$ and $f_{y_{m_\infty},e}$, both depend only on T^* and can be approximated using the expressions shown in Equations (3.36) and (3.37) respectively. This approach has also been used by Churchill *et al.* for developing

general asymptotic solutions for phenomena that vary between limiting cases [16].

$$f_{y_{m_0}}(T^*) = [1 + (C_1 T^*)^{C_3}]^{\frac{C_2}{C_3}} \quad (3.36)$$

$$f_{y_{m_\infty}}(T^*) = \left[1 + \left(\frac{C_1}{T^*} \right)^{C_3} \right]^{\frac{C_2}{C_3}} \quad (3.37)$$

where $f_{y_{m_0}}(T^*)$ is the approximate correction factor for the maximum width for fast heat sources (1), C_1, C_2 , and C_3 are the calibrating constants for the correction factors (1), and $f_{y_{m_\infty}}(T^*)$ is the approximate correction factor for the maximum width for slow heat sources (1). The calibrated form of the isotherm width equation can be expressed for the maximum width of both advection dominant and conduction dominant regimes as follows:

$$\widehat{y_{m_0}}^+ = \widehat{y_{m_0}} f_{y_{m_0}} \quad (3.38)$$

$$\widehat{y_{m_\infty}}^+ = \widehat{y_{m_\infty}} f_{y_{m_\infty}} \quad (3.39)$$

where $\widehat{y_{m_0}}^+$ is the calibrated estimate for maximum isotherm width for fast heat sources (m) and $\widehat{y_{m_\infty}}^+$ is the calibrated estimate for maximum isotherm width for slow heat sources (m). The graphical solution of the calibrated correction factors compared to the exact correction factors is shown in Figure (3.3). Both calibrated factors show excellent agreement for all T^* values, which extends beyond their region of intended use.

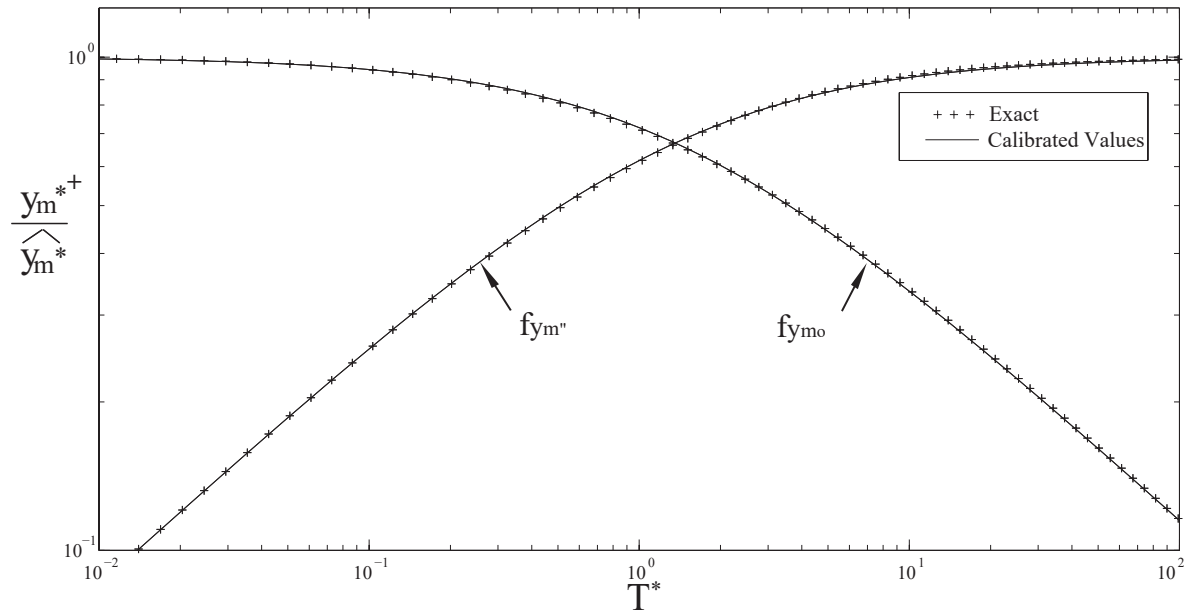


Figure 3.3: Comparison of the exact correction factors to the calibrated correction factors. The maximum error is below 0.8%.

The form of the calibrated factors is such that it matches the behaviour of the exact correction factors in the asymptotes with only slight deviations in the intermediate region around $T^* = 1$. The calibrated correction factor $f_{y_{m_0}}$ tends to 1 at low T^* values ($T^* \ll 1$) where the T^* term is negligible and approaches $(C_1 T^*)^{C_2}$ at high T^* values where the T^* term dominates. For $f_{y_{m\infty}}$ the calibrated approximation tends to 1 as T^* becomes large and approaches $(C_1/T^*)^{C_2}$ at low T^* values.

The calibrated correction factors include three constants to match the behaviour of the exact correction factors. The values of C_1 and C_2 come directly from the derivation shown in step 5, but the constant C_3 has been included to provide an additional degree of manipulation in the intermediate region near $T^* = 1$. This manipulation has been accomplished while preserving the behaviour of the correction factors in the asymptotes of both regimes for both correction factors.

The error between the exact and calibrated factors has been calculated using a ratio

of logs to better represent the difference across large orders of magnitude. The formula for error for $f_{y_{m_0}}$ and $f_{y_{m_\infty}}$ are shown in Equations (3.40) and (3.41).

$$e_{y_{m_0}} = \ln \frac{f_{y_{m_0,e}}(T^*)}{f_{y_{m_0}}(T^*)} \quad (3.40)$$

$$e_{y_{m_\infty}} = \ln \frac{f_{y_{m_\infty,e}}(T^*)}{f_{y_{m_\infty}}(T^*)} \quad (3.41)$$

Using the definition of Equations (3.40) and (3.41), plots such as the one in Figure (3.4) can be generated for a wide range of C_3 values. It is noted that the maximum and minimum observed in Figure (3.4) are symmetric about the T^* axis.

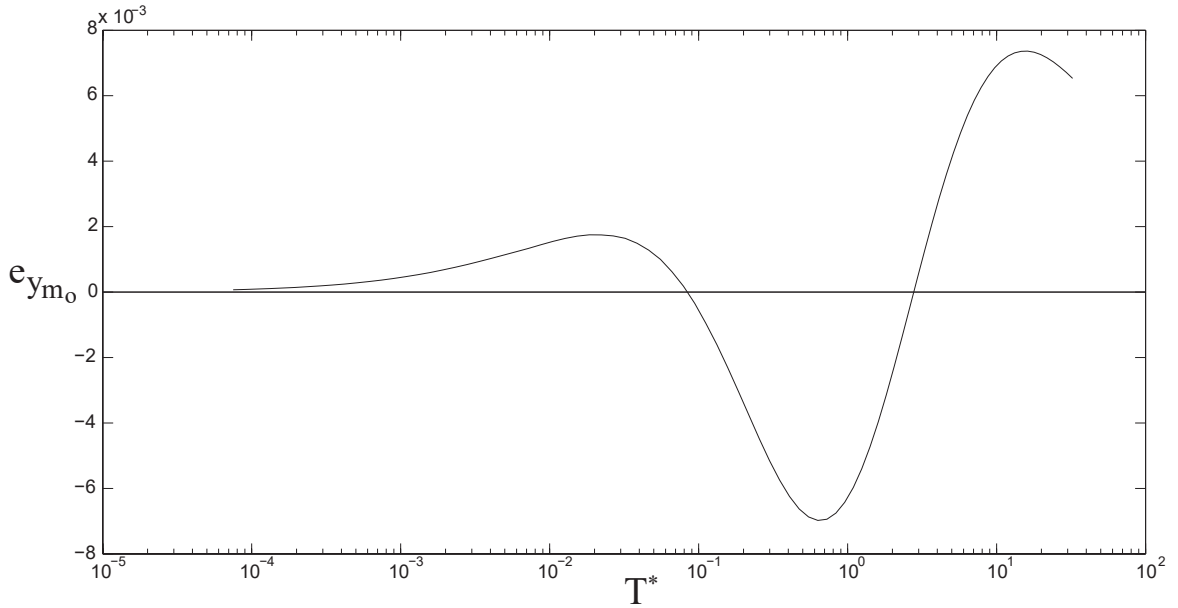


Figure 3.4: Error as a function of T^* for $f_{y_{m_0}}$ and $C_3 = 0.865$

The absolute maximum error for a large range of C_3 values was then plotted to determine a C_3 that minimizes the maximum error. A minimum was identified at $C_3 = 0.865$ correct to three significant digits for $f_{y_{m_0}}$ and $f_{y_{m_\infty}}$. The graph for error minimization of

$f_{y_{m_0}}$ is shown in Figure (3.5).

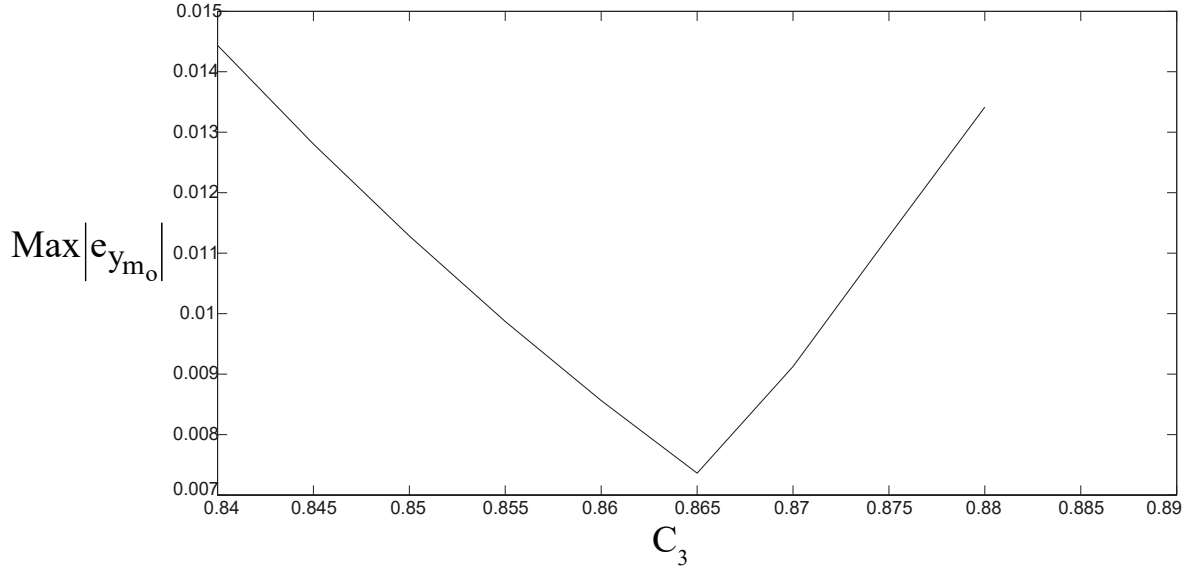


Figure 3.5: Identification of C_3 to minimize the maximum absolute error of $f_{y_{m_0}}$

This approach to calibrating the correction factors has been highly successful, as shown by the excellent fit of the exact and calibrated values in Figure (3.3). The maximum absolute error for both correction curves is less than 0.8% corresponding to an accuracy of at least 99.2% for any isotherm. Table 3.1 summarizes the values of C_1 , C_2 , and optimized C_3 for both correction factors.

Table 3.1: Values of optimized calibration constants for $f_{y_{m_0}}$ and $f_{y_{m_\infty}}$

Approximate Correction Factor	Equation Number	C_1	C_2	C_3
$f_{y_{m_0}}$	(3.36)	$\frac{2}{e}$	-0.5	0.865
$f_{y_{m_\infty}}$	(3.37)	$\frac{e}{2}$	-0.5	0.865

Sample Calculation

To demonstrate the procedure for applying correction factors, a sample welding scenario is presented to calculate the width of the 800 °C isotherm during welding of AISI 1010 carbon steel with no preheat. Recommended welding parameters for GMAW of carbon and low alloy steels using 100% CO₂ shielding gas from the Lincoln GMAW welding catalogue have been selected for this example [17]. Parameters for 3 mm plate and 0.9 mm diameter electrode are: 21 V DC+, 0.5 m/min travel speed, and approximately 160 A. The arc efficiency for this process has been cited as 85% [18]. Relevant material data for AISI 1010 at 300 K include $\alpha = 18.8 \times 10^{-6}$ m²/s and $k = 63.9$ W/mK [19].

The first step using this approach is to determine the T^* value for the particular problem, which is done using Equation (3.11). The value of T^* was calculated to be 0.492.

$$T^* = (T - T_0) \frac{4\pi k \alpha}{\eta Q U} \quad (3.11)$$

$$T^* = (1073 \text{ K} - 298 \text{ K}) \frac{4\pi(63.9 \text{ W/mK})(18.8 \times 10^{-6} \text{ m}^2/\text{s})}{(0.85)[(21 \text{ V})(160 \text{ A})](0.00833 \text{ m/s})}$$

$$T^* = 0.492$$

Since this value is lower than one, advection is the dominating phenomenon. Equation (3.23) is used to calculate the estimate of isotherm width \widehat{y}_{m_0} , which is 5.520 mm

for this example.

$$\widehat{y}_{m_0} = \sqrt{\frac{2e^{-1}\alpha\eta Q}{\pi kU(T - T_0)}} \quad (3.23)$$

$$\widehat{y}_{m_0} = \sqrt{\frac{2(e^{-1})(18.8 \times 10^{-6} \text{ m}^2/\text{s})(0.85)[(21 \text{ V})(160 \text{ A})]}{(\pi)(63.9 \text{ W/mK})(0.00833 \text{ m/s})(1073 \text{ K} - 298 \text{ K})}}$$

$$\widehat{y}_{m_0} = 5.520 \text{ mm}$$

The correction factor for low T^* values, $f_{y_{m_0}}(T^*)$, is found using Equation (3.36) and the calibrated constants in Table 1. $f_{y_{m_0}}(T^*)$ is shown to be 0.818 for a T^* value of 0.492.

$$f_{y_{m_0}}(T^*) = [1 + (C_1 T^*)^{C_3}]^{\frac{C_2}{C_3}} \quad (3.36)$$

$$f_{y_{m_0}}(0.492) = \left\{ 1 + \left[\frac{2}{e}(0.492) \right]^{0.865} \right\}^{\frac{-0.5}{0.865}}$$

$$f_{y_{m_0}}(0.492) = 0.818$$

Combining the estimate \widehat{y}_{m_0} and the correction factor $f_{y_{m_0}}(T^*)$ using Equation (3.36), we find that the calibrated estimate for maximum width of the 800 °C isotherm from the origin is 4.517 mm.

$$\widehat{y}_{m_0}^+ = \widehat{y}_{m_0} f_{y_{m_0}} \quad (3.38)$$

$$\widehat{y}_{m_0}^+ = (5.520 \text{ mm})(0.818)$$

$$\widehat{y}_{m_0}^+ = 4.517 \text{ mm}$$

The application of the MRC approach to isotherm width has been demonstrated using the series of equations shown in this sample calculation and information that is known prior to welding. The general nature of the developed expressions allows this approach to be extended to any number of welding processes, materials, and parameter combinations as an excellent starting point approximation of isotherm width prior to experimental trials.

3.5 Discussion

The MRC approach provides for the first time a framework for systematically determining reliable estimates for characteristic values of welding systems that match the exact solution. The rigorous systematic aspect of this work relies on representing system behaviour in the asymptotic cases using scaling estimates, and applying correction factors to account for deviations from the asymptotic limit.

Based on the analysis of maximum isotherm width presented here, there is error associated with neglecting the secondary terms in the scaling expressions. For this simple uncoupled example, the exclusion of either advection or conduction was shown to have a negligible impact in the asymptotic cases where the scaling estimates match the ex-

act solution. The implementation of calibrated correction factors compensated for the intermediate regime where advection and conduction are of comparable magnitude and resulted in a maximum error of 0.8% between the estimate and exact solution for any isotherm. Unexpectedly, the correction factors $f_{y_{m_0}}$ and $f_{y_{m_\infty}}$ had excellent agreement across all T^* values, which implies they could be successfully used outside of their intended dominant regime.

3.6 Conclusions

A six step Minimal Representation and Calibration approach was presented as a promising alternative to current welding procedure development techniques. The six steps are:

1. List all physics considered relevant
2. Identify dominant factors
3. Solve approximate problem considering only dominant factors
4. Check for self-consistency
5. Compare predictions to “reality”
6. Calibrate predictions

The MRC approach was applied to determine the maximum isotherm width from Rosenthal’s thick plate solution for a point heat source (Equation (3.2)). Through a series of non-dimensional transformations, a set of two independent dimensionless groups were identified that completely characterized the maximum width of any isotherm (x^* , y^*). Two regimes for the dimensionless dependent group T^* were present based on the dominant physics governing system behaviour in the regime. At low values of T^* ($T^* \ll 1$),

advection was dominant, and at high T^* ($T^* \gg 1$) conduction controlled maximum isotherm width. Considering the isotherm shape difference in the respective T^* regimes, two scaling laws, one for each regime, were derived, which captured the exact isotherm width as a function of only T^* . The results of these derivations are shown in Equations (3.24) and (3.30) for low and high T^* respectively. The developed asymptotic expressions were based only on process variables that are typically known prior to welding allowing them to be used for predictive purposes prior to experimental trials.

As part of the MRC methodology, correction factors were derived to ensure an exact match of the asymptotic expression to the exact solution for isotherm width for both T^* regimes. The derived factors were also estimated as power laws, which depended only on T^* and 3 scaling constants. The values of the constants were chosen to minimize the maximum error between the exact and estimate solutions for isotherm width. These calibrated correction factors yielded a maximum error of less than 0.8% demonstrating an excellent agreement between the asymptotic expressions and actual solution for any isotherm. An example problem using tabulated welding parameters for a GMAW bead on plate weld demonstrated the straight forward application of the developed expressions to a real world welding problem.

Overall, the isotherm width problem shows that the MRC approach can be used to tackle complex welding problems in a formal way. It is reasonable to believe that this methodology can be successfully applied to more complex multicoupled, multiphysics systems.

3.7 Acknowledgements

This work was partially supported by the Natural Sciences and Engineering Research Council of Canada (NSERC). Valuable discussions and feedback from N. Barnes are

gratefully acknowledged. Special thanks to Marcio Correa de Carvalho for his help with translation of parts of this work into Portuguese.

3.8 Appendix 3.1 Application of the MRC Approach to Laser Cladding of Ni-WC

As an addendum to the published work, this appendix outlines the application of the MRC approach in this work to the laser cladding experiments presented in Chapters (2) and (4) (the same experimental set). The motivating factor for the development of formulae for maximum width of a point heat source was to produce estimates for the maximum width of laser clad isotherms for this work. The results of this implementation are presented here as an important developmental step and point of comparison to the results calculated considering a distributed heat source in Chapter (4).

For the range of laser powers, powder feed rates, and travel speeds in the laser cladding experiments depositing Ni-WC onto 4145-MOD steel outlined in Sections 2.3 and Sections 4.3, the value of T^* from Equation (3.11) was calculated for the melting isotherm. For each of the 13 test clads the following parameters were in common and necessary for the T^* determination:

- The melting temperature T_m was taken to be the equilibrium solidus temperature of the 4145-MOD steel (1692 K or 1419 °C). Although the laser cladding process is a highly non-equilibrium process, the equilibrium solidus is used to approximate the unknown melting temperature at the fast heating rates associated with cladding. Selection of the solidus rather than the liquidus did not impact the results.
- The thermal conductivity and thermal diffusivity of the 4145-MOD steel were calculated for the clad isotherm shown in detail in Appendix A:

For 1692 K: $k_{eff} = 30.15$ W/mK and $\alpha_{eff} = 5.34 \times 10^{-6}$ m²/s.

- A thermal efficiency factor η_{th} of 0.3 or 30% was taken to represent the absorption of the steel of the 10.6 μ m CO₂ laser wavelength from literature in the absence of fundamental theoretical formulae [20]. Typically thermal efficiency is a fitting parameter in numerical models of the process [21, 22].

The calculated value of T^* for both isotherms of interest was determined to be much less than 1, indicating dominant advective heat transfer mechanism for the material and conditions tested here. The results of the melting temperature analysis are summarized in Table (3.2). Values of $\widehat{y_{m_0}}$, $f_{y_{m_0}}$, and $\widehat{y_{m_0}}^+$ have also been calculated for each test bead.

Table 3.2: Parameters to predict the maximum width of the melting isotherm for experimental cladding trials of Ni-WC on 4145-MOD steel

Bead Number	Laser Power Q (kW)	Powder Feed Rate \dot{m}_p (g/min)	Travel Speed U (mm/s)	Preheat Temp T_0 (K)	Dimensionless Temperature T^* Eq. (3.11) (1)	Maximum Width Estimate $\widehat{y_{m_0,b}}$ Eq. (3.23) (mm)	Correction Factor $f_{y_{m_0,b}}$ Eq. (3.36) (1)	Calibrated Width Estimate $\widehat{y_{m_0,b}}^+$ Eq. (3.38) (mm)
Bead 1	4.98	49.20	25.45	530	0.0618	1.449	0.962	1.394
Bead 2	3.09	49.20	25.45	530	0.0997	1.114	0.944	1.078
Bead 3	3.99	49.20	25.45	535	0.0769	1.300	0.955	1.241
Bead 4	3.99	49.20	19.09	531	0.1028	1.498	0.943	1.413
Bead 5	3.99	28.80	25.45	541	0.0764	1.303	0.955	1.245
Bead 6	3.99	49.20	31.81	537	0.0613	1.164	0.962	1.120
Bead 7	4.54	49.20	25.45	536	0.0675	1.387	0.959	1.331
Bead 8	3.53	49.20	25.45	537	0.0867	1.223	0.950	1.163
Bead 9	3.98	49.20	12.73	536	0.1539	1.837	0.921	1.693
Bead 10	3.98	62.95	25.45	537	0.0769	1.299	0.955	1.241
Bead 11	3.98	42.25	25.45	538	0.0769	1.300	0.955	1.241
Bead 12	3.98	49.20	38.18	540	0.0511	1.062	0.968	1.028
Bead 13	3.98	68.30	25.45	537	0.0769	1.299	0.955	1.240

Table (3.3) compares the measured values of the clad width deposited using the conditions outlined in Chapters (2) and (4) to the results of the MRC approach applied to maximum width of a Rosenthal isotherm presented in Chapter (3). Data for two width measurement techniques are presented. The first technique measures the width as the horizontal distance between the clad toes from the cross section of the bead. A schematic of this measurement is shown in Figure (4.4), and a typical Ni-WC cross section is presented in Figure (4.12). The second technique considers the width as the average of the a surface image of the bead measuring both the visible area and length in the image. An example of this is shown in Figure (4.11). Of the two techniques, the stereo photo measurements are considered to be more accurate because it provides an averaged length rather than a single point value.

Table 3.3: Comparison of measured Ni-WC bead width to predictions produced from the MRC approach applied to a Rosenthal isotherm

Bead Number	Cross Section Measured Width $2y_{m_{o,b}}$ (mm)	Stereo Photo Measured Width $2y_{m_{o,b}}$ (mm)	Calculated Width $2\widehat{y_{m_{o,b}}}$ ⁺ (mm)	Cross Section Percent Difference (%)	Stereo Photo Percent Difference (%)
Bead 1	4.084	3.873	2.791	31.64	27.91
Bead 2	2.034	1.933	2.157	-6.09	-11.62
Bead 3	3.753	3.502	2.484	33.81	29.07
Bead 4	4.233	3.917	2.828	33.20	27.80
Bead 5	4.243	3.820	2.492	41.27	34.76
Bead 6	3.390	3.029	2.242	33.85	25.96
Bead 7	3.489	3.402	2.664	23.64	21.69
Bead 8	3.323	3.334	2.328	29.93	30.17
Bead 9	4.450	4.156	3.389	23.85	18.47
Bead 10	3.754	3.453	2.484	33.84	28.07
Bead 11	3.820	3.653	2.484	34.97	31.99
Bead 12	2.446	2.458	2.057	15.87	16.28
Bead 13	3.646	3.065	2.483	31.89	18.98

Figures (3.6), (3.7), and (3.8) show the individual test parameter effect on measured bead width for the laser power, powder feed rate, and travel speed test blocks respectively. The error analysis for the measured independent and dependent variables is discussed in detail in Appendix 3.2. It is relevant to note that this level of parameter measurement and empirical trend determination represents the limit of typical industrial understanding of the process. The error analysis for both the measured widths, calculated width, and process variables (Q , \dot{m}_p , and U) is discussed in detail in Appendix B of this thesis. The x-axis error bars for Figures (3.7), and (3.8) are sufficiently small that they do not appear beyond the size of the data point marker. Table (3.4) below presents the total uncertainty for all values in Figures (3.6) through (3.10).

Table 3.4: Total uncertainty for the measured bead width, calculated bead width, and experimental process variables

Bead Number	Laser Power Uncertainty $\pm\epsilon_Q$ (kW)	Powder Feed Uncertainty $\pm\epsilon_{\dot{m}_p}$ (g/min)	Travel Speed Uncertainty $\pm\epsilon_U$ ($\times 10^3$ m/min)	Cross Section Measured Width Uncertainty $\pm\epsilon_{2y_{m_{o,b}}}$ (mm)	Stereo Photo Measured Width Uncertainty $\pm\epsilon_{2y_{m_{o,b}}}$ (mm)	Calculated Width Uncertainty $\pm\epsilon_{2\widehat{y_{m_{o,b}}}}$ (mm)
Bead 1	0.274	0.090	1.4536	0.300	0.295	0.0164
Bead 2	0.170	0.090	1.4536	0.149	0.152	0.0197
Bead 3	0.219	0.090	1.4536	0.276	0.275	0.0180
Bead 4	0.219	0.090	1.4489	0.311	0.307	0.0269
Bead 5	0.219	0.053	1.4536	0.312	0.300	0.0178
Bead 6	0.219	0.090	1.4597	0.249	0.238	0.0131
Bead 7	0.250	0.090	1.4536	0.256	0.267	0.0170
Bead 8	0.194	0.090	1.4536	0.244	0.376	0.0188
Bead 9	0.219	0.090	1.4456	0.327	0.316	0.0471
Bead 10	0.219	0.116	1.4536	0.276	0.271	0.0180
Bead 11	0.219	0.078	1.4536	0.281	0.287	0.0179
Bead 12	0.219	0.090	1.4670	0.180	0.187	0.0101
Bead 13	0.219	0.125	1.4536	0.268	0.241	0.0180

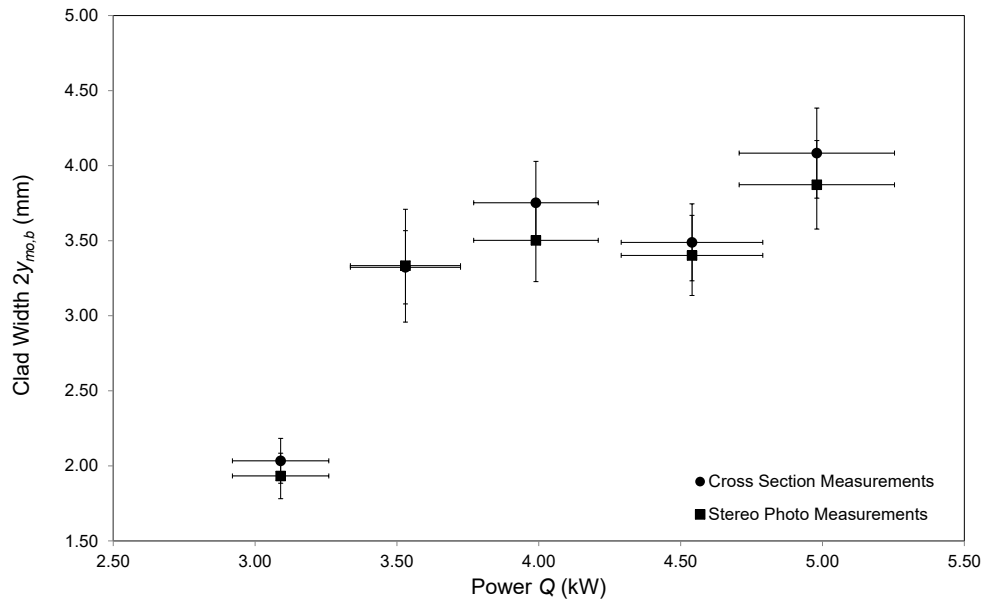


Figure 3.6: Effect of laser power on the measured bead width of Ni-WC deposited on a 4145-MOD steel substrate. Powder feed rate and travel speed were held constant at 49.20 g/min and 25.45 mm/s respectively.

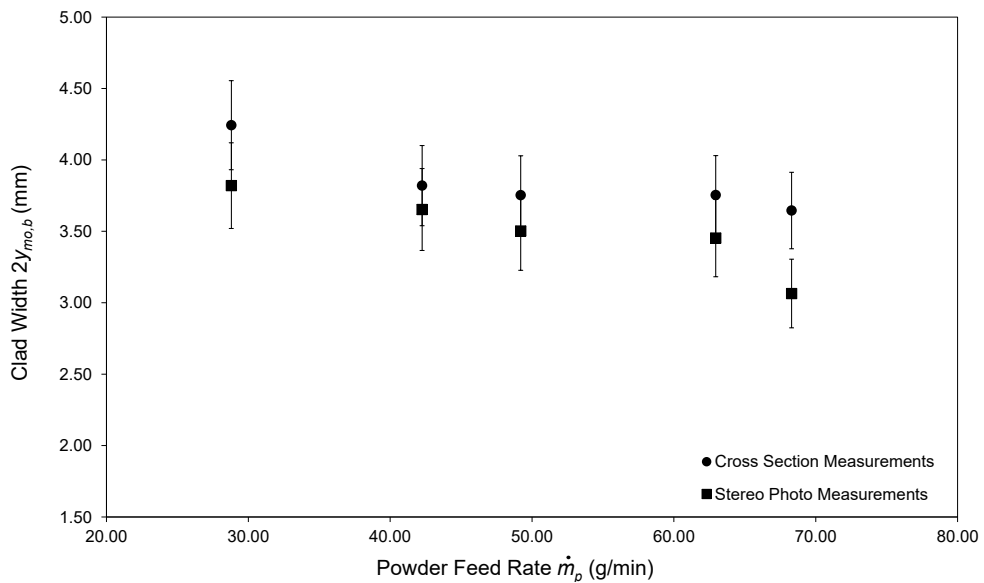


Figure 3.7: Effect of powder feed rate on the measured bead width of Ni-WC deposited on a 4145-MOD steel substrate. Laser power and travel speed were held constant at 3.99 kW and 25.45 mm/s respectively.

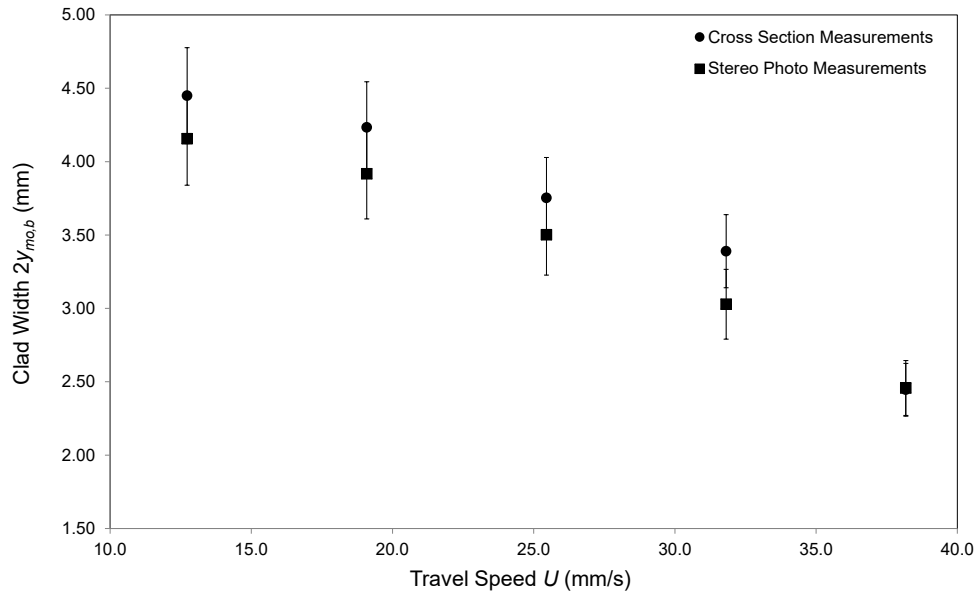


Figure 3.8: Effect of travel speed on the measured bead width of Ni-WC deposited on a 4145-MOD steel substrate. Laser power and powder feed rate were held constant at 3.99 kW and 49.20 g/min respectively.

Within the parameter window tested, Figures (3.6), (3.7), and (3.8) show an increasing trend in width with increasing laser power, a limited effect with respect to increases in powder feed rate, and a decrease in width with increasing travel speed. Figures (3.9) and (3.10) show the calculated width compared to the measured width for the cross section and stereo photo measurements respectively. In these plots, the tests are split into their respective test blocks (power, powder feed rate, and travel speed) in order to more clearly observe trends in each block.

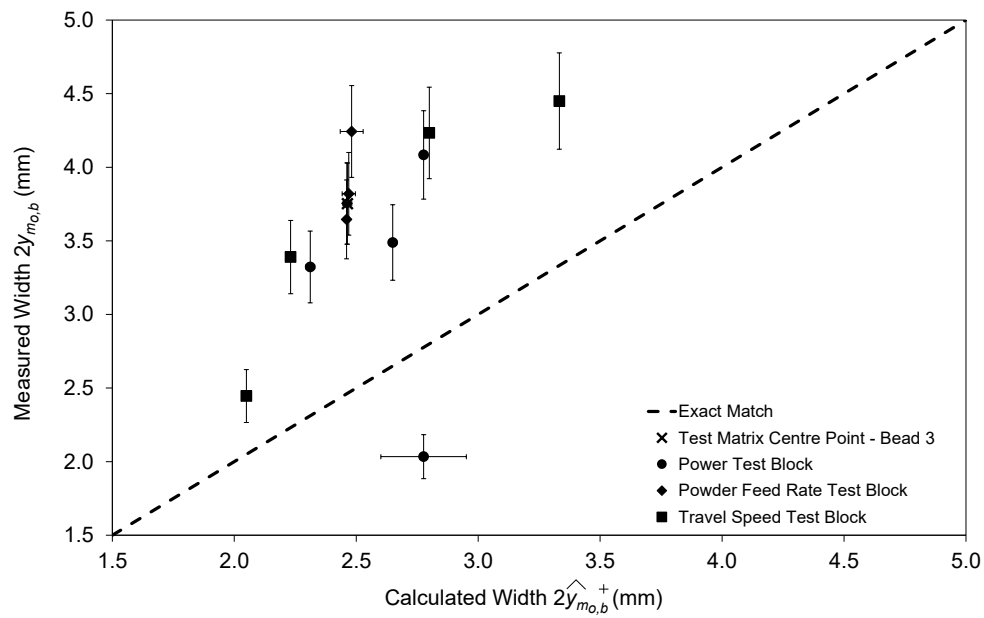


Figure 3.9: Comparison of cross section measured bead width to the calculation based on a Rosenthal heat source.

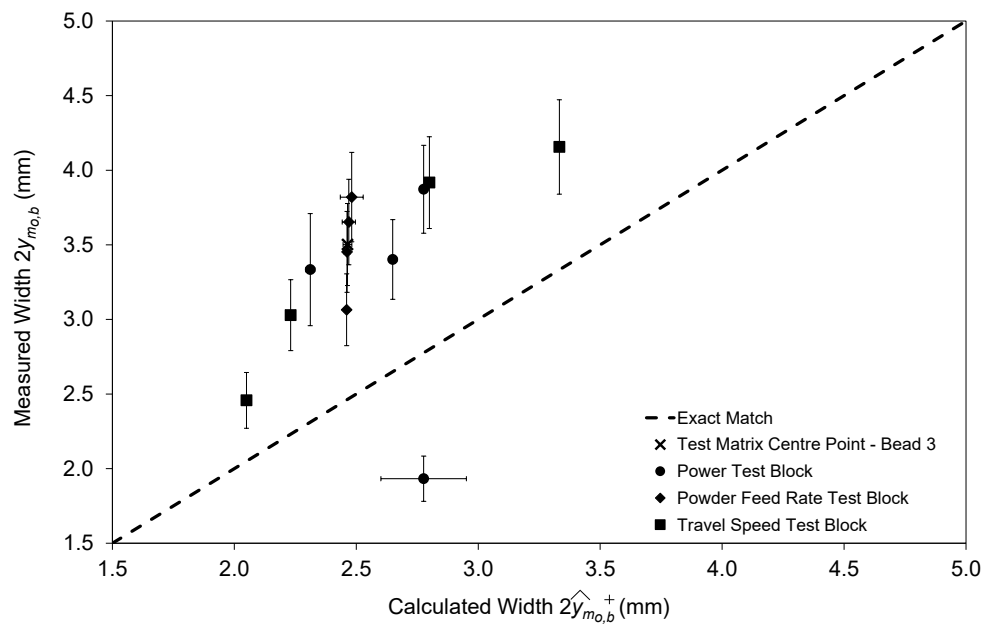


Figure 3.10: Comparison of stereo photo measured bead width to the calculation based on a Rosenthal heat source.

Both Figure (3.9) and Figure (3.10) show that the low power test (Bead 2) over predicts the bead width using this Rosenthal based approach. This is likely due to a change in process physics that has not been accounted for, most likely related to the reduced ability to form a stable clad pool and increased loss of powders as a result of reduced molten pool area. All other tests show a reasonably consistent prediction that is narrower than the measured width. While Rosenthal's approach is not meant for estimates near the heat source in the proximity of melting where fluid flow and other process physics influence the heat transfer in the pool, it is remarkable that the simplest possible representation of a welding system captures the bead width to within nearly 30% for what is considered a large parameter variation for depositing Ni-WC. The consistent under prediction strongly supports incorporating an additional degree of freedom to improve the model predictions. The next logical step is to move from a point heat source to a distributed heat source, which intuitively should increase the model's calculated estimates and improve the agreement with the experiments. The results of the distributed heat source analysis for a Gaussian heat distribution are shown in detail in Chapter (4) for the same set of experiments presented here. Another parameter relationship of note in Figures (3.9) and (3.10) is the effect of powder feed rate on the bead width. The calculated value remains the same for all tests despite changes in the measured values for the beads, which presents itself as a vertical line in both graphs. The reason for this is clearly that the powder feed rate does not have an impact on the heat transfer aspects of the process directly (\dot{m}_p does not appear in any equation for isotherm width); however, it is expected that once an expression for thermal efficiency is developed that incorporates the role of powder absorption and substrate shadowing rather than the literature value of 30% used here, the role of powder feed rate effect on the width of the bead will be realized in the model.

Other important points of discussion are that the heat transfer analysis presented here

in no way involves the Ni-WC coating. Material properties and temperature ranges are determined by the substrate rather than the coating material. A selection of the solidus temperature was done arbitrarily over the liquidus, acknowledging the short solidification range of the 4145-MOD steel presented in Table (7.2) in Appendix A and had a limited effect on the results when applied. Table (3.2) shows that the wide experimental range for the three test variables represents a small dimensionless temperature range (0.05 to 0.16). The fundamental advantage of this approach for analysis of the maximum isotherm width is that the problem has been distilled to depend on only a single parameter, and future experimental testing matrices will consider systematic variations in T^* (for which the problem truly depends) rather than changes in the individual process parameters (q , \dot{m}_p , U) in this analysis.

3.9 References

- [1] T.W. Eagar. Welding and Joining: Moving from Art to Science. *Welding Journal*, pages 49–55, 1995.
- [2] P. F. Mendez. Synthesis and Generalization of Welding Fundamentals to Design New Welding Technologies: Status, Challenges and a Promising Approach. *Science and Technology of Welding and Joining*, 16:348–356, 2011.
- [3] P. F. Mendez. Generalization and Communication of Welding Simulations and Experiments using Scaling Analysis. *Phase Transformations and Complex Properties Research Group*, 7 July, 2011.
- [4] D. Rosenthal. The Theory of Moving Sources of Heat and Its Application to Metal Treatments. *Transactions of the A.S.M.E.*, pages 849–866, 1946.
- [5] D. Rosenthal. Mathematical Theory of Heat Distribution during Welding and Cutting. *Welding Journal*, 20:220–234, 1941.
- [6] M.F. Ashby and K.E. Easterling. The Transformation Hardening of Steel Surface by Laser Beams. *Acta Metallurgica*, 32:1935–1948, 1984.

- [7] O. Grong and N. Christiansen. Effects of Weaving on Temperature Distribution in Fusion Welding. *Materials Science and Technology*, 2:967–973, 1986.
- [8] O. Myher and O. Grong. Dimensional Maps for Heat Flow Analyses in Fusion Welding. *Acta Metallurgica and Materialia*, 38:449–460, 1990.
- [9] P.S. Myers, O.A. Uyehara, and G.L Borman. Fundamentals of Heat Flow in Welding. *Welding Research Bulletin*, pages 1–46, 1967.
- [10] Karem E. Tello, Satya S. Gajapathi, and P. F. Mendez. Generalization and Communication of Welding Simulations and Experiments using Scaling Analysis. pages 249–258. Trends in Welding Research, Proceedings of the 9th International Conference, ASM International, 2012.
- [11] W.D. Pilkey and D.F. Pilkey. *Peterson’s Stress Concentration Factors*. John Wiley Sons, Inc., 3rd edition, 2008.
- [12] S.F. Hoerner. *Fluid-Dynamic Drag*. Hoerner Fluid Dynamics, 1965.
- [13] *Quality Bearing Components Catalog B620*, 2012.
- [14] *Handbook of Metric Drive Components D805*, 2010.
- [15] P. F. Mendez. Characteristic Values in the Scaling of Differential Equations in Engineering. *Journal of Applied Mechanics*, 77:6–17, 2010.
- [16] S. W. Churchill and R. Usagi. A General Expression for the Correlation of Rates of Transfer and Other Phenomena. *AIChE*, 18(6):1121–1127, 1972.
- [17] F. Armao, L. Byall, D. Kotecki, and D. Miller. *Gas Metal Arc Welding Guidelines*. Lincoln Electric.
- [18] J. N. Dupont and A. R. Marder. Thermal Efficiency of Arc Welding Processes. *Welding Journal*, 74(12):406–416, 1995.
- [19] F.P. Incropera, D.P. Dewitt, T.L. Bergman, and A.S. Lavine. *Fundamentals of Heat and Mass Transfer*. John Wiley and Sons, Sixth edition, 2007.
- [20] M. Schneider. *Laser Cladding with Powder*. PhD thesis, University of Twente, March 1998.
- [21] M. Picasso, C. F. Marsden, J. D. Wagnière, A. Frenk, and M. Rappaz. A Simple but Realistic Model for Laser Cladding. *Metallurgical and Materials Transactions B*, 25B:281–291, 1994.
- [22] A.F.A. Hoadley and M. Rappaz. A Thermal Model of Laser Cladding by Powder Injection. *Metallurgical Transactions B*, 23B(12):631–642, 1992.

Chapter 4

First Order Prediction of Bead Width and Height in Coaxial Laser Cladding

4.1 Introduction

Laser cladding with a powder feed is now an established technology for applying wear and corrosion resistant overlays for applications in the natural resource extraction industries in Alberta [1]. These applications range from dimensional repair of worn equipment to surface modification for improved performance of new parts used in extreme environments. The geometry of the deposited coating is an important consideration for the economics of the process. Practitioners must consider maximizing the lifetime of the component without exceeding dimensional tolerances for precision equipment that can be as small as 10 microns (0.0005”). Engineers must decide a set of parameters to accomplish the proper overlay with the minimum of waste material in lost powders or machining of excessive clad. The machining operation can be especially expensive for the case of wear resistant overlays. There are currently no general and easily applicable solutions for engineers to determine these process parameters without trial and error experimentation to target a specific coating size.

The focus of this analysis is the laser deposition of nickel tungsten carbide (Ni-WC) overlays. The Ni-WC powder blend contains two parts: a primarily Ni powder (referred to hereafter as metal powder), which composes the metallic matrix and ceramic tungsten carbide particles, which serve as the primary wear resistant phase in the overlay. The carbides must remain un-melted during the cladding process. Although the microstructural aspects of the Ni-WC are not a focus of this analysis, it is important to note that the WC symbol in Ni-WC does not directly refer to the stoichiometric 1:1 form of the carbide only and is used interchangeably with WC, W_2C and the non-stoichiometric WC_{1-x} . The carbide form used in this analysis is the non-stoichiometric WC_{1-x} .

The goal of this work is to present a new approach to modelling the width and height of a deposited bead. The ability to predict geometry also requires an understanding of the process “catchment efficiency”, which describes the fraction of the powder feed that contributes to the formation of the clad build-up [1–3].

Many researchers in the last 30 years have presented various approaches to predicting bead geometry, and the important papers are summarized below divided into those who have studied width and height and those who have modelled catchment efficiency directly. The work that has been done on predicting bead features can be sub categorized into those who have developed numerical models, those who have developed analytical models, and those who have developed experimentally based correlations. Among the numerical approaches, Hoadley and Rappaz developed a two-dimensional finite element model for laser cladding that predicts a linear relationship between bead height and the process inputs laser power and travel speed [4]. A comprehensive numerical solution was published by Picasso *et. al*, which decoupled the heat and mass transfer phenomena in laser cladding to predict process parameters for a given beam geometry and experimental setup in off-axis powder feed laser cladding [5]. Han *et al.* also presented a comprehensive numerical approach to modelling temperature fields and bead geometry

considering melting, solidification, evaporation, evolution of the free surface, and powder injection [6]. Process maps for laser cladding features were developed by Fathi *et al.* using a moving heat source method to predict temperature fields, melt pool depth, and dilution as a function of clad height and clad width [7]. Kumar and Roy presented correlations for process parameters effects on dilution, which incorporated dimensionless expressions to model the melt pool and deposited coating height [8]. A combined CFD, attenuation, and thermal model was proposed by Taberner *et al.* to predict height and width, which was experimentally validated using a nickel based superalloy [9]. Finally, Balu *et al.* have studied the temperature gradients and coating profile of Ni-WC clad onto a 4140 substrate using a finite element heat transfer model [10].

In the early 1990's Lemoine *et al.* published two papers on analytical modelling of the cross section of laser cladding for continuous [11] and pulsed [12] heat sources using an energy balance. Analytical models for clad geometry have been proposed by Colaço *et al.* who experimentally observed a linear relationship between bead width and travel speed. Their work assumed that the clad surface profile was given by the segment of a circle [13]. An analytical model for track geometry was introduced by Pinkerton and Li based on mass and energy balances using a circular approximation for the bead profile, which matched well with experiments for 316L and H13 tool steels [14]. Lalas *et al.* presented an analytical model based on surface tension differences between the clad and substrate, which was shown to work well for low process speeds [15]. A similar approach was used by Cheikh *et al.* who built a model based on surface tensions forces assuming a circular cross section [16]. Their work was validated using a low power (≤ 1 kW) cladding of 316L stainless steel on a low carbon substrate. The limitations of the majority of these analytical models are the required inputs for parameters such as catchment efficiency that are typically assumed or experimentally determined, and their inability to generate results that work for a wide range of laser powers, powder feed rates, travel speeds, and

material combinations. Previous work by Peyre *et al.* incorporated a combined analytical-numerical model to predict geometries and thermal fields in laser cladding applied to graded or single crystal materials, which was validated with a TA6V alloy [17].

Experimental based analyses for coating geometry have been completed by de Oliveira *et al.* who presented correlations for bead width and height as functions of laser power, powder feed rate, and travel speed raised to experimentally determined coefficients for 316 L stainless steel [18]. A similar approach was used by Davim who performed experiments using Diamalloy 2002 clad onto a 100Mn Cr W4-DIN substrate [19]. Nenadl *et al.* applied this regression technique to predict width and height for overlapping clads with optimal results for a parabolic assumption of the clad bead profile [20].

Contributions to the understanding of catchment efficiency in literature can also be grouped into two categories: those who present models of catchment efficiency and those who experimentally explore laser cladding parameters to optimize efficiency.

Among models of efficiency, Picasso *et al.* developed a numerical algorithm to compute powder efficiency accounting for the angular dependence of laser power absorption and melt pool shape based on a Gaussian heat distribution [5]. This model incorporated a ratio of the melt pool area to the powder jet area approximated as ellipses similar to the approach presented in this work. Lin and Steen presented a model of efficiency based on the geometry of the powder stream at the nozzle focus point, molten pool, and the degree of overlap between the powder stream and molten pool [21]. Frenk *et al.* proposed a model of efficiency for off-axis laser cladding with a theoretical maximum mass efficiency of 69% that was experimentally validated [22]. Partes studied the effects of melt pool geometry and nozzle alignment on catchment efficiency taking into account particle time of flight and surface melting under the beam [23].

Researchers that have studied parameter optimization for laser cladding of homogeneous alloys include de Oliviera *et al.* who analyzed the effect of laser power, powder

feed rate, and substrate travel speed on powder efficiency and proposed experimentally determined correlations to fit 316 L stainless steel cladding trials [18]. Gremaud *et al.* determined the optimal efficiency for thin walled structures made of single stacked laser clad beads. This work explored the effect of travel speed and powder feed rate on efficiency for a variety of alloys [24]. A select few researchers have also studied the catchment efficiency of laser cladding of Ni-WC. Zhou *et al.* studied the effect of laser spot dimensions with laser induction hybrid cladding on efficiency of Ni-WC coatings, but did not directly report values for efficiency. Increases in bead width and height were qualitatively correlated to increased capture efficiency [25]. Angelastro *et al.* optimized the process parameters of power, powder feed rate, and travel speed for a multilayer clad of Ni-WC with Co and Cr additions reporting only an overall value for deposition efficiency [26]. Only the recent work of Farahmand and Kovacevic has discriminated between the efficiency of the carbide and metal matrix for Ni-WC overlays for induction assisted cladding [27].

Previous work by several authors [13–16] shows that, for typical bead sizes, capillary forces are dominant over gravity, and the cross section of the bead can be approximated by a segment of a circle. For the small fractions of a circle typically involved, a segment of a circle and a parabola are nearly identical [20] with the advantage that a parabolic cross section results in a much simpler calculation of the cross sectional area without a loss of accuracy as shown in Appendix 4.1. Using this knowledge, the cross section of a single bead can be fully defined by the width and height. This work presents new predictions for height and width of a clad bead from fundamental concepts. The developed expressions are then compared with 13 experimental clad beads of Ni-WC deposited using a CO₂ laser. Laser power, powder feed rate, and travel speed are varied to study the effects of each parameter on bead geometry independently.

4.2 List of Symbols

Symbol	Unit	Description
A	m^2	Area of the clad bead
α	$\text{m}^2 \text{s}^{-1}$	Thermal diffusivity
c_P	$\text{J kg}^{-1}\text{K}^{-1}$	Heat capacity at constant pressure
d_p	m	Diameter of the powder cloud at the cladding nozzle working distance
η_{th}	1	Total thermal efficiency of the cladding process
η_m	1	Total combined catchment efficiency of the carbide and metal powders
η_{m_c}	1	Catchment efficiency of the carbide powders
η_{m_m}	1	Catchment efficiency of the metal powders
$f_{v_{c_b}}$	1	Volume fraction of carbide in the clad bead
h_m	m	Maximum height of the clad bead
k	$\text{W m}^{-1} \text{K}^{-1}$	Thermal conductivity
l_{s_c}	mm	Resolution of the microscope scale bar calibration sample
l_{s_m}	pixels	Variation in measured length of the Photoshop TM scale bar
m_p	kg	Total mass transfer of the powder feed
m_{c_p}	kg	Mass of carbide in the powder feed
m_{m_p}	kg	Mass density of metal powder in the powder feed
q	W	Nominal laser power
R	m	Circle radius whose segment approximates the bead profile
r_p	m	Radius of the powder cloud at the cladding nozzle working distance
ρ	kg m^{-3}	Density
ρ_c	kg m^{-3}	Density of the carbide
ρ_m	kg m^{-3}	Density of the metal powders
S	m	Sum of the comparison of experimental to theoretical values
σ	m	Beam distribution diameter
t	s	Time
t_p	s	Time for the powder collection test
τ	1	Dimensionless time
T	K	Isotherm temperature
T_0	K	Preheat temperature
T_m	K	Melting temperature
U	m s^{-1}	Substrate travel speed
W_f	1	Weight fraction
x, y, z	m	Cartesian coordinates
$1 - x$	1	Stoichiometry of carbon phase in the WC_{1-x} phase
y_m	m	Maximum width of an isotherm
z_m	m	Maximum depth of an isotherm

Symbol	Description
Superscripts	
$\hat{}$	Calculated value
\cdot	Rate
$*$	Dimensionless value
Subscripts	
b	Clad bead
d	Dilution area
eff	Effective value. For thermophysical properties, this represents the average value between the preheat temperature and the target isotherm temperature
HAZ	Heat affected zone (HAZ)
$melt$	Melting isotherm
Ni	Metal powers (also referred to as primarily nickel matrix)
r	Reinforcement area
t	Total area
WC	Tungsten carbide (WC) phase

4.3 Experimental Setup

4.3.1 Laser Cladding Equipment

The experimental setup consisted the following equipment:

- 6.0 kW CO₂ laser cladding system with a 10.6 μm wavelength.
- Water cooled copper mirror optics with a final beam focusing mirror focal length of 345 mm (13.595”).
- Continuous coaxial powder feeding nozzle capable of feed rates up to 150 g/min.
- Volumetrically controlled disk feeder set with an Ar carrier gas flow rate of 6.5 L/min.
- CNC controlled x-y lathe bed positioning system for cylindrical substrates with a mounted four jaw chuck headstock and tailstock spindle support.

4.3.2 Powder Feed

The powder feed used in this analysis was a mixture of cast spherical fused tungsten carbide and a Ni-Cr-B-Si blend of metals comprising the metal powders. The two component powders were mixed to achieve a target 60%-40% weight fraction of carbide to metal powder respectively. Size range, reported manufacturer hardness range, weight fractions, and densities are listed in Table 4.1.

Table 4.1: Properties of powders used in the experiments

Component	Size Range (μm)	Expected Hardness Range in the Deposit (HV)	Weight Fraction W_f (%)	Density ρ (kg/m^3)
Carbide Powder	45-106	2700-3500	62.60	16,896*
Metal Powder	53-150	425	37.40	8100

* Calculated from a theoretical crystal structure analysis of WC_{1-x} by Wood *et. al* [28].

4.3.3 Experimental Matrix

The parameters tested were laser power q , powder feed rate \dot{m}_p , and travel speed U because there is direct control over them. It is generally accepted that these parameters have the largest influence on the process. The test matrix is set up as a modified fractional factorial design with 5 levels for each of the 3 factors. The centre point (Bead 3), which represents industrial parameters, is common to all three test blocks totalling 13 experiments. This design only considers the main effects and does not consider the combined effects of a full factorial analysis, but these interactions effects do not affect the conclusions obtained. To eliminate procedural bias the test order was randomized by assigning each test a random number and sorting the tests low to high. The target and measured values for each parameter are summarized in Table 4.2. Additional testing and

repetition at each parameter level was not possible due to the nature of using industrial production equipment for testing and allotted experiment time limited to a single day.

Table 4.2: Experimental matrix for cladding of Ni-WC onto a 4145-MOD substrate for all beads. Target preheat was 260 °C (500 °F)

Bead Number	Laser Power q (kW)		Powder Feed Rate \dot{m}_p (g/min)		Target Travel Speed U (mm/s)		Average Temperature (°C)
	Target	Measured	Target	Measured	Target	Measured	Measured
Bead 1*†	5.0	4.98	50	49.20	25.40	25.45	257
Bead 2*	3.0	3.09	50	49.20	25.40	25.45	257
Bead 3*	4.0	3.99	50	49.20	25.40	25.45	261
Bead 4	4.0	3.99	50	49.20	19.05	19.09	258
Bead 5†	4.0	3.99	30	28.80	25.40	25.45	268
Bead 6†	4.0	3.99	50	49.20	31.75	71.81	264
Bead 7*	4.5	4.54	50	49.20	25.40	25.45	263
Bead 8*	3.5	3.53	50	49.20	25.40	25.45	264
Bead 9*	4.0	3.98	50	49.20	12.70	12.73	263
Bead 10†	4.0	3.98	60	62.95	25.40	25.45	264
Bead 11†	4.0	3.98	40	42.25	25.40	25.45	264
Bead 12	4.0	3.98	50	49.20	38.10	38.18	267
Bead 13†	4.0	3.98	70	68.30	25.40	25.45	263

* Laser power measurement performed immediately before test.

† Powder feed rate measurement performed immediately before test.

4.3.4 Cladding Procedure

The substrate material was a 4145 MOD cylinder with dimensions 254 mm (10”) in length, 20.3 mm (0.8”) thick, and 165 mm (6.5”) on the outer diameter. The loaded sample was centered to within 25 μm (0.001”) using a rotational alignment dial indicator. Cladding was performed 19 mm (0.75”) out of focus beyond the focal point conforming to typical industrial practices. The outer surface of the cylinder was prepared with an initial acetone wash to remove oil and grease followed by manual grinding between passes to remove remaining contaminants. A preheat of 260°C (500 F) was applied to the

rotating substrate using a type-K contact thermocouple at the 0° , 90° , 180° , and 270° positions on the cylinder along the rotation direction. These temperature measurements were performed along the centreline of the upcoming bead. Some variation in preheat temperatures was observed across the four measured points, but values within 25°C of each other and the target preheat temperature were taken as acceptable.

Calibration of the laser power and powder feed rates was performed at the beginning of the experiment and before trials with a parameter change to confirm levels at the substrate. Laser power was measured using a 10 kW Comet 10K-HD power probe, and feed rate was measured by manually capturing the powder flow for $t_p = 2$ min, measuring the accumulated mass, and reporting a per minute average rate. Prior to the start of

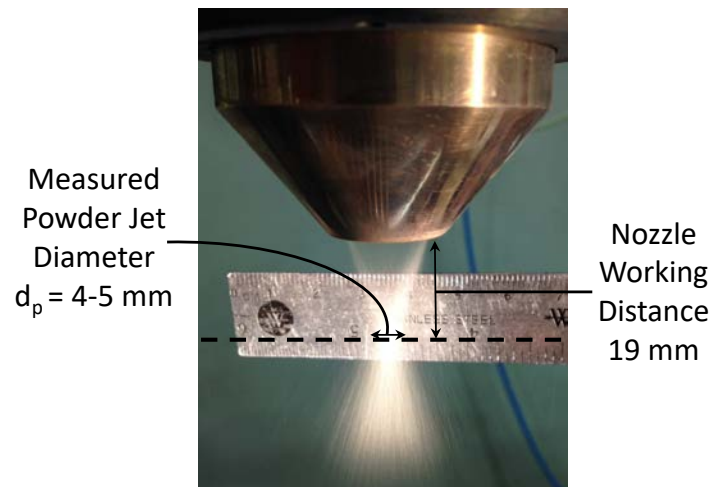


Figure 4.1: Photo of the powder cloud showing the powder jet focus at the nozzle working distance for the experimental trials.

The laser power, powder feed, and substrate rotation were programmed to begin simultaneously with the shutter closed. This momentarily delayed the start of cladding and allowed the parameters time to ramp up to test levels. At the same time, an Ar shield gas purge began with the shield gas flow rate set at 45 cfh for the remainder of the test. After a 5 second waiting period, the shutter was opened and the cladding began. A 360° bead was deposited with a continuous 2 mm helical pitch followed immediately and 180° overlapping bead without interruption. The overlapping beads were not included as part of this study. A 12.5 mm (0.5”) gap between bead centres was left for post-clad sectioning, and beads were placed 51 mm (2”) away from the edges of the coupon to prevent heat accumulation effects. Once the 180° overlapping bead was completed, the shutter was closed effectively stopping the clad process while the laser power and powder feed rate ramped down. The travel speed was set to shift rapidly to the maximum value of 1500°/min to complete the second full rotation and place the starting point directly beneath the nozzle. Following the completion of rotation, a thermocouple was used to measure the temperature of the crown of the bead for 5 minutes. Figure (4.2) summarizes the timeline of the experiments as described above. Figure (4.3) shows an example of the in-process Ni-WC clad deposit highlighting the rotation direction of the cylinder.

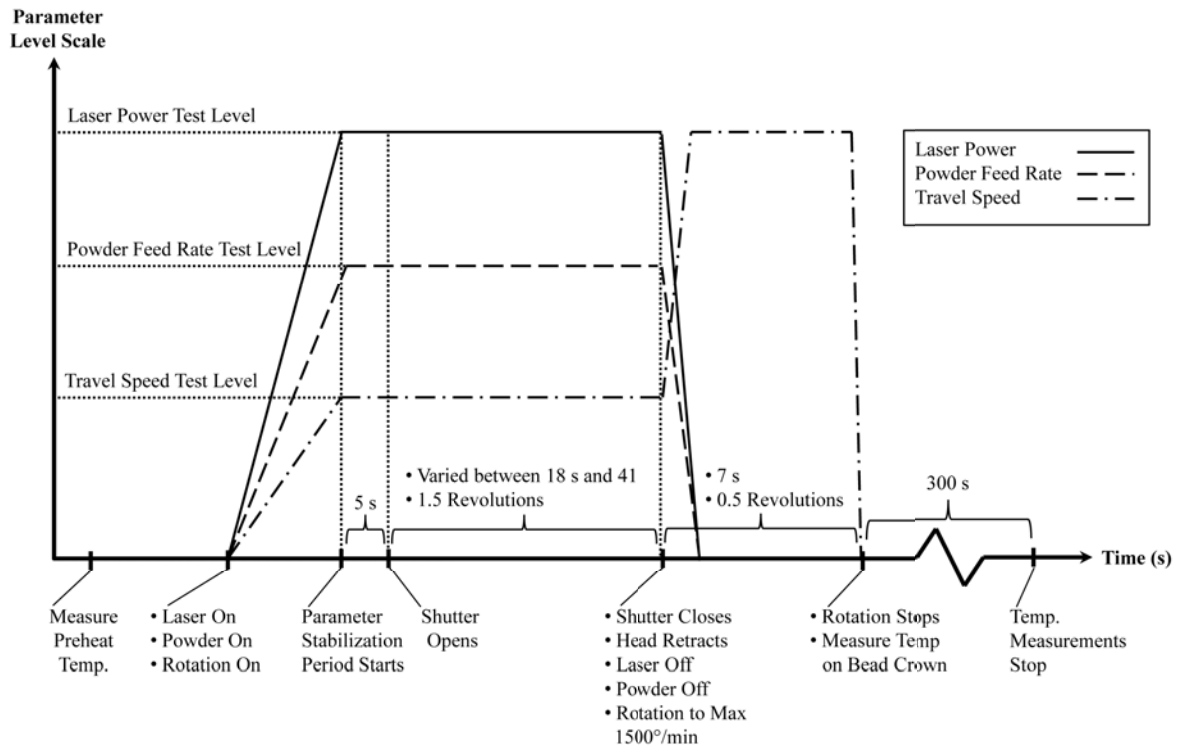


Figure 4.2: Procedural timeline for the cladding experiments.

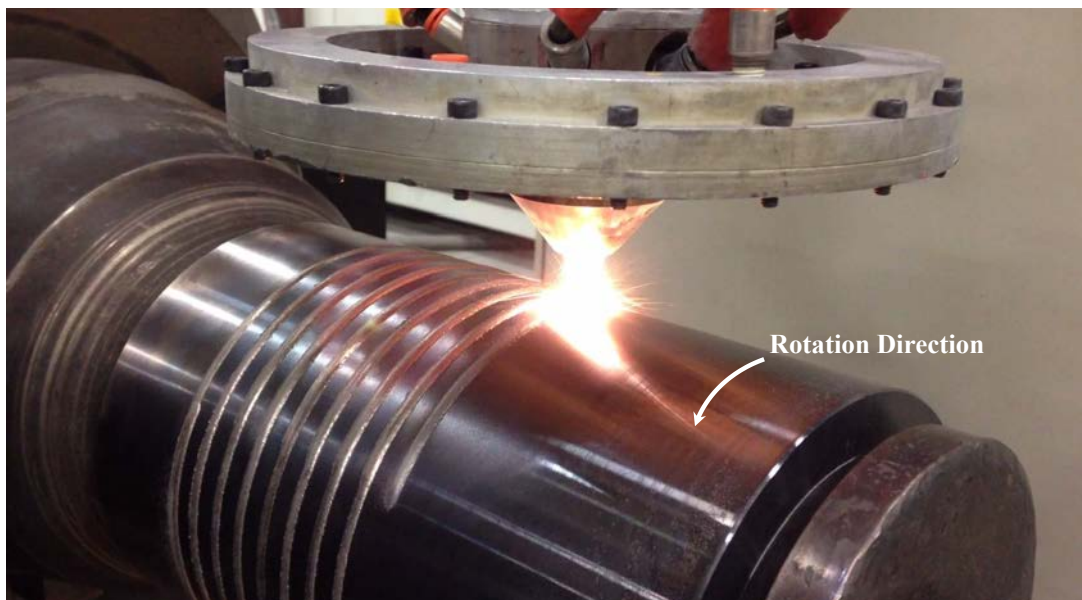


Figure 4.3: Laser cladding during the Bead 9 run.

4.3.5 Test Coupon Preparation and Analysis

Photos of the pre-sectioned beads were taken using a Nikon SMZ 745T stereomicroscope at the 270° position relative to top-dead centre of the start of the bead. These surface photos were used to get an average bead width measurement from the visible bead area using Adobe PhotoshopTM. This area was determined by analyzing pixels of the selected region and converting pixel measurements to an actual area using the image scale bar of known length. This area is then divided by the bead length in the photo to provide a bead width averaged over the visible length of the bead. This method was considered to be more representative of the bead width than measurements traditionally taken from cross section samples, which were subject to visible variation based on the location of the cut. The digital measurements were used as the measured width values y_m for this analysis.

All test beads were then sectioned from the 270° position from the start of the bead using a wet saw, mounted into a Bakelite puck, polished to a $0.04 \mu\text{m}$ finish, and etched with 3% Nital solution for 5 seconds. The etch revealed the HAZ isotherm clearly, but had little to no effect on the overlay microstructure. Micrographs of the samples were taken using a Nikon Eclipse MA200 inverted microscope and stitched together to create panoramas of the entire cross section using PhotoshopTM. The maximum height of the clad h_m , maximum width of the HAZ, maximum depth of the HAZ, reinforcement area A_r , and total area A_t were measured. Due to the presence of machining marks on the sample surface, a straight line drawn between the clad toes was used to divide above and below surface levels. These areas and features are shown in Figure (4.4).

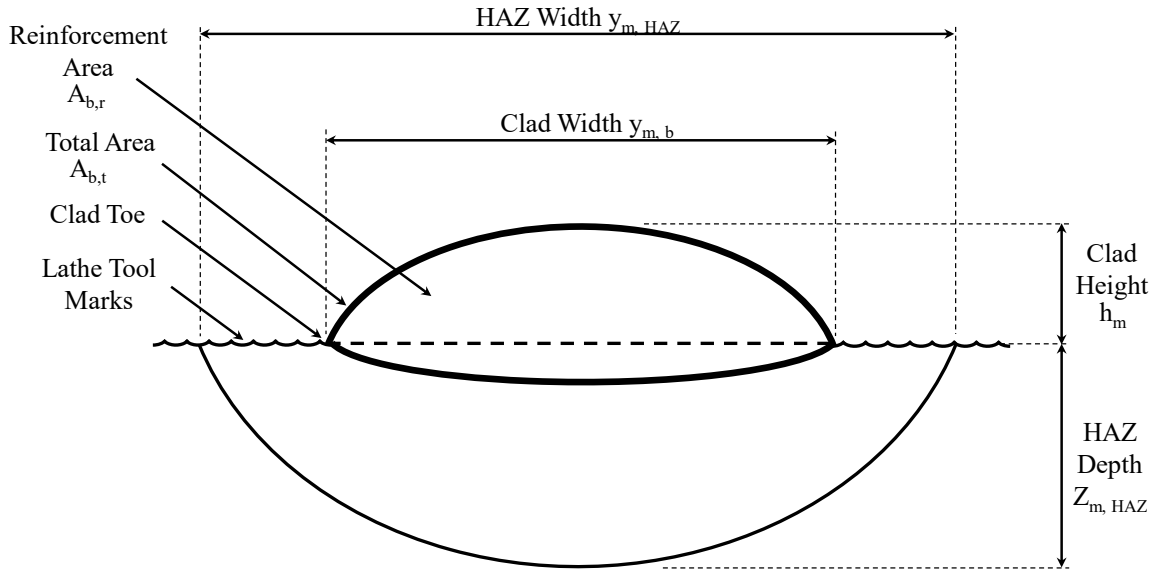


Figure 4.4: Schematic of a cross section of a deposited clad bead from the experiments.

The area fraction of the carbide, $f_{v_{cb}}$, was measured using a PythonTM script developed at the Canadian Centre for Welding and Joining that identified the carbides based on colour contrast with the matrix. The clad area was isolated from the remainder of the cross section, and the brightness was adjusted to maximize the contrast difference between the two components.

4.4 Thermal Analysis for Bead Width

There is general agreement in literature that the geometry of the molten region during cladding dictates the width of the bead [4–7, 9, 13–17, 23, 29]. By decoupling the heat and mass transfer aspects of the process and considering only the temperature profile of the substrate, the pool can be mathematically represented using previously developed solutions. The maximum isotherm width for a point heat source is analyzed in detail in [30]. A point heat source analysis predicts that the maximum bead width is in some cases

smaller than the beam focus, which suggests a point heat source is not the best approach. The next step in accuracy improvement of the analysis is the Gaussian heat source developed by Eagar [31] consistent with the lowest order fundamental mode TEM₀₀ beam. The use of a Gaussian heat source is only because it introduces an additional degree of freedom for a heat source of finite size. For this analysis the beam has previously been characterized as the TEM_{01*} mode, the "doughnut hole" mode, which has two peaks and a dip in intensity in the centre, but has a much closer profile to the Gaussian distribution than the point heat source. A schematic of the beam, clad pool, and distributed heat source is shown in Figure (4.5).

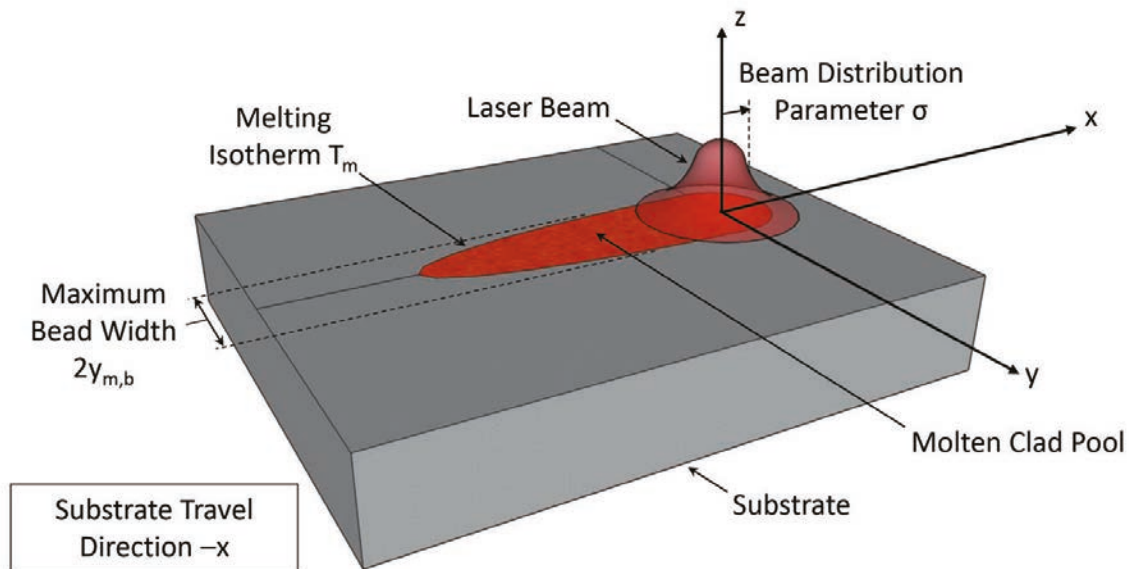


Figure 4.5: Schematic of the laser cladding process without powder.

In 1983 Eagar and Tsai published a dimensionless general solution for isotherm geometry for a travelling Gaussian heat distribution shown in Equation (4.1) [31]. The notation from Wood *et. al* has been applied to Equation (4.1) for consistency with the work presented here [30]. While Equation (4.1) does not account for the effects of fluid flow in the molten pool, there is evidence to support that the role of convection is not

dominate due to the presence of solid particles in the melt pool for Ni-WC cladding, which is the focus of Chapter (5).

$$T^* = \frac{1}{\sqrt{2\pi}} \int_0^\infty d\tau \frac{\tau^{-\frac{1}{2}}}{\tau + \sigma^{*2}} e^{-\frac{x^{*2} + y^{*2} + 2x^*\tau + \tau^2}{2\tau + 2\sigma^{*2}} - \frac{z^{*2}}{2\tau}} \quad (4.1)$$

where T^* is the definition for dimensionless temperature developed in Wood *et. al* [30] (Equation (4.2)), τ is the dimensionless time (Equation (4.3)), σ^* is the dimensionless distribution parameter (Equation(4.4)), x^* is the dimensionless distance x (Equation (4.5)), y^* is the dimensionless distance y (Equation (4.6)), and z^* is the dimensionless distance z (Equation (4.7)).

$$T^* = (T - T_0) \frac{4\pi k_{eff} \alpha_{eff}}{\eta_{th} q_{eff} U} \quad (4.2)$$

where T is the isotherm temperature (K), T_0 is the preheat temperature (K), k_{eff} is the effective thermal conductivity of the substrate (W/mK), α_{eff} is the effective thermal diffusivity of the substrate (m^2/s), η_{th} is the effective thermal efficiency of the cladding process, q_{eff} is the effective laser power described in detail in a subsequent section (W), and U is the travel speed (m/s). Equations (4.3) and (4.4) show the formulae for dimensionless time and dimensionless distribution parameter respectively.

$$\tau = \frac{U^2 t}{2\alpha_{eff}} \quad (4.3)$$

$$\sigma^* = \frac{U\sigma}{2\alpha_{eff}} \quad (4.4)$$

where t is time (s), σ is the beam distribution parameter, which represents the location measured from the origin where the beam power falls to $1/e^2$ of its maximum value (m). The dimensionless Cartesian coordinates x^* , y^* , and z^* are shown in Equations (4.5), (4.6), and (4.7).

$$x^* = \frac{Ux}{2\alpha_{eff}} \quad (4.5)$$

$$y^* = \frac{Uy}{2\alpha_{eff}} \quad (4.6)$$

$$z^* = \frac{Uz}{2\alpha_{eff}} \quad (4.7)$$

where x is the distance in the x direction (m), y is the distance in the y direction (m), and z is the distance in the z direction (m). The dimensionless distances x^* , y^* , and z^* are shown below in Equations (4.5), (4.6), and (4.7) respectively. Reliable material properties as a function of temperature namely thermal conductivity k , specific heat capacity c_P , density ρ and thermal diffusivity α are necessary to convert the general, dimensionless results of Equations (4.1) and (4.2) to dimensional values that can be used by engineers in practice. The approach in this work is to use a single value that represents an average from the target process preheat temperature 260°C (533 K) up to the A_{e_1} temperature 708°C (981 K) for the HAZ isotherm. A similar approach is used for the melting isotherm taking an average value from the preheat temperature up to melting temperature of the 4145-MOD substrate. For this work the melting temperature was taken as the equilibrium solidus temperature 1419°C (1692 K). The choice of solidus compared to liquidus did not have an meaningful effect on the results obtained due to the narrow range of melting for the substrate alloy. Though laser cladding is a highly non-equilibrium process with heating

rates on the order of thousands of degrees per second [32], the equilibrium values serve as a good starting point estimate. The procedure of averaging of parameters over ranges of hundreds of degrees did not have an order of magnitude effect on the results between the HAZ and melting effective values. The effective values used in this analysis are listed below in Table 4.3. A detailed review of the methods and models used to produce these thermophysical property values has been included in Appendix 4.2 as-published and in Appendix A in complete detail.

Table 4.3: Effective thermophysical properties of 4145-MOD steel

Target Isotherm	Temperature Range (K)	Effective Thermal Conductivity k_{eff} (W/mK)	Effective Specific Heat Capacity $c_{P_{eff}}$ (J/kgK)	Effective Density ρ_{eff} (kg/m ³)	Effective Thermal Diffusivity α_{eff} (m ² /s)
HAZ	533-981	32.52	737.61	7689	$5.73 * 10^{-6}$
Melting	533-1692	30.15	743.97	7590	$5.34 * 10^{-6}$

4.4.1 Calculation of Isotherm Width and Depth

The calculation of maximum isotherm width and depth (\widehat{y}_m^* and \widehat{z}_m^*) corresponds to solving Equation (4.1) for y^* at $z^* = 0$ and z^* at $y^* = 0$ respectively. A MATLABTM optimization algorithm was developed to compute the integral in Equation (4.1), solve implicitly for y^* and z^* , and identify the exact maximum values for all possible solutions of Eagar's equation. The algorithm has three steps and incorporates the program's built in non-linear solvers *fminsearch* and *fzero*. The unconstrained non-linear optimization function *fminsearch* finds the local minimum of a objective function of several variables from an initial estimate [33]. The non-linear solver *fzero* finds the roots or zeros of an objective function given a starting point estimate [34]. For the analysis here, the limits of integration for Equation (4.1) were taken between $\tau = 0$ and $\tau = 50$, which previous work has shown satisfies the infinite limit computationally for the peak temperature of

the integral. The dimensional distribution parameter was not directly measured but was calculated from experimental data to be 1.62 mm, which is described in detail in Step 3 in a subsequent section. The convergence criterion for all objective functions and target variables was set at 10^{-6} . The first two steps for the algorithm for \widehat{y}_m^* are as follows:

Step 1. Input values of T^* and x^* to the function, which outputs the corresponding \widehat{y}^* as a solution to Equation (4.1). Step 1 uses *fzero* to identify the \widehat{y}^* that forces the input value of T^* to the script to equal the calculated T^* from Equation (4.1). The objective function for *fzero* is shown in Equation (4.8).

$$\widehat{T}_i^* = T_{input}^* - \widehat{T}^* \quad (4.8)$$

where \widehat{T}_i^* is the calculated value for T^* for iteration i , T_{input}^* is the input value of T^* to the script, and \widehat{T}^* is the calculated value of T^* from Equation (4.1). The seed for \widehat{y}^* was chosen to be $1/T^*$, which represents the a solution for maximum width developed by Wood *et. al* for slow moving heat sources [30].

Step 2. For an input of T^* , Step 2 outputs the maximum \widehat{y}^* , \widehat{y}_m^* , by repeatedly calling Step 1 with an input x^* , solving Equation (4.1), returning the corresponding \widehat{y}^* , and testing using *fminsearch* whether or not the returned \widehat{y}^* was the minimum value representing the location of maximum width. The objective function for *fminsearch* is shown in Equation (4.9):

$$\widehat{y}_i^* = -\max(\widehat{y}^*) \quad (4.9)$$

If \widehat{y}_{i+1}^* is less than \widehat{y}_i^* , *fminsearch* selects a new adjacent x^* , iteratively solving until a local minimum is found. The surface isotherm is known to have a single

minimum value at \widehat{y}_m^* , therefore the returned value represents the global minimum. The negative in Equation (4.9) is necessary to compute the solution on the $-y^*$ axis. The seed for x^* was chosen to be 0 because all isotherms cross the y^* axis.

The algorithm for \widehat{z}_m^* uses a parallel approach to \widehat{y}_m^* with a few modifications: Equation (4.1) is solved with $y^* = 0$, $z^* = 0$ is the seed for Step 1 and $\max(\widehat{z}^*)$ is the objective function for Step 2. It is noted that the maximum \widehat{x}^* calculated from the \widehat{y}_m^* algorithm, $\widehat{x}_{m_y}^*$, was distinguished from the maximum \widehat{x}^* calculated from the \widehat{z}_m^* algorithm, $\widehat{x}_{m_z}^*$. These two x^* values were indeed different, indicating that the x^* coordinate corresponding to the maximum width does not coincide with the x^* coordinate of the maximum depth.

Determination of T^* in Equation (4.2) as part of the solution algorithm for maximum width and depth requires a value for the thermal efficiency, which presents the fraction of the total thermal energy imparted to the substrate from the process either directly from the laser beam exposure or preheat of the in-flight powders. The thermal efficiency has been taken to be 0.3 for this analysis as reported for CO₂ laser cladding on a steel substrate [35]. This literature value for thermal efficiency is used in the absence of a fundamental expression for thermal efficiency which is widely agreed to vary with laser power, powder feed rate, travel speed, laser wavelength, and substrate material. Typically, η_{th} is a fitting parameter for similar numerical analyses where the heat source geometry and isotherm temperature are known, which is not the case in this analysis.

Figure (4.6) shows a graphic of the dimensionless surface and centreline isotherms for the melting isotherm of Bead 3. The x^* , y^* coordinates of the maximum are directly output from the optimization, which are easily converted to dimensional coordinates using Equations (4.5) and (4.6).

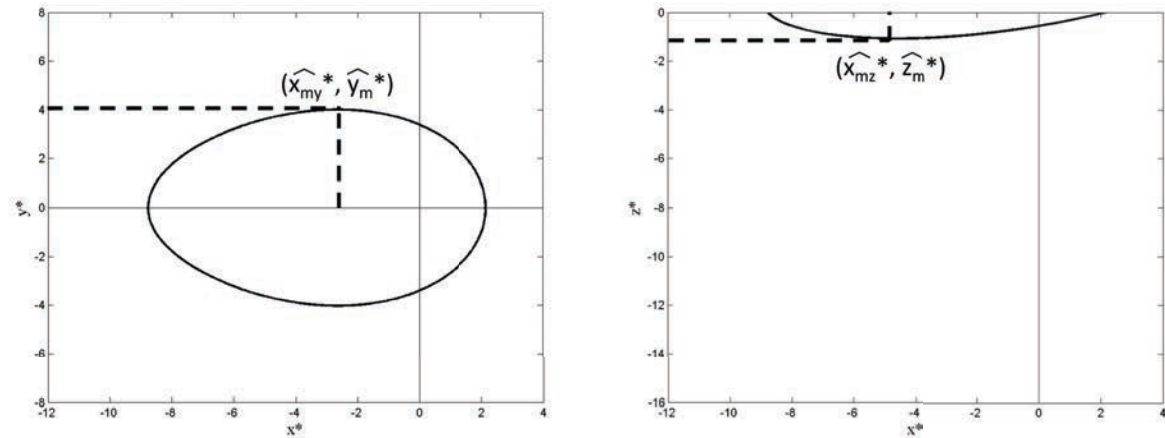


Figure 4.6: Left: Dimensionless surface isotherm showing the location of maximum width for Bead 3. Right: Dimensionless centreline isotherm showing the maximum depth location for Bead 3. Both figures use the Bead 3 parameters from Table 4.2.

4.4.2 Effect of the Bead on Heat Transfer

The formation of a continuous bead during the cladding process provides an additional channel for the dissipation of heat from the laser. Until now this effect has not been quantified for any welding process. The effect is expected to be small, and it is analyzed in detail below. Figure (4.7) schematically outlines the heat conduction pathways of the process showing the conduction through the reinforcement q_r .

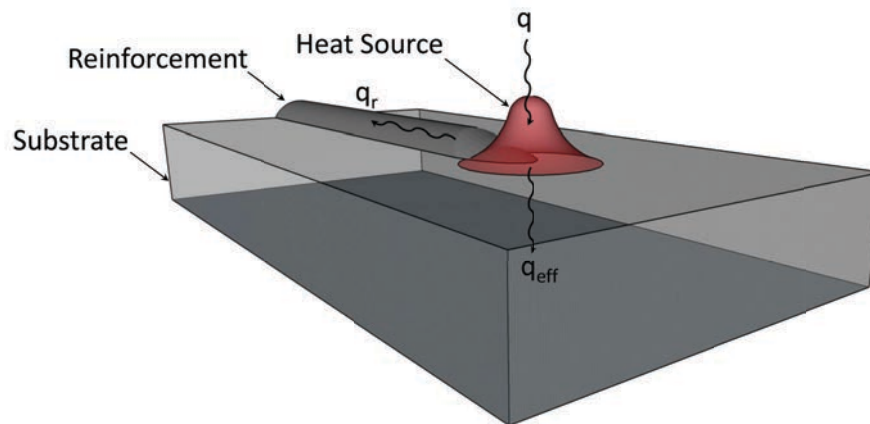


Figure 4.7: Schematic of heat conduction through the bead reinforcement during laser cladding.

Equation (4.10) presents an expression for a q_{eff} that accounts for heat conduction through the bead. This equation is based on approximating the isotherms using a point heat source on a thick plate.

$$q_{eff} = q \left(1 - \frac{1}{2\pi} k_r^* A_{b,r}^* T^{*2} \right) \quad (4.10)$$

where q_{eff} is the effective input power of the process (W), q is the nominal laser power, k_r^* is the dimensionless conduction ratio (Equation (4.11)), and $A_{b,r}^*$ is the dimensionless reinforcement area (Equation (4.13)).

$$k_r^* = \frac{k_r}{k} \quad (4.11)$$

where k_r is the thermal conductivity of the deposited clad bead (W/mK), which in this work represents a solid matrix of Ni interspersed with uniformly distributed spheres of WC. Maxwell presented the following equation to represent the effective conductivity for this case [36]:

$$k_r = \left[\frac{2k_{WC} + k_{Ni} + f_{v_{cb}}(k_{WC} - k_{Ni})}{2k_{WC} + k_{Ni} - 2f_{v_{cb}}(k_{WC} - k_{Ni})} \right] k_{Ni} \quad (4.12)$$

where k_{WC} is the conductivity of the WC spheres in the clad, k_{Ni} is the conductivity of the primarily nickel metal powders in the clad, and $f_{v_{cb}}$ is the volume fraction of carbide in the deposited clad. The values used for this analysis were $k_{WC,melt} = 64.32$ W/mK and $k_{Ni,melt} = 37.00$ W/mK for the melting isotherm, and $k_{WC,HAZ} = 70.04$ W/mK and $k_{Ni,HAZ} = 41.68$ W/mK for the optimized HAZ isotherm (1228 K). The description of the HAZ isotherm calculation is described in detail in a subsequent section, and the full discussion of the effective conductivities for WC and Ni is included in Appendix 4.2

(as-published/abbreviated) and Appendix A (complete).

$$A_{b,r}^* = \frac{A_{b,r}U^2}{4\alpha_{eff}^2} \quad (4.13)$$

where $A_{b,r}$ is the bead reinforcement area defined in Figure (4.4) (mm^2). Equation (4.10) is valid when the reinforcement is isothermal, which must satisfy the condition $\frac{1}{2}A_{b,r}^*T^* < 1$. This condition was met for all tests for both the HAZ and melting isotherms. The q_{eff} for the HAZ was found to be greater than 99% of q for all tests. For the melting isotherm, the q_{eff} was greater than 97% of the nominal power.

4.4.3 Estimation of the Beam Distribution Parameter σ

This work did not have a beam profilometer to characterize the laser power density and measure the distribution parameter directly. The σ was estimated by determining the value that minimized the difference between the predicted and measured widths and depths of the HAZ isotherm for all 13 experimental trials. The temperature of the HAZ isotherm (T_{HAZ}) was unknown because of the highly non-equilibrium conditions of the cladding process, which preliminary calculations show were on the order of thousands of degrees per second [32]. The HAZ temperature was left as an unknown in the algorithm shown below in Step 3. All dimensionless solutions from Steps 1 and 2 were converted to dimensional values to be able to solve for the single $\hat{\sigma}$ and $\widehat{T_{HAZ}}$ common to all experiments.

Step 3. Input values of $y_{m,HAZ}^*$, $z_{m,HAZ}^*$, T_0 , η_{th} , $k_{eff,HAZ}$, $\alpha_{eff,HAZ}$, $q_{eff,HAZ}$, U to the function.

The outputs are single values for $\hat{\sigma}$ and $\widehat{T_{HAZ}}$ that minimize the sum of the natural logs of the difference between the calculated and measured values of width and

depth for the HAZ, S , using *fminsearch* for $n = 13$ experiments:

$$S = \sum_{i=1}^n \left\{ \left[\ln \left(\frac{\widehat{y_{m,HAZ}}}{y_{m,HAZ}} \right) \right]^2 + \left[\ln \left(\frac{\widehat{z_{m,HAZ}}}{z_{m,HAZ}} \right) \right]^2 \right\} \quad (4.14)$$

where S is the total value of the sum of the differences between the calculated and measured widths and depths for the HAZ, $\widehat{y_{m,HAZ}}$ is the calculated value of maximum width for the HAZ, $y_{m,HAZ}$ is the measured value of maximum width for the HAZ, $\widehat{z_{m,HAZ}}$ is the calculated value of maximum depth for the HAZ, $z_{m,HAZ}$ is the measured value of maximum width for the HAZ. The seed values for σ and T_{HAZ} were 1 mm and the 4145-MOD A_{e1} temperature 981 K. Step 3 makes continuous calls to Steps 1 and 2 in order to calculate values for $\widehat{y_{m,HAZ}}$ and $\widehat{z_{m,HAZ}}$.

The optimized values for $\widehat{\sigma}$ and $\widehat{T_{HAZ}}$ were 1.62 mm and 1228 K respectively. The findings for sigma were compared to burn marks into acrylic plastic at the same working distance. The second order moment of the beam, which represents the beam diameter from ISO-11146-1, has a value of $4\widehat{\sigma}$ and is shown in Figure (4.8) [37]. The match between the burn

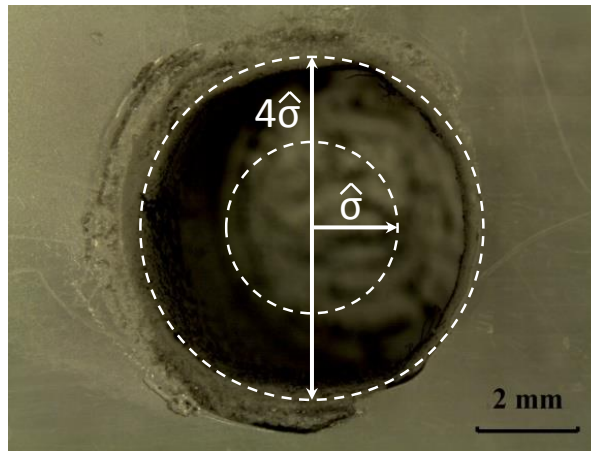


Figure 4.8: Comparison of the calculated σ to burn marks made on an acrylic substrate. The working distance was 19 mm matching the experimental trials.

4.5 Estimation of Catchment Efficiency η_m

The catchment efficiency in laser cladding represents the fraction of process powders that fall inside the weld pool and stick to the molten surface contributing to the formation of the clad bead. In some literature models of efficiency, the molten pool has been approximated by the beam area [3, 21, 38]. Figure (4.9) below shows a comparison of the projected laser area assumption of the molten pool to a typical isotherm generated in this work. The visual comparison suggests that the laser beam spot is not the best approximation of the molten pool, which is critical to this analysis of efficiency.

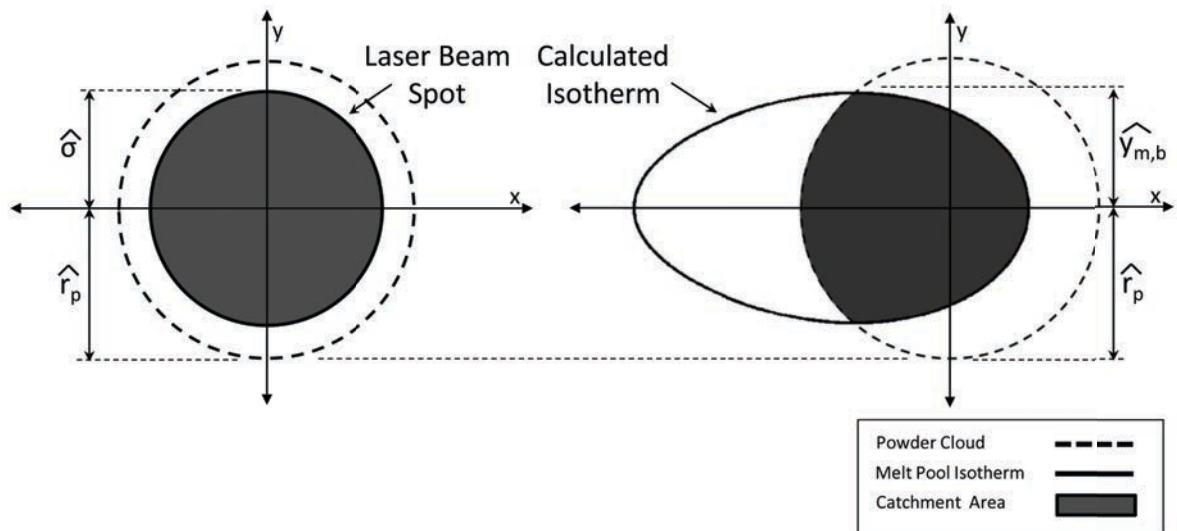


Figure 4.9: Left: Overlap of the powder cloud with the beam spot approximation for the melting isotherm. Right: Overlap of the powder cloud with the experimental matrix centre point melting isotherm (Bead 3) calculated from this work. The dimensions are to scale with $\widehat{\sigma} = 1.62$ mm, $\widehat{y}_{m,b} = 1.69$ mm, and $\widehat{r}_p = 1.77$ mm.

This work presents a new approach to determine these important areas as a fundamental part of our understanding of catchment efficiency in coaxial laser cladding. In this analysis three important assumptions are made:

- All powders that contact the molten pool adhere to the surface.

- All solid particles colliding with the unmelted substrate surface are lost and do not become part of the bead.
- The powder is evenly distributed across the powder cloud.

These assumptions of powders surface interactions are typical of existing models in literature [3, 21]. Balu *et. al* have shown for a coaxial powder feed of Ni-WC with similar size and composition to the powder used in this work that the powder cloud concentration profile is normally distributed [39]. For this iteration of the catchment model, the simplification of the powder distribution is made as an alternative to the complexity required to simultaneously solve the integral of the powder distribution and the integral of the implicit function describing the melt pool (Equation (4.1)).

For the Ni-WC powder used in this work, the authors have previously shown that the catchment efficiency of the metal powder, η_{m_m} , and the catchment efficiency of the carbide, η_{m_c} , were different depending on the powder feed rate of the process [28]. The aim of this estimation of efficiency is to predict the total catchment efficiency, η_m of the combined powder components to compare to Equation (4.15) proposed in the author's previous work [28].

$$\eta_m = \frac{U}{\dot{m}_p} [A_{b,t} f_{v_{c_b}} \rho_c + A_{b,r} (1 - f_{v_{c_b}}) \rho_m] \quad (4.15)$$

where η_m is the total catchment efficiency of the powders, $A_{b,t}$ is the total area of the clad bead, and where ρ_c and ρ_m are the density of the carbide and metal powders respectively from Table 4.1.

The model of catchment efficiency presented here is based on an approximation for a point heat source isotherm. The intersection of the melting temperature isotherm with the powder cloud area is represented as half the area of an ellipse whose major axis is

the twice radius of the powder jet and minor axis is the total weld pool width. This model assumes that the molten pool area ahead of the heat source is small relative to the overlapping area in the bead tail, which is typically the case for these isotherms. Figure (4.10) schematically shows the area approximations of the model relative to a point heat source isotherm.

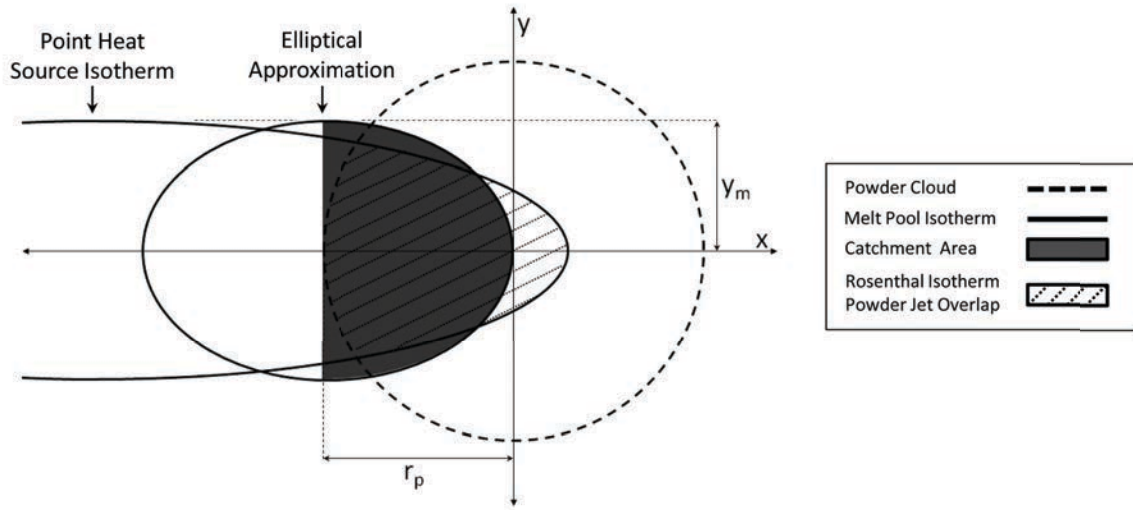


Figure 4.10: Proposed elliptical approximation of the catchment area compared with a Rosenthal isotherm overlapping the projected powder cloud area.

This ratio of the elliptical area of the molten pool to the total circular area of the powder cloud simplifies to the relation presented in Equation (4.16). The only two parameters necessary to predict catchment efficiency are the width of the molten pool y_m calculated from the Gaussian heat source and the radius of the powder jet.

$$\widehat{\eta}_m = \frac{\widehat{y}_{m,b}}{2\widehat{r}_p} \quad (4.16)$$

where $\widehat{\eta}_m$ is the calculated overall catchment efficiency, $\widehat{y}_{m,b}$ is the calculated value of dimensional width for the clad, \widehat{r}_p is the calculated value for the radius of the powder jet. The value of r_p could not be measured directly with the precision necessary to obtain

accurate values for the model. Powder radius was left as an adjustment parameter, and a value was selected that minimized the difference between the model and experiments. The value for \widehat{r}_p was determined to be 1.77 mm, which is comparable to the measured range of 2-2.5 mm.

4.6 Prediction of Bead Height h_m

It has been observed that the shape of the crown is similar for nearly all clads. The curvature of the bead profile has previously been modelled as parabolic, sinusoidal, and a circular arc [13,20]. Nenadl *et. al* proposed that the parabolic profile was the best fit for modelling overlapping beads geometries [20]. Using the simple geometric relation between the area, width, and height of a parabola, the reinforcement area of the bead can be expressed as:

$$\widehat{A}_{b,r} = \frac{4}{3} \widehat{y}_{m,b} \widehat{h}_m \quad (4.17)$$

where $\widehat{A}_{b,r}$ is the calculated value for the bead reinforcement area and \widehat{h}_m is the calculated maximum height of the bead (m). The height of a clad bead can be ascertained by combining three concepts: a mass balance of the process, an understanding of the bead profile of a cross section, and the catchment efficiency of the process. Using a mass balance similar to Colaço *et. al* [13], the reinforcement area of the bead can be shown to be a function of the mass transfer rate \dot{m}_p , travel speed U , component powder densities ρ_c , ρ_m and the catchment efficiency $\widehat{\eta}_m$ of the process shown in Equation (4.18).

$$\widehat{A}_{b,r} = \frac{\widehat{\eta}_m \dot{m}_p}{[f_{v_{c_b}} \rho_c + (1 - f_{v_{c_b}}) \rho_m] U} \quad (4.18)$$

Combining Equations (4.16), (4.17), and (4.18), we arrive at an expression to predict maximum bead height that depends only on parameters known prior to cladding.

$$\widehat{h}_m = \frac{3\dot{m}_p}{8U [f_{v_{c_b}}\rho_c + (1 - f_{v_{c_b}})\rho_m] \widehat{r}_p} \quad (4.19)$$

4.7 Comparison with Experiments

The surface measurements for width were taken from stereo photographs of the beads prior to sectioning, such as the one shown in Figure (4.11). The area outlined in white is

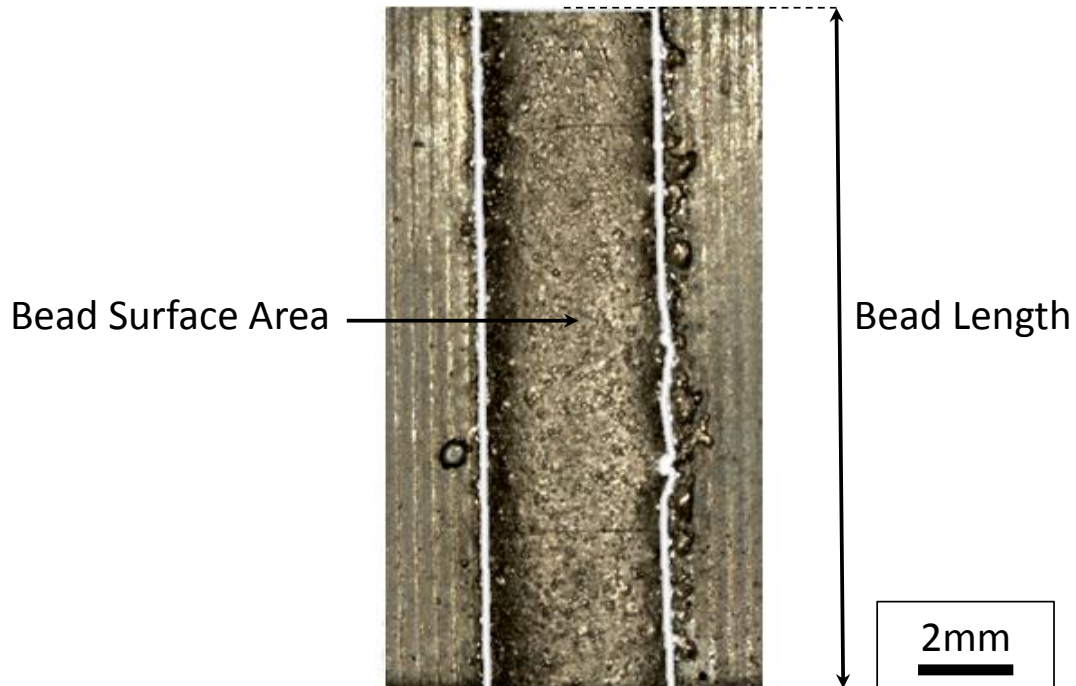


Figure 4.11: Stereomicrograph of the Bead 3 surface finish of the clad used to calculate an average width over the visible length of the bead.

The measurements of all remaining bead features required direct measurements from cross sections of the experimental beads. Figure (4.12) shows a typical cross section of a Ni-WC clad.

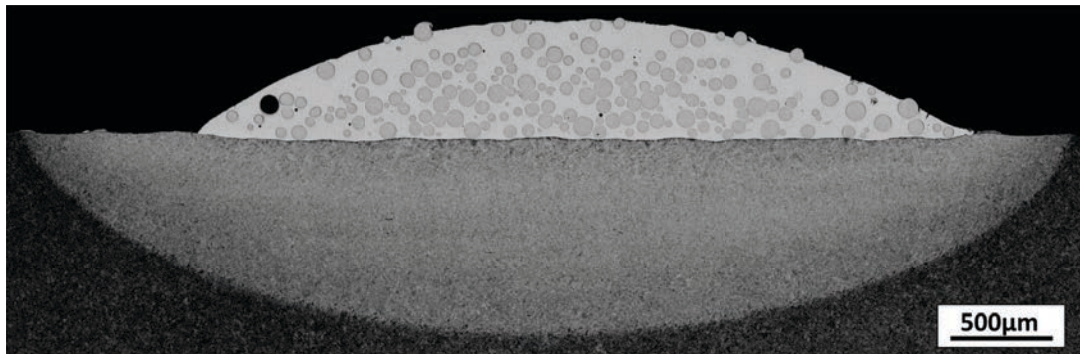


Figure 4.12: Cross section of Bead 3 etched with 3% Nital for 5 seconds.

Voids in clad bead were also occasionally observed. These features were typically accounted for as matrix material in the calculations, which is a reasonable approximation for beads with low porosity such as those in this work. Figure (4.13) shows the output of the PythonTM script highlighting the carbide area. The carbide colouration is randomly generated by the program.



Figure 4.13: Python script output showing carbide area for Bead 3.

Table 4.4 shows the measured values of reinforcement area, total area, and volume fraction of carbide used in subsequent calculations for this analysis. Table 4.5 summarizes the measured values for HAZ width, HAZ depth, bead width, catchment efficiency (Equation (4.15)), and height from the 13 experimental tests.

Table 4.4: Bead area and carbide volume fraction measurements for the experimental test beads

Bead Number	Total Area $A_{b,t}$ (mm ²)	Reinforcement Area $A_{b,r}$ (mm ²)	Carbide Volume Fraction $f_{v_{cb}}$ (%)
Bead 1	1.89	1.65	33.64
Bead 2	0.72	0.68	30.05
Bead 3	1.52	1.40	28.48
Bead 4	2.27	2.11	29.30
Bead 5	1.19	0.85	20.27
Bead 6	1.02	0.95	34.42
Bead 7	1.46	1.38	34.29
Bead 8	1.19	1.12	38.04
Bead 9	3.59	3.42	34.71
Bead 10	1.90	1.79	36.39
Bead 11	1.37	1.16	36.26
Bead 12	0.67	0.65	37.48
Bead 13	1.96	1.88	38.56

Table 4.5: Measured HAZ dimensions, clad dimensions, and catchment efficiency for the experimental clad beads

Bead Number	HAZ Width $2y_{m,HAZ}$ (mm)	HAZ Depth $z_{m,HAZ}$ (mm)	Clad Width $2y_{m,b}$ (mm)	Catchment Efficiency η_m (Equation (4.15)) (%)	Clad Height h_m (mm)
Bead 1	4.93	-1.08	3.87	60.89	0.59
Bead 2	4.28	-0.72	1.93	23.42	0.49
Bead 3	5.03	-1.00	3.50	47.80	0.49
Bead 4	5.36	-1.14	3.92	54.24	0.72
Bead 5	5.22	-1.16	3.82	50.67	0.31
Bead 6	4.81	-0.85	3.03	42.75	0.42
Bead 7	4.87	-1.03	3.40	48.96	0.55
Bead 8	4.84	-0.90	3.33	41.18	0.49
Bead 9	5.47	-1.39	4.16	60.71	1.12
Bead 10	4.96	-0.95	3.45	50.68	0.69
Bead 11	5.09	-1.09	3.65	52.04	0.45
Bead 12	4.45	-0.71	2.46	35.00	0.39
Bead 13	4.80	-0.88	3.06	49.45	0.76

The results of the isotherm calculation for maximum width and depth for the HAZ and melt, catchment efficiency from Equation (4.16), and the height from Equation (4.19) are summarized in Table (4.6).

Table 4.6: Calculated dimensions and catchment efficiency for the experimental clad beads

Bead Number	HAZ Width $2\widehat{y}_{m,HAZ}$ (mm)	HAZ Depth $\widehat{z}_{m,HAZ}$ (mm)	Melt Width $2\widehat{y}_{m,b}$ (mm)	Melt Depth $\widehat{z}_{m,b}$ (mm)	Catchment Efficiency $\widehat{\eta}_m$ (Equation (4.16)) (%)	Clad Height \widehat{h}_m (Equation (4.19)) (mm)
Bead 1	5.40	-1.24	4.11	-0.68	58.15	0.62
Bead 2	4.12	-0.70	2.23	-0.20	31.96	0.64
Bead 3	4.85	-0.98	3.37	-0.45	47.71	0.65
Bead 4	5.25	-1.22	3.83	-0.62	54.23	0.85
Bead 5	4.90	-1.00	3.42	-0.46	48.38	0.41
Bead 6	4.56	-0.82	2.99	-0.33	42.37	0.49
Bead 7	5.20	-1.14	3.83	-0.59	54.28	0.62
Bead 8	4.53	-0.85	2.91	-0.33	41.16	0.60
Bead 9	5.86	-1.62	4.46	-0.91	63.12	1.23
Bead 10	4.85	-0.98	3.37	-0.45	47.65	0.77
Bead 11	4.87	-0.99	3.39	-0.46	47.92	0.52
Bead 12	4.30	-0.69	2.64	-0.25	37.39	0.40
Bead 13	4.85	-0.98	3.36	-0.45	47.57	0.83

To visualize the fit of the models for bead width, catchment efficiency, and bead height the calculated values were plotted against the measured values from experiments in Figures (4.14), (4.15), and (4.16) respectively. A dotted line has been included in all figures to show the theoretical exact match of the model predictions to the experiments measurements. The uncertainty for the measured values in this work was estimated using standard techniques described in Beckwith *et al.*, which is presented in Table (4.7) for the values in Figures (4.14) through (4.16). The uncertainty in the optimized calculated bead width and optimized radius of the powder cloud was taken to be 0, which is reflected in the absence of x-axis error bars in Figure (4.14) and x and y-axis error bars in Figure (4.15). The complete uncertainty analysis is outlined in Appendix B of this thesis.

Table 4.7: Total uncertainty for measured and calculated parameters for bead width, catchment efficiency, and height

Bead Number	Stereo Photo Measured Width Uncertainty $\pm\epsilon_{2y_{m_{o,b}}}$ (mm)	Measured Catchment Efficiency Uncertainty $\pm\epsilon_{\eta_m}$ (%)	Measured Height Uncertainty $\pm\epsilon_{h_m}$ (mm)	Calculated Height Uncertainty $\pm\epsilon_{\widehat{h_m}}$ (mm)
Bead 1	0.295	4.79	0.044	0.042
Bead 2	0.152	1.82	0.036	0.047
Bead 3	0.275	3.72	0.036	0.049
Bead 4	0.307	4.22	0.053	0.064
Bead 5	0.300	3.99	0.023	0.041
Bead 6	0.238	3.35	0.031	0.033
Bead 7	0.267	3.83	0.040	0.041
Bead 8	0.376	3.26	0.036	0.037
Bead 9	0.316	4.75	0.082	0.081
Bead 10	0.271	3.99	0.051	0.050
Bead 11	0.287	4.14	0.033	0.033
Bead 12	0.187	2.75	0.029	0.025
Bead 13	0.241	3.91	0.056	0.051

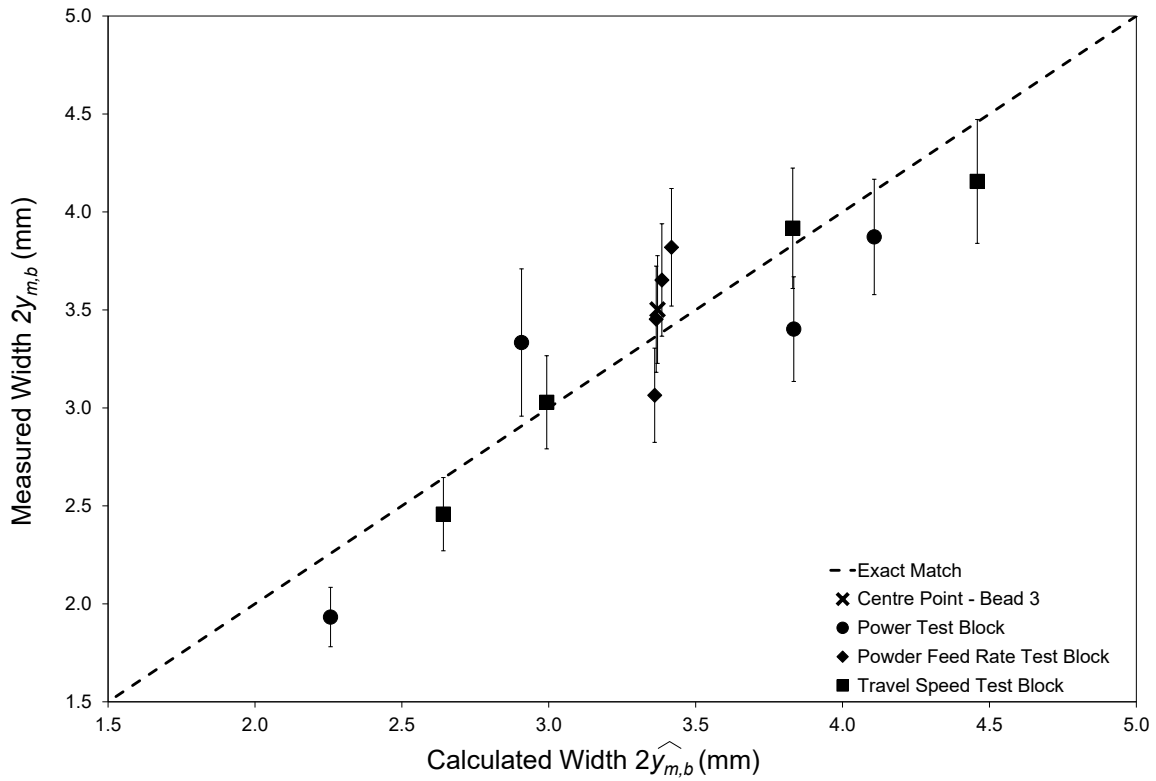


Figure 4.14: Comparison of measured bead width to the calculation based on a Gaussian heat source.

Figure (4.14) shows an overall good fit for all the experiments with some scatter both high and low for all test blocks. The maximum deviation was 17% under prediction for the low power setting with most tests falling within the $\pm 10\%$ range. The powder feed rate test block showed that increasing powder feed rate decreased the measured value of bead width.

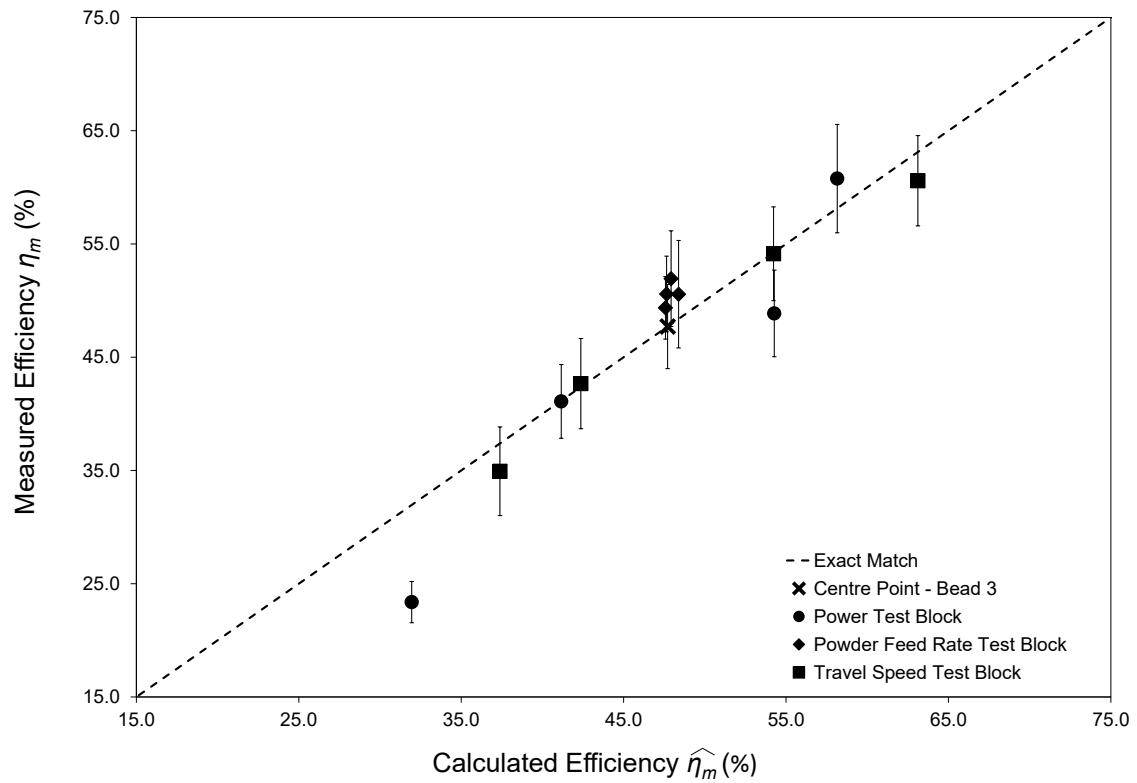


Figure 4.15: Comparison of measured catchment efficiency to the calculated catchment efficiency predicted by Equation (4.16).

Figure (4.15) shows that the model proposed in Equation (4.16) is a good fit across all three test blocks. The low power test sample at 3 kW over predicted the efficiency by 37% and but the remaining samples were consistently within $\pm 10\%$. The powder feed rate tests were shown to slightly under predict efficiency (within 5%), and the overall efficiency was insensitive to powder feed rate in the parameter range tested.

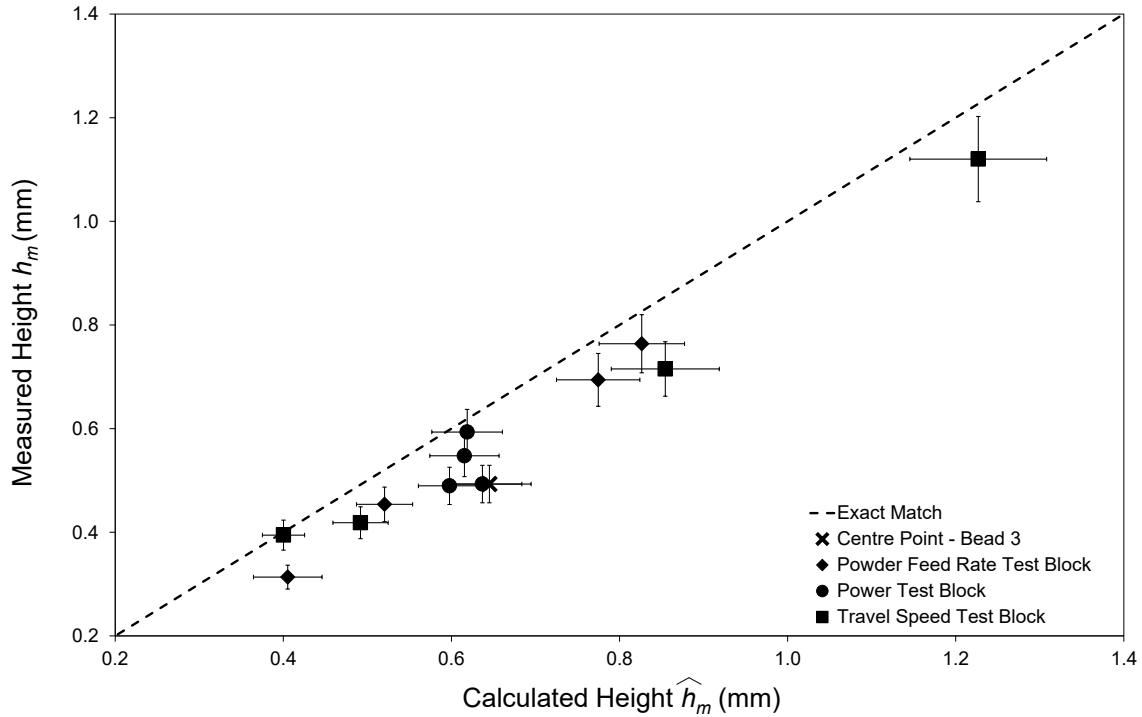


Figure 4.16: Comparison of measured height to the calculated height from Equation (4.19).

Figure (4.16) shows that the calculated value of h_m was higher than the measured value for all experiments by approximately 20%. The power test block demonstrated that power did not have a significant effect on the bead height. Higher powder feed rates were shown to increase the bead height with an approximately linear trend consistent with Equation (4.19). Increasing travel speed resulted in decreased height as predicted by the inverse relationship shown by the model.

4.8 Discussion

The effects of velocity on bead width are well described by the isotherm calculations in this work. These findings agree with the work of Colaço *et al.* who experimentally determined a linear decrease in width with increasing travel speed [13]. The overall trend with

increased laser power increasing the observed bead width is shown by the model, but the scatter can be attributed to the unknown role of beam attenuation by the powder particles, which has not been incorporated into this iteration of model development. Increased powder feed rate slightly decreased the measured width of the clads; this behaviour is not captured by the model and again supports the conclusion that beam-particle interactions should be considered in calculations of bead width. Energy requirements heating the powder particles up to cladding temperatures (melting only for the metal powders) may also play a role in the decreased width.

The calculated value of catchment efficiency, which scales with the calculated value of bead width, mirrored the effects of increased power and travel speed effects shown for bead width. The model worked well in the parameter ranges tested with the exception of the 3.0 kW (low power) test where the calculated value of efficiency was substantially higher. This behaviour suggests a change in the physics of the process under these conditions, which needs to be explored further. Overall catchment efficiency of the Ni-WC was shown to be relatively insensitive to changes in powder feed rate. This insensitivity is reflected in the small effects of powder feed rate on calculated bead width shown in Figure (4.14). The visualisation of area overlaps in this work suggests that back feeding into the pool may dramatically improve the process efficiency. A tilt of the powder feed towards the back of the pool, which changes the circular projected powder jet area to an elliptical shape may also be beneficial.

Nearly all values calculated for the height of the beads were between 10 and 20% higher than the measured cross sections. This systematic deviation is acknowledged, but the explanation for this behaviour will be the subject of future analysis. Changes in laser power did not have a large effect on the bead height. Increases in powder feed rate were shown to increase the bead height, which intuitively makes sense considering the linear relationships between powder feed rate and bead reinforcement area from the

mass balance (Equation (4.18)), the linear relationship between reinforcement area and bead height predicted by the parabolic profile calculation, and the relative insensitivity of catchment efficiency to changes in powder feed rate. Height was shown to be inversely proportional to the travel speed, which is predicted by Equation (4.19).

The laser cladding process is fully coupled, but the model presented here does not incorporate all couplings yet and is therefore not self-consistent. Thermal efficiency was assumed to be 30% as reported in literature for CO₂ laser cladding [35], but the thermal efficiency depends on process parameters including the bead width. Future iterations should incorporate temperature measurements from thermocouples or thermal imaging to calibrate the actual thermal efficiency of the process. Some important parameters were not measured directly in this work. The beam radius and powder radius were left as adjustment parameters to better fit the model to the experiments. While the values obtained are reasonable compared to available measurements, full characterization of both the beam and powder cloud will be necessary to obtain and validate a model to predict bead geometry directly from theory.

Some major questions remain about the process, which will need to be addressed. The effects of powder feed rate on powder jet focus and powder distribution should be quantified for single and multicomponent flows such as the Ni-WC system in this work. It is possible that the distribution of the nickel and carbide are in fact different based on the density differences between the components. The catchment efficiency model presented here is based on a point heat source analysis, which has shown to underpredict maximum bead width, a fundamental part of the calculation of efficiency. As the distribution expands, there is likely a point where the contribution of molten area ahead of the heat source becomes significant. Thermal efficiency considerations, which were not included as part of this work, need to be quantified to account for the clear indications of powder-beam interaction effects.

The expressions developed here should be synthesized and generalized similar to what has been done for the point heat source [30]. A set of simple equations with appropriate correction factors could replace the numerical requirement for calculation of Gaussian isotherms. This achievement would unlock for engineers a practical and easily applied method for predicting bead width, which now is limited to experts who are familiar with the numerical procedures currently available in literature and demonstrated in this work.

4.9 Conclusions

Clad bead geometry can be estimated using the following fundamental principles:

- Bead width and height completely define the bead geometry for practical aspects in single bead deposition.
- Bead height can be calculated from knowledge of catchment efficiency and bead width.
- Bead width can be approximated using a Gaussian heat source heat conduction model.
- Catchment efficiency can be approximated by the fraction of the molten surface in the cross section of the powder jets.

Predictions for bead width, catchment efficiency and bead height were tested against 13 beads of Ni-WC powder deposited using a CO₂ laser with a range of power levels, powder feed rates, and travel speeds. All predictions were shown to be in good agreement with the experimental beads generally to within $\pm 10\%$.

4.10 Acknowledgements

The authors wish to acknowledge Apollo Clad Laser Cladding, a division of Apollo Machine and Welding Ltd. who was instrumental in sharing their knowledge, equipment, and powder blends. The authors also acknowledge NSERC for providing project funding for this research. Student scholarships from the American Welding Society and Canadian Welding Association were gratefully received.

4.11 Appendix 4.1 Bead Area Approximation

It has been observed that the gentle curvature of the bead profile for laser clad beads is geometrically similar for a wide range of parameters. For typical bead sizes, capillary forces are dominant over gravity, and the cross section of the bead can be described by a segment of a circle. For the small fractions of a circle typically involved, a segment of a circle and a parabola are nearly identical [20]. (Equation (4.17)) shows that width and height multiplied by a 4/3 constant fully defines the cross sectional area for the parabolic case. For a circular area, Colaço *et al.* presented the following two expressions to calculate the area based purely on geometric considerations [13]:

$$h_m = R - \sqrt{R^2 - y_m^2} \quad (4.20)$$

$$A_{b,r} = y_m \sqrt{R^2 - y_m^2} + R^2 \arcsin\left(\frac{y_m}{R}\right) + 2y_m(h_m - R) \quad (4.21)$$

where R is the radius of the circle whose circular segment defines the cross sectional profile of the clad bead. It is noted that the y_m defined by Colaço represents the entire width, and the definition of full bead width in this analysis $2y_m$ has been substituted

into Equation (4.21) to be consistent with the notation presented here. Equation (4.20) was solved numerically using MATLABTM to identify R for the 13 experimental trials. Equation (4.21) was then used to solve for the bead area using experimentally measured values of bead width (stereo measurement) and height from Table (4.5). Figure (4.17) shows the reinforcement areas for both the parabolic and circular area calculations compared to the actual measured reinforcement areas from the experimental Ni-WC clads. Total uncertainty values for the measured reinforcement area, calculated parabolic bead area, and calculated circular bead area are shown in Table (4.8). The uncertainty analysis is outlined in detail in Appendix B, which additionally includes the exhaustive list of measured and calculated areas.

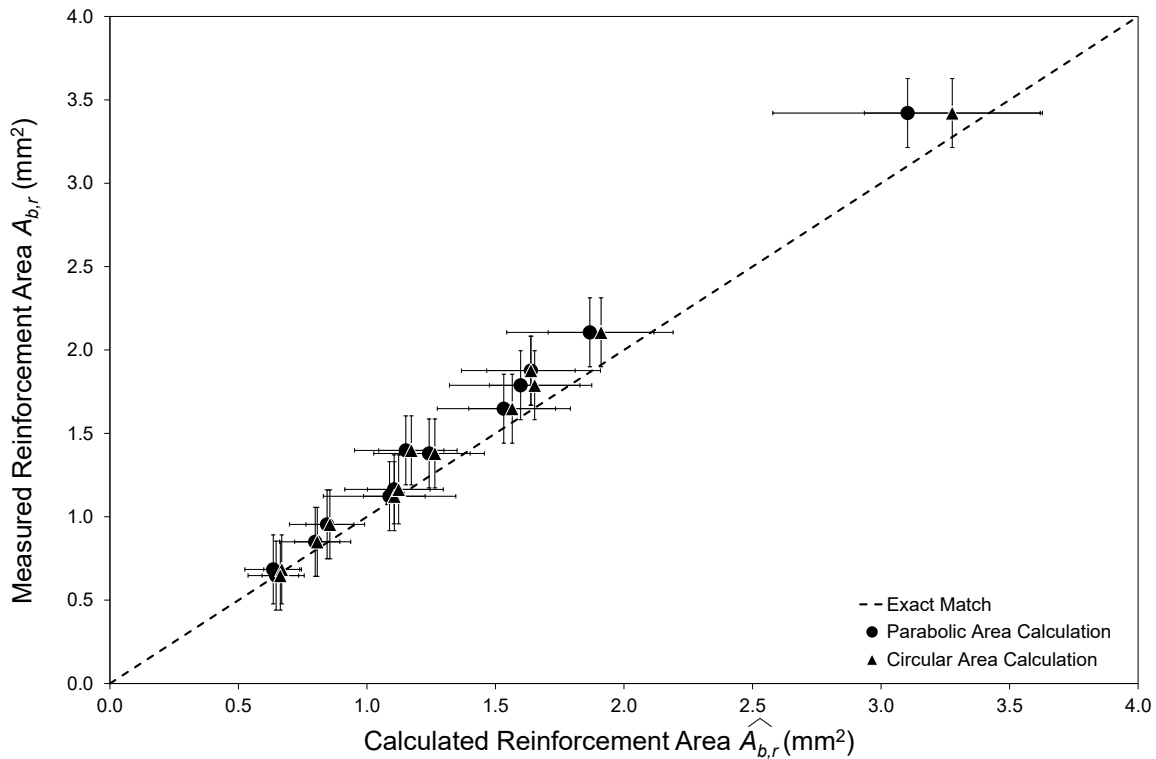


Figure 4.17: Comparison of the measured bead reinforcement area to parabola and circle area approximations.

Table 4.8: Total uncertainty for measured and calculated reinforcement area

Bead Number	Measured Reinforcement Area Uncertainty	Calculated Parabolic Reinforcement Area Uncertainty	Calculated Circular Reinforcement Area Uncertainty
	$\pm \epsilon_{A_{br}}$ (mm ²)	$\pm \epsilon_{\widehat{A_{br}}}$ (mm ²)	$\pm \epsilon_{\widehat{A_{br}}}$ (mm ²)
Bead 1	0.178	0.225	0.169
Bead 2	0.074	0.093	0.070
Bead 3	0.151	0.169	0.127
Bead 4	0.228	0.274	0.206
Bead 5	0.092	0.117	0.088
Bead 6	0.103	0.124	0.093
Bead 7	0.149	0.183	0.137
Bead 8	0.122	0.160	0.120
Bead 9	0.370	0.456	0.342
Bead 10	0.194	0.235	0.176
Bead 11	0.126	0.163	0.122
Bead 12	0.070	0.095	0.071
Bead 13	0.203	0.229	0.172

Both area calculation techniques compared excellently to the experimental results in this work. Figure (4.17) demonstrates that the parabolic approach can be implemented as an alternative to the circular calculation for simplicity in calculation without a loss of accuracy.

4.12 Appendix 4.2 Material Properties as a Function of Temperature

Reliable material properties as a function of temperature namely thermal conductivity k , specific heat capacity c_P , density ρ and thermal diffusivity α are necessary to convert the general, dimensionless results this work to dimensional values to be used in practice. A single value was used to represent the effective property as an average between the pre-

heat 260°C (533 K) and target isotherm temperatures. In this work these temperatures were the A_{e1} temperature 708°C (981 K) and the solidus temperature 1419°C (1692 K) modelled using the thermodynamic computational software package ThermoCalcTM.

Thermal conductivity of the 4145-MOD substrate was calculated using the model proposed by Mills for steel alloys [40]. Heat capacity was calculated as the enthalpy change with respect to temperature from ThermoCalcTM, and density was calculated as the ratio of molar mass to the molar volume also determined using ThermoCalcTM. The effective values for k , c_p and ρ were then used to calculate the effective diffusivity α_{eff} using Equation (4.22) [41]. Effective values for all values are listed in Table 4.3. Figure (4.18) shows the property data for the entire temperature range of interest and the effective values taken for both the HAZ and melting isotherm.

$$\alpha_{eff} = \frac{k_{eff}}{\rho_{eff}c_{p_{eff}}} \quad (4.22)$$

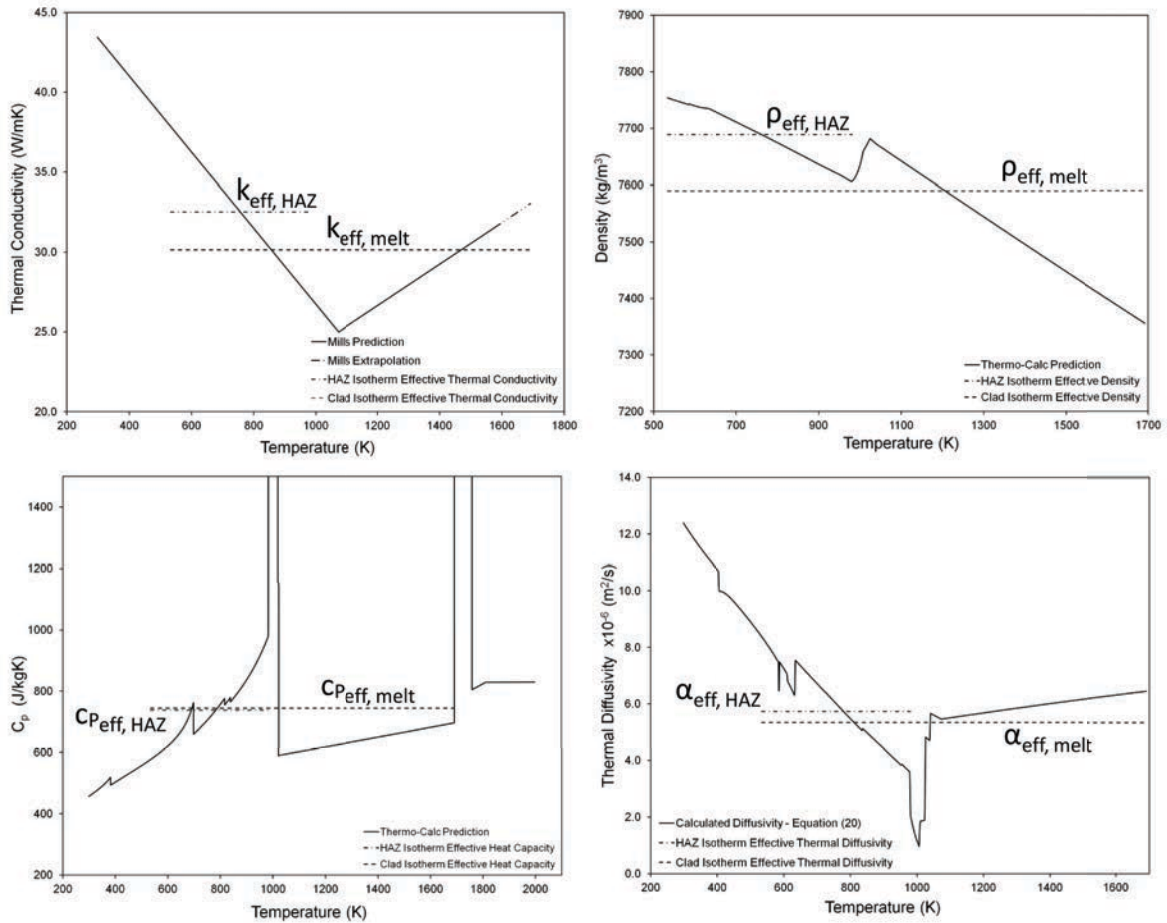


Figure 4.18: Temperature dependence of 4145-MOD steel thermal conductivity (top left), density (top right), heat capacity (bottom left), and thermal diffusivity (bottom right) showing effective values for the HAZ and clad melt isotherms.

Thermal conductivity values for the Ni-WC clads were also necessary for the effective power analysis in this work to account for bead reinforcement conduction. For Ni, the Mills model proposed for Ni-based superalloys was used [40] to predict a value for the matrix powders. For WC, data was available from the JAHM database above 800 K [42], and a room temperature value was reported by Lui *et. at* for WC as 110 W/mK [43]. An interpolation between the available data from JAHM and the reported room temperature value by Lui *et. at* was used to fill in the missing data gap. Although this data is for cemented carbides and not the uniform metastable WC_{1-x} used in this analysis, it is

the best available for the material. Figure (4.19) shows the conductivity data for the temperature range between 533 K and 1692 K with effective values in the temperature range for both the HAZ and melting isotherms. It is important to note that the HAZ temperature used as the peak temperature for both the WC and Ni was the calculated value 1228 K.

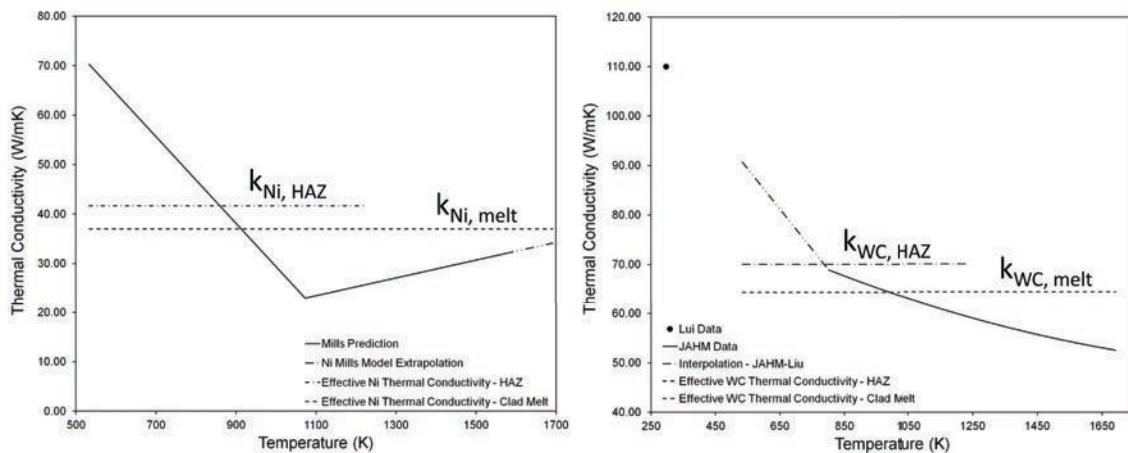


Figure 4.19: Left: Temperature dependence of Ni thermal conductivity. Right: WC thermal conductivity as a function of temperature. Both graphs show effective properties for the calculated HAZ (1228 K) and melting isotherm.

4.13 References

- [1] P.F. Mendez, N. Barnes, K. Bell, S. D. Borle, S. S. Gajapathi, S. D. Guest, H. Izadi, A. Kamyabi Gol, and G. Wood. Welding Processes for Wear Resistant Overlays. *Journal of Manufacturing Processes*, 16:4–25, 2013.
- [2] S.D. Guest. *Depositing Ni-WC Wear Resistant Overlays with Hot-Wire Assist Technology*. PhD thesis, University of Alberta, 2014.
- [3] J. Lin. A Simple Model of Powder Catchment in Coaxial Laser Cladding. *Optics & Laser Technology*, 31:233–238, 1999.
- [4] A.F.A. Hoadley and M. Rappaz. A Thermal Model of Laser Cladding by Powder Injection. *Metallurgical Transactions B*, 23B(12):631–642, 1992.

- [5] M. Picasso, C. F. Marsden, J. D. Wagnière, A. Frenk, and M. Rappaz. A Simple but Realistic Model for Laser Cladding. *Metallurgical and Materials Transactions B*, 25B:281–291, 1994.
- [6] L. Han, F.W. Liou, and K.M. Phatak. Modelling of Laser Cladding with Powder Injection. *Metallurgical and Materials Transactions B*, 35B:1139–1150, 2004.
- [7] A. Fathi, E. Toyserkani, A. Khajepour, and M. Durali. Prediction of Melt Pool Depth and Dilution in Laser Powder Deposition. *Journal of Applied Physics D: Applied Physics*, 39:2613–2623, 2006.
- [8] S. Kumar and S. Roy. Development of a Theoretical Process Map for Laser Cladding using Two-Dimensional Conduction Heat Transfer Model. *Computational Materials Science*, 41:457–466, 2008.
- [9] I. Taberbero, A. Lamikiz, S. Martinez, E. Ukar, and L.N. López de Lacalle. Geometric Modelling of Added Layers by Coaxial Laser Cladding. *Physics Procedia*, 39:913–920, 2012.
- [10] P. Balu, S. Hamid, and R. Kovacevic. Finite Element Modeling of Heat Transfer in Single and Multilayered Deposits of Ni-WC Produced by the Laser-Based Powder Deposition Process. *International Journal of Advanced Manufacturing Technology*, 68:85–98, 2013.
- [11] F. Lemoine, D. Grevey, and A. Vannes. Cross-Section Modeling Laser Cladding. pages 203–212. Proceedings of SPIE - The International Society for Optical Engineering, December 1993.
- [12] F. Lemoine, D. Grevey, and A. Vannes. Cross-Section Modeling of Pulsed Nd:YAG Laser Cladding. In *Laser Materials Processing and Machining*, volume 2246, pages 37–44. Proceedings of SPIE - The International Society for Optical Engineering, November 1994.
- [13] R. Colaço, L. Costa, R. Guerra, and R. Vilar. A Simple Correlation Between the Geometry of Laser Cladding Tracks and the Process Parameters. In *Laser Processing: Surface Treatment and Film Deposition*, pages 421–429. Kluwer Academic Publishers, Netherlands, 1996.
- [14] A.J. Pinkerton and L. Lin. Modelling the Geometry of a Moving Laser Melt Pool and Deposition Track via Energy and Mass Balances. *Journal of Physics D: Applied Physics*, 27:1885–1895, 2004.
- [15] C. Lalas, K. Tsirbas, K. Salonitis, and G. Chryssolouris. An Analytical Model of the Laser Clad Geometry. *International Journal of Advanced Manufacturing Technology*, 32:34–41, 2007.

- [16] H. E. Cheikh, B. Courant, J.-Y. Hascoët, and R. Guillén. Prediction and Analytical Description of the Single Laser Track Geometry in Direct Laser Fabrication from Process Parameters and Energy Balance Reasoning. *Journal of Materials Processing Technology*, 212:1832–1839, 2012.
- [17] P. Peyre, P. Aubry, R. Fabbro, R. Neveu, and A. Longeut. Analytical and Numerical Modelling of the Direct Metal Deposition Laser Process. *Journal of Applied Physics D: Applied Physics*, 41:1–10, 2008.
- [18] U. de Oliveira, V. Ocelík, and J. Th. M. De Hosson. Analysis of Coaxial Laser Cladding Processing Conditions. *Surface and Coatings Technology*, 197:127–136, 2005.
- [19] J.P. Davim, C. Oliveira, and A. Cardoso. Predicting the Geometric Form of Clad in Laser Cladding by Powder Using Multiple Regression Analysis (MRA). *Materials and Design*, 29:554–557, 2008.
- [20] O. Nenadl, V. Ocelík, A. Palavra, and J.Th.M De Hosson. The Prediction of Coating Geometry from Main Processing Parameter in Laser Cladding. *Physics Procedia*, 56:220–227, 2014.
- [21] J. Lin and W. M. Steen. Powder Flow and Catchment during Coaxial Laser Cladding. In *Lasers in Materials Processing*, volume 3097, pages 517–524. The International Society for Optical Engineering, 1997.
- [22] A. Frenk, M. Vandyoussefi, J. D. Wagnière, A. Zryd, and W. Kurz. Analysis of the Laser-Cladding Process for Stellite on Steel. *Metallurgical and Materials Transactions B*, 28B:501–508, 1997.
- [23] K. Partes. Analytical Model of the Catchment Efficiency in High Speed Laser Cladding. *Surface & Coatings Technology*, 204:366–371, 2009.
- [24] M. Gremaud, J. D. Wagnière, A. Zryd, and W. Kurz. Laser Metal Forming: Process Fundamentals. *Surface Engineering*, 12(3):251–259, 1996.
- [25] S. Zhou, Y. Huang, and X. Zeng. A Study of Ni-Based WC Composite Coatings by Laser Induction Hybrid Rapid Cladding with Elliptical Spot. *Applied Surface Sciences*, 254:3110–3119, 2008.
- [26] A. Angelastro, S. L. Campanelli, G. Casalino, and A. D. Ludovico. Optimization of Ni-Based WC/Co/Cr Composite Coatings Produced by Multilayer Laser Cladding. *Advances in Materials Science and Engineering*, pages 1–7, 2013.
- [27] P. Farahmand and R. Kovacevic. Laser Cladding Assisted with an Induction Heater (LCAIH) of Ni-60%WC Coating. *Journal of Materials Processing Technology*, 222:244–258, 2015.

- [28] G. Wood and P.F. Mendez. Disaggregated Metal and Carbide Catchment Efficiencies in Laser Cladding of Nickel-Tungsten Carbide. *Welding Journal*, 94(11):343–350, 2015.
- [29] V.M. Weerasinghe and W.M. Steen. Laser Cladding of Blown Powder. *Metal Construction*, 19:1344–1351, 1987.
- [30] G. Wood, S. Islam, and P.F. Mendez. Calibrated Expressions for Welding and their Application to Isotherm Width in a Thick Plate. *Soldagem and Inspeçao*, 19(3):212–220, 2014.
- [31] T.W. Eagar and N.S. Tsai. Temperature Fields Produced by Traveling Distributed Heat Sources. *Welding Journal*, 62(12):346–355, 1983.
- [32] S. Gajapathi. Laser Heat Treatment and Laser Cladding Report. 2012.
- [33] MathWorks Inc. Documentation: `fminsearch`, 2015.
- [34] MathWorks Inc. Documentation: `fzero`, 2015.
- [35] M. Schneider. *Laser Cladding with Powder*. PhD thesis, University of Twente, March 1998.
- [36] J. C. Maxwell. *A Treatise on Electricity and Magnetism*, volume 1. Literary Licensing LLC, 1873.
- [37] ISO 11146-1: Test Methods for Laser Beam Widths, Divergence Angles and Beam Propagation Ratios, Jan 15, 2005.
- [38] E. Toyserkani, A. Khajepour, and S. Corbin. *Laser Cladding*. CRC Press LLC, 2005.
- [39] P. Balu, P. Leggett, and R. Kovacevic. Parametric Study on Coaxial Multi-Material Powder Flow in Laser-Based Powder Deposition Process. *Journal of Materials Processing Technology*, 212:1589–1610, 2012.
- [40] K.C. Mills, A.P. Day, and P.N. Queded. Details of METALS Model to Calculate the Thermophysical Properties of Alloys, 2002.
- [41] F.P. Incropera, D.P. Dewitt, T.L. Bergman, and A.S. Lavine. *Fundamentals of Heat and Mass Transfer*. John Wiley and Sons, Sixth edition, 2007.
- [42] JAHM Software, I., Material Property Database (MPDB), 2003.
- [43] K. Liu, X.P. Li, M. Rahman, and X.D. Liu. CBN Tool Wear in Ductile Cutting of Tungsten Carbide. *Wear*, 255:1344–1351, 2003.

Chapter 5

Role of Thermocapillary Flows in the Laser Cladding of Nickel-Tungsten Carbide Alloys

5.1 Introduction

Laser cladding is an overlay deposition technology in which metallic or composite coatings are metallurgically bonded to a substrate in near-net shape geometry using a laser heat source. These value added coatings, commonly referred to as “clads”, are applied for improved wear or corrosion resistance, or dimensional repairs of high value components. Typical clads are on the order of 3 to 4 millimeters in width and one millimeter in height, and by overlapping clad beads it is possible to create protective material coatings encompassing entire surfaces. Laser cladding relies on a highly localized laser heat source to melt a substrate creating a liquid melt pool similar to traditional welding processes. A powder substrate is supplied to the pool from a lateral or coaxial feed system using a carrier gas. The solid powder interacts with the beam and melts as it penetrates the molten surface of the clad pool. The substrate is manipulated using a computer numeric controlled (CNC) system, and as the stationary beam traverses across the moving surface, the molten pool solidifies creating the clad layer.

The particular weld pool under consideration in this work is the composite nickel-tungsten carbide (Ni-WC) overlay system. This material consists of a two component mixture of Ni-Cr-B-Si pre-alloyed powders (primarily Ni as represented in the designation) and cast spherical fused tungsten carbides (WC). During welding, the Ni-Cr-B-Si powders melt to form liquid matrix component of the system, while the tungsten carbides remain solid throughout the cladding thermocycle, which is necessary to maintain the integrity and performance of the reinforcing carbide phase. This rapid thermocycle is a major benefit of using laser heat sources compared to arc based welding techniques for depositing Ni-WC alloys. To this point, it is not clear what effect this solid phase fraction has on the heat transfer of the liquid melt, particularly its impact on molten flows in the laser clad pool. Thermocapillary flows arise in laser cladding (as well as other welding processes) because of temperature dependent surface tension variation over the free surface of the pool [1, 2]. These surface tension gradients create a shear condition at the surface that typically drives fluid motion from the lower surface tension region directly beneath the heat source to the higher surface tension regions at the solid-liquid interface (subject to change based on presence/role of surface active elements). The resultant flows represent a convective heat transfer mechanism in the pool, which normally contributes significantly to the overall transfer of heat in the molten region. The heat transfer of the melt dictates the geometry of the clad bead, primarily the width of the deposit for typical low dilution, low penetration clads.

For coaxial laser cladding, the complexity of thermocapillary action is compounded with the addition of externally fed powders which depress the free surface of the pool and brings an additional momentum contribution to the system [3]. In some cases, as for the Ni-WC composite studied in this work, the effect of high (upwards of 50%) solid fraction in the melt pool remains unknown. With the complexities of the coupled-physics of the process, there has been a plethora of models of the molten clad pool geometry each with

their own unique approach and simplifications, some of which are described below. The role of convection in the clad pool has been a more prevalent part of many of the state of the art numerical models, but for composite materials it may be possible that the role of convection is minimal based on the presence of high fraction of solid particles in the molten pool. These solid particles, which remain solid during the thermocycle, should disrupt the thermocapillary flows thereby reducing the importance of the convective heat transfer mechanism in the melt. This work attempts to address for the first time the relative importance of thermocapillary flows in modelling of the clad pool geometry for this particular high solid fraction target system. The simplicity in modelling without a loss in accuracy of the prediction has been a fundamental part of the author's previous works [4–6].

There has not been consistent agreement in literature regarding the need for accounting for convection in modelling the geometry of the molten clad pool. Authors have argued that for typical process conditions, convection does not meaningfully change the prediction for pool geometry significantly but does have a lesser effect in reducing surface temperatures [2, 7, 8]. Of those who have incorporated thermocapillary flows into modelling of molten clad pool geometry, there are two distinct groups: those who apply a conduction models with a modified thermal conductivity in the melt and those who simultaneously solve continuity, momentum, and energy balances with varying complexities in material properties and boundary conditions. Both groups rely on finite element/numerical simulations to solve either 2D or 3D models typically for Gaussian or uniform heat distributions. The key authors are summarized below.

Reviews by Mazumder *et al.* [9], Mackwood and Crafer [10], and Pinkerton [8] highlight the development of models that have incorporated Marangoni flows. To narrow the scope, the models discussed here are limited to conduction mode cladding models and not key-hole laser welding and hybrid-laser models, which must consider different

physical phenomena. Toyserkani *et al.*, Fathi *et al.*, and Amara *et al.* presented conduction based heat transfer models of a Gaussian intensity distribution applying a corrected thermal conductivity in calculating the melt pool boundaries [3, 11–13]. This modified conductivity is typically in the range of at least twice the stationary melt conductivity [3, 13]. Farahmand and Kovacevic used a slightly different approach incorporating a three dimensional thermal conductivity factor to account fluid flow in their transient 3D uncoupled model for single and multitrack clad beads [14]. In a book detailing the physical mechanisms in a variety of laser materials processes, Guldesch and Smurov identify this modified conductivity approach as the simplest method of incorporating mass transfer effects on heat transfer in the surface layer during cladding [15].

Of those who have incorporated convection directly into the governing equations of the problem, most notable is Picasso and Hoadley, some of the earliest and most cited authors for development of clad pool geometry models for laser cladding. Their work presented a two dimensional model for laser cladding that solved temperature and velocity fields simultaneously considering powder injection forces with the assumption that the powder melts instantaneously at the melt surface [16]. The authors concluded that fluid flow and the effects of powder injection are important in determining the melt pool shape and temperature fields during single-layer cladding. In 2004, Han *et al.* presented a comprehensive 3D model incorporating Maragoni shear stress, powder injection, together with energy balances at the liquid-vapor and solid-liquid interfaces [17]. Other similar approaches have been applied by Bhat and Majumdar [18], Taberner [19], Akbari *et al.* [20], and Lee *et al.* [21]. Few authors have also presented a dimensionless characterizations of the weld pool during laser processing. Guldesch and Smurov state in their book on physics of welding that for fluids under certain dimensionless conditions convective terms in the Naive-Stokes equations can be neglected and convection can be neglected overall in the heat transfer analysis of the laser clad pool [15]. In 1984 and 1988, Chan, Mazumder,

and Chen produced models that incorporated asymptotic solutions for thermocapillary flows into predictions of surface temperature, pool shape, and cooling rates as a function of the Prandtl number [22,23]. Wei *et al.* discuss the melt pool shape, surface velocities, and maximum temperatures in the pool determined as a function of Marangoni, Prandlt, Peclet, and Stefan dimensionless groups. Their work highlights the practical importance of revealing physical mechanisms, but focuses on quantitative predictions of the fusion zone shapes [24,25].

Only Balu *et al.* have presented a finite element model of heat transfer in single and multilayered deposits of Ni-WC taking into account convective heat transfer in the weld pool [26]. Their results related process variables to cooling rates in the pool and associated dissolution of the carbide phases, but they did not focus on the role of the WC phase on convection in the melt. It remains unknown if a threshold of the solid phase can significantly limit the role of convection in the clad pool or if convection must be accounted for to obtain meaningful predictions of the melt geometry. This work addresses the role of thermocapillary flows in coaxial laser cladding of a composite Ni-WC using a framework presented by Rivas and Ostrarch [1]. The thermophysical properties of the composite clad pool are addressed considering the two components of the clad powder feed, and the dimensionless analysis of Rivas is applied to typical cladding conditions to characterize the role of convection during laser cladding of this alloy system.

List of Symbols

Symbol	Unit	Description
A	1	Aspect ratio
α	$\text{m}^2 \text{s}^{-1}$	Thermal diffusivity
B	1	Constant from Thomas relation for effective viscosity
β	K^{-1}	Coefficient of thermal expansion
C	1	Constant from Thomas relation for effective viscosity
c_p	$\text{J kg}^{-1} \text{K}^{-1}$	Heat capacity at constant pressure
D	m	Depth of the fluid cavity
δ_t	m	Thermal boundary layer thickness
E	J mol^{-1}	Activation energy
η	1	Efficiency
F	$\text{J}^{1/2} \text{K}^{-1/2} \text{mol}^{-1/6}$	Constant from Kaptay's unified equation for viscosity
$f_{v_{c_b}}$	1	Volume fraction of carbide in the clad bead
G	J mol^{-1}	Free energy
γ	J mol^{-1}	Surface energy
H	J mol^{-1}	Molar enthalpy
I	1	Constant from Kaptay's unified equation for viscosity
k	$\text{W m}^{-1} \text{K}^{-1}$	Thermal conductivity
L	m	Length of the fluid cavity
\mathcal{L}	m	Beam distribution parameter
L_o	$\text{W } \Omega \text{K}^{-2}$	Theoretical constant in the Wiedemann-Franz-Lorenz Rule
M	g mol^{-1}	Molar mass
Ma	1	Marangoni number, a Peclet number for thermocapillary flows
μ	Pa s	Dynamic viscosity
N	atoms mol^{-1}	Avogadro's number
ν	$\text{m}^2 \text{s}^{-1}$	Kinematic viscosity
P	Pa	Pressure
ϕ	$^\circ$	Divergence angle of the laser beam
Pr	1	Prandtl number
Q	W	Nominal laser power
$Q(X)$	W m^{-2}	Heat flux distribution
Q_0	W m^{-2}	Maximum of the heat flux distribution located at the centreline
Re_σ	1	Reynolds number for thermocapillary flows
ρ	kg m^{-3}	Density
ρ_e	Ωm	Electrical resistivity
σ_T	$\text{N m}^{-1} \text{K}^{-1}$	Surface tension coefficient
T	K	Temperature
ΔT^*	K	Temperature difference between T_0 and T_s for Regime III
U_s^*	m s^{-1}	Reference velocity in the viscous boundary layer
V	m^3	Volume
x, y, z	m	Cartesian coordinates

Symbol	Description
Subscripts	
<i>C</i>	Carbon
<i>c</i>	Tungsten carbide
<i>eff</i>	Effective value
<i>f</i>	Focus point
<i>i</i>	Data point i
<i>L</i>	Linear
<i>m</i>	Ni-Cr-B-Si metal powders
<i>melt</i>	Melting
<i>mol</i>	Molar quantity
<i>s</i>	Surface
<i>T</i>	Function of temperature
<i>th</i>	Thermal
0	Reference
<i>V</i>	Volumetric
<i>W</i>	Tungsten

5.2 Methodology

The analysis of composite clad pool phenomena here is based on the work of Rivas and Ostrarch, who presented formulae to characterize the role of the different physical mechanisms (conduction and convection) in low Prandtl number fluids, such as liquid metals, through dimensional analysis and asymptotic considerations [1]. Their methodology builds from an existing weld cavity geometry to reveal the relative importance of heat transfer mechanisms in specific regions of the melt from dimensionless criterion. Rivas' analysis framework is best suited for the analysis of composites here because it follows the same method of characterizing phenomena in an existing molten pool. Other authors have used a slightly different approach to produce predictions of width and depth of the pool from dimensional analysis [22–25].

Rivas' approach to characterising thermocapillary flows considers a series of simplifying assumptions to a rectangular approximation of the weld pool. Rivas' methodology

ranks the relative contributions of momentum driven and thermally driven phenomena in the weld pool, and then categorizes “regimes” that define the physically meaningful effects that results from the dominant physics. The benefit of this approach is its ability characterize physical phenomena without solving the relevant differential equations related to continuity, momentum, and energy, which requires numerical analysis. Rivas also presents estimates of characteristic values of a particular regime, which provide simple expressions for points of interest in the domain of the problem such as maxima of the thermal and flow fields. The problem formation and approximations, dimensionless groups, regimes characterization and characteristic values presented by Rivas that serve as the foundation of this analysis on thermocapillary flows in laser cladding of composite materials are outlined below.

5.2.1 Problem Formulation

The problem configuration originally proposed by Rivas and Ostrach is taken to represent a typical laser cladding molten pool [1]. The weld pool is considered a rectangular cavity with depth D and length L filled with a fluid having constant density, kinematic viscosity, and thermal diffusivity. The fluid is subject to an imposed symmetrical heat flux on the surface denoted $Q(X)$ with a maximum value at the centreline Q_0 and a distribution parameter \mathcal{L} . T_0 , the reference temperature, is considered to be the melting temperature of the substrate material. The symmetry of the cavity and the heat source makes it possible to consider only half of the domain of the problem. Other important conditions are:

1. Constant properties of the fluid with respect to temperature with the exception of surface tension
2. Linearly decreasing surface tension with increasing temperature

3. Negligible properties of the passive gas in contact with the free surface
4. Buoyancy, frictional heating and electromagnetic effects are not considered
5. The boundary layer between liquid and solid is omitted

In reality the problem of a molten weld pool formed during laser cladding has key differences than the configuration proposed by Rivas. The molten clad pool exists almost completely above the substrate surface contrary to typical molten pools for traditional welding processes, which involve penetrating subsurface fluid flows. The height of the cavity D is taken as the measured height of a solidified bead. The penetration of the pool, d , is not considered in the cavity height as $d \ll D$ under typical laser cladding conditions [27]. The width of the cavity is taken as half the width of the molten pool measured from the width of the solidified bead. The original problem configuration compared to a representation of laser cladding is schematically shown in Figure (5.1).

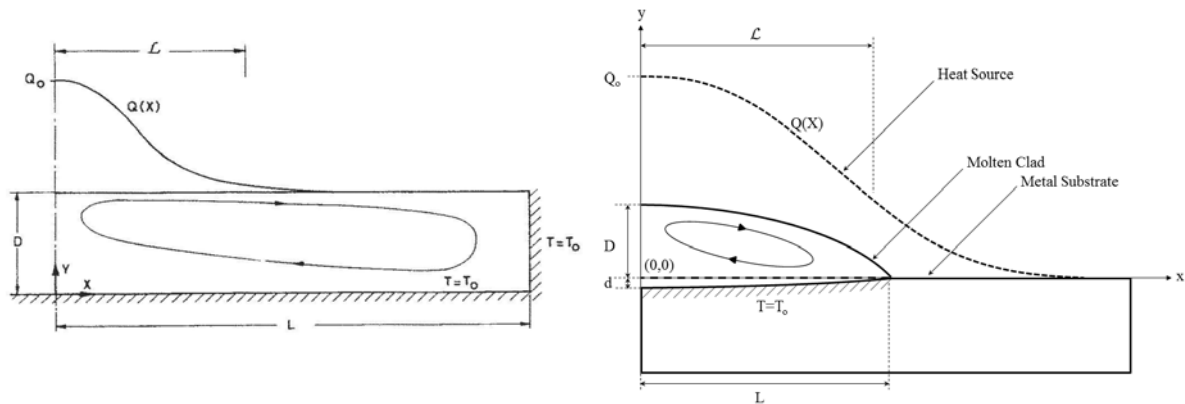


Figure 5.1: Left: Rivas system coordinates and problem configuration [1]. Right: Laser cladding pool showing the largely above surface pool geometry of the process.

Figure (5.1) highlights additional differences between the two system configurations. The clad pool has curvature of its molten surface rather than the rigid square fluid container. In their paper, Rivas and Ostrarch also outline that the problem is formulated

such that the distribution of the heat flux is smaller than the length of the molten pool ($\mathcal{L} < L$), which is not typically the case in laser cladding. The cladding process also requires the addition of external mass to create the surface layer, which comes in the form of forced-fed powders that impinge on the surface of the molten clad pool. These particles deform the free surface of the melt and bring a disruptive momentum contribution and thermal contribution that is not considered in this preliminary analysis. To maintain consistency with Rivas' boundary conditions and conclusions about the physics of the process, the geometry of the surface clad pool (width L and depth D) are taken to represent Rivas proposed problem configuration as a first approximation of composite clad pool phenomena.

5.2.2 Regimes and Dimensionless Groups for Characterizing Low-Prandtl-Number Thermocapillary Flows

Rivas' analysis applies to low-Prandtl number fluids. The Prandtl number ($\text{Pr} = \nu/\alpha$) is the dimensionless ratio of kinematic viscosity and thermal diffusivity. Values for liquid metals typical fall into the $\text{Pr} \ll 1$ range satisfying Rivas' preliminary condition [28]. Rivas' work outlines three regimes for low-Prandtl-number systems that characterize the presence and relative importance of the forces acting in the weld pool. The balance of these forces determines whether thermal and/or viscous boundary layers will form under conditions dictated by dimensionless groups, which characterize the relative magnitudes of these phenomena. A summary of each regime is shown below [4]:

- **Regime I:** Labelled the viscous regime, where viscous forces dominate through the fluid volume. Conduction is the dominant heat transfer mechanism.
- **Regime II:** Flow boundary layer regime. Inertial forces dominate the volume, but a viscous boundary layer forms at the surface. Conduction is still the dominant

heat transfer mechanism throughout the volume of the liquid and in the boundary layer.

- **Regime III:** Flow and thermal boundary layer regime, where both a viscous and thermal boundary layer exist simultaneously. Inertial forces dominate the volume, and convection is the dominant heat transfer mechanism; however, conduction dominates in the thermal boundary layer at the surface. By definition, the viscous boundary layer is smaller than the thermal boundary layer in this regime.

There are three dimensionless numbers that completely describe the formulation of the problem, which are: the Prandtl number Pr (Equation (5.1)), the Reynolds number for thermocapillary flows Re_σ (Equation (5.2)), and the aspect ratio A (Equation (5.3)) defined below [4]. Definitions of thermophysical properties available from this analysis have been substituted in the equations presented here.

$$\text{Pr} = \frac{c_{p\text{eff}} \mu_{\text{eff}}}{k_{\text{eff}}} \quad (5.1)$$

$$\text{Re}_\sigma = \frac{\sigma_{T\text{eff}} Q_0 D^2 \rho_{\text{eff}}}{k_{\text{eff}} \mu_{\text{eff}}^2} \quad (5.2)$$

$$A = \frac{D}{\mathcal{L}} \quad (5.3)$$

where $c_{p\text{eff}}$ is the effective specific heat capacity of the clad pool (J/kgK), μ_{eff} is the effective dynamic viscosity of the pool (Pa·s), and k_{eff} is the effective thermal conductivity (W/mK). The value $\sigma_{T\text{eff}}$ represents the effective surface tension temperature coefficient (N/mK), Q_0 is the maximum value of the heat flux distribution (W/m²), D is the height of the fluid cavity or molten clad pool in this work (m), and ρ_{eff} is the effective density

of the composite pool (kg/m^3). For Equation (5.3), \mathcal{L} is the heat flux distribution parameter (m). Values with the subscript “eff” indicate the value that considers both the composite nature of the pool and its temperature dependence. The identification of these three numbers allows for the creation of a process map to identify the regime of the target system.

Three dimensionless groups are presented by Rivas, which depend directly on the above defined dimensionless numbers that characterize the three proposed regimes. The formulas for each group come from the coefficients of the terms in the dimensionless form of the Naive Stokes, continuity, and energy differential equations. These are presented in detail in the Appendix of Rivas’ paper [1]. Table (5.1) summarizes the mathematical requirements for the non-dimensional groups for each regime, the physical regions present, and the dominant heat transfer mechanism in each physical region. Figure (5.6) presented later in this analysis shows how these groups and the equalities outlined by Rivas describe the boundaries for a process map, which allows simple graphical identification of the target system’s regime.

Table 5.1: Regime classification for low Pr thermocapillary flows [1]

Regime	Dimensionless Group			Dominant Heat Transfer Mechanism		
	$A^2\text{Re}_\sigma$	$\text{Pr}A^2\text{Re}_\sigma$	$\text{Pr}(A^2\text{Re}_\sigma)^{1/3}$	Core	Viscous Layer	Thermal Layer
I	≤ 1	$\ll 1$	N/A	Conduction	N/A	N/A
II	$\gg 1$	~ 1	$\lesssim 1$	Conduction	Conduction	N/A
III	$\gg 1$	$\gg 1$	$\gg 1$	Convection	Conduction	Conduction

5.2.3 Characteristic Values of Regime III

In each regime, estimates for characteristic values of interest in the domain are presented by Rivas for the thermal and flow fields. Important characteristic values for this analysis

are the thermal boundary layer size and the temperature differential across this boundary layer for Regime III, which will be shown to apply to the conditions and material of the target system here. The estimate for thickness of the thermal boundary layer is defined in Equations (5.4) as follows:

$$\delta_t = \frac{D}{(Pr^3 A^2 Re_\sigma)^{1/4}} \quad (5.4)$$

where δ_t is the thickness of the thermal boundary layer at the liquid surface (m). A secondary thermal boundary layer exists between the solid-liquid interface, which has not been incorporated into Rivas' analysis. Wei *et al.* have proposed the following estimate for the boundary layer thickness at this interface [24]:

$$\delta_{t_{s-l}} = \sqrt{\frac{\alpha_{eff} D}{U_s^*}} \quad (5.5)$$

where $\delta_{t_{s-l}}$ is the thickness of the thermal boundary at the solid-liquid interface (m), and U_s^* is the characteristic velocity in the viscous boundary layer of Regime III. Notation from this analysis has been substituted into the formula for consistency. Wei's expression relies on the assumption that transverse conduction as the same magnitude as stream-wise (downward) convection. The characteristics velocity in the viscous boundary layer is shown in Equation (5.6).

$$U_s^* = \left(\frac{\sigma_{T_{eff}} Q_0}{\mu_{eff} \rho_{eff} c_{p_{eff}}} \right)^{1/2} \quad (5.6)$$

$$(5.7)$$

The temperature difference between the surface and core region via conduction through

the thermal boundary layer for Regime III is shown below in Equation (5.8).

$$\Delta T^* = \frac{Q_0 \delta t}{k_{eff}} \quad (5.8)$$

where ΔT^* is this temperature gradient through the thermal boundary layer (K). An alternative form of Equation (5.8) is proposed for this work, which substitutes the process parameters into the definition for δ_t for clarity in the material property analysis outlined in the subsequent section. Equation (5.8) becomes the following:

$$\Delta T^* = \left(\frac{\mathcal{L}^2 Q_0^3}{\rho_{eff} C_{p_{eff}}^3 \sigma_{T_{eff}} \mu_{eff}} \right)^{1/4} \quad (5.9)$$

5.3 Target System

The target system considered here comes from previous experimental analyses using a CO₂ laser and Ni-WC alloy system [5, 6, 29]. Described in this section are the experimental conditions, pertinent measurement of the deposited clad bead, the laser beam characteristics, reference temperatures in the clad pool, constituents of the composite clad pool, and the material properties calculated as functions of both composition and temperature for this evaluation of fluid flow.

5.3.1 Experiments and Cross Section Measurements

A 6.0 kW coaxial CO₂ laser was used to deposit Ni-WC onto a 4145-MOD steel substrate using a range of laser powers, powder feed rates, and travel speeds. A single test bead from the experiments described in Chapters 2 and 4 has been used for the analysis of fluid flow here, which represents the typical industrial parameters for direct cladding of Ni-WC on chrome-moly steels: 4.0 kW laser power, 50 g/min powder feed rate, and 25.4 mm/s

travel speed with a target preheat of 260°C (500°F). Measured tests values are shown in Table 4.2 Additional repetitions of the test parameters for statistical significance were not possible due to limited time available for use of the production laser system.

For this analysis of thermocapillary flows, the geometry of the solidified clad bead must be known and is taken to represent the geometry of the fluid cavity (Figure (5.1)). The relevant parameters are the bead height, width, and carbide volume fraction in the solidified clad. The cross section of the clad deposited using the above described parameters is shown in Figure (5.2), and Figure (5.3) shows the visualized results of the carbide volume fraction analysis using a PythonTM image processing script having a randomly generated colour scheme. Assuming an isotropic distribution of carbides, the area fraction is taken to represent the volume fraction of the reinforcing phase in the entire deposit. The measurements for D , L , and $f_{v_{cb}}$ for the solidified clad are summarized in

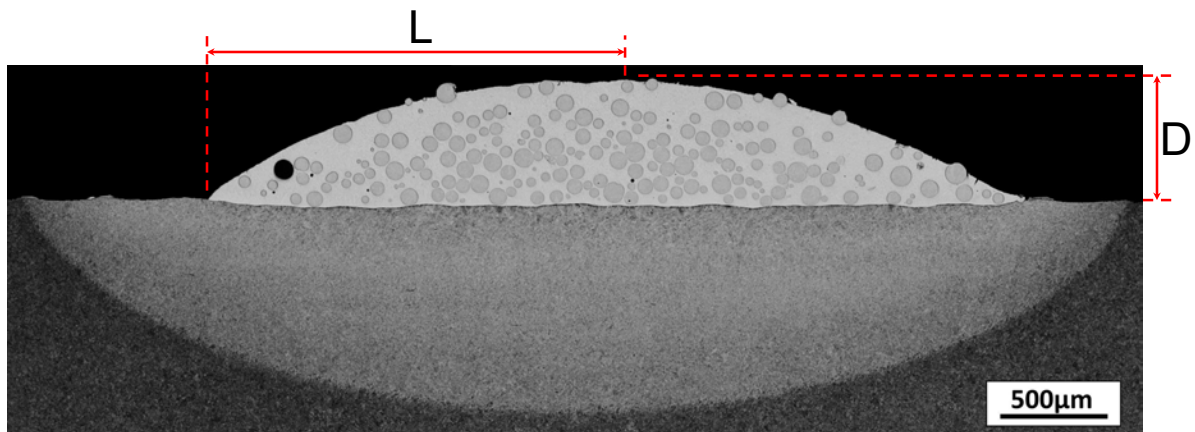


Figure 5.2: Cross section of the solidified Ni-WC clad from this work etched with 3% Nital for 5 seconds.

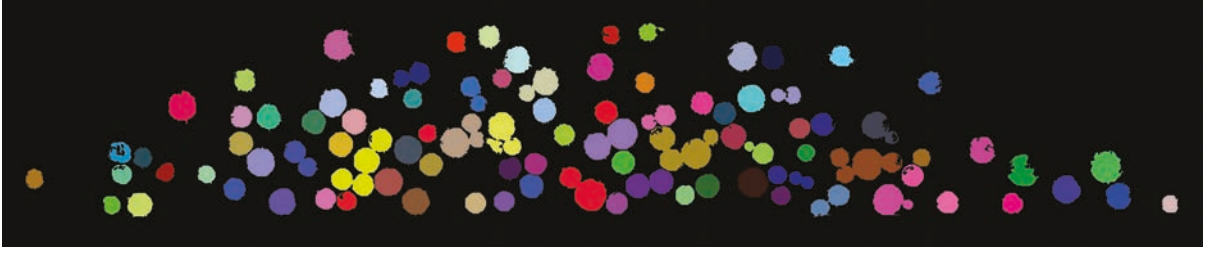


Figure 5.3: Python script output showing carbide area for the Ni-WC laser clad in this analysis.

Table 5.2: Bead cross sectional measurements used in calculations of characteristic values of thermocapillary flows in this work

Variable	Units	Value	Description
D	(mm)	0.49	Measured height of the bead cross section taken as the height of the fluid cavity.
L	(mm)	1.62	Measured value of half the width of the cross section used to represent half the width of the fluid cavity.
$f_{v_{cb}}$	(1)	0.386	Measured volume fraction of tungsten carbides in the deposited clad bead

5.3.2 Heat Source Characterization

The important parameters of the laser for this work are the beam power, thermal efficiency, characteristic length, and characteristic power of the beam's distribution. Each parameter of the heat source is described in detail below. For the experimental trial considered here, the target beam power was 4000 W. The beam power was tested at the substrate using a 10 kW Comet 10K-HD power probe, a calibrated copper calorimeter, to be 3990 W. This value is used in subsequent calculations as the beam power Q . The thermal efficiency factor is considered to be the literature value for steel absorption at $10.6\mu\text{m}$ wavelength, which is 0.3 or 30% reported by Schneider [30]. This literature value is taken in the absence of empirical expressions or easily implemented predictive models

for thermal efficiency of laser cladding as a function of the major process parameters (laser power, powder feed rate, and travel speed).

The characteristic length of the heat flux distribution \mathcal{L} is taken as the beam distribution parameter or standard deviation of the beam. This value has been measured using a PH0053 Ophir laser beam sampler, USBNanoScan-Pyro Sensor with 20 mm aperture and 25 μm slits, and a LBS-100-IR 0.5 beam attenuator to be 1.242 mm at the laser working distance of 19.05 mm below the nozzle level, which corresponds to a mirror working distance of 345.31 mm. The results of this characterization are shown in detail Appendix 5.1. Shown below in Figure (5.4) is the global caustic energy distribution of the beam produced by the profiler. The beam shows an irregular distribution with non-symmetric spike on one side. For the calculations in this analysis, the beam is modelled as having a Gaussian intensity to provide simple expressions for the peak power of the distribution Q_0 and characteristic length \mathcal{L} while satisfying the conditions for Rivas' symmetric heat source distribution in the problem formulation.

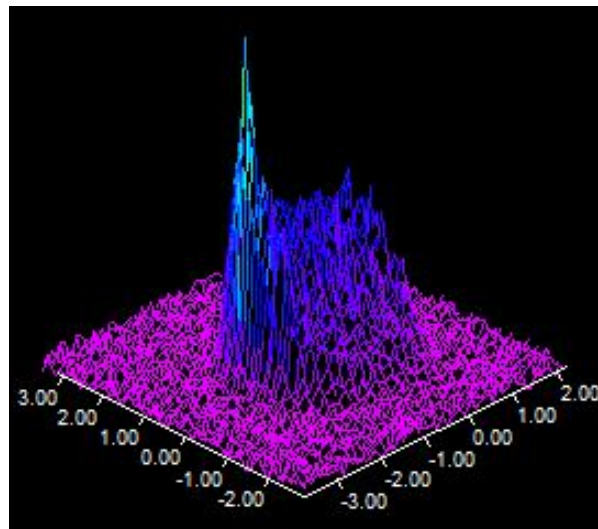


Figure 5.4: Global caustic of the CO₂ laser beam in this work. Spatial units are in mm, and the relative power intensity (vertical axis) corresponds to a total laser power of 4 kW laser power.

For a Gaussian distribution, the characteristic power is taken as the peak value of the distribution, which is described as follows:

$$Q_0 = \frac{\eta_{th}Q}{2\pi\mathcal{L}^2} \quad (5.10)$$

where η_{th} is the thermal efficiency of the laser cladding process (1), Q is the total power of the laser (W), and \mathcal{L} is the standard deviation of the Gaussian distribution. Table (5.3) summarizes the values of Q , η_{th} , \mathcal{L} , and Q_0 calculated using Equation (5.10) that fully define the heat source for this analysis of fluid flows in laser cladding.

Table 5.3: Parameters characterizing the heat source and power absorption during laser cladding

Parameter	Units	Value	Description
η_{th}	(1)	0.3	Literature value of absorption for a CO ₂ laser beam on a steel substrate during cladding. [30]
Q	(W)	3990	Measured beam power at the substrate.
\mathcal{L}	(mm)	1.242	Measured beam distribution parameter.
Q_0	(kW/m ²)	123568	Peak power of the Gaussian intensity distribution.

5.3.3 Reference Temperature for Regime III

The value of ΔT^* in Equation (5.8) describes the temperature difference through the thermal boundary layer thickness present in Regime III. This formula represents the temperature difference between the core and surface developed as a result of conduction in this layer. The core temperature is effectively a constant value T_0 through its thickness as a result of convection and heat redistribution. The value of T_0 for this analysis comes from the melting temperature of the 4145-MOD steel substrate, which has been computed using ThermoCalcTM software to be 1692 K representing the solidus temperature of the

steel. ΔT^* represents the appropriate temperature range for the effective thermophysical material properties. The surface temperature can therefore be represented as:

$$T_s = T_0 + \Delta T^* \quad (5.11)$$

As a result of the dependency of ΔT^* (Equation (5.9)) on the process parameters an iterative approach is adopted to determine the appropriate temperature range for each property for the range of solid phase fractions considered in this analysis. Starting with melting temperature values for c_p , μ , and ρ (σ_T is defined as the change with respect to temperature and is taken as a single constant value), ΔT^* is calculated, and this new value is then used to compute the updated material property values. The iterative process is repeated until ΔT^* converged to within 1 K, which occurs after 4 or 5 iterations for all volume fractions considered in this work. The values of the ΔT^* and T_s are summarized below in Table (5.4). The literature data and available literature models used to produce these temperature values and the resulting material properties are summarized in the material property section and outlined in detail in Appendix 5.2.

Table 5.4: Values for the effective heat capacity analysis of a Ni-WC composite clad pool. T_0 is 1692 K for all solid fractions analyzed here.

Deposited Carbide Volume Fraction $f_{v_{cb}}$ (1)	Regime III Cavity Temperature Differential ΔT^* (K)	Molten Pool Surface Temperature T_s (K)
0	983.4	2675
0.386	798.2	2490
0.5	630.6	2323

5.3.4 Clad Pool Constituents

The clad pool is a composite mixture of Ni-Cr-B-Si powders and cast spherical fused tungsten carbides (WC_{1-x}), most often represented as Ni-WC. The carbide phase in this work has previously been characterized as the metastable high hardness $WC_{0.604}$ or $\sim WC_{0.6}$ phase [5]. The chemistry of the metal powders and tungsten carbides has been included in Table (5.5) [31]. The effects of substrate dilution of primarily iron into the nickel-based melt likely did not have a significant effect the chemistry of the clad pool. The dilution of the cladding process is typically less than 5%, and can be as low as 1%, and for the purposes of this analysis the deposited chemistry was considered to match the chemistry of the feed components.

Table 5.5: Chemistry data for the components of the Ni-WC powders used in this analysis

Element	W	C	Cr	Si	B	Fe	O	Ni	Other
Source	wt%	wt%	wt%						
Metal Powder MTR	-	0.25	7.44	3.39	1.58	2.43	0.022	84.89	-
WC_{1-x}	95.5	3.8	-	-	-	-	-	-	0.7

The two component powders were mixed together by the sponsor in 62.60% to 37.4% weight fractions of carbide to metal powder respectively. The size of the carbides varies between 45 μm and 150 μm . It is important to note that the initial weight fractions in the feed serves as an upper bound on the balance of carbide in the final coating. In practice 65% by weight (50% by volume) represents the limit of industrially observed fully densified clads.

5.4 Ni-WC Clad Pool Material Properties

The relevant physical properties for this work on thermocapillary flows are: heat capacity c_p , viscosity μ , thermal conductivity k , surface tension coefficient σ_T , and density ρ . The evaluation of material properties for the composite Ni-WC system is accomplished considering each property as a functions of both temperature and relative phase fraction in the clad pool. The strategy is to calculate properties for each constituent taking a single average across the clad pool temperature range (Equation (5.8)), which changes significantly based on the constituent fraction in the pool shown in Table (5.4). Data for the materials in this analysis is largely unavailable; therefore, data for pure nickel and stoichiometric tungsten carbide are taken to approximate the material properties here. A combination of thermodynamic modelling using ThermoCalcTM, literature data [32], and material property models presented by Mills [33] and Iida [34] have been employed to obtain the best possible estimates for the temperature dependence of the nickel and tungsten carbide constituents. Single values for $c_{P_{eff}}$ and ρ_{eff} are combined using a rule of mixture approach. A combined reinforcement conductivity for Ni-WC has been determined considering a matrix of pure nickel interspersed with uniformly distributed spheres of WC. For this scenario Maxwell's equation for conductivity of heterogeneous media applies [35]. The surface tension coefficient is considered to be a constant value taken from data for a nickel-silicon binary presented by Keene [36]. This estimate considers the effect of the solid phase fraction on the surface tension to be negligible. Viscosity is this only parameter in this analysis that is not bound between the property values of the constituents. As shown in the analysis below, it has the potential to change orders of magnitude at high solid fraction in the molten pool while simultaneously having a one to one correspondence with the Prandtl number and an inverse square relationship to the Reynolds number for thermocapillary flows. The approach to quantify this effect is

summarized below as the most critical material property value of this composite analysis. A more detailed summary of the values for $c_{P_{eff}}$, k_{eff} , σ_T , and ρ_{eff} is included in Appendix 5.2. Section 5.4.2 presents a summary of all material properties for the solid fractions used in this work.

5.4.1 Effective Viscosity μ_{eff}

Viscosity of the composite pool is accounted for considering an increase viscous effect of the solid reinforcing phase on the molten fluid using the semi-empirical Thomas equation shown in Equation (5.12) [37]. Thomas' equation applies to uniform spheres in a Newtonian fluid, which fits well with the small size range of the spherical WC particles in the Ni-WC powders in this work (45 μm -106 μm). The first two terms represent Einstein's solution for a dilute suspension of spheres [38]. The $f_{v_{cb}}^2$ term accounts for interaction effects between particles in more concentrated suspensions, and the exponential term includes two fitting parameters that compensate for higher order particle interactions (up to $f_{v_{cb}}^7$ described by Thomas), which become dominate at higher volume fractions ($\geq 40\%$) [37]. This equation was shown by Thomas' to adequately reproduce experimental data from an 8 term power series form of the viscosity-particle concentration relationship to within a variance of fit of 0.152. The simplicity of the Equation (5.12) containing only two fitting parameters compared to several coefficients in the 8 terms power series is superior for the simple but accurate approach in this work and is the preferred final form of the relation presented by Thomas. Notation from the list of symbols defined in this work has been substituted in Equation (5.12) for consistency with this analysis.

$$\mu_{eff}/\mu_m = 1 + 2.5f_{v_{cb}} + 10.05f_{v_{cb}}^2 + Be^{Cf_{v_{cb}}} \quad (5.12)$$

where μ_{eff} is the effective viscosity of the composite pool (Pa·s), μ_m is the effective viscosity of the molten Ni-Cr-B-Si powders (Pa·s), and B and C are experimental fitting parameters (1). The best fit is obtained by Thomas with values of B and C of 0.00273 and 16.6 respectively [37]. No data on the viscosity of the Ni-Cr-B-Si alloy chemistry is available directly, and therefore the liquid component of the pool is modelled as pure nickel, which composes approximately 85 wt% (75 mol%) of the pool. Data for Ni viscosity extending the entire temperature range of this work is unavailable in literature, and Equation (5.13), presented in Mills' book on thermophysical properties of materials, is used to predict viscosity up to the temperatures of this analysis [33].

$$\mu_{Ni} = 10^{(-0.5038+2029/T)} \quad (5.13)$$

The units of μ_{Ni} from Equation (5.13) are mPa·s. Figure (5.5) shows the dependence of viscosity on solid fraction from Equation (5.12). The effective values are highlighted in the figure, and the summarized below in Table (5.6) for all for all three volume fractions considered in this analysis.

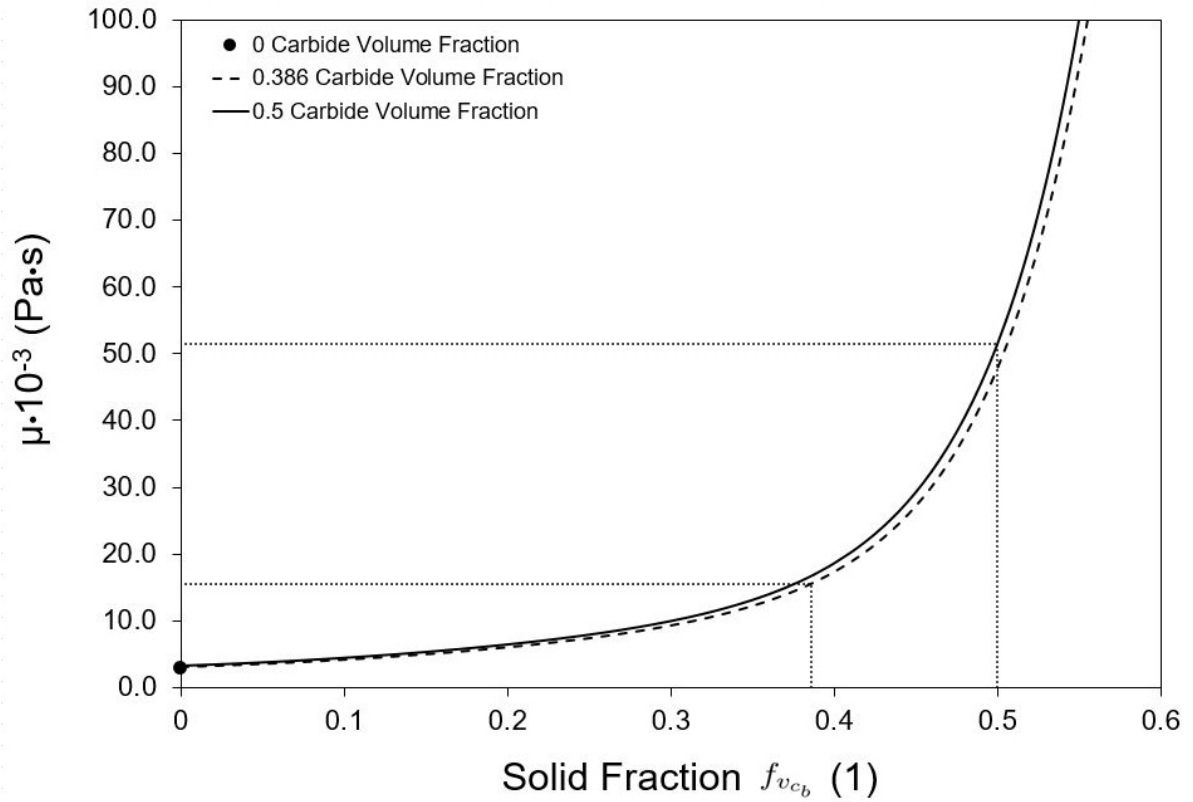


Figure 5.5: The effect of carbide volume fraction on the effective viscosity of the molten pool.

Table 5.6: Values for the effective viscosity analysis of a Ni-WC composite clad pool

Deposited Carbide Volume Fraction $f_{v_{cb}}$ (1)	Metal Powder Viscosity μ_m (Pa·s)	Effective Clad Pool Viscosity μ_{eff} (Pa·s)
0	2.812×10^{-3}	2.812×10^{-3}
0.386	3.029×10^{-3}	1.550×10^{-2}
0.5	3.267×10^{-3}	5.145×10^{-2}

5.4.2 Effective Values Summary

Table (5.7) summarizes the effective material property values used in this analysis of fluid flow for each of the three values of $f_{v_{cb}}$ under consideration here.

Table 5.7: Effective thermophysical properties for the composite Ni-WC pool used in this analysis of thermocapillary flows

Solid Fraction $f_{v_{cb}}$ (1)	ΔT^* (K)	$c_{p_{eff}}$ (J/kgK)	μ_{eff} (Pa·s)	k_{eff} (W/mK)	$\sigma_{T_{eff}}$ (N/mK)	ρ_{eff} (kg/m ³)
0	983	798.21	2.812×10^{-3}	65.06	2.964×10^{-4}	7336.5
0.386	790	521.27	1.599×10^{-2}	56.36	2.964×10^{-4}	11110
0.500	631	463.51	5.145×10^{-2}	55.61	2.964×10^{-4}	12151

5.5 Results

The first step in this analysis of thermocapillary flows is to determine the Pr number for the Ni-WC clad pool to satisfy Rivas' primary condition for this analysis. Values for the Re_σ and A quantities have been calculated for the range of solid fractions considered in this work (0% up to 50%). These results are summarized in Table (5.8) from Equations (5.1), (5.2), and (5.3). It is important to note that these calculations have been done using the measured geometry of the experimental clad and experimental cladding conditions in Tables (5.2) and (5.3) respectively applied to the hypothetical solid fractions considered here.

Table 5.8: Summary of the dimensionless quantities to characterize thermocapillary flows for typical laser cladding conditions of Ni-WC

Dimesionless Quantity	$f_{v_{cb}} = 0$	$f_{v_{cb}} = 0.386$	$f_{v_{cb}} = 0.5$
Pr	0.0345	0.1479	0.4713
Re_σ	125405	6778.5	799.03
A	0.3946	0.3946	0.3946

Figure (5.6) displays a process map of the problem or a graphic representation of the conditions for Regime I, II, and III. The dots correspond to the different Ni-WC clad carbide volume fractions in this analysis. The dashed lines represent the boundaries of the particular regime, which come from the relationships between Pr , Re_σ , and A shown in Table (5.1). Boundaries for $A = 1$, and $A = 0.4$ (corresponding to the experimental clad in this work) are shown against the log scale Pr - Re_σ plot in the figure. All plotted values for Ni-WC laser clad overlays in this work fall very close to the Regime II/III boundary with point $f_{v_{cb}} = 0$ nearly on the boundary line itself.

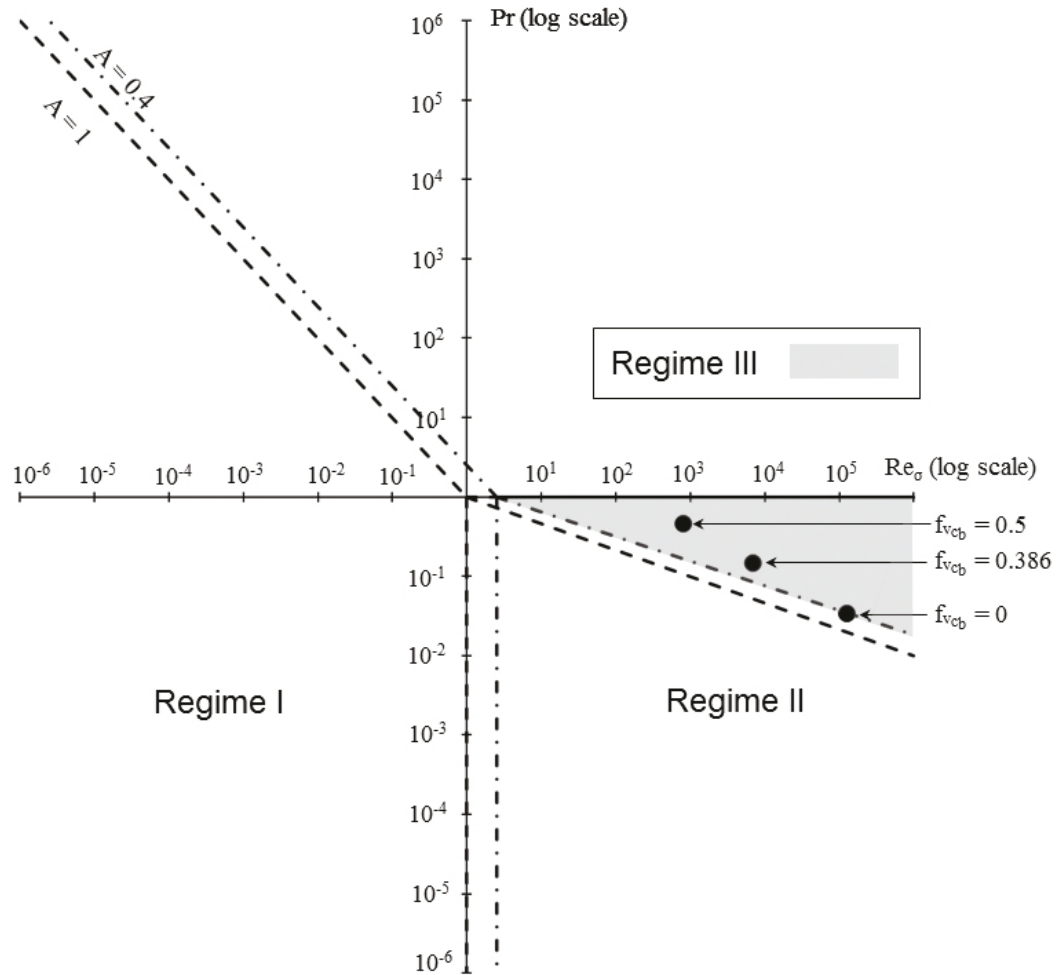


Figure 5.6: Process map for thermocapillary flows. The dashed lines indicate a boundaries of the Rivas' regimes defined by the conditions in Table (5.1). The shaded area in the plot corresponds to the $A=0.4$, which applies to all the cases considered here. The dot labelled " $f_{v_{cb}} = 0$ " corresponds to the conditions $Pr = 0.03$ and $Re_{\sigma} = 125405$. The dot labelled " $f_{v_{cb}} = 0.386$ " corresponds to the conditions $Pr = 0.15$ and $Re_{\sigma} = 6779$. The dot labelled " $f_{v_{cb}} = 0.5$ " corresponds to the conditions $Pr = 0.47$ and $Re_{\sigma} = 799$.

The calculated values of the Pr number for all solid fractions in this analysis meet the conditions for low Pr number fluids required by Rivas' analysis ($Pr \ll 1$). As shown in the figure, all three cases are adjacent to the Regime II/III boundary with the experimental 38.6% and 50% solid fractions within the Regime III region. This classification indicates that both a viscous and thermal boundary layer are present in the fluid cavity. The

results of the calculated characteristic values for Regime III presented in Section 2.3 are shown in Table (5.9) for $f_{v_{cb}} = 0.5$ and $f_{v_{cb}} = 0.386$.

Table 5.9: Summary of the characteristic values for laser cladding of Ni-WC presented in Section 2.3

Reference Quantity	Equation Number	$f_{v_{cb}} = 0.386$		$f_{v_{cb}} = 0.5$	
δ_t	(5.4)	3.605×10^{-4} m	0.3605 mm	2.579×10^{-4} m	0.2579 mm
U_s^*	(5.6)	6.289×10^{-1} m/s	628.9 mm/s	0.3556 m/s	355.6 mm/s
$\delta_{t_{s-l}}$	(5.5)	8.7082×10^{-5} m	0.0871 mm	1.112×10^{-4} m	0.1112 mm

5.6 Discussion

The classification of Regime III for the experimental clad ($f_{v_{cb}} = 0.386$) is an unexpected result. It had been initially hypothesized that the presence of high volume fraction of carbides in the molten clad pool would increase the effective viscosity to the point where it could be classified as a Regime I or II, where fluid flow is secondary to heat conduction. The positions of the points in Figure (5.6) show that for the cladding conditions considered here the Reynolds number is a minimum of two orders of magnitude higher than the requirement for Regime I at $A = 0.4$, but it is borderline with Regime II. The practical implication of this conclusion is that convection cannot be immediately discarded.

It was determined that the majority of the pool is contained within the thermal boundary layers shown in Table (5.9). For the experimental clad (38.6% solid fraction), 89.5% of the pool thickness is within these two boundary layers, and for the hypothetical 50% case this value was found to be 73.8%. These thicknesses are substantial and support the argument for considering conduction as a more significant heat transfer mechanism in a typical Ni-WC clad pool [39].

The nature of this analysis does not consider the disruptive effects of the forced-fed

powders penetrating and deforming the surface of the melt at velocities of the order of a meter per second, which is the same order of magnitude as the speeds of the convective flows. In a similar dimensionless based analysis of heat transfer in laser cladding, Kumar and Roy justify their simplifying assumption of negligible convection in the molten pool because of high velocity of the impinging particles and high fraction of solid particles undergoing solidification in the melt [40]. Future work is necessary to evaluate the role of convection quantitatively in these high solid fraction composite coatings. The evidence presented in this analysis suggests that the role of convection is not dominant.

5.7 Conclusions

An analysis of fluid flow in laser cladding of Ni-WC has been conducted based on the thermocapillary flow analysis developed by Rivas and Ostrach for low-Pr number fluids [1]. The analysis indicates that:

- A Ni-WC clad pool under typical laser cladding conditions containing as much as 50% solid fraction of carbide (maximum amount of typical industrial applications) can be characterized as a low Pr number fluid.
- Asymptotic analysis indicates that the weld pool during laser cladding is in a borderline case between conduction and convective heat transfer mechanisms. Rivas' analysis indicates that this borderline condition is still dominated by conduction with fluid flow playing a secondary role.
- The combined thermal boundary layer thicknesses (surface and solid-liquid interface) was calculated to be 89.5% of the cavity depth. Heat conduction is dominant in this boundary layer region supporting the argument that conduction plays a more significant role than convection in laser cladding under the conditions tested.

5.8 Acknowledgements

The authors wish to acknowledge Apollo Clad Laser Cladding, a division of Apollo Machine and Welding Ltd. who was instrumental in sharing their knowledge, equipment, and powder blends. The authors also acknowledge NSERC for providing project funding for this research. Student scholarships from the American Welding Society and Canadian Welding Association were gratefully received.

5.9 Appendix 5.1 CO₂ Laser Beam Characterization

Figure (5.7) shows the two dimensional map produced by the profiler that identified the divergence angle and beam radius at various plane locations for a 4 kW power output of the 10.6 μm CO₂ laser beam. Highlighted in the image are the divergence angle ϕ and minimum radius at the beam focus point labelled $4\sigma_{min}$. This notation is used to signify that the measurement is for the second moment, which represents the 4σ value (2σ on either side of the centreline marked 0 on the x-axis) of the beam.

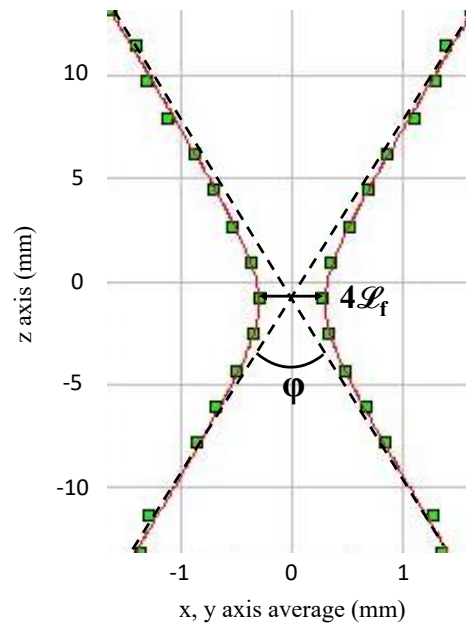


Figure 5.7: Second moment of the beam profile results for the CO₂ laser in this work. Units are in mm, and the y to x scale is 5:1 to emphasize the divergence angle ϕ .

The typical working distance of the laser is 19.05 mm (0.75 in) below the $4\mathcal{L}_f$ value in Figure (5.7). With a measured $4\mathcal{L}_f$ value of 0.600 mm and ϕ of 13.08°, the \mathcal{L} value of beam at the working distance of the experiment was calculated to be 1.242 mm. The procedure and definitions for the beam are outlined fully in ISO-11146-1 [41].

5.10 Appendix 5.2 Material Properties for the Composite Clad Pool

Outlined in this appendix is additional information about the individual material properties for the Ni-Cr-B-Si metal powders and WC particles used to determine effective material properties for this analysis of fluid flow. Presented in this appendix are literature thermophysical data for Ni and WC that corroborate the selected constituent

material properties as well as models presented in reputable sources. Formulae for the effective property values are proposed for each of the following properties: heat capacity ($c_{p_{eff}}$), viscosity (μ_{eff}), thermal conductivity (k_{eff}), surface tension coefficient ($\sigma_{T_{eff}}$), and density (ρ_{eff}), summarized in the body of this work in Table (5.7). The presented trends and effective values in this appendix are demonstrated for $f_{v_{c_b}} = 0.5$, but parallel analysis have been conducted for $f_{v_{c_b}} = 0$ and $f_{v_{c_b}} = 0.386$.

5.10.1 Effective Heat Capacity $c_{p_{eff}}$

The heat capacity of the molten pool is taken as a rule of mixtures considering the heat capacity of both the Ni-Cr-B-Si matrix and WC phases as functions of temperature. The temperature range of interest is considered to be the temperature difference through the thermal boundary layer. The temperature of the core region is taken as the solidus temperature of the 4145-MOD steel (1692 K). The maximum temperature at the surface of the 50% volume fraction carbide (65% weight fraction) clad pool is 2323 K. The rule of mixtures equation for effective heat capacity in this work is shown in Equation (5.14).

$$c_{p_{eff}} = (1 - f_{m_{c_b}})c_{p_m} + f_{m_{c_b}}c_{p_c} \quad (5.14)$$

Values for specific heat capacity of molten matrix are not reported by any source but have been determined using ThermoCalcTM nickel alloy database TTNi8. The molar enthalpy has been calculated for a range of temperatures from 1000 K to 3000 K for the Ni-Cr-B-Si MTR reported chemistry. The calculated equilibrium solidus temperature and liquidus temperatures are 1171 K and 1513 K respectively, which represents a wider solidification range than that reported by the manufacturer Hogänäs (1279 K and 1323 K) determined using differential scanning calorimetry (DSC) [42]. Equation (5.15) has been

used to calculate the c_p from the enthalpy data output in one degree increments.

$$c_{p_i} = \frac{1}{M_m} \frac{H_{mol_{i+1}} - H_{mol_{i-1}}}{T_{i+1} - T_{i-1}} \quad (5.15)$$

where c_{p_i} is the specific heat capacity at data point i (J/kgK), M_m is the molar mass of the Ni-Cr-B-Si metal powders (kg/mol), $H_{mol_{i+1}}$ is the molar enthalpy at data point $i+1$ (J/molK), $H_{mol_{i-1}}$ is the molar enthalpy at data point $i-1$ (J/molK), T_{i+1} is the temperature at data point $i+1$ (K), and T_{i-1} is the temperature at data point $i-1$ (K). M_m has been computed using ThermoCalcTM to be 51.95 g/mol. Figure (5.8) shows the molar enthalpy output from ThermoCalcTM from 1600 K to 2400 K, which encompasses the temperature range of interest for this analysis.

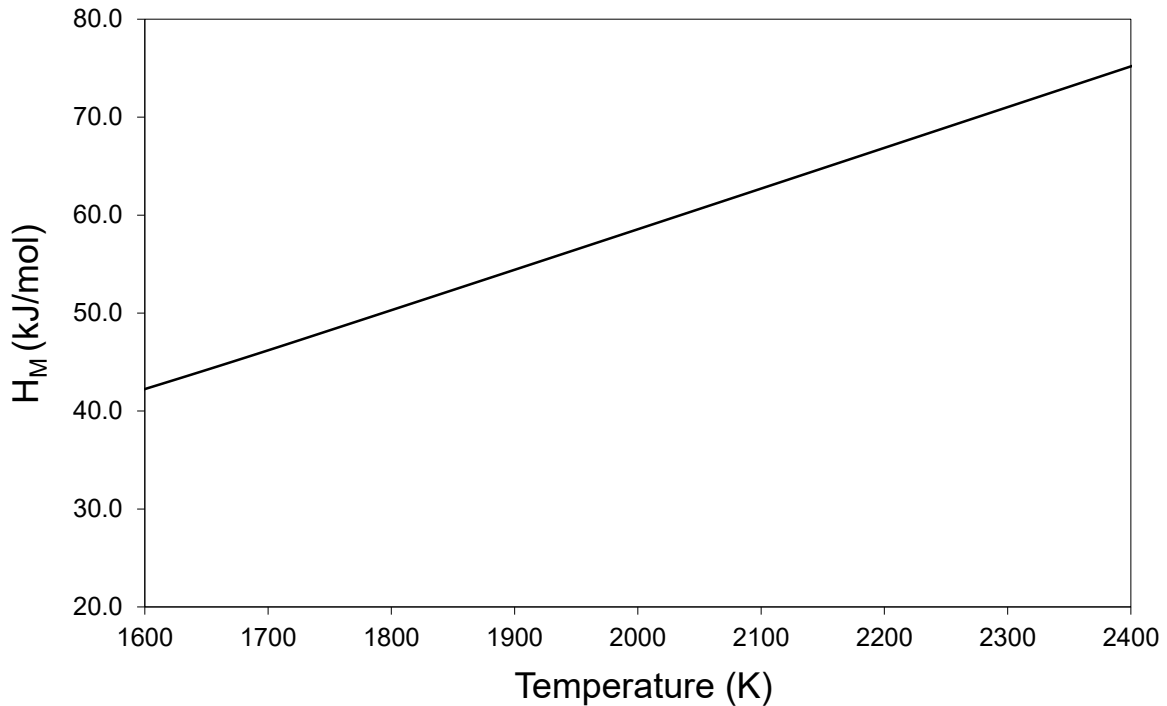


Figure 5.8: Molar enthalpy of the Ni-Cr-B-Si matrix used in this work as a function of temperature from ThermoCalcTM.

Using Equation (5.15), Figure (5.9) has been generated to show heat capacity as a

function of temperature for the Ni-Cr-B-Si matrix. Values for pure liquid nickel from the JAHM database are also included for comparison, which are uniform in the liquid phase across the entire temperature range [32]. The effective value for the molten metal matrix specific heat capacity is 796.74 J/kgK, which comes from the ThermoCalcTM data.

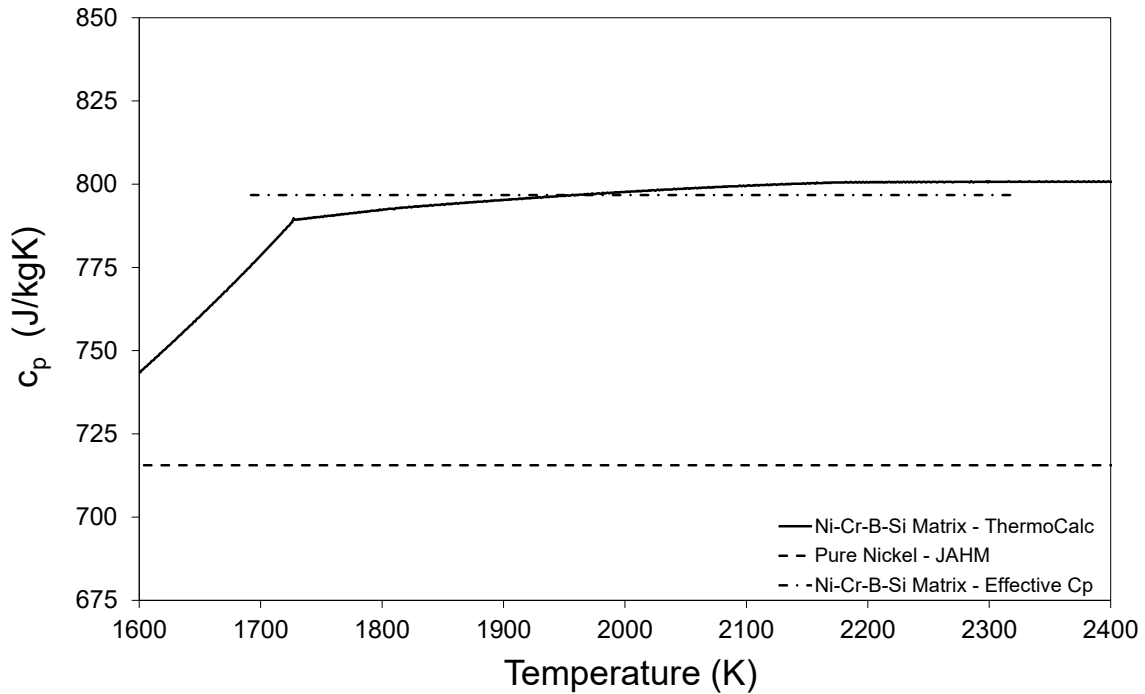


Figure 5.9: Specific heat capacity of Ni-Cr-B-Si matrix used in this work as a function of temperature showing the effective value used in this work.

Values for c_p of WC are reported directly in the JAHM database for the entire temperature range considered here [32]. This source is the most complete available to calculate the value of c_{pe} . The chemistry of the JAHM source is 93.9 wt% W and 6.1 wt% C, which is higher than the carbides in this work reported in Table (5.5) but is still within the same phase boundaries for the applicable temperatures [43]. An effective value of 287.83 J/kgK is calculated for c_{pe} between 1692 K and 2323 K. Figure (5.10) shows these

values along with additional data from Touloukian [44], which supports the increasing slope of heat capacity with respect to increasing temperature in this range.

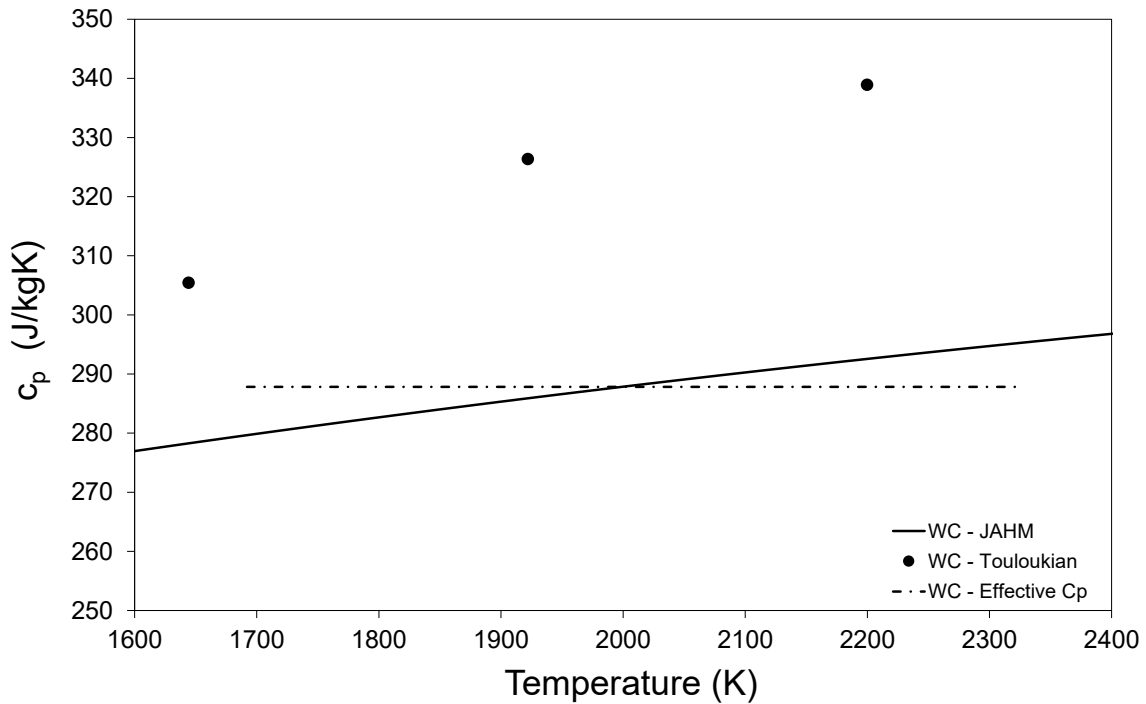


Figure 5.10: Specific heat capacity of WC as a function of temperature showing the effective value used in this work.

Data for the heat capacity of WC as a function of temperature from the JAHM database [32] (93.9 wt%W and 6.1 wt%C) and Touloukian's TPRC Data Series for Specific Heat of Nonmetallic Solids [44] (93.9 wt%W and 6.15 wt%C) is shown in Figure (5.11) against data for a non-stoichiometric carbide $W_2C_{0.833}$ from Grønvold *et. al* [45]. It is likely that the actual heat capacity of the $WC_{0.6}$ used in this work would fall between the data for WC and $W_2C_{0.833}$ ($\sim WC_{0.4}$), but more importantly not substantially different as to effect the results of this work in a meaningful way.

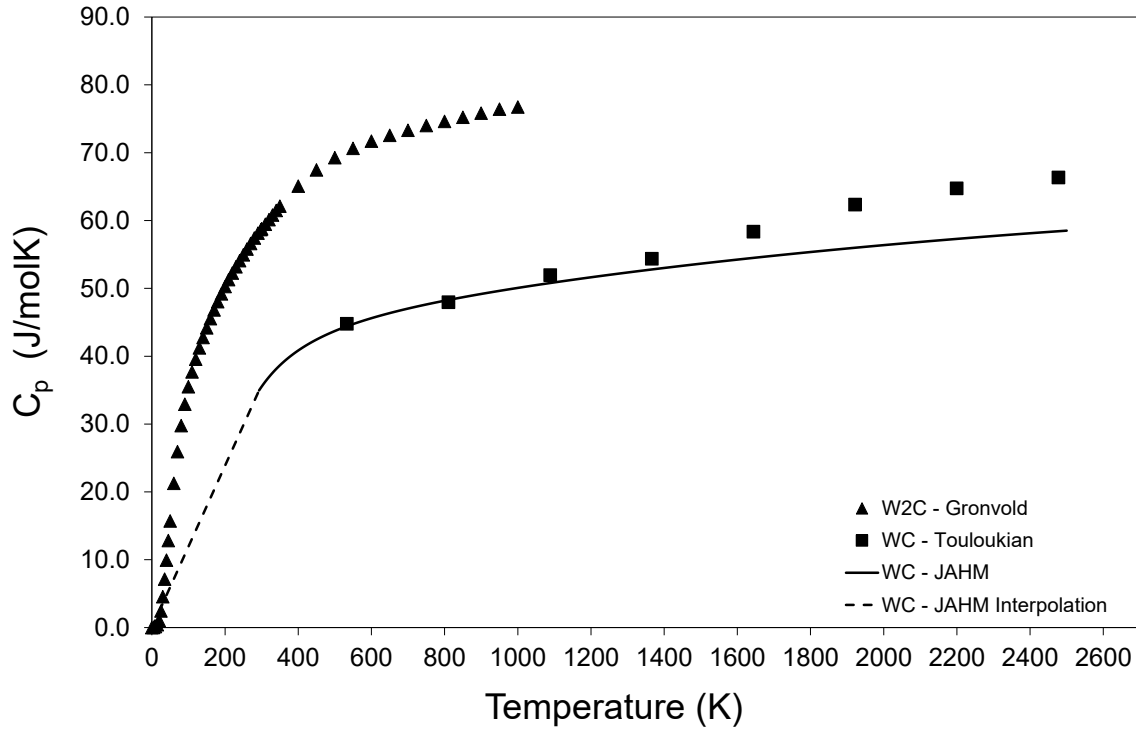


Figure 5.11: Heat capacity of WC as a function of temperature for different stoichiometries of the compound.

Combining c_{pm} , c_{pc} , and $f_{m_{cb}} = 0.655$ into Equation (5.14), the final value of specific heat for the Ni-WC molten clad pool is 463.51 J/kgK.

5.10.2 Effective Viscosity μ_{eff}

No data on the viscosity of the Ni-Cr-B-Si alloy chemistry was available, and therefore the liquid component of the pool is modelled as pure nickel. A series of equations in literature to predict the temperature dependence of viscosity of nickel have been applied and compared against available literature data. Firstly, the JAHM database contains limited data between 1667 K and 1930 K [32]. A paper by Assael *et al.* also contains tabular data for nickel viscosity up to 2100 K [46]. Figure (5.12) is included from Iida and Guthrie's book "The Physical Properties of Liquid Metals", which contains a summary

of viscosity data for nickel determined using a variety of methods [34].

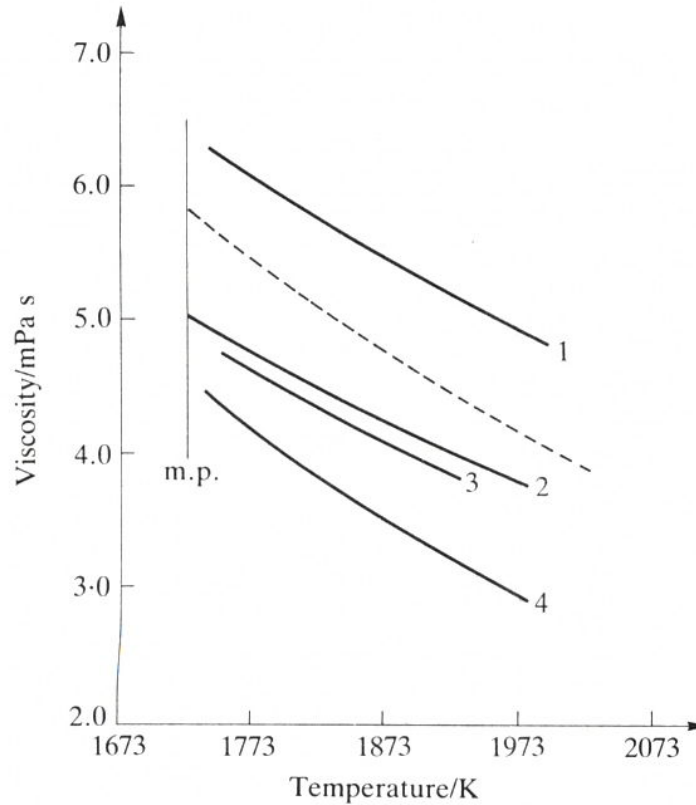


Figure 5.12: Experimental data for viscosity of pure nickel as a function of temperature summarized by Iida and Guthrie (Figure 6.27) [34].

Figure (5.12) shows a large variation in measured viscosity data, which is only available for a limited range of temperatures. To obtain data extending the entire range of this work, Models from literature are applied to predict the temperature dependence of viscosity. Mills book on thermophysical properties of materials presents Equation (5.13) to predict viscosity of nickel [33] (no temperature range of limited applicability in the liquid phase is stated).

$$\mu_{Ni} = 10^{(-0.5038+2029/T)} \quad (5.13)$$

The ASM handbooks present Equations (5.16) and (5.17) to predict viscosity of pure metals as a function of temperature based on work from Iida and Guthrie [47, 48].

$$\mu_T = \mu_0 \exp\left(\frac{2.65T_{melt}^{1.27}}{RT}\right) \quad (5.16)$$

where μ_T is the viscosity at temperature T (Pa·s), μ_0 is the reference viscosity (Pa·s), and R is the real gas constant (8.314 J/molK). The reference viscosity is normally taken at the melting temperature as follows:

$$\mu_0 = \frac{\mu_{melt}}{\exp\left(\frac{2.65T_{melt}^{0.27}}{R}\right)} \quad (5.17)$$

where μ_{melt} is the viscosity at the melting temperature (Pa·s) and T_{melt} is the melting temperature (K). The Andrade equation is also presented in several sources as an alternative equation to model viscosity of metal liquids [33, 34, 47]. Andrade's equation relates the molar volume and molar mass of the pure metal to a temperature dependant viscosity [49]. In 2005, George Kaptay presented a unified equation for viscosity of pure liquid metals, which supports Andrade's results combining the concept of energy activation with Andrade's free volume concept [50]. Kaptay's unified equation is presented in Equation (5.18).

$$\mu_T = F \left(\frac{M_{Ni}^{1/2}}{V_{melt}^{2/3}} \right) T^{1/2} \exp\left(I \frac{T_{melt}}{T} \right) \quad (5.18)$$

where F and I are fitting constants with values $1.80(\pm 0.39) \times 10^{-8}$ (J/Kmol^{1/3})^{1/2} and $2.34(\pm 0.20)$ respectively, M_{Ni} is the molar mass of nickel [51], and V_{melt} is the molar volume of the nickel liquid at the melting temperature (m³/mol) [32]. Smithell presented

a model for pure liquid metal viscosity shown in Equation (5.19) [52].

$$\mu_T = \mu_o \exp\left(\frac{E}{RT}\right) \quad (5.19)$$

where E is activation energy (J/mol). Values for μ_o and E of nickel were reported to be 0.1663×10^{-3} Pa·s and 50,200 J/mol. Figure (5.13) summarizes the data from Equations (5.13), (5.16), (5.18), (5.19) and available experimental sources. The decreasing trends for all sources agree well between 1600 K and 2400 K. The effective value for viscosity for the molten matrix, μ_m , is taken as the average from the Mills model prediction between 1728 K (melting temperature of nickel) and 2323 K. This value is 3.267×10^{-3} Pa·s. The discrepancy between the substrate melting temperature 1692 K (T_0) and the melting temperature of pure nickel (1728 K) is noted, but has a nearly negligible effect on the calculated effective value across a temperature range of hundreds of degrees. The remainder of the determination of μ_{eff} is highlighted in the body of the paper.

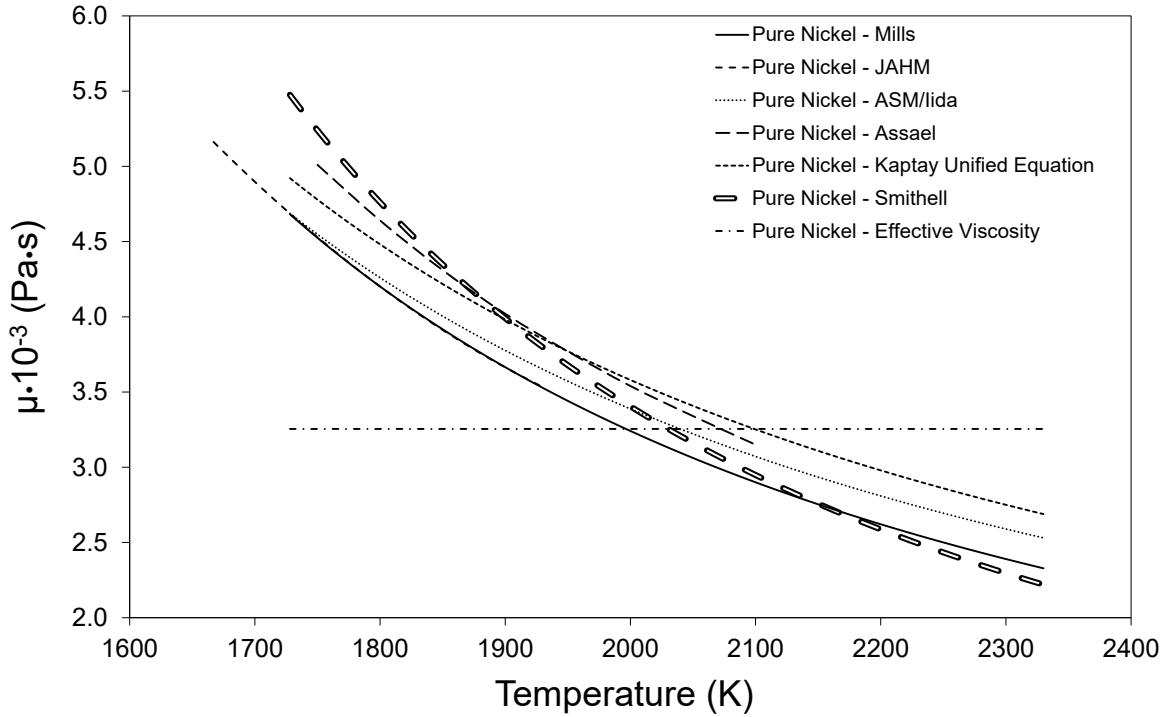


Figure 5.13: Viscosity of pure nickel as a function of temperature showing the effective value used in this work.

5.10.3 Effective Thermal Conductivity k_{eff}

Previous analyses by the author have incorporated a combined reinforcement conductivity for Ni-WC considering a matrix of nickel interspersed with uniformly distributed spheres of WC [6]. For this scenario Maxwell's equation for conductivity of heterogeneous media applies shown in Equation (5.20) [35].

$$k_{eff} = \left[\frac{2k_c + k_m + f_{v_{cb}}(k_c - k_m)}{2k_c + k_m - 2f_{v_{cb}}(k_c - k_m)} \right] k_m \quad (5.20)$$

Data for the thermal conductivity of the molten Ni-Cr-B-Si metal powders is unavailable at any temperature; therefore, values for pure nickel are used as an estimate for the matrix alloy. Values are reported directly for elemental nickel from the JAHM

database [32] and Mills book on thermophysical properties of commercial alloys [33]. Thermal conductivity of the matrix is also estimated using the Wiedemann-Franz-Lorenz (WFL) rule shown in Equation (5.21).

$$k_m = \frac{L_0 T}{\rho_e} \quad (5.21)$$

where L_0 is a constant with a theoretical value of $2.445 \times 10^{-8} \text{ W}\Omega/\text{K}^2$ and ρ_e is the electrical resistivity (Ωm). The WFL rule is typically shown with electrical conductivity σ_e , but the simple inverse relationship between electrical conductivity and resistivity ($\sigma_e = 1/\rho_e$) is substituted into Equation (5.21) to be consistent with available resistivity data for pure nickel. Iida and Guthrie summarize experimental data for the resistivity of liquid nickel as a function of temperature between 1728 K and 1973 K as the linear relationship shown in Equation (5.22) [53].

$$\rho_{eT} = (1.27 \times 10^{-10})T + 6.3 \times 10^{-7} \quad (5.22)$$

where ρ_{eT} is the electrical resistivity of pure nickel as a function of temperature (Ωm). The effective value for thermal conductivity for this analysis is taken as the average temperature between 1728 K (the melting temperature of pure nickel) and 2323 K from the JAHM data, which was the most complete resource and fell between Mills reported values and the WFL calculation. The effective thermal conductivity of the metal powders, k_m , is found to be 61.31 W/mK. Figure (5.14) shows the available data sets for pure nickel, the WFL rule calculation (Equation (5.21)), and the effective average value for the molten Ni-Cr-B-Si metal powders.

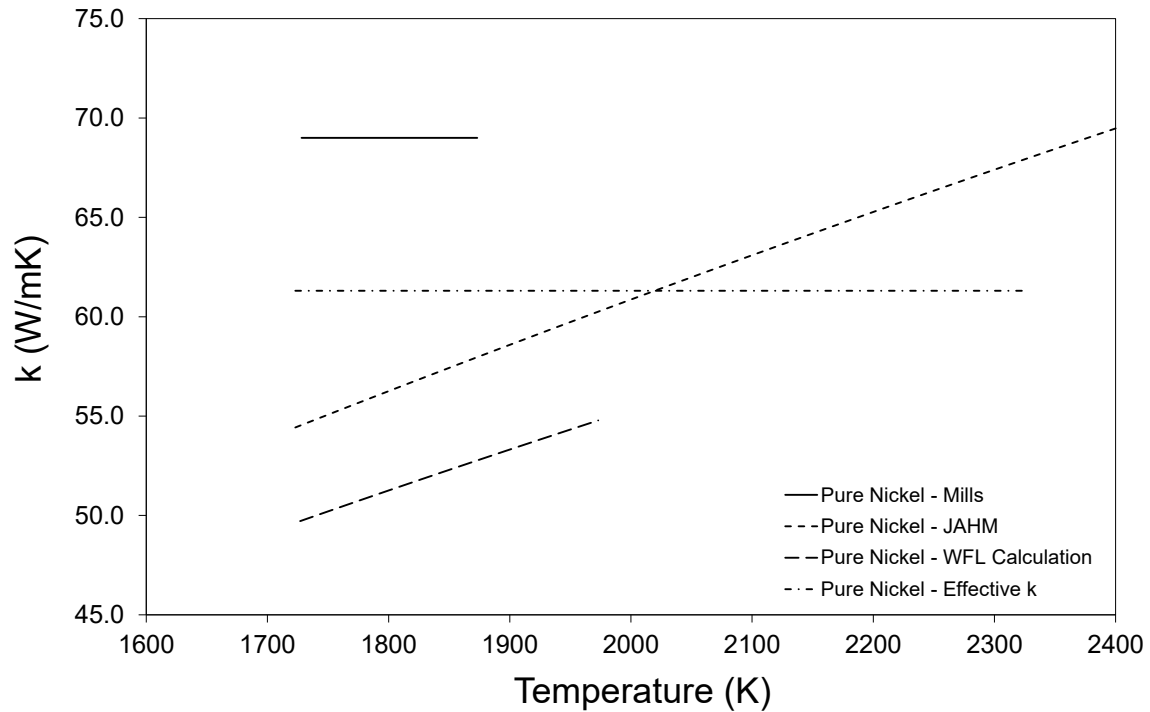


Figure 5.14: Thermal conductivity as a function of temperature showing the effective value for the Ni-Cr-B-Si powders used in this work.

Data for high temperature thermal conductivity of WC is only available in the JAHM database up to 1900 K. The effective value is taken at 1900 K as close to the midpoint of the temperature range as possible in what is a decreasing trend asymptotically approaching a value around 48 W/mK around 2200 K. The effective value for k_c is 50.57 W/mK shown in Figure (5.15)

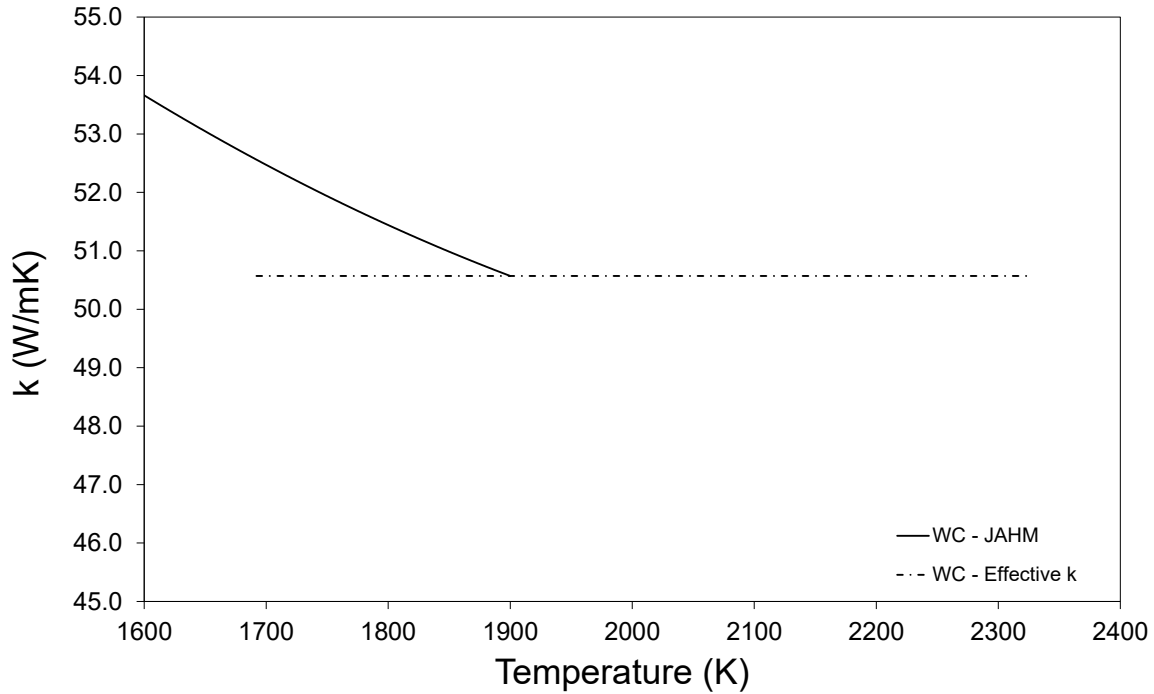


Figure 5.15: Thermal conductivity as a function of temperature showing the effective value for the tungsten carbide powders used in this work.

Using Equation (5.20), $k_m = 61.31$ W/mK, $k_c = 50.57$ W/mK, and $f_{v_{cb}} = 0.5$, the effective composite thermal conductivity between 1692 K and 2323 K is calculated to be 55.61 W/mK.

5.10.4 Effective Surface Tension Coefficient $\sigma_{T_{eff}}$

The surface tension coefficient of the Ni-WC composite has been determined by considering the surface tension effects of the liquid phase only assuming a negligible effect on the surface tension from the solid phase fraction in the pool. Numerous studies have been done looking at the surface properties of nickel and its alloys. A summary of the values reported in literature for the surface tension coefficients for nickel and binary nickel

alloys has been included in Table (5.10). All sources agree that a linear temperature dependence of the surface tension coefficient can be implemented for temperatures near melting.

Table 5.10: Literature surface tension values for nickel and nickel based alloys

Alloy (wt%)	$d\sigma/dT^*$ (mN/mK)	Measurement Technique	Temperature Range (K)	Year	Reference
Nickel	0.21 ± 0.43	Sessile Drop	1689-1898	1970	Fraser [54]
96.5%Ni-3.5%Si	-0.296^\dagger	Unavailable	Unavailable	1971	Shergin [36]
Nickel	-1.76	Sessile Drop	1728-1773	1976	Ahmad [55]
Nickel	-0.38	Unavailable	Unavailable	1992	Smithell [52]
Nickel	-0.460	Sessile Drop/Model	1773-1873	2005	Xiao [56]
95%Ni-5%Cr	-0.900	Sessile Drop/Model	1773-1873	2005	Xiao [56]
90%Ni-10%Cr	-0.417	Sessile Drop/Model	1773-1873	2005	Xiao [56]
Nickel	-0.33	Electromag Levitation	1448-1928	2005	Brillo [57]
75%Ni-25%Fe	-0.276	Electromag Levitation	1750-2000	2005	Brillo [57]

* Negative value for the surface tension coefficient indicates a decrease in surface tension with increasing temperature

† Calculation for this value is shown in this section

The most valuable reference for surface tension coefficients comes from a review paper by Keene in 1987 who refers to the work of Shergin *et al.* from the USSR. In 1971 Shergin *et al.* reported the change in surface tension coefficient for the entire nickel-silicon binary, which is shown below in Figure (5.16). The shift in slope around 70 at%Ni has also been observed by Vasiliu and Eermenko [58]. The line drawn at 93 at%Ni in Figure (5.16) represents the 3.5 wt%Si for the Ni-Cr-B-Si alloy powder under consideration in this work assuming the balance as nickel. The value of the surface tension coefficient has been identified using linear interpolation between 90 at%Ni and 100 at%Ni on the graph, which is reasonable based on the linear trend in high nickel content region of the curve (>80 at%Ni). This value for the metal powders is -0.296 mN/mK.

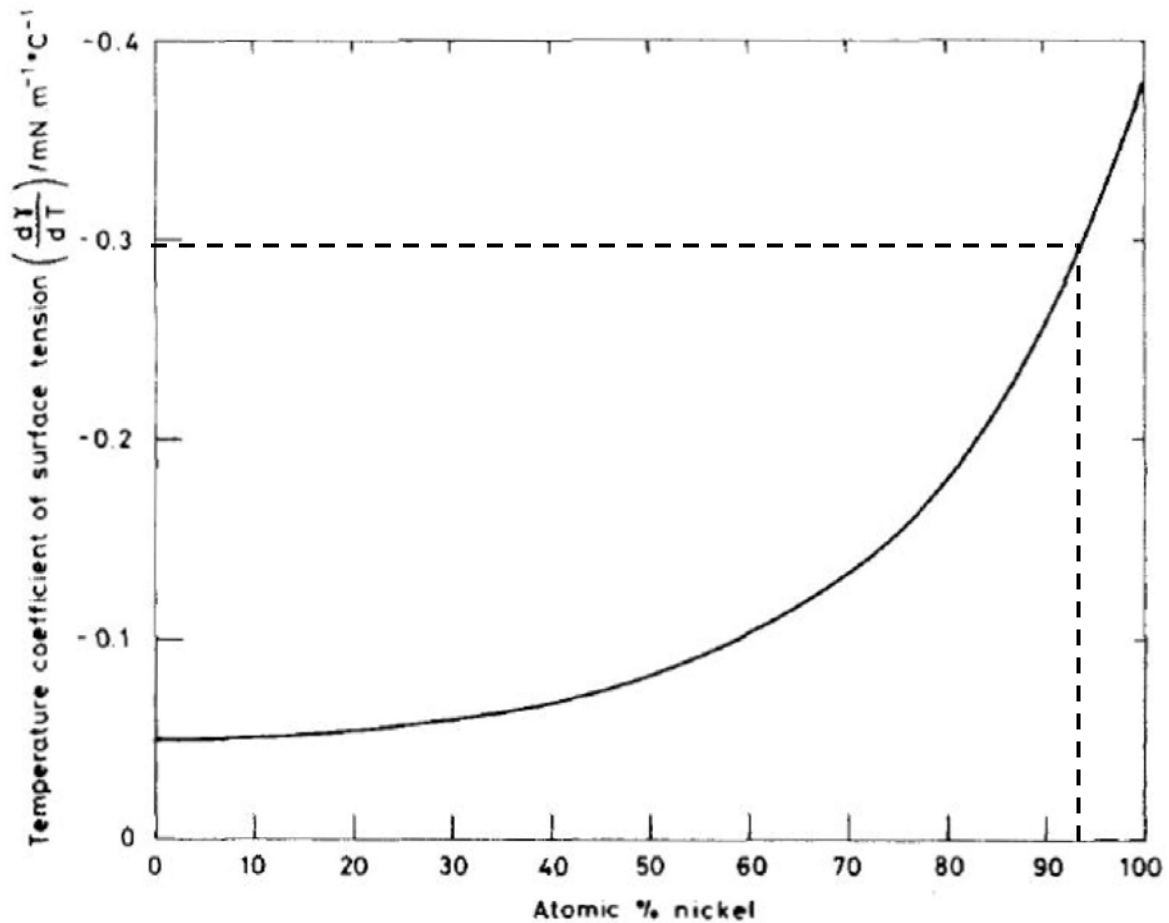


Figure 5.16: Surface tension coefficient of Ni-Si binary alloys [36]. Original work by Shergin *et al.*

The effects of alloying elements on the surface tension of nickel is only available from a select few sources. Most notable is a book titled “Surface Phenomena in Fusion Welding Processes” by German Deyev and Dmitriy Deyev, where effects of chromium, iron, and carbon in concentrations similar to the metal matrix compositions of this work are stated to have only small individual effects on the surface tension of nickel alloys [59]. German and Dmitriy Deyev also reported that silicon along with copper, sulfur, tellurium, and selenium were surface active elements for a nickel system [59]. It is unknown whether or not the composition additions have the same minimal effect on the surface tension

coefficient as they do on the surface tension directly for the temperatures in this work. It is reasonable to approximate the Ni-Cr-B-Si system as a Ni-Si binary, which accounts for the only reported surface active element in the melt. Data for combined elemental effects on the surface tension coefficient of nickel based alloys is non-existent. Oxygen, which is present in small quantities shown in the MTR data in Table (5.5), is a strong surfactant in iron alloys and has been shown to decrease the surface tension of pure liquid nickel at elevated temperatures [60]. Again, it is unclear whether the trends for oxygen content on the surface tension coefficient are the same. The effect of boron is likely to be similar to that of carbon, which does not play a large role in surface tension in concentrations of a few weight percent. Further research into individual and combined elemental effects may provide an improved estimate of the surface tension coefficient of the Ni-Cr-B-Si alloy, but it is not expected to have an order of magnitude effect relevant to the dimensionless characterization of the system in this work.

5.10.5 Density ρ_{eff}

The effective density of the molten pool was taken as a rule of mixtures considering the density of both the Ni-Cr-B-Si matrix and WC phases as functions of temperature, which is shown mathematically in Equation (5.23).

$$\rho_{eff} = (1 - f_{v_{c_b}})\rho_m + f_{v_{c_b}}\rho_c \quad (5.23)$$

Density data for the matrix chemistry as a function of temperature is unavailable and is approximated by pure nickel values. The density of liquid nickel as a function of temperature, similar to that of many metallic liquids, has been shown to have a linearly decreasing relationship with increasing temperature. Data from the JAHM database is available for liquid nickel density up to 2370 K [32]. Mill's reports the following equation

to calculate liquid nickel density [33]:

$$\rho_T = 7850 - 1.20(T - 1728) \quad (5.24)$$

where ρ_T is the density at temperature T (kg/m^3). Iida and Gunther use a slightly different formula for density prediction shown in Equation (5.25) [34].

$$\rho_T = 7900 - 1.19(T - 1728) \quad (5.25)$$

The CRC Handbook also contains data on the density of molten elements and representative salts [61]. Equation (5.26) shows the proposed formula for liquid nickel density:

$$\rho_T = 7810 - 0.726(T - 1728) \quad (5.26)$$

The maximum temperature that the CRC handbook recommends for Equation (5.26) is 1973 K. Smithell's metal reference book uses the following relation to predict liquid nickel density:

$$\rho_T = 7905 - 1.160(T - 1727) \quad (5.27)$$

Figure (5.17) summarizes the sources for liquid nickel density. There is a small discrepancy between the slope of Mills, Iida, and Smithell data compared to JAHM and the CRC Handbook likely due to variation in purity of the nickel in each case. The effective value for the density of the Ni-Cr-B-Si metal powders, ρ_m is calculated from JAHM's database for $f_{v_{c_b}} = 0.5$. For 38.6% and 0% volume fraction of carbide, Iida's model has been used to reach the necessary temperatures for the analysis. From the JAHM database the value for ρ_m at 50% carbide fraction is $7631.3 \text{ kg}/\text{m}^3$.

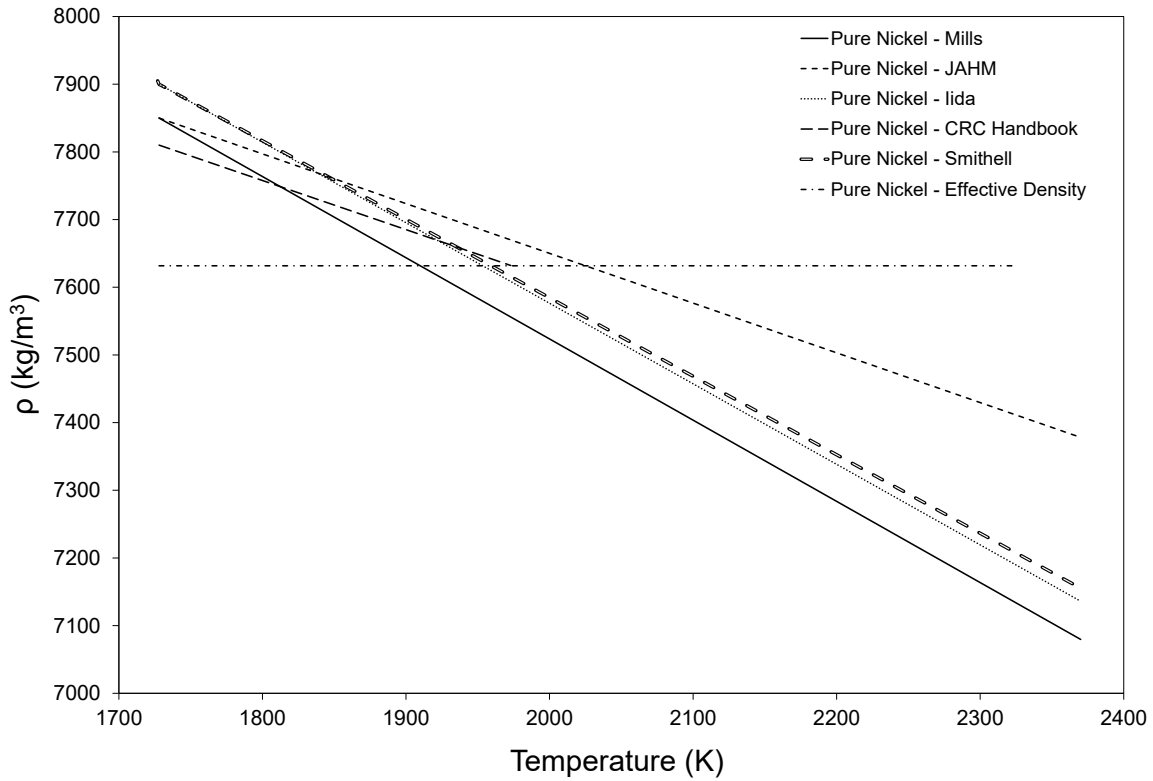


Figure 5.17: Density of liquid nickel as a function temperature showing the effective value for ρ_m used in this work.

No data for temperature dependent density of WC has been found in any source; however a model for density of solid materials as a function of temperature is proposed by Mills [33], which incorporates the coefficient of thermal expansion as follows:

$$\rho_T = \frac{\rho_{298}}{1 + 3\beta_L(T - 298)} \quad (5.28)$$

This equation assumes isotropic expansion and small dimensional changes, β_V can be approximated by $3\beta_L$ [62]. Data for the linear thermal expansion of WC from room temperature up to 2000 K is reported by Touloukian [63], which is shown below in Figure (5.18). Touloukian reported recommended values for the a-axis and c-axis of the crystal separately, as well as for polycrystalline WC. For the cubic B1 rock salt structure

of the $WC_{0.6}$, the relationship for the a-axis is used corresponding to the cubic crystal. The a-axis linear thermal expansion coefficient as a function of temperature is shown in Equation (5.29). The WC chemistry to generate the a-axis data has been reported as 93.6 wt%W, 6.24 wt%C, and 0.16 wt% other elements. The reported uncertainty in the reported values for all recommended values of linear thermal expansion is $\pm 5\%$.

$$\beta_L = -0.110 \times 10^{-6} + 3.409 \times 10^{-10}T + 1.276 \times 10^{-13}T^2 - 2.453 \times 10^{-17}T^3 \quad (5.29)$$

The value of β_L at 2000 K, the peak temperature available from the Touloukian, is 0.886×10^{-6} (mm/mm). This value has been used for all calculations of WC density as the most likely representative value and closest data point to the midpoint of a linearly decreasing density trend with increasing temperature.

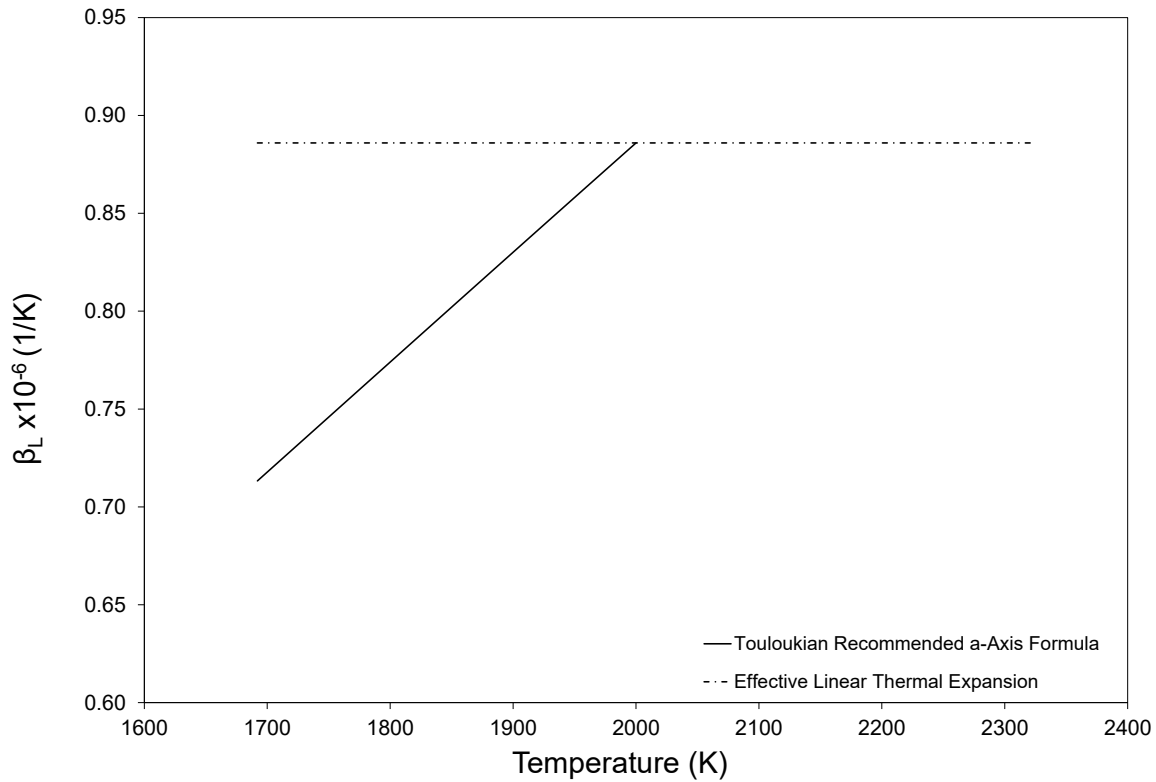


Figure 5.18: Thermal expansion of WC as a function temperature for the a-axis of the crystal.

Combining Equation (5.28), Figure (5.18), and $\rho_{298} = 16896 \text{ kg/m}^3$ for $\text{WC}_{0.6}$ from previous analyses by the author [29], Figure (5.19) has been generated, which predicts the temperature dependence of density for WC. The effective value for ρ_c is taken at 2000 K from Figure (5.19), which is 16670 kg/m^3 .

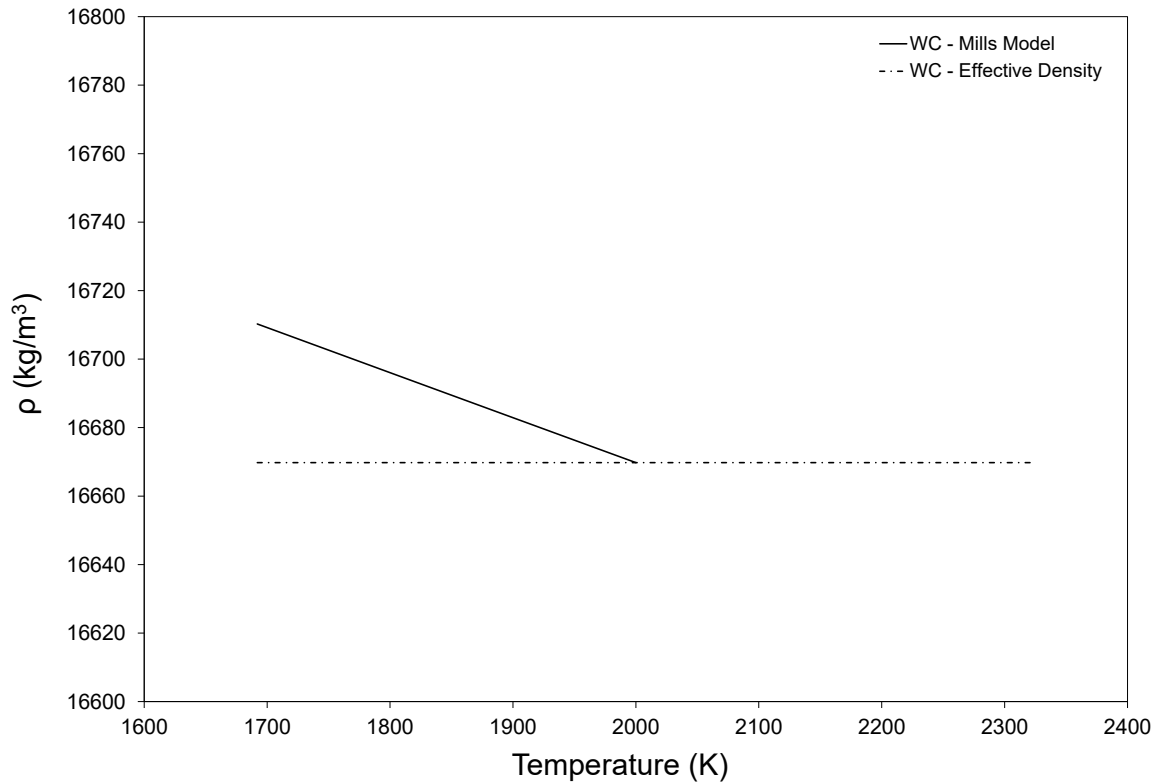


Figure 5.19: Density of WC as a function temperature showing the effective value for ρ_c used in this work.

The final effective value of density for the Ni-WC composite molten pool from Equation (5.23) is 12151 kg/m^3 .

5.11 References

- [1] D. Rivas and S. Ostrach. Scaling of Low-Prandtl-Number Thermocapillary Flows. *International Journal of Heat and Mass Transfer*, 35(6):1469–1479, 1992.
- [2] S. Kumar and S. Roy. Development of Theoretical Process Maps to Study the Role of Powder Preheating in Laser Cladding. *Computational Materials Science*, 37:425–433, 2006.
- [3] E. Toyserkani, A. Khajepour, and S. Corbin. *Laser Cladding*. CRC Press LLC, 2005.
- [4] P.F. Mendez. *Order of Magnitude Scaling of Complex Engineering Problems, and its Application to High Productivity Arc Welding*. PhD thesis, Massachusetts Institute of Technology, June 1999.
- [5] G. Wood, S. Islam, and P.F. Mendez. Calibrated Expressions for Welding and their Application to Isotherm Width in a Thick Plate. *Soldagem and Inspeçao*, 19(3):212–220, 2014.
- [6] G. Wood and P.F. Mendez. First Order Prediction of Bead Width and Height in Coaxial Laser Cladding. Numerical Analysis of Weldability, IIW Commision IX, WG Mathematical Modelling of Weld Phenomena, 2015. Submitted.
- [7] John Dowden, editor. *The Theory of Laser Materials Processing*. Springer, 2009.
- [8] A.J. Pinkerton and L. Lin. Modelling the Geometry of a Moving Laser Melt Pool and Deposition Track via Energy and Mass Balances. *Journal of Physics D: Applied Physics*, 27:1885–1895, 2004.
- [9] J. Mazumder, P.S. Mohanty, and A. Kar. Mathematical Modelling of Laser Materials Processes. *International Journal of Materials and Product Technology*, 11(3–4):193–252, 1996.
- [10] A.P. Mackwood and R.C. Crafer. Thermal Modelling of Laser Welding and Related Processes: A Literature Review. *Optics and Laser Technology*, 37:99–115, 2005.
- [11] E. Toyserkani, A. Khajepour, and S. Corbin. Three-Dimensional Finite Element Modeling of Laser Cladding by Powder Injection: Effects of Powder Feedrate and Travel Speed on the Process. *Journal of Laser Applications*, 15(153):1306–1318, 2003.
- [12] A. Fathi, E. Toyserkani, A. Khajepour, and M. Durali. Prediction of Melt Pool Depth and Dilution in Laser Powder Deposition. *Journal of Applied Physics D: Applied Physics*, 39:2613–2623, 2006.

- [13] E.H. Amara, F. Hamadi, L. Achab, and O. Boumia. Numerical Modelling of the Laser Cladding Process using a Dynamic Mesh Approach. *Journal of Achievements in Materials and Manufacturing Engineering*, 15:100–106, 2006.
- [14] P. Farahmand and R. Kovacevic. An Experimental-Numerical Investigation of Heat Distribution and Stress Field in Single- and Multi-Track Laser Cladding by a High-Power Direct Diode Laser. *Optics and Laser Technology*, 62:154–168, 2014.
- [15] G.G. Guldesh and I. Smurov. *Physics of Laser Materials Processing*. Springer, 2011.
- [16] M. Picasso, C. F. Marsden, J. D. Wagnière, A. Frenk, and M. Rappaz. A Simple but Realistic Model for Laser Cladding. *Metallurgical and Materials Transactions B*, 25B:281–291, 1994.
- [17] L. Han, F.W. Liou, and K.M. Phatak. Modelling of Laser Cladding with Powder Injection. *Metallurgical and Materials Transactions B*, 35B:1139–1150, 2004.
- [18] K. Bhat and P. Majumdar. Transport Phenomena in Surface Alloying of Metals Irradiated By High Energy Laser Beam. *Advances in Modern Mechanical Engineering*, pages 11–24, 2003.
- [19] I. Taberero, A. Lamikiz, S. Martinez, E. Ukar, and L.N. López de Lacalle. Geometric Modelling of Added Layers by Coaxial Laser Cladding. *Physics Procedia*, 39:913–920, 2012.
- [20] M. Akbari, S. Saedodin, D. Toghraie, R. Shoja-Razavi, and F. Kowsari. Experimental and Numerical Investigation of Temperature Distribution and Melt Pool Geometry during Pulsed Laser Welding of Ti6Al4V Alloy. *Optics and Laser Technology*, 59:52–59, 2014.
- [21] Y.S. Lee, M. Nordin, S.S. Babu, and D.F. Farson. Influence of Fluid Convection on Weld Pool Formation in Laser Cladding. *Welding Journal*, 93:292–300, 2014.
- [22] C. Chan, J. Mazumder, and M.M. Chen. A Two-Dimensional Transient Model for Convection in Laser Melted Pool. *Metallurgical Transactions A*, 15A:2175–2184, 1984.
- [23] C. Chan, J. Mazumder, and M.M. Chen. Asymptotic Solution fo Thermocapillary Flow at High and Low Prandlt Numbers Due to Concentrated Surface Heating. *Transactions of the ASME*, 110:140–146, 1988.
- [24] P.S. Wei, H.J. Liu, and C.L. Lin. Scaling Weld or Melt Pool Shape Induced by Thermocapillary Convection. *International Journal of Heat and Mass Transfer*, 55:2328–2337, 2012.
- [25] P.S. Wei and H.J. Liu. Scaling Thermocapillary Weld Pool Shape and Transport Variables in Metals. *Welding Journal*, 91:187–192, 2012.

- [26] P. Balu, S. Hamid, and R. Kovacevic. Finite Element Modeling of Heat Transfer in Single and Multilayered Deposits of Ni-WC Produced by the Laser-Based Powder Deposition Process. *International Journal of Advanced Manufacturing Technology*, 68:85–98, 2013.
- [27] L. St-Georges. Development and Characterization of Composite Ni-Cr + WC Laser Cladding. *Wear*, 263:562–566, 2007.
- [28] F.P. Incropera, D.P. Dewitt, T.L. Bergman, and A.S. Lavine. *Fundamentals of Heat and Mass Transfer*. John Wiley and Sons, Sixth edition, 2007.
- [29] G. Wood and P.F. Mendez. Disaggregated Metal and Carbide Catchment Efficiencies in Laser Cladding of Nickel-Tungsten Carbide. *Welding Journal*, 94(11):343–350, 2015.
- [30] M. Schneider. *Laser Cladding with Powder*. PhD thesis, University of Twente, March 1998.
- [31] Thermal Surfacing Marine and Offshore Industry Solutions, Hogänäs AB, 2013.
- [32] JAHM Software, I., Material Property Database (MPDB), 2003.
- [33] K.C. Mills, A.P. Day, and P.N. Queded. Details of METALS Model to Calculate the Thermophysical Properties of Alloys, 2002.
- [34] T. Iida and R.I.L. Guthrie. *The Physical Properties of Liquid Metals*. Oxford Science Publications, 1988.
- [35] J. C. Maxwell. *A Treatise on Electricity and Magnetism*, volume 1. Literary Licensing LLC, 1873.
- [36] B.J. Keene. A Review of the Surface Tension of Silicon and its Binary Alloys with Reference to Marangoni Flow. *Surface and Interface Analysis*, 10:367–383, 1987.
- [37] D. G. Thomas. Transport Characteristics of Suspension: VIII. A Note on the Viscosity of Newtonian Suspensions of Uniform Spherical Particles. *Journal of Colloid Science*, 20:267–277, 1965.
- [38] A. Einstein. *A New Determination of Molecular Dynamics*. PhD thesis, University of Zurich, 1905.
- [39] P.F. Mendez and T.W. Eagar. Order of Magnitude Scaling: A Systematic Approach to Approximation and Asymptotic Scaling of Equations in Engineering. *Journal of Applied Mechanics*, 80(1):1–9, 2012.
- [40] S. Kumar and S. Roy. Development of a Theoretical Process Map for Laser Cladding using Two-Dimensional Conduction Heat Transfer Model. *Computational Materials Science*, 41:457–466, 2008.

- [41] ISO 11146-1: Test Methods for Laser Beam Widths, Divergence Angles and Beam Propagation Ratios, Jan 15, 2005.
- [42] R. Seger. *Effect of Tungsten Carbides Properties of Overlay Welded WC/NiSiB Composite Coatings*. Hogänäs, 2013.
- [43] A.S. Kurlov and A.I. Gusev. Phases and Equilibria in the W–C and W–Co–C Systems. In *Tungsten Carbides: Structure, Properties and Application in Hardmetals*, pages 5–56. Springer International Publishing, Switzerland, 2013.
- [44] Y.S. Touloukian and E.H. Buyco. *Thermophysical Properties of Matter*, volume 5 of *The TPRC Data Series*. Plenum Publishing Corp., 1970.
- [45] F. Grønvold, S. Stølen, E.F. Westrum Jr., A.K. Labban, and B. Uhrenius. Heat Capacity and Thermodynamic Properties of Ditungsten Carbide, W_2C_{1-x} , from 10 to 1000 K. *Thermochimica Acta*, 129:115–125, 1988.
- [46] M.J. Assael, A.E. Kalyva, K.D. Antoniadis, R.M. Banish, I. Egry, J. Wu, E. Kaschnitz, and W.A. Wakeham. Reference Data for the Density and Viscosity of Liquid Antimony, Bismuth, Lead, Nickel and Silver. *High Temperatures-High Pressures*, 41:161–184, 2012.
- [47] J.J. Valencia and P.N. Quested. Thermophysical properties. In *ASM Handbook*, volume 15, chapter Casting, pages 468–481. ASM International, 2008.
- [48] T. Iida, R. Guthrie, M. Isac, and N. Tripathi. Accurate Predictions for the Viscosities of Several Liquid Transition Metals, Plus Barium and Strontium. *Metallurgical and Materials Transactions B*, 37B:403–412, 2006.
- [49] E.N. da C. Andrade. LVIII. A Theory of the Viscosity of Liquids. Part II. *The London, Edinburgh, and Dublin Philosophical Magazine and Journal of Science*, 17:698–723, 1934.
- [50] G. Kaptay. A Unified Equation for the Viscosity of Pure Liquid Metals. *Z. Metallkd*, 96:1–8, 2005.
- [51] J. Meija. Standard Atomic Weights. *Pure and Applied Chemistry*, 2013.
- [52] *Smithells Metals Reference Book*. Butterworth Heinemann, 7 edition, 1992.
- [53] T. Iida and R.I.L. Guthrie. *The Thermophysical Properties of Metallic Liquids: Fundamentals*, volume 1. Oxford, 2015.
- [54] M. Fraser. *Surface Tension Measurements on Pure Liquid Iron and Nickel by the Oscillating Drop Technique*. PhD thesis, McMaster University, 1970.

- [55] U.M. Ahmad and L.E. Murr. Surface Free Energy of Nickel and Stainless Steel at Temperatures Above the Melting Point. *Journal of Materials Science*, 11:224–230, 1976.
- [56] Y. Wei, K.T. Chong, T. Takahashi, S. Liu, Z. Li, Z. Jiang, and J.Y. Choi, editors. *Surface Tension of Molten Nickel-Chromium Alloy*, volume 6040. Proceedings of SPIE, 2005.
- [57] J. Brillo and I. Egry. Surface Tension of Nickel, Copper, Iron and their Binary Alloys. *Journal of Materials Science*, 40:2213–2216, 2005.
- [58] M.I. Vasiliu and V.N. Eremenko. The Surface Tension of Liquid Nickel-Silicon Alloys. *Poroshkovaya Metallurgiya*, 3(27):80–82, 1964.
- [59] G.F. Deyev and D. Deyev. *Surface Phenomena in Fusion Welding Processes*. CRC Press, 2005.
- [60] I. Syhan and I. Egry. The Surface Tension of Undercooled Binary Iron and Nickel Alloys and the Effect of Oxygen on the Surface Tension of Fe and Ni. *International Journal of Thermophysics*, 20(4):1017–1028, 1999.
- [61] D.R. Lide, editor. *CRC Handbook of Chemistry and Physics*. CRC press, 84 edition, 2003.
- [62] ASM International. Thermal expansion. In *Thermal Properties of Metals*, chapter 2, pages 9–16. ASM International, 2002.
- [63] Y.S. Touloukian and E.H. Buyco. *Thermophysical Properties of Matter*, volume 13 of *The TPRC Data Series*. Plenum Publishing Corp., 1977.

Chapter 6

Conclusions and Future Work

6.1 Conclusions

For the first time, formulae for the mass transfer efficiency (catchment efficiency) of the individual components of a composite overlay system were proposed. Three expressions, one for each of the deposited components and an overall efficiency, were presented based on fundamental mass balance principles and measurements from the cross section of a deposited overlay. Experiments of coaxial laser cladding of nickel-tungsten carbide deposited under a range of laser powers, powder feed rates, and travel speeds, showed that the component catchment efficiencies for the nickel-based metal powders and tungsten carbides were different. In the case of the powder feed rate analysis, it was discovered that the trends in metal powder and carbide efficiency were different and that changes in powder feed rate could alter the balance of carbide in the deposited clad without affecting the overall catchment efficiency.

The Minimal Representation and Calibration (MRC) approach was applied to the point heat source approximation for welding heat sources proposed by Rosenthal [1]. Conduction and advection were established as the two relevant physical mechanisms that describe the heat transfer under Rosenthal's simplified problem formulation. Two regimes were identified based on the value of the dimensionless temperature T^* relative

to unity for the particular system: advection dominant regime (fast heat sources) for the case of $T^* \ll 1$ and the conduction dominant regime (slow heat sources $T^* \gg 1$). Estimates of maximum width in the form of analytical equations were proposed for both regimes for any isotherm directly from known process parameters. Calibrated correction factors were proposed to minimize the maximum error of the analytical expressions to the exact solution from Rosenthal's formula, which were shown to have a maximum error of 0.8% across the entire T^* domain. These expressions were applied to calculate the maximum width of the melting isotherm of a 4145-MOD steel substrate used in the Ni-WC cladding trials in this work. It was shown that for the range of laser powers (3-5 kW), powder feed rates (30-70 g/min), and travel speed (12.7-38.1 mm/s), the process could be characterized as advection dominant for all tests. The analytical expressions for maximum isotherm width predicted the actual width to consistently within 70% of the measured values from the experimental tests.

A numerical solution to the dimensionless Gaussian heat source equation proposed by Eagar and Tsai was developed using MATLABTM software [2]. The multi-level optimization algorithm solved for the values of the maximum width and depth for the HAZ and determined values for the beam distribution parameter and HAZ isotherm temperature that minimized the difference between the experimental measurements of Ni-WC bead geometry and the prediction from Eagar's formula. The thermal efficiency of the process in this analysis was taken to be the reported literature value of 30% for mild to medium steel. This value represented the fraction of the total laser power that was absorbed by the steel for the 10.6 μm beam. The optimized beam distribution parameter was calculated to be 1.62 mm, which was consistent with industrial characterizations using a plastic burn technique. The optimized HAZ temperature was calculated to be 1228 K, which was higher than the 981 K Ae_1 temperature, but is consistent with delayed transformations at high heat rates associated with laser processes. The results were then used

to compute the geometry of the melting isotherm, which was shown to be with $\pm 10\%$ of experimental values for the same experiments in Chapter (3).

A new model for catchment efficiency was developed for coaxial laser cladding, which depended only on the maximum width of the molten pool and the radius of the powder jet. An optimized value of 1.77 mm for the powder cloud radius was computed to produce the optimal match between the model and experiments. The proposed radius value was consistent with photos of the focal point of the powder cloud stream.

An expression for the height of the clad bead was developed using a parabolic estimate for the surface profile of the bead. This parabolic expression has a simple mathematical relationship between the cross sectional area to the width and height purely considering the geometry. Combining the catchment efficiency model, a mass balance for the powders in the deposited bead, and the parabolic expression, an equation for the bead height is presented in terms of process parameters known prior to cladding. This expression was shown to consistently predict the crown height to within 10%.

The role of convection in the heat transfer of the nickel-tungsten carbide system under typical industrial laser cladding conditions was evaluated for the first time. Using a methodology proposed by Rivas and Ostrach [3], the Prandtl number (Pr), Reynolds number for thermocapillary flows (Re_σ), and dimensionless aspect ratio (A) were calculated and demonstrated that the laser clad bead in this analysis was a borderline Regime II/III fluid. This classification indicates that the bead is transitioning from a system with a viscous boundary layer and conduction dominant core to a system with both a thermal and viscous boundary layer and a convection dominant core region. In Regime III conduction is still the dominant heat transfer mechanisms in the thermal and viscous boundary layers. Calculations for the boundary layer thickness showed that combined solid-liquid and surface thermal boundaries accounted for 89.5% of the cavity thickness for the experimental clad bead containing 38.6% volume fraction of carbides.

This supports that conduction is a more significant heat transfer mechanism in these overlays under typical industrial conditions.

6.2 Future Work

To more fully satisfy the objectives of predicting bead geometry in a quick, accurate, and general way the following aspects of this analysis are proposed:

- Perform additional test clads to provide statistical support for the experimental measurements
- Test new substrates and overlays to verify the generality of the proposed models in this work.
- Measure the radius of the powder cloud and beam distribution parameter directly to validate optimized values.
- Apply a scaling approach to the Gaussian heat source to make direct analytical estimates of characteristic values similar to the point heat source in this work.
- Explore the application of the scaling approach to catchment efficiency to obtain a more physically meaningful model.
- Address the role of convection in purely molten, single phase clad pools to quantify its effect on bead geometry.
- Develop an expression to predict the thermal efficiency in terms of the process parameters to address the role of the powder particles/cloud in the heat transfer of the process.

- Explore predicting bead geometry for overlapping and multilayer beads based on the results for single beads in this work.

6.3 References

- [1] D. Rosenthal. The Theory of Moving Sources of Heat and Its Application to Metal Treatments. *Transactions of the A.S.M.E.*, pages 849–866, 1946.
- [2] T.W. Eagar and N.S. Tsai. Temperature Fields Produced by Traveling Distributed Heat Sources. *Welding Journal*, 62(12):346–355, 1983.
- [3] D. Rivas and S. Ostrach. Scaling of Low-Prandtl-Number Thermocapillary Flows. *International Journal of Heat and Mass Transfer*, 35(6):1469–1479, 1992.

Bibliography

- [1] D. Rivas and S. Ostrach. Scaling of Low-Prandtl-Number Thermocapillary Flows. *International Journal of Heat and Mass Transfer*, 35(6):1469–1479, 1992.
- [2] T. Iida and R.I.L. Guthrie. *The Physical Properties of Liquid Metals*. Oxford Science Publications, 1988.
- [3] B.J. Keene. A Review of the Surface Tension of Silicon and its Binary Alloys with Reference to Marangoni Flow. *Surface and Interface Analysis*, 10:367–383, 1987.
- [4] P.F. Mendez, N. Barnes, K. Bell, S. D. Borle, S. S. Gajapathi, S. D. Guest, H. Izadi, A. Kamyabi Gol, and G. Wood. Welding Processes for Wear Resistant Overlays. *Journal of Manufacturing Processes*, 16:4–25, 2013.
- [5] E. Toyserkani, A. Khajepour, and S. Corbin. *Laser Cladding*. CRC Press LLC, 2005.
- [6] A.F.A. Hoadley and M. Rappaz. A Thermal Model of Laser Cladding by Powder Injection. *Metallurgical Transactions B*, 23B(12):631–642, 1992.
- [7] R. Colaço, L. Costa, R. Guerra, and R. Vilar. A Simple Correlation Between the Geometry of Laser Cladding Tracks and the Process Parameters. In *Laser Processing: Surface Treatment and Film Deposition*, pages 421–429. Kluwer Academic Publishers, Netherlands, 1996.
- [8] V.M. Weerasinghe and W.M. Steen. Laser Cladding of Blown Powder. *Metal Construction*, 19:1344–1351, 1987.
- [9] A.J. Pinkerton and L. Lin. Modelling the Geometry of a Moving Laser Melt Pool and Deposition Track via Energy and Mass Balances. *Journal of Physics D: Applied Physics*, 27:1885–1895, 2004.
- [10] E.H. Amara, F. Hamadi, L. Achab, and O. Boumia. Numerical Modelling of the Laser Cladding Process using a Dynamic Mesh Approach. *Journal of Achievements in Materials and Manufacturing Engineering*, 15:100–106, 2006.

- [11] P. Farahmand and R. Kovacevic. An Experimental-Numerical Investigation of Heat Distribution and Stress Field in Single- and Multi-Track Laser Cladding by a High-Power Direct Diode Laser. *Optics and Laser Technology*, 62:154–168, 2014.
- [12] A. Fathi, E. Toyserkani, A. Khajepour, and M. Durali. Prediction of Melt Pool Depth and Dilution in Laser Powder Deposition. *Journal of Applied Physics D: Applied Physics*, 39:2613–2623, 2006.
- [13] E. Toyserkani, A. Khajepour, and S. Corbin. Three-Dimensional Finite Element Modeling of Laser Cladding by Powder Injection: Effects of Powder Feedrate and Travel Speed on the Process. *Journal of Laser Applications*, 15(153):1306–1318, 2003.
- [14] L. Han, F.W. Liou, and K.M. Phatak. Modelling of Laser Cladding with Powder Injection. *Metallurgical and Materials Transactions B*, 35B:1139–1150, 2004.
- [15] Y.S. Lee, M. Nordin, S.S. Babu, and D.F. Farson. Influence of Fluid Convection on Weld Pool Formation in Laser Cladding. *Welding Journal*, 93:292–300, 2014.
- [16] M. Picasso, C. F. Marsden, J. D. Wagnière, A. Frenk, and M. Rappaz. A Simple but Realistic Model for Laser Cladding. *Metallurgical and Materials Transactions B*, 25B:281–291, 1994.
- [17] I. Taberero, A. Lamikiz, S. Martinez, E. Ukar, and L.N. López de Lacalle. Geometric Modelling of Added Layers by Coaxial Laser Cladding. *Physics Procedia*, 39:913–920, 2012.
- [18] H. E. Cheikh, B. Courant, J.-Y. Hascoët, and R. Guillén. Prediction and Analytical Description of the Single Laser Track Geometry in Direct Laser Fabrication from Process Parameters and Energy Balance Reasoning. *Journal of Materials Processing Technology*, 212:1832–1839, 2012.
- [19] C. Lalas, K. Tsirbas, K. Salonitis, and G. Chryssolouris. An Analytical Model of the Laser Clad Geometry. *International Journal of Advanced Manufacturing Technology*, 32:34–41, 2007.
- [20] F. Lemoine, D. Grevey, and A. Vannes. Cross-Section Modeling Laser Cladding. pages 203–212. Proceedings of SPIE - The International Society for Optical Engineering, December 1993.
- [21] F. Lemoine, D. Grevey, and A. Vannes. Cross-Section Modeling of Pulsed Nd:YAG Laser Cladding. In *Laser Materials Processing and Machining*, volume 2246, pages 37–44. Proceedings of SPIE - The International Society for Optical Engineering, November 1994.

- [22] J.P. Davim, C. Oliveira, and A. Cardoso. Predicting the Geometric Form of Clad in Laser Cladding by Powder Using Multiple Regression Analysis (MRA). *Materials and Design*, 29:554–557, 2008.
- [23] O. Nenadl, V. Ocelík, A. Palavra, and J.Th.M De Hosson. The Prediction of Coating Geometry from Main Processing Parameter in Laser Cladding. *Physics Procedia*, 56:220–227, 2014.
- [24] U. de Oliveira, V. Ocelík, and J. Th. M. De Hosson. Analysis of Coaxial Laser Cladding Processing Conditions. *Surface and Coatings Technology*, 197:127–136, 2005.
- [25] D. Ding, Z. Pan, D. Cuiuri, H. Li, S. van Duin, and N. Larkin. Bead Modelling and Implementation of Adaptive MAT Path in Wire and Arc Additive Manufacturing. *Robotics and Computer-Integrated Manufacturing*, 39:32–42, 2016.
- [26] P. Peyre, P. Aubry, R. Fabbro, R. Neveu, and A. Longeue. Analytical and Numerical Modelling of the Direct Metal Deposition Laser Process. *Journal of Applied Physics D: Applied Physics*, 41:1–10, 2008.
- [27] G. G. Roy, R. Nandan, and T. Debroy. Dimensionless Correlation to Estimate Peak Temperature During Friction Stir Welding. *Science and Technology of Welding and Joining*, 11(5):606–608, 2006.
- [28] P. W. Fuerschbach and G. R. Eisler. Determination of Material Properties for Welding Models by Means of Arc Weld Experiments. Number 5, pages 15–19. Trends in Welding Research, Proceedings of the 6th International Conference, 2002.
- [29] P. F. Mendez. Synthesis and Generalization of Welding Fundamentals to Design New Welding Technologies: Status, Challenges and a Promising Approach. *Science and Technology of Welding and Joining*, 16:348–356, 2011.
- [30] Karem E. Tello, Satya S. Gajapathi, and P. F. Mendez. Generalization and Communication of Welding Simulations and Experiments using Scaling Analysis. pages 249–258. Trends in Welding Research, Proceedings of the 9th International Conference, ASM International, 2012.
- [31] P.F. Mendez and T.W. Eagar. Order of Magnitude Scaling: A Systematic Approach to Approximation and Asymptotic Scaling of Equations in Engineering. *Journal of Applied Mechanics*, 80(1):1–9, 2012.
- [32] T.W. Eagar and N.S. Tsai. Temperature Fields Produced by Traveling Distributed Heat Sources. *Welding Journal*, 62(12):346–355, 1983.
- [33] S.D. Guest. *Depositing Ni-WC Wear Resistant Overlays with Hot-Wire Assist Technology*. PhD thesis, University of Alberta, 2014.

- [34] J. Lin. A Simple Model of Powder Catchment in Coaxial Laser Cladding. *Optics & Laser Technology*, 31:233–238, 1999.
- [35] J. Lin and W. M. Steen. Powder Flow and Catchment during Coaxial Laser Cladding. In *Lasers in Materials Processing*, volume 3097, pages 517–524. The International Society for Optical Engineering, 1997.
- [36] A. Frenk, M. Vandyoussefi, J. D. Wagnière, A. Zryd, and W. Kurz. Analysis of the Laser-Cladding Process for Stellite on Steel. *Metallurgical and Materials Transactions B*, 28B:501–508, 1997.
- [37] K. Partes. Analytical Model of the Catchment Efficiency in High Speed Laser Cladding. *Surface & Coatings Technology*, 204:366–371, 2009.
- [38] M. Gremaud, J. D. Wagnière, A. Zryd, and W. Kurz. Laser Metal Forming: Process Fundamentals. *Surface Engineering*, 12(3):251–259, 1996.
- [39] S. Zhou, Y. Huang, and X. Zeng. A Study of Ni-Based WC Composite Coatings by Laser Induction Hybrid Rapid Cladding with Elliptical Spot. *Applied Surface Sciences*, 254:3110–3119, 2008.
- [40] A. Angelastro, S. L. Campanelli, G. Casalino, and A. D. Ludovico. Optimization of Ni-Based WC/Co/Cr Composite Coatings Produced by Multilayer Laser Cladding. *Advances in Materials Science and Engineering*, pages 1–7, 2013.
- [41] L. St-Georges. Development and Characterization of Composite Ni-Cr + WC Laser Cladding. *Wear*, 263:562–566, 2007.
- [42] T.G. Beckwith, R.D. Marangoni, and J.H. Leinhard V. *Mechanical Measurements*. Pearson Prentice Hall, 6 edition, 2007.
- [43] S. Kumar and S. Roy. Development of Theoretical Process Maps to Study the Role of Powder Preheating in Laser Cladding. *Computational Materials Science*, 37:425–433, 2006.
- [44] S. D. Guest, J. Chapuis, G. Wood, and P.F. Mendez. Non-Wetting Behaviour of Tungsten Carbide Powders in Nickel Weld Pool: New Loss Mechanism in GMAW Overlays. *Science and Technology of Welding and Joining*, 19(2):133–141, 2014.
- [45] A.S. Kurlov and A.I. Gusev. Phases and Equilibria in the W–C and W–Co–C Systems. In *Tungsten Carbides: Structure, Properties and Application in Hardmetals*, pages 5–56. Springer International Publishing, Switzerland, 2013.
- [46] A.A. Rempel. Atomic and Vacancy Ordering in Nonstoichiometric Carbides. *Physics - Uspekhi*, 39(1):31–56, 1996.

- [47] A. S. Kurllov and A. I. Gusev. Phase Equilibria in the W-C System and Tungsten Carbides. *Russian Chemical Reviews*, 75(7):617–636, 2010.
- [48] R. V. Sara. Phase Equilibria in the System Tungsten-Carbon. *Journal of The American Ceramic Society*, 5:251–257, 1965.
- [49] T.W. Eagar. Welding and Joining: Moving from Art to Science. *Welding Journal*, pages 49–55, 1995.
- [50] P. F. Mendez. Generalization and Communication of Welding Simulations and Experiments using Scaling Analysis. *Phase Transformations and Complex Properties Research Group*, 7 July, 2011.
- [51] D. Rosenthal. The Theory of Moving Sources of Heat and Its Application to Metal Treatments. *Transactions of the A.S.M.E.*, pages 849–866, 1946.
- [52] D. Rosenthal. Mathematical Theory of Heat Distribution during Welding and Cutting. *Welding Journal*, 20:220–234, 1941.
- [53] M.F. Ashby and K.E. Easterling. The Transformation Hardening of Steel Surface by Laser Beams. *Acta Metallurgica*, 32:1935–1948, 1984.
- [54] O. Grong and N. Christiansen. Effects of Weaving on Temperature Distribution in Fusion Welding. *Materials Science and Technology*, 2:967–973, 1986.
- [55] O. Myher and O. Grong. Dimensional Maps for Heat Flow Analyses in Fusion Welding. *Acta Metallurgica and Materialia*, 38:449–460, 1990.
- [56] P.S. Myers, O.A. Uyehara, and G.L Borman. Fundamentals of Heat Flow in Welding. *Welding Research Bulletin*, pages 1–46, 1967.
- [57] W.D. Pilkey and D.F. Pilkey. *Peterson's Stress Concentration Factors*. John Wiley Sons, Inc., 3rd edition, 2008.
- [58] S.F. Hoerner. *Fluid-Dynamic Drag*. Hoerner Fluid Dynamics, 1965.
- [59] *Quality Bearing Components Catalog B620*, 2012.
- [60] *Handbook of Metric Drive Components D805*, 2010.
- [61] P. F. Mendez. Characteristic Values in the Scaling of Differential Equations in Engineering. *Journal of Applied Mechanics*, 77:6–17, 2010.
- [62] S. W. Churchill and R. Usagi. A General Expression for the Correlation of Rates of Transfer and Other Phenomena. *AIChE*, 18(6):1121–1127, 1972.
- [63] F. Armao, L. Byall, D. Kotecki, and D. Miller. *Gas Metal Arc Welding Guidelines*. Lincoln Electric.

- [64] J. N. Dupont and A. R. Marder. Thermal Efficiency of Arc Welding Processes. *Welding Journal*, 74(12):406–416, 1995.
- [65] F.P. Incropera, D.P. Dewitt, T.L. Bergman, and A.S. Lavine. *Fundamentals of Heat and Mass Transfer*. John Wiley and Sons, Sixth edition, 2007.
- [66] M. Schneider. *Laser Cladding with Powder*. PhD thesis, University of Twente, March 1998.
- [67] S. Kumar and S. Roy. Development of a Theoretical Process Map for Laser Cladding using Two-Dimensional Conduction Heat Transfer Model. *Computational Materials Science*, 41:457–466, 2008.
- [68] P. Balu, S. Hamid, and R. Kovacevic. Finite Element Modeling of Heat Transfer in Single and Multilayered Deposits of Ni-WC Produced by the Laser-Based Powder Deposition Process. *International Journal of Advanced Manufacturing Technology*, 68:85–98, 2013.
- [69] P. Farahmand and R. Kovacevic. Laser Cladding Assisted with an Induction Heater (LCAIH) of Ni-60%WC Coating. *Journal of Materials Processing Technology*, 222:244–258, 2015.
- [70] G. Wood and P.F. Mendez. Disaggregated Metal and Carbide Catchment Efficiencies in Laser Cladding of Nickel-Tungsten Carbide. *Welding Journal*, 94(11):343–350, 2015.
- [71] G. Wood, S. Islam, and P.F. Mendez. Calibrated Expressions for Welding and their Application to Isotherm Width in a Thick Plate. *Soldagem and Inspeção*, 19(3):212–220, 2014.
- [72] S. Gajapathi. Laser Heat Treatment and Laser Cladding Report. 2012.
- [73] MathWorks Inc. Documentation: fminsearch, 2015.
- [74] MathWorks Inc. Documentation: fzero, 2015.
- [75] J. C. Maxwell. *A Treatise on Electricity and Magnetism*, volume 1. Literary Licensing LLC, 1873.
- [76] ISO 11146-1: Test Methods for Laser Beam Widths, Divergence Angles and Beam Propagation Ratios, Jan 15, 2005.
- [77] P. Balu, P. Leggett, and R. Kovacevic. Parametric Study on Coaxial Multi-Material Powder Flow in Laser-Based Powder Deposition Process. *Journal of Materials Processing Technology*, 212:1589–1610, 2012.

- [78] K.C. Mills, A.P. Day, and P.N. Queded. Details of METALS Model to Calculate the Thermophysical Properties of Alloys, 2002.
- [79] JAHM Software, I., Material Property Database (MPDB), 2003.
- [80] K. Liu, X.P. Li, M. Rahman, and X.D. Liu. CBN Tool Wear in Ductile Cutting of Tungsten Carbide. *Wear*, 255:1344–1351, 2003.
- [81] P.F. Mendez. *Order of Magnitude Scaling of Complex Engineering Problems, and its Application to High Productivity Arc Welding*. PhD thesis, Massachusetts Institute of Technology, June 1999.
- [82] G. Wood and P.F. Mendez. First Order Prediction of Bead Width and Height in Coaxial Laser Cladding. Numerical Analysis of Weldability, IIW Commission IX, WG Mathematical Modelling of Weld Phenomena, 2015. Submitted.
- [83] John Dowden, editor. *The Theory of Laser Materials Processing*. Springer, 2009.
- [84] J. Mazumder, P.S. Mohanty, and A. Kar. Mathematical Modelling of Laser Materials Processes. *International Journal of Materials and Product Technology*, 11(3–4):193–252, 1996.
- [85] A.P. Mackwood and R.C. Crafer. Thermal Modelling of Laser Welding and Related Processes: A Literature Review. *Optics and Laser Technology*, 37:99–115, 2005.
- [86] G.G. Guldes and I. Smurov. *Physics of Laser Materials Processing*. Springer, 2011.
- [87] K. Bhat and P. Majumdar. Transport Phenomena in Surface Alloying of Metals Irradiated By High Energy Laser Beam. *Advances in Modern Mechanical Engineering*, pages 11–24, 2003.
- [88] M. Akbari, S. Saedodin, D. Toghraie, R. Shoja-Razavi, and F. Kowsari. Experimental and Numerical Investigation of Temperature Distribution and Melt Pool Geometry during Pulsed Laser Welding of Ti6Al4V Alloy. *Optics and Laser Technology*, 59:52–59, 2014.
- [89] C. Chan, J. Mazumder, and M.M. Chen. A Two-Dimensional Transient Model for Convection in Laser Melted Pool. *Metallurgical Transactions A*, 15A:2175–2184, 1984.
- [90] C. Chan, J. Mazumder, and M.M. Chen. Asymptotic Solution fo Thermocapillary Flow at High and Low Prandlt Numbers Due to Concentrated Surface Heating. *Transactions of the ASME*, 110:140–146, 1988.

- [91] P.S. Wei, H.J. Liu, and C.L. Lin. Scaling Weld or Melt Pool Shape Induced by Thermocapillary Convection. *International Journal of Heat and Mass Transfer*, 55:2328–2337, 2012.
- [92] P.S. Wei and H.J. Liu. Scaling Thermocapillary Weld Pool Shape and Transport Variables in Metals. *Welding Journal*, 91:187–192, 2012.
- [93] Thermal Surfacing Marine and Offshore Industry Solutions, Hogänäs AB, 2013.
- [94] D. G. Thomas. Transport Characteristics of Suspension: VIII. A Note on the Viscosity of Newtonian Suspensions of Uniform Spherical Particles. *Journal of Colloid Science*, 20:267–277, 1965.
- [95] A. Einstein. *A New Determination of Molecular Dynamics*. PhD thesis, University of Zurich, 1905.
- [96] R. Seger. *Effect of Tungsten Carbides Properties of Overlay Welded WC/NiSiB Composite Coatings*. Hogänäs, 2013.
- [97] Y.S. Touloukian and E.H. Buyco. *Thermophysical Properties of Matter*, volume 5 of *The TPRC Data Series*. Plenum Publishing Corp., 1970.
- [98] F. Grønvold, S. Stølen, E.F. Westrum Jr., A.K. Labban, and B. Uhrenius. Heat Capacity and Thermodynamic Properties of Ditungsten Carbide, W_2C_{1-x} , from 10 to 1000 K. *Thermochimica Acta*, 129:115–125, 1988.
- [99] M.J. Assael, A.E. Kalyva, K.D. Antoniadis, R.M. Banish, I. Egry, J. Wu, E. Kaschnitz, and W.A. Wakeham. Reference Data for the Density and Viscosity of Liquid Antimony, Bismuth, Lead, Nickel and Silver. *High Temperatures-High Pressures*, 41:161–184, 2012.
- [100] J.J. Valencia and P.N. Quedsted. Thermophysical properties. In *ASM Handbook*, volume 15, chapter Casting, pages 468–481. ASM International, 2008.
- [101] T. Iida, R. Guthrie, M. Isac, and N. Tripathi. Accurate Predictions for the Viscosities of Several Liquid Transition Metals, Plus Barium and Strontium. *Metallurgical and Materials Transactions B*, 37B:403–412, 2006.
- [102] E.N. da C. Andrade. LVIII. A Theory of the Viscosity of Liquids. Part II. *The London, Edinburgh, and Dublin Philosophical Magazine and Journal of Science*, 17:698–723, 1934.
- [103] G. Kaptay. A Unified Equation for the Viscosity of Pure Liquid Metals. *Z. Metallkd*, 96:1–8, 2005.
- [104] J. Meija. Standard Atomic Weights. *Pure and Applied Chemistry*, 2013.

- [105] *Smithells Metals Reference Book*. Butterworth Heinemann, 7 edition, 1992.
- [106] T. Iida and R.I.L. Guthrie. *The Thermophysical Properties of Metallic Liquids: Fundamentals*, volume 1. Oxford, 2015.
- [107] M. Fraser. *Surface Tension Measurements on Pure Liquid Iron and Nickel by the Oscillating Drop Technique*. PhD thesis, McMaster University, 1970.
- [108] U.M. Ahmad and L.E. Murr. Surface Free Energy of Nickel and Stainless Steel at Temperatures Above the Melting Point. *Journal of Materials Science*, 11:224–230, 1976.
- [109] Y. Wei, K.T. Chong, T. Takahashi, S. Liu, Z. Li, Z. Jiang, and J.Y. Choi, editors. *Surface Tension of Molten Nickel-Chromium Alloy*, volume 6040. Proceedings of SPIE, 2005.
- [110] J. Brillo and I. Egry. Surface Tension of Nickel, Copper, Iron and their Binary Alloys. *Journal of Materials Science*, 40:2213–2216, 2005.
- [111] M.I. Vasiliu and V.N. Eremenko. The Surface Tension of Liquid Nickel-Silicon Alloys. *Poroshkovaya Metallurgiya*, 3(27):80–82, 1964.
- [112] G.F. Deyev and D. Deyev. *Surface Phenomena in Fusion Welding Processes*. CRC Press, 2005.
- [113] I. Syhan and I. Egry. The Surface Tension of Undercooled Binary Iron and Nickel Alloys and the Effect of Oxygen on the Surface Tension of Fe and Ni. *International Journal of Thermophysics*, 20(4):1017–1028, 1999.
- [114] D.R. Lide, editor. *CRC Handbook of Chemistry and Physics*. CRC press, 84 edition, 2003.
- [115] ASM International. Thermal expansion. In *Thermal Properties of Metals*, chapter 2, pages 9–16. ASM International, 2002.
- [116] Y.S. Touloukian and E.H. Buyco. *Thermophysical Properties of Matter*, volume 13 of *The TPRC Data Series*. Plenum Publishing Corp., 1977.
- [117] J.A.J. Robinson, A.T. Dinsdale, L.A. Chapman, P.N. Quested, J.A. Gisby, and K.C Mills. *The Prediction of Thermophysical Properties of Steels and Slags*. 2001.
- [118] J.V. Sengers and M. Klein, editors. *The Technological Importance of Accurate Thermophysical Property Information*. American Society of Mechanical Engineers, National Bureau of Standards, 1979.
- [119] M.J. Peet, H.S. Hasan, and H.K.D.H. Bhadeshia. Prediction of Thermal Conductivity of Steel. *International Journal of Heat and Mass Transfer*, 54:2602–2608, 2011.

- [120] Z. Guo, N. Saunders, P. Miodownik, and J. Schille. Modelling Phase Transformations and Material Properties Critical to the Prediction of Distortion during Heat Treatment of Steels. *Int. J. Microstructure and Material Properties*, 4(2):187–195, 2009.
- [121] I.S. Cho, S.M. Yoo, V.M. Golod, K.D. Savyelyev, C.H. Lim, and J.K. Choi. Calculation of Thermophysical Properties of Iron Casting Alloys. *International Journal of Cast Metals Research*, 22(1–4):43–46, 2009.
- [122] J. Miettinen. Calculation of Solidification-Related Thermophysical Properties for Steels. *Metallurgical and Materials Transactions B*, 28B:281–297, 1997.
- [123] Alloy 4145 / 4145 MOD in bar, Castle Metals, 2015. <http://www.amcastle.com/stock/alloysteel/grade4145unsg41450alloybar.aspx>.
- [124] Alloy 4145 Modified API Spec. 7, Bohler Uddeholm, 2013. http://www.buau.com.au/media/4145H_2013.pdf.
- [125] AISI 4145 Alloy Steel, West Yorkshire Steel, 2015. <http://www.westyorkssteel.com/alloysteel/oilandgas/aisi4145/>.
- [126] A. Kamyabi-Gol. *Quantification of Phase Transformations using Calorimetry as an Alternative to Dilatometry*. PhD thesis, University of Alberta, 2015.
- [127] AISI 4145 Alloy Steel (UNS G41450), AZO Materials, 2015. <http://www.azom.com/article.aspx?ArticleID=6664>.
- [128] SAE-AISI 4145 SCM445, G41450 Cr-Mo Steel, MakeItFrom, 2015. <http://www.makeitfrom.com/material-properties/SAE-AISI-4145-SCM445-G41450-Cr-Mo-Steel/>.
- [129] SAE 4145 Chemical Composition, Mechanical Properties, and Heat Treatment, Jiangyou Longhai Steel, 2015. <http://www.steelgr.com/SteelGrades/CarbonSteel/sae4145.html>.
- [130] Y.S. Touloukian, R.W. Poewll, C.Y. Ho, and M.C. Nicolaou. *Therophysical Properties of Matter*, volume 3 of *The TPRC Data Series*. IFI/Plenum, 1973.
- [131] AISI 4140 (Oil-Hardening Cr-Mo Steel). ASM International, 1988.
- [132] AISI 4140 4140H, Engineering Properties of Steel. pages 113–116. ASM International, 1982.
- [133] AISI 4140, efunda, 2015. http://www.efunda.com/materials/alloys/alloy_steels/show_alloy.cfm?ID=aisi_4140&show_prop=elec&Page_Title=Alloy%20Steel%20aisi%204140.

- [134] Sommer. Material Data Sheet 4140, Application Institute for the Optimisation of Material, Process and Heat Treatment Applications, 2012.
- [135] AISI 4140 Steel, annealed at 815°C (1500°F) furnace cooled 11°C (20°F)/hour to 665°C (1230°F), air cooled, 25 mm (1 in.) round, MatWeb, 2015. <http://www.matweb.com/search/datasheet.aspx?matguid=7b75475aa1bc41618788f63c6500d36b&ckck=1>.
- [136] LSS 4140 and 4142HT Alloy Steels, Latrobe Specialty Steel Company, 2006. www.latrobesteel.com.
- [137] Evitherm, Material Property Database (MPDB), 2015. <http://ib.ptb.de/evitherm/evitherm.jsp?restart>.
- [138] 42CrMo4 Quality, Lucefin Group. http://www.lucefin.com/wp-content/files_mf/0242crmo472.pdf.
- [139] W.F. Gale and T.C. Totemeier, editors. *General Physical Properties*. Butterworth Heinemann, eighth edition, 2004.
- [140] Y.S. Touloukian and E.H. Buyco. *Therophysical Properties of Matter*, volume 4 of *The TPRC Data Series*. Plenum Publishing Corp., 1971.
- [141] M. Niffenegger and K. Reichlin. The Proper Use of Thermal Expansion Coefficients in Finite Element Calculations. *Nuclear Engineering and Design*, 243:356–359, 2012.
- [142] Y.S. Touloukian, R.W. Poewll, C.Y. Ho, and M.C. Nicolaou. *Therophysical Properties of Matter*, volume 10 of *The TPRC Data Series*. IFI/Plenum, 1973.
- [143] R.J. Kosinski. A Literature Review on Reaction Time, 2013.

Appendix A. Thermophysical Properties of 4145-MOD Steel

7.1 Introduction

Reliable thermophysical data is fundamentally important to modelling of heat transfer phenomena. The success of these predictive models hinges on the quality of data used in their development [1]. Application of Rosenthal's thick plate solution requires inputs of thermal conductivity, k , and thermal diffusivity, α , to predict welding isotherm geometries [2]. This data is often difficult to find even for commonly used materials and is complicated by the inherent temperature dependence of these quantities. The need for this data was recognized by the US Department of Commerce in 1979 in conference proceedings titled "The Technological Importance of Accurate Thermophysical Property Information" where the engineering and economic impacts of this issue were discussed [3]. Despite the recognition of the need for reliable property data over 35 years ago, the situation has not improved dramatically and those engaged in modelling have limited resources to draw upon for this vital information.

Models of thermophysical properties exist in literature using a variety of thermodynamic simulations techniques or commercial softwares for predictions [1, 4–7]. Models such as these are limited by their experimentally validated databases and the cost and availability of the software. This work attempts to summarize available reported experi-

mental data for 4145-MOD and similar steel chemistries to predict and select appropriate values for solid state heat transfer modelling of laser cladding processes in the temperature range between a preheat of 533 K (260°C) and solidus 1692 K (1419°C).

7.2 List of Symbols

Symbol	Unit	Meaning
A_{e_1}	K	Austentite transformation start temperature (equilibrium heating conditions)
A_{e_3}	K	Austentite transformation finish temperature (equilibrium heating conditions)
α	$\text{m}^2 \text{s}^{-1}$	Thermal diffusivity
α_{eff}	$\text{m}^2 \text{s}^{-1}$	Effective thermal diffusivity between T_p and T_s
$\alpha(T)$	$\text{m}^2 \text{s}^{-1}$	Thermal diffusivity as a function of temperature
α_T	$\text{m}^2 \text{s}^{-1}$	Thermal diffusivity at temperature T
$\overline{\beta_L}$	K^{-1}	Mean linear coefficient of thermal expansion between T_i and T_o
$\overline{\beta_L}(T)$	K^{-1}	Mean linear coefficient of thermal expansion as a function of temperature
$\overline{\beta_V}$	K^{-1}	Mean volumetric coefficient of thermal expansion between T_i and T_o
c_p	$\text{J kg}^{-1} \text{K}^{-1}$	Specific heat capacity
$c_{p_{eff}}$	$\text{J kg}^{-1} \text{K}^{-1}$	Effective specific heat capacity between T_p and T_s
c_{p_i}	$\text{J mol}^{-1} \text{K}^{-1}$	Molar heat capacity at data point i
$c_p(T)$	$\text{J kg}^{-1} \text{K}^{-1}$	Specific heat capacity as a function of temperature
H_i	J mol^{-1}	Molar enthalpy at data point i
H_M	J mol^{-1}	Molar enthalpy
H_p	$\text{J kg}^{-1} \text{K}^{-1}$	Molar enthalpy at the preheat temperature
H_s	$\text{J kg}^{-1} \text{K}^{-1}$	Molar enthalpy at the solidus temperature
k	$\text{W m}^{-1} \text{K}^{-1}$	Thermal conductivity
k_{eff}	$\text{W m}^{-1} \text{K}^{-1}$	Effective thermal conductivity between T_p and T_s
$k(T)$	$\text{W m}^{-1} \text{K}^{-1}$	Thermal conductivity as a function of temperature
k_T	$\text{W m}^{-1} \text{K}^{-1}$	Thermal conductivity at temperature T
l_i	m	Length of the dilatometry sample at T_i
l_o	m	Initial length of the dilatometry sample
Δl	m	Difference between l_i and l_o
M_{eff}	kg mol^{-1}	Molecular weight of compound
M_i	kg mol^{-1}	Molecular weight of element i
m_i	g	Mass of element i
m_t	g	Total mass of the compound
n_i	mol	Moles of element i
n_t	mol	Total moles of the compound
ρ	kg m^{-3}	Density
ρ_{eff}	kg m^{-3}	Effective density between T_p and T_s
$\rho(T)$	kg m^{-3}	Density as a function of temperature
ρ_T	kg m^{-3}	Density at temperature T
T	K	Temperature
T_i	K	Temperature at data point i
T_l	K	Liquidus temperature
T_o	K	Room temperature
T_p	K	Preheat temperature
T_s	K	Solidus temperature
$V_M(T)$	$\text{m}^3 \text{mol}^{-1}$	Molar volume as a function of temperature
V_{MT}	$\text{m}^3 \text{mol}^{-1}$	Molar volume at temperature T
W_i	1	Weight fraction of element i
x_i	1	Mole fraction of element i

7.3 Chemistry, Heat Treatment, and Applications of 4145-MOD Steel

7.3.1 Chemistry

4145-MOD steel is a low alloy, medium-carbon, Cr-Mo steel grade. Its higher carbon content compared to 4140 improves hardenability for thick sections [8]. The MOD aspect comes from alloying with higher levels of Mn, Cr or Mo to further improve through hardening characteristics [8]. The major alloying elements of 4145-MOD used for the preliminary cladding experiments are summarized below in Table 7.1. Trace amounts of Sn, Al, H, B, Nb, Ti, and V were also present but were not included in the thermodynamic analysis in this work. The presence of these elements lead to the prediction of several unobserved carbide phases that would prevent successful equilibrium calculations between 1000 K and room temperature. The complete chemistry of 4145-MOD as reported in the materials test report (MTR) is included in Appendix A.1.

Table 7.1: Composition of 4145-MOD steel used in preliminary experiments

C wt%	Cr wt%	Mn wt%	Mo wt%	Si wt%	Ni wt%	Cu wt%	P wt%	S wt%
0.47	1.18	1.13	0.34	0.24	0.24	0.16	0.008	0.006

7.3.2 Heat Treatment

Material microstructure will influence thermophysical properties, and the heat treatment of the experimental substrate is included here. However, the limited amount of data available for this alloy did not allow the distinction between heat treatment conditions effects on material properties, and required consideration of similar chemistries to

estimate property values. 4145-MOD steel typically undergoes a quench and tempered heat treatment to reach through hardness levels between 30 and 36 HRc [9]. The specific substrate heat treatment schedule outlined in the MTR in Appendix A.1 is summarized as follows:

- Austenitize at 1153 K (880°C) for 1 hour
- Water quench to 304 K (31°C)
- Temper at 893 K (620°C) for 1 hour
- Air cool to room temperature

7.3.3 Applications

4145-MOD is commonly used for a wide variety of oil and gas sector applications. Its through-hardening characteristics, moderate machinability, and wear resistance make it an excellent option for gears, shafts for hydraulic presses, rolls for paper mills, oil well tool joints, tool holders, drill collars, and piston rods [8, 10].

7.4 4145-MOD Transformation Temperatures

Equilibrium transformation temperatures for the experimental 4145-MOD substrate were determined using ThermoCalcTM and are summarized in Table 7.2.

Table 7.2: Transformation temperatures of 4145-MOD

Transformation Temperature Label	Equilibrium Temperature	
	(K)	(°C)
A_{e_1}	981	708
A_{e_3}	1021	748
T_s	1692	1419
T_l	1760	1487

The alloying elements shown in Table 7.1 excluding S and P were used to determine transformation temperatures to be consistent with all thermophysical properties modelled in ThermoCalcTM. The inclusion of all elements resulted in the formation of several unlikely low temperature phases (below A_{e_1}), which prevented the program from reaching a solution in this range. Another important consideration was the inclusion of only ferrite, austenite, and cementite phases present in the solid. This assumption was made based on previous work on 41XX alloys, where $M_{23}C_6$, M_7C_3 , and MC phases were thermodynamically stable but not observed [11]. The absence of these phases is linked to the highly non-equilibrium conditions of the quench and temper treatment for the 41XX grade alloys described previously. An 18 K reduction in the A_{e_3} temperature was the only effect of these simplifications.

7.5 4145-MOD Thermal Conductivity

Thermal conductivity values for 4145-MOD were reported at room temperature by two sources as 42.6 W/mK and 43 W/mK [12, 13]. Values outside of room temperature were not found in any thermodynamic database, literature reference, or online data sheet. A Chinese steel supplier reported their product with a conductivity of $25 \text{ Wm}^{-1}\text{K}^{-1}$, but this value was suspect based on further research into similar 41XX alloys [14].

Mills et al. developed a model to predict thermal conductivity of steels as a function

of temperature from trends reported in literature [15]. It was observed that thermal conductivity could vary by nearly an order of magnitude, the slope could change signs depending on the level of alloying, and that conductivity reached a constant value near 1073 K (800°C) then would increase with increasing temperature. Mills' approach obtained the electronic conduction and lattice conduction contributions to conductivity at 298 K (25°C) separately using a combination of electrical conductivity data and numerical fitting of data from annealed steels. The following piece-wise equation was proposed:

$$298 \text{ K} < T \leq 1073 \text{ K} : k_T = k_{298} + (25 - k_{298}) \left(\frac{T - 298}{775} \right) \quad (7.1)$$

$$1073 \text{ K} < T \leq 1573 \text{ K} : k_T = 25 + 0.013(T - 1073)$$

where k_T is the thermal conductivity at temperature T (K), k_{298} is the thermal conductivity at 298 K, and T is the temperature (K). There was an error found in the reported high temperature portion of Equation (7.1). Mills stated that $k_T = 25$ W/mK at 1073 K (800°C) and $k_T = 31.5$ W/mK at 1573 K (1300°C). This condition was only satisfied when T-1073 was substituted for T-800 in the 1073 K < T < 1573 K range. This change corrected for the inconsistency in °C and K temperature units between the low and high portions of the equation. A value of 43.35 W/mK was chosen for k_{298} taken from the JAHM database for 4140 [16]. This value corresponded well with the reported room temperature values for 4145-MOD and was from the most complete thermophysical resource. Inputting this value into Equation (7.1), Figure (7.1) was generated. An average of all the model generated values between 533 K (260°C) and 1692 K (1419°C) was taken as the effective thermal conductivity k_{eff} . The average value was calculated to be 30.15 W/mK. It was noted that the average calculated value required extrapolation

of Mills' equation by 119 K to determine k_{1692} , but this represented less than 10% of the values used in the determination of k_{eff} and only raised the average by 0.25 W/mK.

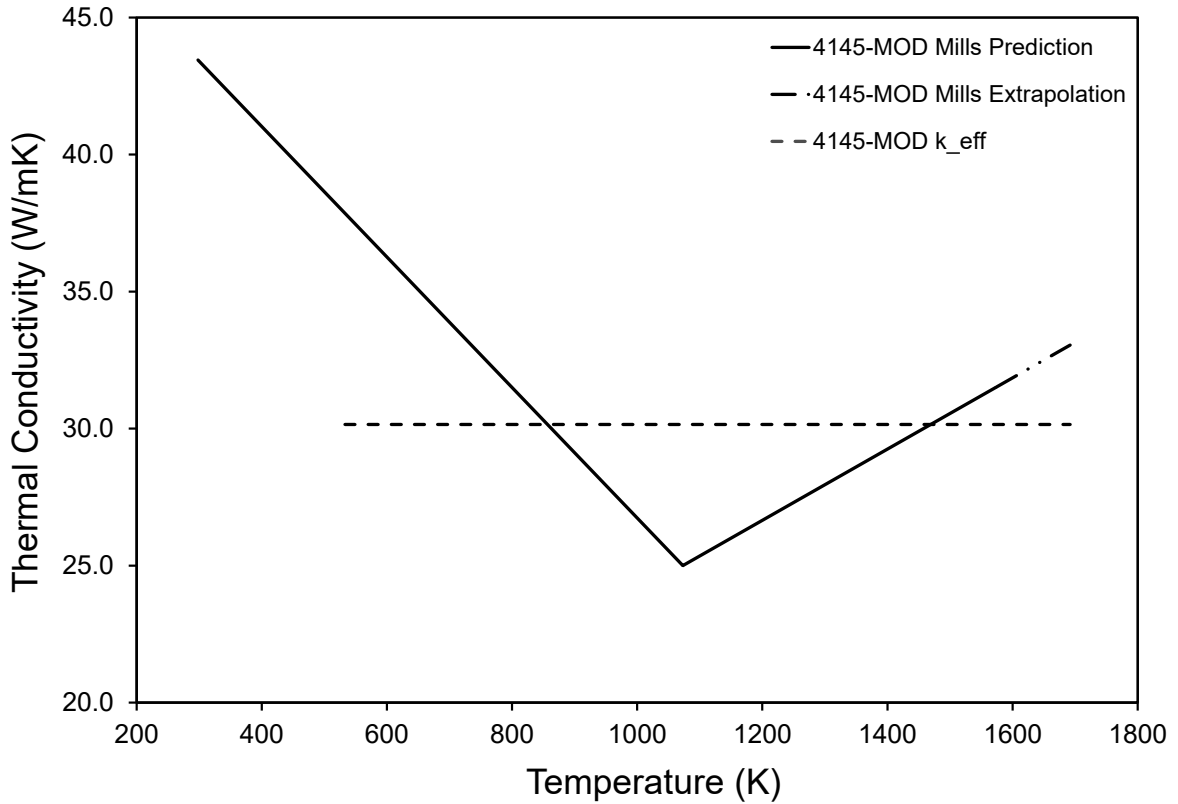


Figure 7.1: Mills model prediction for 4145-MOD thermal conductivity.

Figure (7.2) shows the Mills model conductivity predictions, k_{eff} , and data for similar chemistries to 4145-MOD found in literature [15–26]. Grades 4130, 4140, 42CrMo4 (European designated 4140), 9KhF (Russian grade similar to 4140), and 1%Cr-Mo steel were deemed to have alloying levels similar enough to 4145-MOD for reasonable comparison. Reported literature alloy chemistries are presented in Appendix A.2.

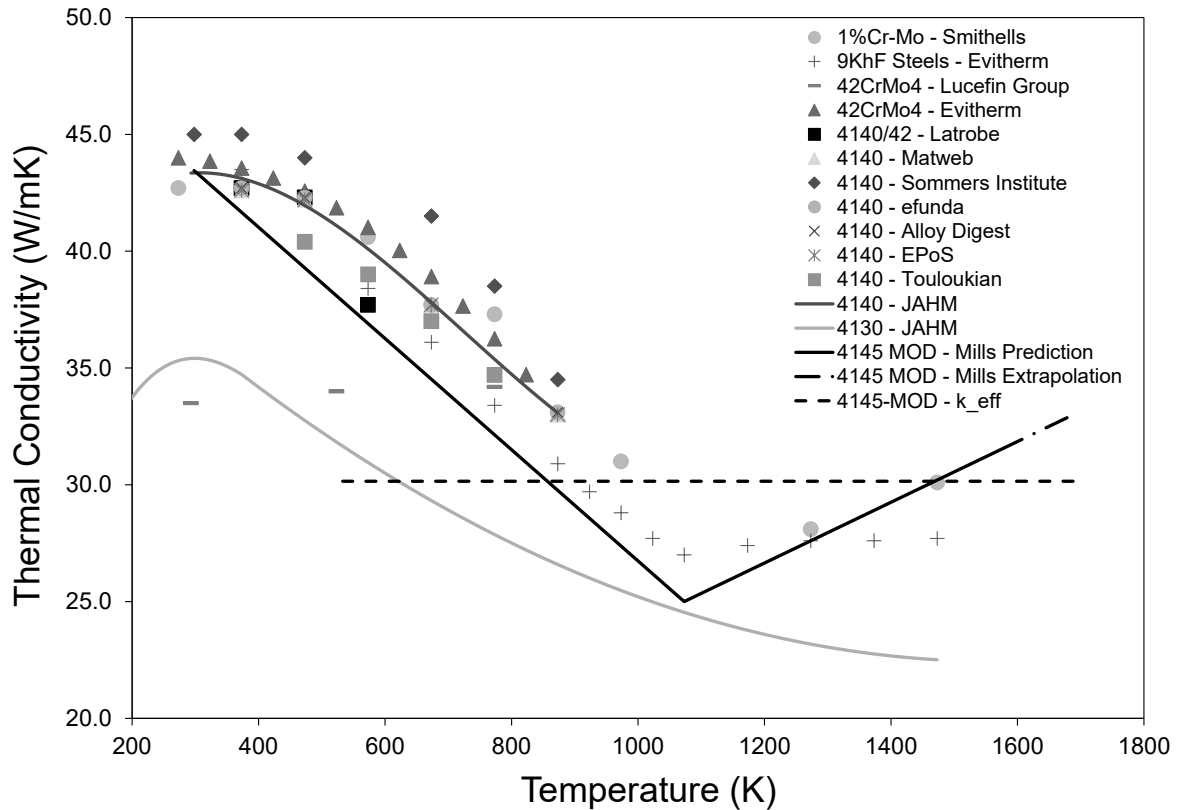


Figure 7.2: Comparison of k_{eff} , Mills model, and literature values of 4145-MOD thermal conductivity.

The model fits the literature data decreasing trend between 298 K (25°C) and 1573 K (1300°C) and demonstrates the same slope change point as the 9KhF steel and 1%Cr-Mo steel. The difference between 4140 and 4130 behaviour suggests higher carbon content increases the thermal conductivity, but there is still some doubt as the accuracy of the models slope increase at 1073 K based on the exponential decay of 4130 conductivity with temperature. The 1%Cr-Mo steel data increases at higher temperatures supporting the models slope prediction. Overall the choice of k_{eff} is reasonable compared to both the model and available literature data.

7.6 4145-MOD Heat Capacity

No values for 4145-MOD heat capacity at any temperature were reported in literature. Heat capacity temperature dependence for 4145-MOD was calculated by first determining enthalpy as a function of temperature from ThermoCalcTM. The data was output as molar enthalpy, which is shown in Figure (7.3) between 298 K (25°C) and 2000 K (1727°C).

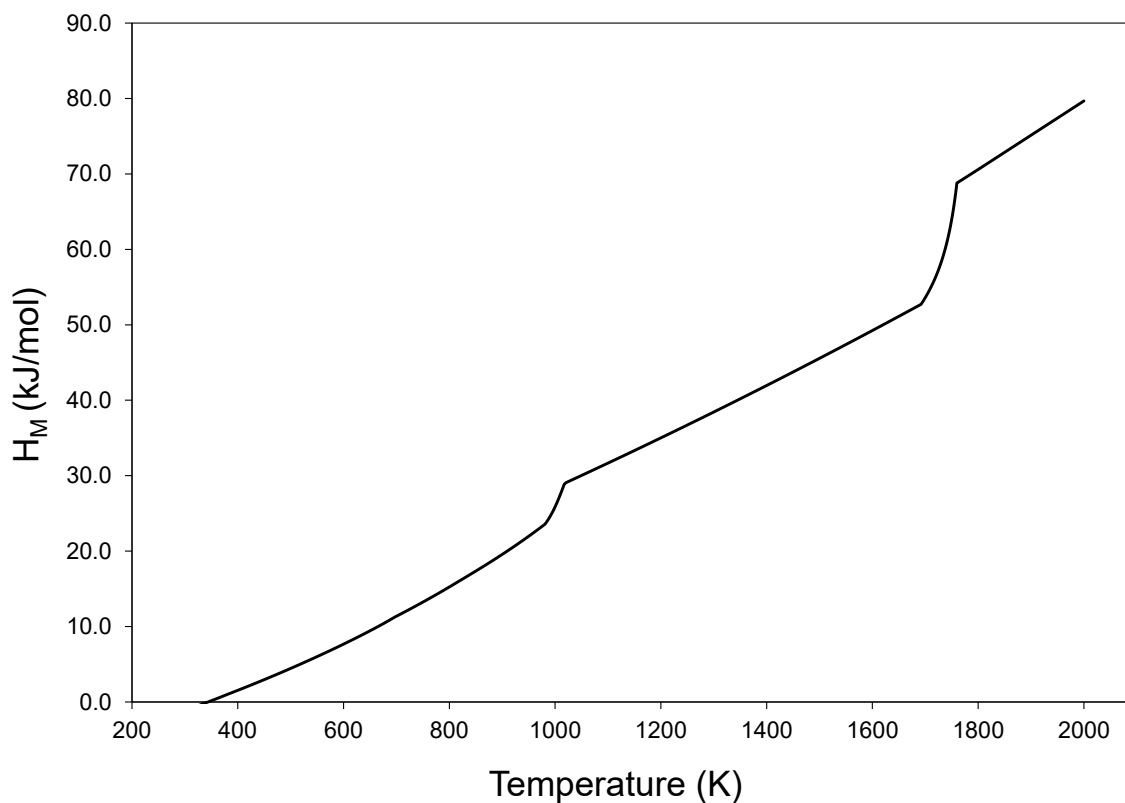


Figure 7.3: Molar enthalpy of 4145-MOD as a function of temperature from ThermoCalcTM.

Molar heat capacity at a given temperature came from the instantaneous slope at any point in Figure (7.3). This slope was approximated using Equation (7.2) below.

$$c_{p_i} = \frac{(H_{i+1}) - (H_{i-1})}{(T_{i+1}) - (T_{i-1})} \quad (7.2)$$

where c_{p_i} is the molar heat capacity at data point i (J/molK), H_{i+1} is the molar enthalpy at data point $i+1$ (J/mol), H_{i-1} is the molar enthalpy at data point $i-1$ (J/mol), T_{i+1} is the temperature at data point $i+1$ (K), T_{i-1} is the temperature at data point $i-1$ (K). The data was output in one degree increments from ThermoCalcTM with the exception of transformation temperatures, which were reported to the thousandth of a degree between the degree increments. Conversion of molar heat capacity to specific heat capacity required the molar mass for 4145-MOD. Equation (7.3) was derived to take available weight percent data from the MTR and convert it to a usable compound molar mass. Elemental molar mass data was taken from the Commission on Isotopic Abundances and Atomic Weights [27]. The derivation for Equation (7.3) is shown in Appendix A.3.

$$M_{eff} = \left[\sum_i \left(\frac{W_i}{M_i} \right) \right]^{-1} \quad (7.3)$$

where M_{eff} is the compound molar mass (g/mol), W_i is the weight fraction of element i , and M_i is the molar mass of element i (g/mol). $M_{4145\ MOD}$ was calculated to be 54.80 g/mol, which was confirmed by ThermoCalcTM as 54.81 g/mol considering only major elements ($> 0.1\text{wt}\%$). Conversion of molar heat capacity to specific heat capacity is accomplished using Equation (7.4).

$$c_p = \frac{c_{p_i}}{M_{4145\ MOD}} \quad (7.4)$$

where c_p is the specific enthalpy (J/kgK). Applying Equation (7.3) to all points in Figure (7.3), the specific heat capacity of 4145-MOD as a function of temperature was determined, which is shown in Figure (7.4).

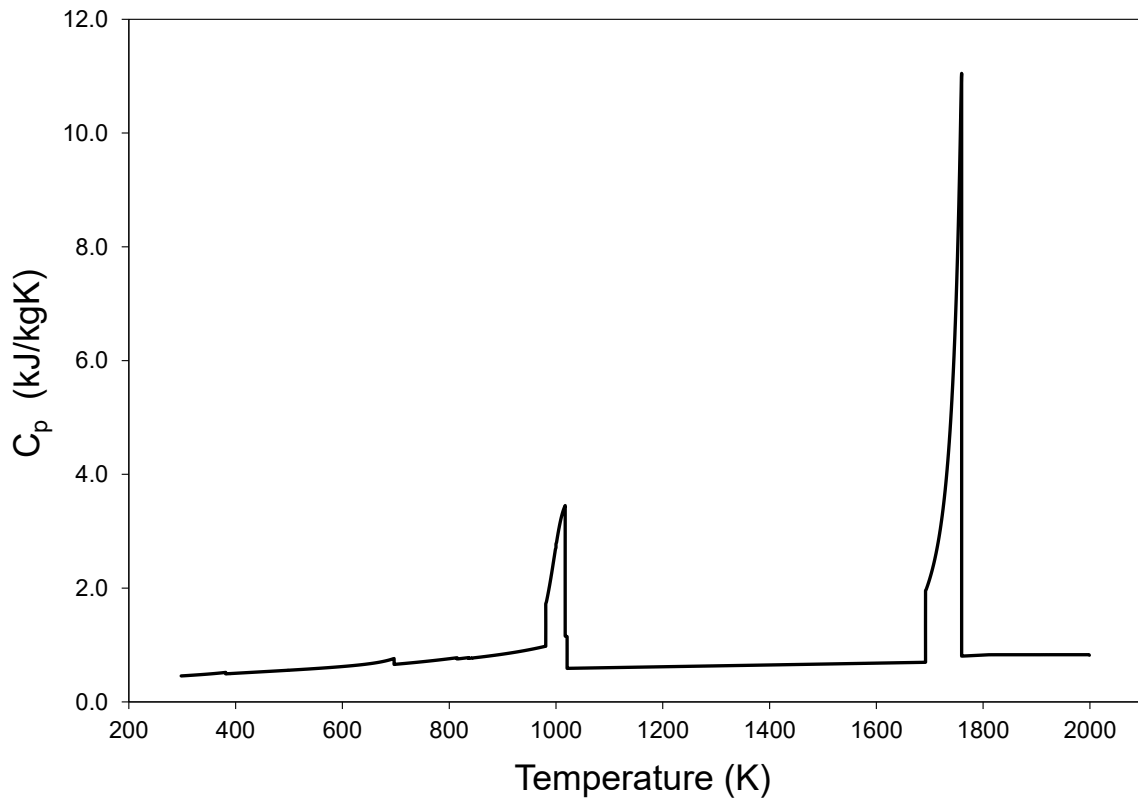


Figure 7.4: Specific heat capacity of 414- MOD calculated from Equation (7.4).

It is difficult to get a sense of the behaviour of c_p at temperatures below 1100 K (827°C) as a result of skewing from phase transformations in Figure (7.4). Figure (7.5) limits the range to 1500 J/kgK and includes the transformations associated with changes in c_p . Ideally, only cementite would have been included in this analysis, but it was not possible to isolate ferrite (BCC) and austenite (FCC) formation from other BCC and FCC carbide phases in ThermoCalcTM. The inclusion of these carbides in the analysis only slightly increases the effective enthalpy.

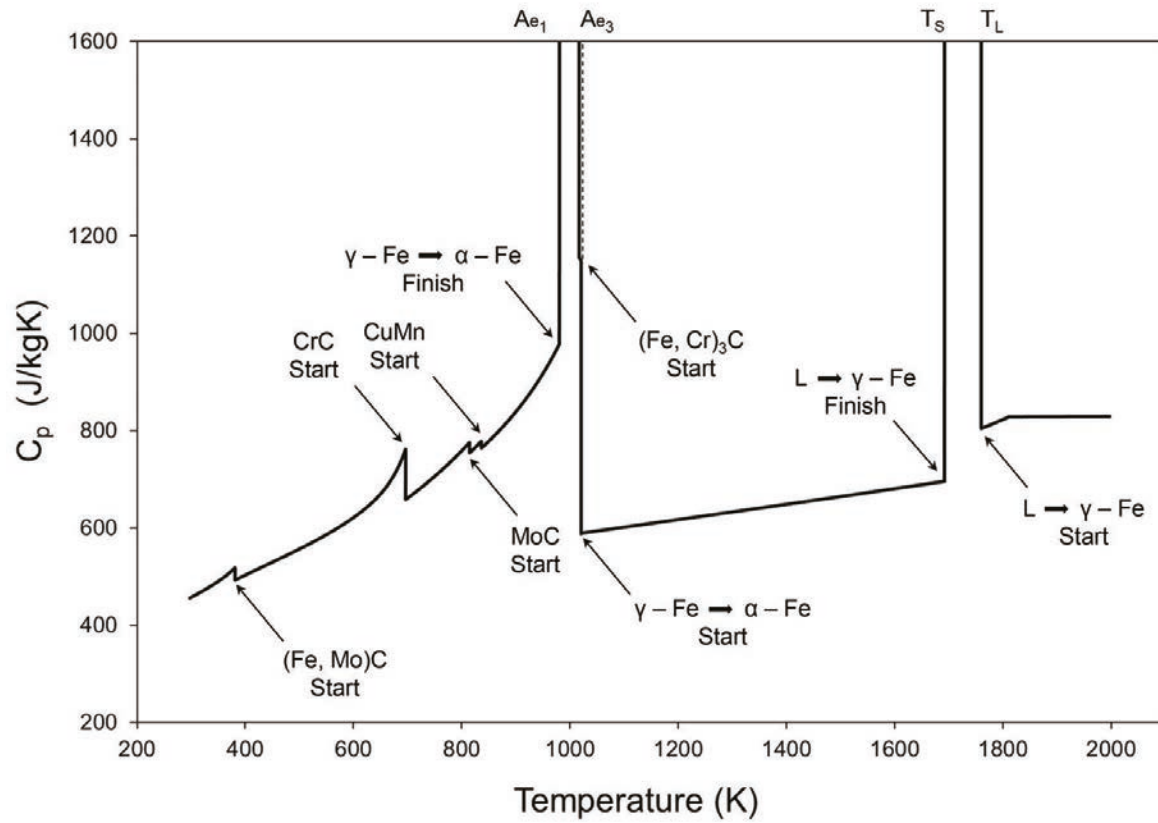


Figure 7.5: Zoomed view of specific heat capacity of 4145-MOD as a function of temperature calculated from Equation (7.4).

Equation (7.5) was used to determine an effective specific heat capacity $c_{p_{eff}}$ between the preheat temperature 533 K (260°C) and solidus temperature 1692 K (1419°C).

$$c_{p_{eff}} = \left[\frac{(H_s) - (H_p)}{(T_s) - (T_p)} \right] \left(\frac{1}{M_{eff}} \right) \quad (7.5)$$

where H_s is the molar enthalpy at the solidus temperature (J/mol), H_p is the molar enthalpy at the preheat temperature (J/mol), T_s is the solidus temperature (K), and T_p is the preheat temperature (K). $c_{p_{eff}}$ was calculated to be 743.97 J/kgK. Figure (7.6) shows the effective value graphically over the temperature range of interest in this analysis (533 K-1692 K).

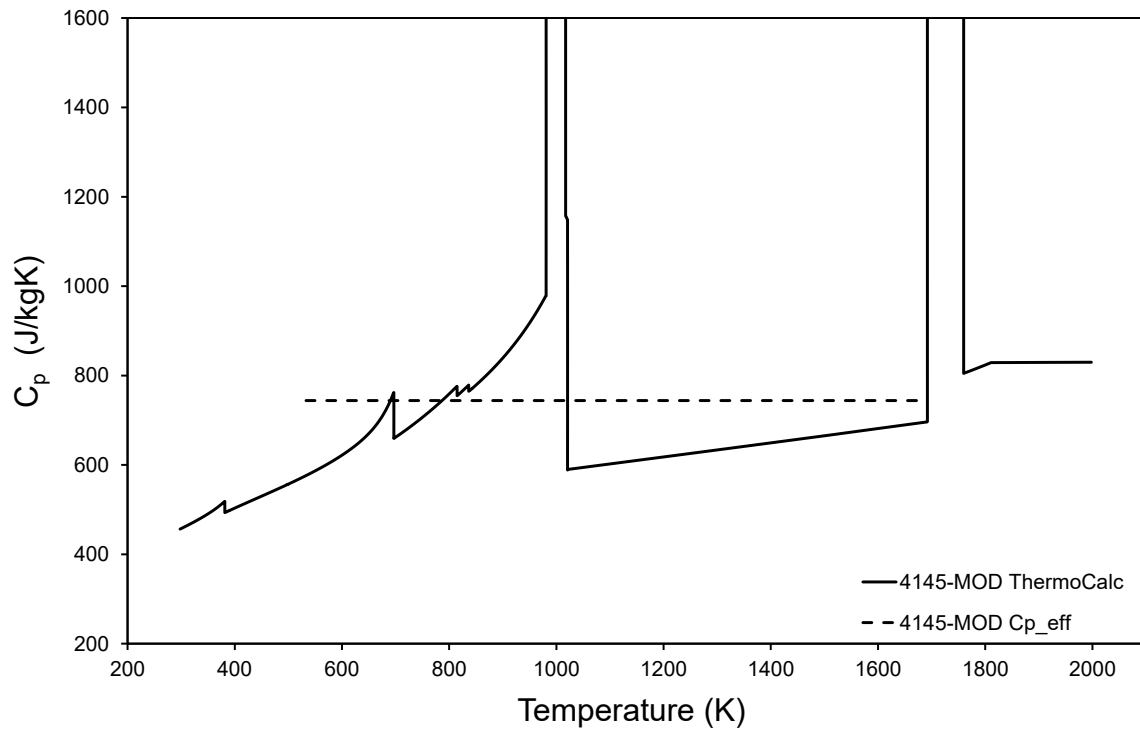


Figure 7.6: Effective specific heat capacity of 4145-MOD determined from ThermoCalcTM.

Figure (7.7) compares the ThermoCalcTM equilibrium predictions for specific heat capacity for 4145-MOD to values for 4140, 4130, and other similar grades from in literature [16,18–22,24,26,28]. Reported chemistries from the available sources are summarized in Appendix A.2.

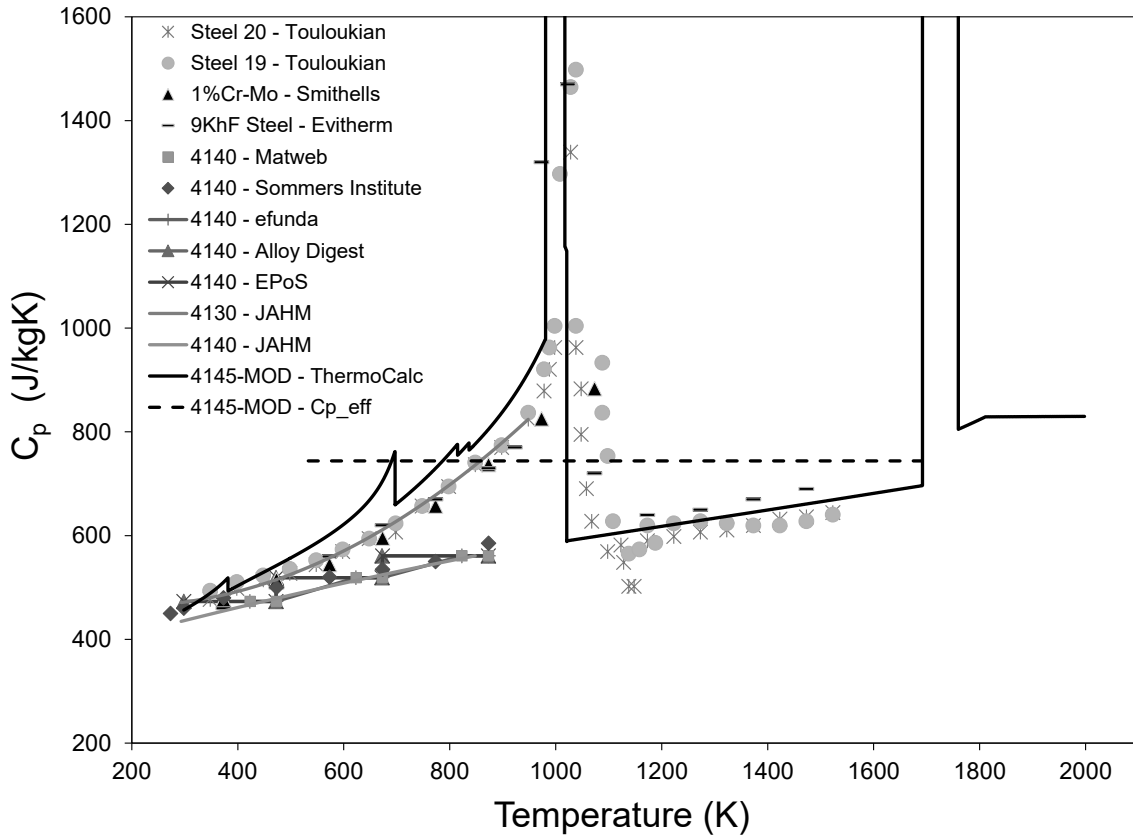


Figure 7.7: Specific heat capacity of 4145-MOD compared to similar steel heat capacities found in literature.

The stepwise values reported [18–20, 22, 24] represent an average across the temperature range and appear to only slightly overpredict the c_p compared to more complete sources for 4140 [16, 21]. The data for 4130 more closely matches the ThermoCalcTM trend for 4145-MOD compared to 4140, which is unexpected considering only C effects. The 4145-MOD trend in c_p matches well with available high temperature data having comparable slopes prior to and following the ferrite to austenite transformation. Only ThermoCalcTM predicts the precipitation of FCC and BCC carbide phases below 1000 K shown in Figure (7.5), which previous work on 4140 steels indicates are not present [11]. These phases have been included in the calculation of $c_{p_{eff}}$ in the form of molar enthalpy because they cannot be isolated from ferrite and austenite in ThermoCalcTM, but do

not contribute significantly compared to the ferrite to austenite transformation. Overall the ThermoCalcTM prediction of 4145-MOD heat capacity matches well with reported literature values for similar chemistries, and the choice of $c_{p_{eff}}$ is reasonable across the temperature range between T_p and T_s .

7.7 4145-MOD Density

4145-MOD density at room temperature was reported as 7850 kg/m³ by several online data sheets [12, 20, 22] and as 7800 kg/m³ [13], but it has not been reported as function of temperature in any resource. Two methods were explored to determine 4145-MOD density temperature dependence: modelling of molar quantities using ThermoCalcTM and dilatometry. These methods are outlined in detail below.

7.7.1 ThermoCalcTM Density

Density as a function of temperature for 4145-MOD can be determined from molar mass and molar volume modelled in ThermoCalcTM. Equation (7.6) shows the relationship between these quantities.

$$\rho(T) = \frac{M_{eff}}{V_M(T)} \quad (7.6)$$

where $\rho(T)$ is the compound density as a function of temperature (kg/m³) and $V_M(T)$ is the compound molar volume as a function of temperature (m³/mol). Equation (7.6) highlights that the change in density is related to the change in molar volume with temperature. Molar mass of the system remains constant, and the value outputted from ThermoCalcTM was 51.81 g/mol using the chemistry in Table (7.1) excluding S and P. Figure (7.8) shows the molar volume temperature dependence of 4145-MOD modelled in

ThermoCalcTM.

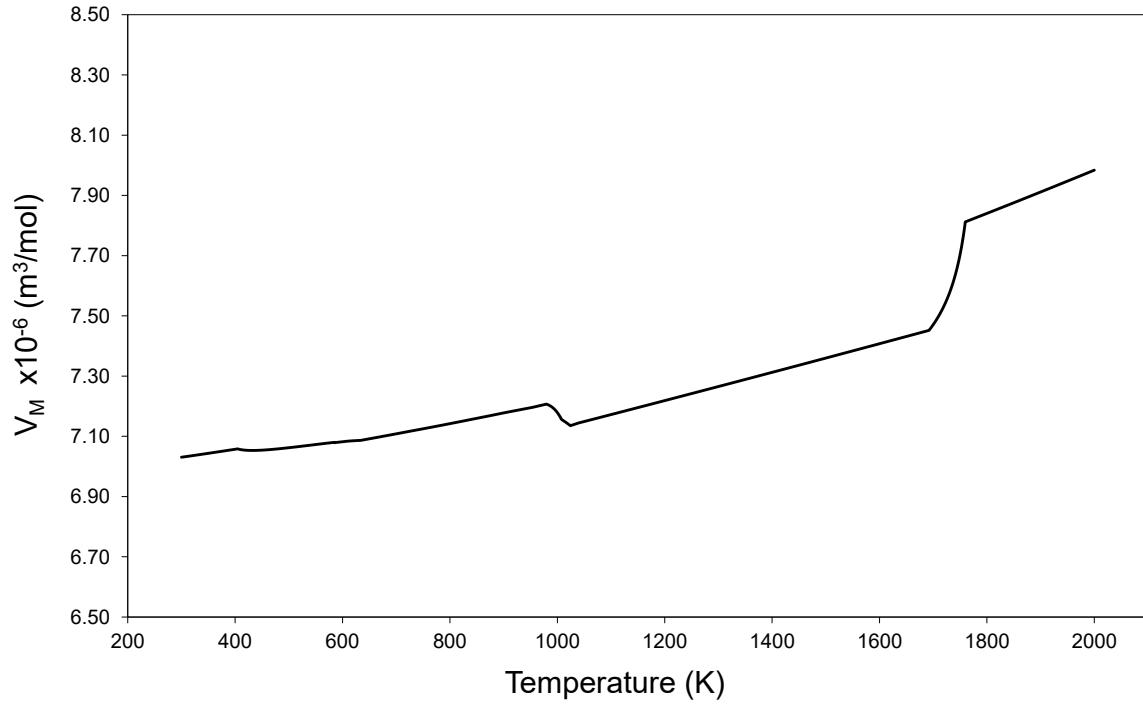


Figure 7.8: Molar volume of 4145-MOD as a function of temperature modelled in ThermoCalcTM.

Applying Equation (7.6) to the data in Figure (7.8) yields a plot of density as a function of temperature shown in Figure (7.9).

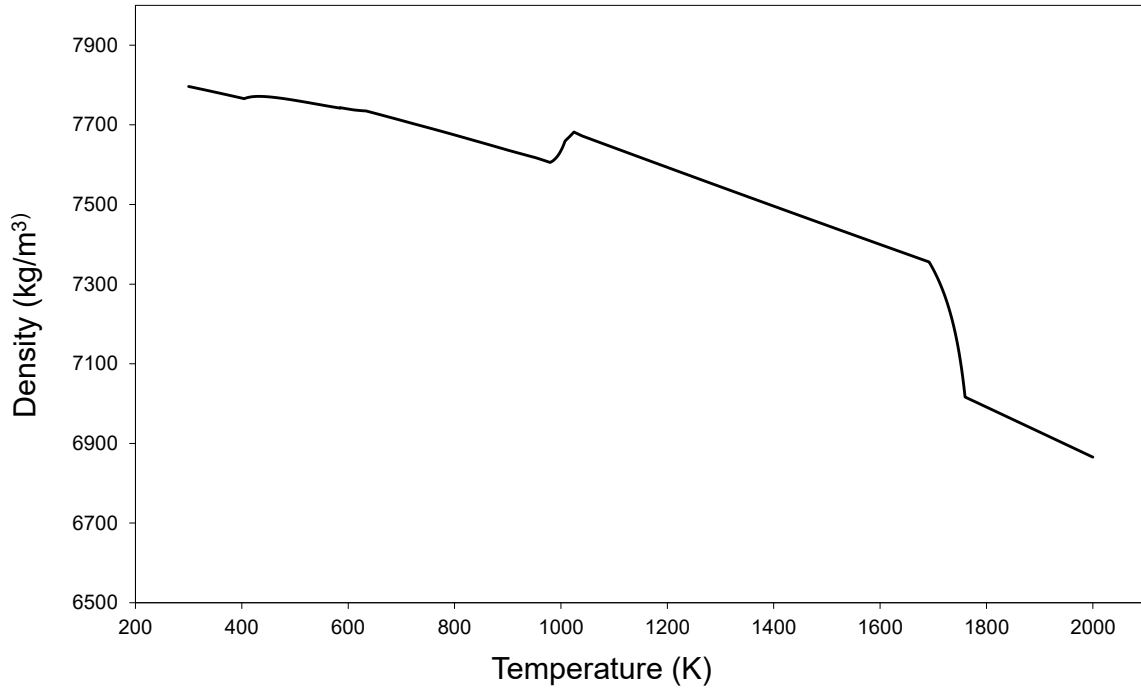


Figure 7.9: Density of 4145-MOD as a function of temperature modelled in ThermoCalcTM.

7.7.2 Calculation of Density from Dilatometry Data

Dilatometry is an experimental alternative to ThermoCalcTM in the determination of temperature effects on material density. Length changes with temperature typically used for identification of phase transformations can be correlated to the mean linear coefficient of thermal expansion using Equation (7.7) [29]. The dilatometer directly reads the change in length Δl , which has been included in Equation (7.7) rather than instantaneous length l_i as reported by Niffengger [29].

$$\overline{\beta}_L = \frac{\Delta l}{l_o(T_i - T_o)} \quad (7.7)$$

where $\overline{\beta}_L$ is the mean coefficient of linear thermal expansion (1/K), Δl is change in length of the sample (m), l_o is the original length of the sample (m), T_i is the tem-

perature at data point i (K), and T_o is the initial temperature of the test sample (K). Assuming isotropic expansion and small dimensional changes, $\overline{\beta_V}$ can be approximated by Equation (7.8) [30].

$$\overline{\beta_V} = (3\overline{\beta_L}) \quad (7.8)$$

where $\overline{\beta_V}$ is the mean volumetric coefficient of thermal expansion (1/K). A model for density was proposed by Mills for the solid state using the molar volume shown in Equation (7.9) [15].

$$V_{M_T} = V_{M_{298}} [1 + \overline{\beta_V}(T - 298)] \quad (7.9)$$

where V_{M_T} is molar volume at temperature T (m^3/mol). Combining the Equations (7.6) and (7.8) with the model proposed by Mills, the following expression was developed to describe density as a function of temperature.

$$\rho_T = \frac{\rho_{298}}{1 + 3\overline{\beta_L}(T - 298)} \quad (7.10)$$

where ρ_T is density at temperature T (kg/m^3).

7.7.3 4145-MOD Dilatometry Experiments

Ten samples were prepared for tests in a RITA L78 high speed dilatometer. The samples were machined directly from the 4145-MOD sample used for preliminary cladding trials. The target geometry was a cylinder with dimensions 10 mm long, 4 mm outer diameter, and 0.85 mm wall thickness. Length measurements were performed using a micrometer with a resolution of 0.01 mm and a high precision balance was used for mass measurements

(0.0001 g). Table (7.3) summarizes the data for all ten samples.

Table 7.3: Geometry, mass, and density of 4145 MOD dilatometry samples

Sample Number	Outer Diameter (mm)	Wall Thickness (mm)	Length (mm)	Volume (mm ³)	Mass (g)	Measured Density (g/mm ³)	Measured Density (kg/m ³)
1	4.04	0.85	10.04	85.53	0.6666	0.007794	7794
2	4.08	0.85	10.00	86.25	0.7060	0.008185	8185
3	3.92	0.80	10.01	78.49	0.6132	0.007812	7812
4	4.05	0.80	10.02	81.84	0.6806	0.008316	8316
5	4.07	0.85	9.96	85.64	0.6946	0.008111	8111
6	4.05	0.85	9.88	84.43	0.6436	0.007623	7623
7	3.95	0.80	10.04	79.48	0.6409	0.008063	8063
8	4.05	0.85	9.78	83.57	0.6680	0.007993	7993
9	3.94	0.75	9.94	74.71	0.5903	0.007901	7901
10	3.87	0.85	10.00	80.64	0.5914	0.007333	7333

No heat treatment was performed on the samples contrary to standard procedure to maintain the quench and tempered microstructure of the substrate. Ten runs were performed using the following heat cycle:

- Heat to 1173 K (900°C) at the trial heat rate
- Hold at 1173 K (900°C) for 5 s
- Cool to room temperature at 600 K/s (600°C/s)

The heating rates were varied for each of the 10 samples between 600 K/s and 0.1 K/s. The experimental heating rates are shown in Table 7.4. Previous work suggested that the heating rate was on the order of thousands of degrees per second. Rates this high were not possible using the dilatometer, and temperatures above 1573 K (1300°C) were not recommended to protect the machine from sample melting and potential resulting damage.

Table 7.4: Heating rate test values for 4145-MOD dilatometry trials

Sample Number	Heating Rate (K/s)
1	600
2	500
3	400
4	200
5	100
6	50
7	10
8	1
9	0.5
10	0.1

The change in length data output from the dilatometer was too large to be included here. Using Equation (7.7), the mean linear coefficient of thermal expansion was calculated for each temperature up to 1173 K (900°C). For heating rates below 1 K/s duplicate measurements at the same temperature had to be removed to avoid a singularity in the $\overline{\beta}_L$ calculation. Figure (7.10) shows $\overline{\beta}_L(T)$ for all samples.

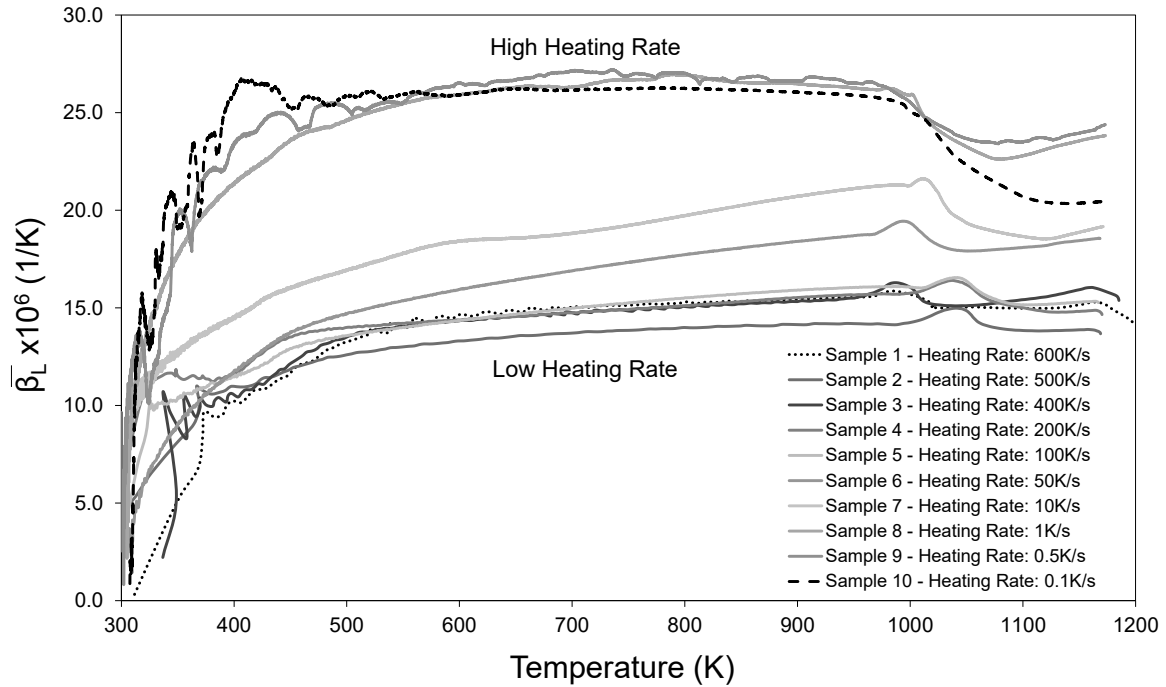


Figure 7.10: Heating rate effects on the mean linear coefficient of thermal expansions of 4145-MOD as a function of temperature.

In general higher heating rate increased $\bar{\beta}_L$. Using the $\bar{\beta}_L(T)$ data, Equation (7.10) was used to determine $\rho(T)$. For this calculation of $\rho(T)$, $\rho_{298} = 7850 \text{ kg/m}^3$ was used [12,20,22] rather than the measured density data from Table 7.3 because of the variation in these measured values. The variation is likely related to the accuracy of the volume measurements of the samples for which small variations make a large difference when scaled up to a bulk value in the m^3 unit system. Figure (7.11) shows the results of those calculations.

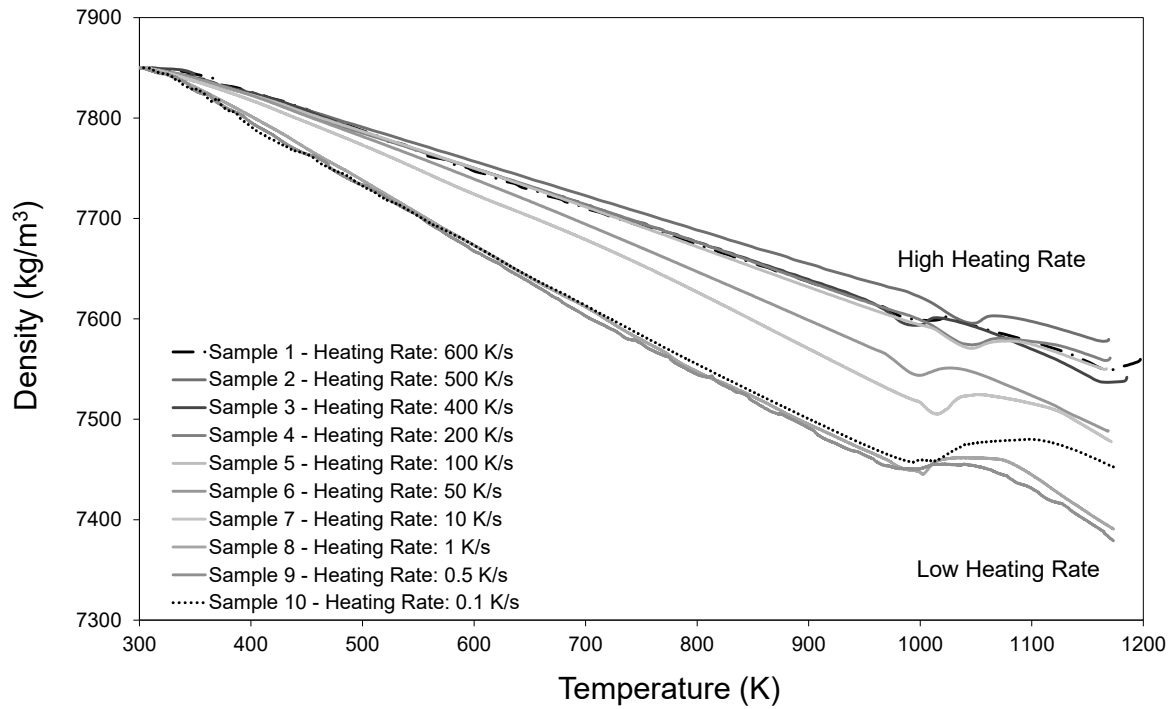


Figure 7.11: 4145-MOD density temperature dependence calculated using Equation (7.10).

Figure (7.11) shows that faster heating rate effectively increased $\rho(T)$ and delayed the start of the ferrite to austenite transformation around 1000 K. This observation can be explained in the context of the time required for atomic realignment and expansion during phase transformations. There is a clear diverging trend in high and low heating rate density with increasing temperature from the dilatometry data, but this understanding goes beyond the scope of this study.

7.7.4 Determination of ρ_{eff} for 4145-MOD

The effective value for 4145-MOD was taken from the ThermoCalcTM generated data for 4145-MOD. In spite of the parallels between high heating rate dilatometry tests and laser cladding processes, the ThermoCalcTM value was used because it was possible to generate data for the entire temperature range of interest. It should be noted that the

selection of reference for effective density would not have a large effect on the resulting value (within 100's of kg/m^3). The value of $7590 \text{ kg}/\text{m}^3$ was taken for ρ_{eff} for this work between 533 K and 1692 K. Only two references were found for comparison of similar chemistry data, one each for 4130 and 4140 [16]. Figure (7.12) shows the ThermoCalcTM simulation, highest and lowest heating rate dilatometry samples, and these literature values. Literature alloy chemistries are listed in Appendix A.2.

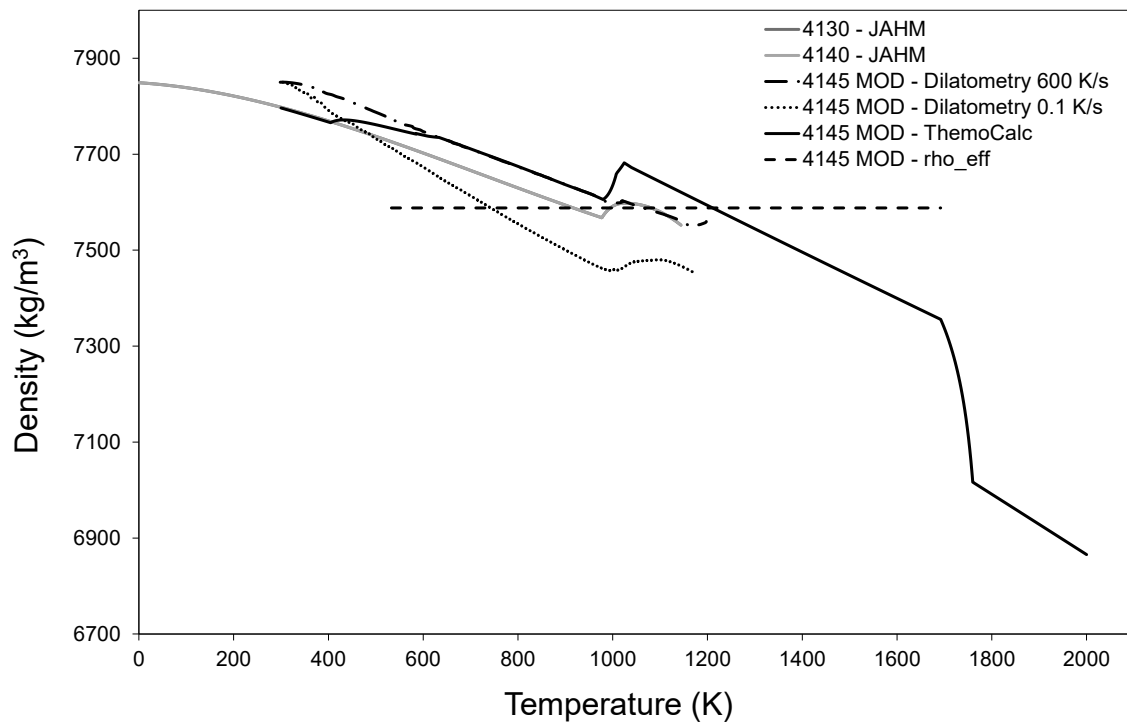


Figure 7.12: Comparison of 4145-MOD densities to similar chemistries in literature.

Figure (7.12) shows that 4130 and 4140 have identical reported density for the entire available temperature range. The location of the A_{C_1} temperature agrees well for all sources, though the curvature varies with sharper features corresponding to more equilibrium treatments. Despite some variation between the sources, overall they demonstrate similar decreasing trends with increasing temperature and comparable locations for the ferrite to austenite transformation. The average ρ_{eff} between T_p and T_s is acceptable

compared to the available literature sources and between the two techniques.

7.8 4145-MOD Thermal Diffusivity

Thermal diffusivity is a key parameter for understanding temperature evolution in welding processes. Thermal diffusivity α is related to k , c_p , and ρ through the relation in Equation (7.11) [31].

$$\alpha = \frac{k}{\rho c_p} \quad (7.11)$$

Similar to all three parameters, α has an inherent temperature dependence. Having determined an effective value for k , c_p and ρ between 533 K (260°C) and 1692 K (1419°C), it follows that the effective diffusivity α_{eff} can be expressed as:

$$\alpha_{eff} = \frac{k_{eff}}{\rho_{eff} c_{p_{eff}}} \quad (7.12)$$

α_{eff} was calculated to be $5.34 \times 10^{-6} \text{ m}^2/\text{s}$ using Equation (7.12). For comparison $\alpha(T)$ was calculated using $k(T)$, $c_p(T)$, and $\rho(T)$ between 298 K (25°C) and 1692 K (1419°C). A second curve for $\alpha(T)$ was also generated using an estimate c_p in the region of the ferrite-austenite phase transformation. This estimate was calculated at each temperature value using linear interpolation between A_{e_1} and A_{e_3} as recommended by Mills [15]. The average α between T_P and T_S was calculated to be $5.78 \times 10^{-6} \text{ m}^2/\text{s}$ and $5.89 \times 10^{-6} \text{ m}^2/\text{s}$ for the $\alpha(T)$ curve using $k(T)$, $c_p(T)$ and $\alpha(T)$ with estimate c_p curves respectively. The calculated value of α_{eff} agrees within 11% of both values using these slightly different techniques. These thermal diffusivity curves and the selected α_{eff} are shown in Figure (7.13).

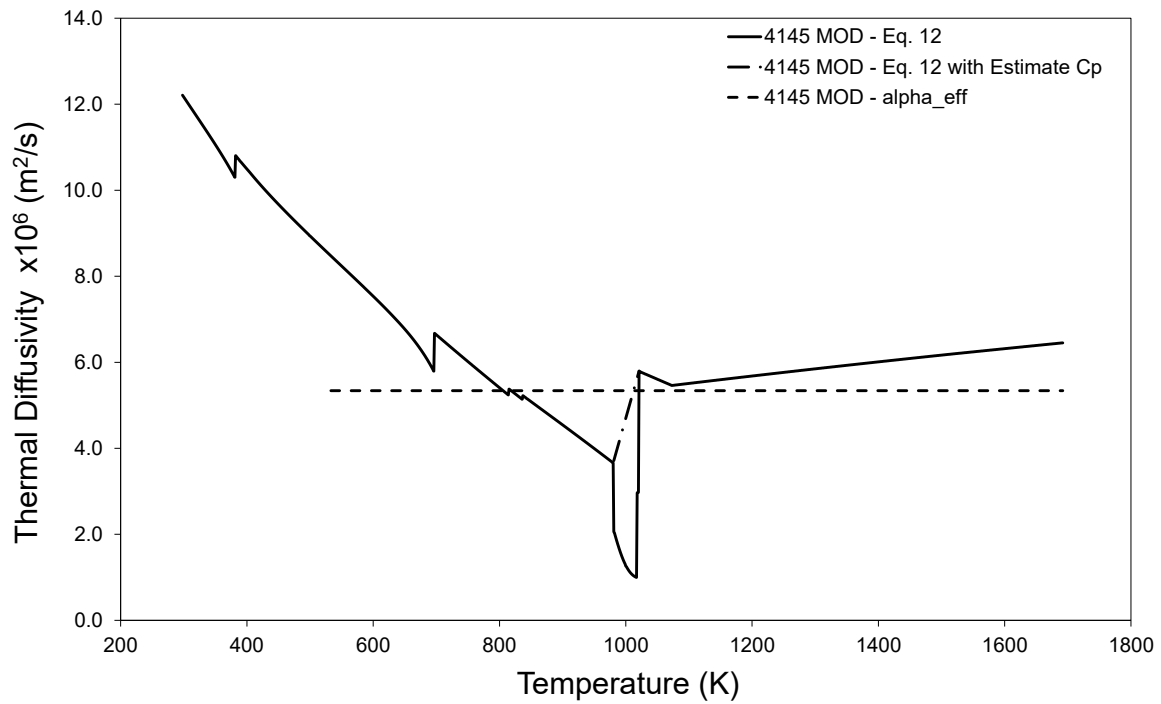


Figure 7.13: Thermal diffusivity of 4145-MOD calculated using Equation (7.11).

No sources directly reported any value for α of 4145-MOD even at room temperature. Available data for 4130 [16,24,32], 42CrMo4 [24], and 9KhF steel [24] is presented below in Figure (7.14) compared against the calculated values in Figure (7.13) and α_{eff} . Chemistry data for these alloys is shown in Appendix A.2.

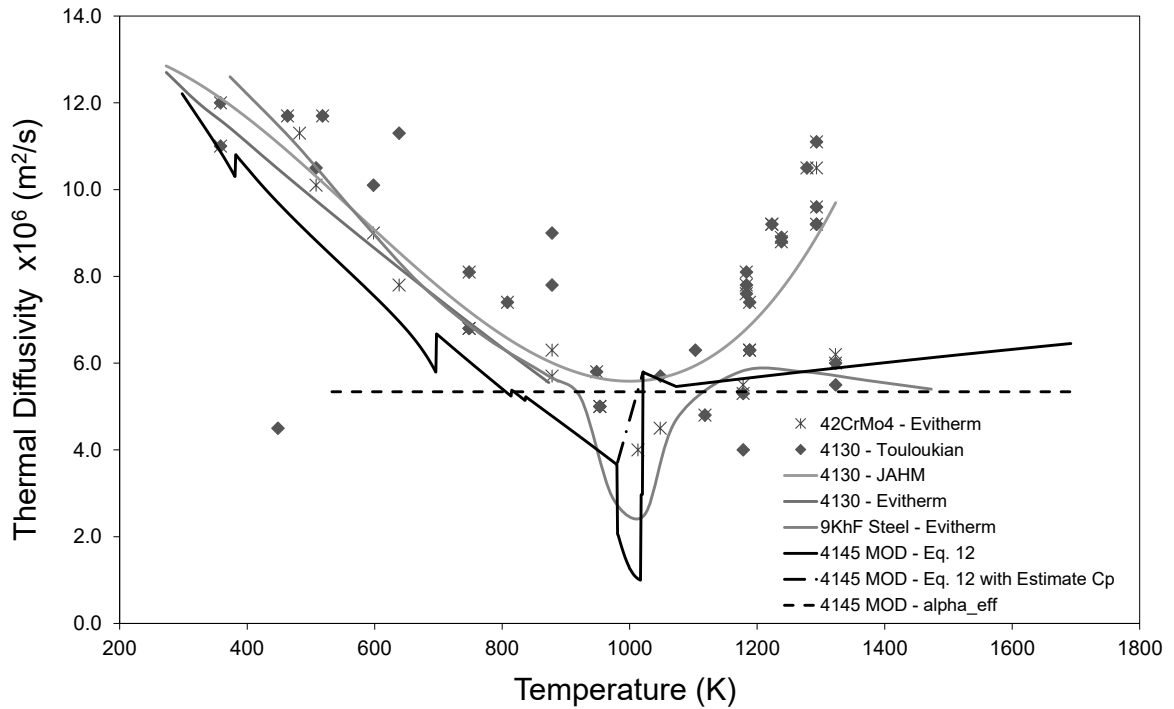


Figure 7.14: Comparison of α_{eff} to thermal diffusivity of alloys having similar chemistries to 4145-MOD.

The decreasing trend in the data is reasonably consistent between all sources until the ferrite-austenite transformation. The clear dip shown by the 4145-MOD - Eq.12 curve and Evitherm's 4130 data [24] is due to the actual C_P in the region of transformation and not an estimate as recommended by Mills [15]. The change in slope at the transformation agrees with behaviour of k in Figure (7.1) near this temperature in the context of Equation (7.11). The trend agreement falls apart around 1100 K (827°C) with multiple sources reporting values for the same material with a spread that makes it difficult to determine the actual trend [24, 32]. Overall α_{eff} is in reasonable agreement with the calculated $\alpha(T)$ curves and sources reported in literature.

7.9 Conclusions

Thermophysical properties of 4145-MOD steel were calculated as a function of temperature between 533 K (260°C) and solidus (1419°C). The temperature range for this analysis corresponds to preheat and solidus temperatures for laser cladding of Ni-WC alloys on 4145-MOD steel. Single values were selected for thermal conductivity, heat capacity, density, and thermal diffusivity using a combination of existing models for steels and thermodynamic calculations. These values were calculated to be:

- $k_{eff} = 30.15 \text{ W/mK}$
- $c_{p_{eff}} = 743.97 \text{ J/kgK}$
- $\rho_{eff} = 7590 \text{ kg/m}^3$
- $\alpha_{eff} = 5.34 \times 10^{-6} \text{ m}^2/\text{s}$

Property values were compared against limited literature data as a function of temperature. No values outside of room temperature were reported for 4145-MOD requiring inclusion of similar chemistries (4130, 4140, 42CrMo4, 9KhF) with available data for comparison. Modelled trends agreed well with reported values at temperatures below 1000 K (727°C). Higher temperature values above the ferrite to austenite transformation showed more variation with some sources reporting contradictory trends.

7.10 Appendix A.1 Materials Testing Report for 4145-MOD Steel



Tata Steel UK Limited
 Stocksbridge
 Sheffield
 S36 2JA
 United Kingdom
 Telephone: +44 (0) 114 2882361
 Fax: +44 (0) 114 2832079
 Website: www.tatasteel.com



INSPECTION CERTIFICATE/TYPE 3.1 to BS EN 10204

HOWCO GROUP PLC HOWCO MATERIALS MANAGEMENT ATTN WILLIAM JACK 3 BLAIRLINN ROAD BLAIRLINN INDUSTRIAL ESTATE CUMBERNAULD G67 2TD	DATE	01/11/14	HOWCO CERTIFIED TRUE COPY
	BY	CHARLEA	CAST No. A0994N/W23613 HG No. 61315
	WO #	99851	CERT No. 61315-1 YRO/No.21080
	PO #	21080	AUTH SIGNATORY Charlene Moon DATE Jan 20 2014

FOR HOWCO PAGE 1 OF 3

Cast No. A0994N	Works Order No. CB860313	Date of Issue 01-NOV-2013
	Customer Order No. EUR-915087	Certificate No. 00461900/1
		Page No. 1 of 3

SPECIFICATIONS ASSOCIATED WITH THIS ORDER -
 HG4145MOD/MT36 BAR REV 1 (2301 CAPABLE) HG001

PRODUCT INFORMATION -
 SIZE - 0171.450 MM DIA
 QUANTITY/WEIGHT - 7 BARS 11.535 TONNES APPROX
 CONDITION OF MATERIAL - COLD STR, H&T, SM TURN, STR REL
 STEELMAKING PROCESS/PROCESS OF MANUFACTURE - Electric VDG Ingot

HEAT TREATMENT OF MATERIAL - W23613
 Continuous Harden at 880°C; for 01:00; time to 02:47; total time 03:47; Water Quenched from 31°C.
 Temper at 620°C; for 01:00; time to 03:21; total time 04:21; Air Cooled.
 Freedom from residual stress

ANALYSIS -

Cast No	C	Si	Mn	P	S	Cr	Mo	Ni	Cu	Sn	Al	H ppm	B	Nb	Ti	V
Cast Analysis																
A0994N	0.47	0.24	1.13	0.008	0.006	1.18	0.34	0.24	0.16	0.020	0.028	1.5	< 0.005	< 0.01	0.01	0.002

Mechanical Test - Tested to ASTM A370 - 12

Test No.	Ingot Id	Ingot Pos.	Sample Pos.	Orient	Temp	0.2% PS	UTS	Elong	R of A	YS/MS
Units					C	PSI	PSI	%	%	
Result	2260783	M	Mid-Radial	Lo	23	129000	151000	20.0	57.0	0.82

Impact Test - Tested to ASTM A370 - 12

Test No	Ingot Id	Ingot Pos.	Sample Pos.	Geometry	Orient	Temp	Imp Mean	Impact	Impact	Impact	Lat Exp	Lat Exp	Lat Exp	% Shear
Units						C	J	J	J	J	mm	mm	mm	%
Result	2260784	M	Mid-Radial	CH2MMV(B)	Lo	23	85	81	87	86	1.02	1.08	1.10	100.0
	2260785	M	Mid-Radial	CH2MMV(B)	Lo	20	75	74	78	74	0.96	0.96	0.92	90.0

Test No	Ingot Id	Ingot Pos.	Sample Pos.	Geometry	Orient	Temp	% Shear	% Shear
Units						C	%	%
Result	2260784	M	Mid-Radial	CH2MMV(B)	Lo	23	100.0	100.0
	2260785	M	Mid-Radial	CH2MMV(B)	Lo	20	100.0	100.0



Tata Steel UK Limited
 Stocksbridge
 Sheffield
 S36 2JA
 United Kingdom
 Telephone: +44 (0) 114 2882361
 Fax: +44 (0) 114 2832079
 Website: www.tatasteel.com

INSPECTION CERTIFICATE/TYPE 3.1 to BS EN10204

Cast No. A0994N	Works Order No. CB860313	Date of Issue 01-NOV-2013
	Customer Order No. EUR-915087	Certificate No. 00461900/1
		Page No. 2 of 3

MacQuaid Ehn Grain Size - Tested to ASTM E112 - 12
 MacQuaid Ehn Grain Size - Carburised at 925 Deg C 8 Hours Furnace Cooled.
 Tested at a magnification of X100

Test No.	Ingot Id	Ingot Pos.	G Size	G Size
Result 2260781			6	8

As Supplied Grain Size - Tested to ASTM E112 - 12
 Magnification X100

Test No.	Ingot Id	Ingot Pos.	G.Size	G Size	Etchant
Result 2260782		M	6	7	NITAL

Jernkontoret Inclusion Count - Tested to ASTM E45 -13

Test No.	Ingot Pos.	A Thin	A Heavy	B Thin	B Heavy	C Thin	C Heavy	D Thin	D Heavy
Result Average		1.13	0.25	0.75	0.00	0.00	0.00	0.63	0.50

Surface Hardness -

Test No.	Ingot Id	Ingot Pos.	Hardness	Hardness
Units			HBW10/3000	HBW10/3000
Result 2260792			302	302

Sub Surface Hardness test -

Test No.	Ingot Id	Ingot Pos.	Mid Radial	1/8" Below
Units			HBW10/3000	HBW10/3000
Result 2260786		M	317	326

Chemical Composition Fomulae -
 Chemical Composition Fomulae P + S

Test No.	Ingot Id	Ingot Pos.	Result
Units			%
Result 2250941			0.0140

HOWCO
CERTIFIED TRUE COPY
 PAGE 2 OF 3
 CERT No. 61315-1

Structure Test - Satisfactory

Ultrasonic Test - Tested to ASTM A388/A388M - 11
 Satisfactory to 6 0mm FBH
 US SATISFACTORY TO API 6A PSL 3+ 4



INSPECTION CERTIFICATE/TYPE 3.1 to BS EN10204

Cast No. A0994N	Works Order No. CB860313	Date of Issue 01-NOV-2013
	Customer Order No. EUR-915087	Certificate No. 00461900/1
		Page No. 3 of 3

Ultrasonic Test - Tested to ASTM A388/A388M - 11
Satisfactory to 3.0mm FBH EXCLUDING AXIAL +/- 10% OF SECTION

MISCELLANEOUS INFORMATION -
PRODUCT HYDROGEN <= 2PPM MAX
START AND FINISH WATER QUENCH TEMPS DO NOT EXCEED 38oC
REDUCTION RATIO: 11.88:1
VAC DEGASSED AND SECONDARY REFINED STEEL
INGOT ROUTE
Furnaces calibrated to an in-house procedure using MIL-H-6875 and ASTM A991 methodology
Material type tested satisfactorily
Method of Analysis
- Elemental Analysis (combustion/fusion) tested at our Rotherham laboratory C S H
- Atomic Emission Spectroscopy (OES) tested at our Rotherham laboratory Si Mn P Cr Mo Ni Cu Sn Al B Nb Ti V
Radioactivity < 0.1Bq/g on ladle sample.
This product is mercury free.
No weld repair carried out on this product.
Our quality management system is accredited to the following standards : ISO9001 and AS/EN9100.
Our environmental management system is accredited to ISO14001.

AUTHORISED SIGNATURE -
Certified by our Stocksbridge Works that, unless otherwise stated above, the whole of the above mentioned materials have been manufactured, tested & inspected in accordance with the terms of the acknowledged contract/order applicable thereto and conform fully to the standards/specifications quoted hereon.
Approved Signatory - Lee Ibbitson - Certification and Accreditation Manager

Signed.....

For Tata Steel UK Limited

This inspection certificate shall not be reproduced except in full, without the written approval of Tata Steel UK Limited
End Of Certificate

HOWCO
CERTIFIED TRUE COPY
PAGE 3 OF 3
CERT No. 61315-1

7.11 Appendix A.2 Literature Alloy Chemistries

Table (7.5) summarizes the reported chemistries for all literature sources compared against 4145-MOD. Iron is not included, but makes up the balance of all compositions.

Table 7.5: Composition of steel chemistries from literature used as comparison for 4145-MOD thermophysical properties

Grade	Ref	C wt%	Cr wt%	Mn wt%	Mo wt%	Si wt%	Ni wt%	P wt%	S wt%
4145	[12]	0.43-0.48	0.80-1.10	0.75-1.00	0.15-0.25	0.15-0.30		0.035*	0.040*
4145	[13]	0.43-0.48	0.80-1.10	0.75-1.00	0.15-0.25	0.15-0.35		0.035	0.040
4145	[14]	0.48-0.53	0.80-1.10	0.75-1.00	0.15-0.25	0.15-0.35		0.035*	0.040*
4140	[16]	0.4	1	0.25		0.25			
4130	[16]	0.3	1	0.5	0.2	0.25			
4140	[17]	0.38-0.43	0.8-1.10	0.25-1.50			0.20-0.35	0.1*	0.040*
4140	[18]	0.38-0.43	0.80-1.10	0.75-1.00	0.15-0.25	0.15-0.30		0.04*	0.035*
4140	[19]	0.38-0.43	0.80-1.10	0.75-1.10	0.15-0.25	0.15-0.30		0.035*	0.040*
4140	[20]	0.38-0.43	0.80-1.10	0.75-1.10	0.15-0.25	0.15-0.30		0.035*	0.040*
4140	[21]	0.38-0.43	0.80-1.10	0.75-1.00	0.15-0.25	0.025*	0.25*	0.025*	0.025*
4140	[22]	0.38-0.43	0.80-1.10	0.75-1.0	0.15-0.25	0.15-0.30		0.035*	0.040*
4140/42	[23]	0.40	1.00	1.00	0.20	0.25			
42CrMo4	[24]	0.39	1.11	0.56		0.3		0.011	0.023
42CrMo4	[25]	0.38-0.45	0.90-1.20	0.60-0.90	0.15-0.30	0.40*		0.035*	0.035*
9KhF Steel	[24]	0.80-0.90	0.40-0.70	0.30-0.60	0.15*	0.15-0.35	0.35*	0.030*	0.030*
1%Cr-Mo	[26]	0.28-0.33	0.8-1.1	0.4-0.6	0.15-0.25	0.2-0.35			
Steel 20	[28]	0.35	0.88	0.59	0.20	0.21	0.26	0.028	0.031
Steel 19	[28]	0.315	1.09	0.69	0.012	0.2	0.073	0.039	0.036
4130	[32]	0.28-0.33	0.80-1.10	0.40-0.60	0.15-0.25	0.20-0.35		0.040	0.040

* Indicates a maximum allowable level rather than a measured wt%

7.12 Appendix A.3 Derivation for Compound Molar Mass

This section outlines the derivation for compound molar mass from individual elemental weight percent values.

$$W_i = \frac{m_i}{m_t} \quad (7.13)$$

The mass of an individual element in the compound is related to molar mass through Equation (7.14).

$$m_i = M_i \times n_i \quad (7.14)$$

The number of moles of element i depends on the mole fraction as follows:

$$n_i = x_i \times n_t \quad (7.15)$$

Substituting Equations (7.14) and (7.15) into Equation (7.13) and rearranging yields:

$$\frac{m_t}{n_t} = \frac{M_i \times x_i}{W_i} \quad (7.16)$$

Compound molar mass represents the total mass over the total number of moles shown below.

$$M_{eff} = \frac{m_t}{n_t} \quad (7.17)$$

Replacing Equation (7.17) into Equation (7.16) results in the following definition for M_{eff} :

$$M_{eff} = \frac{M_i \times x_i}{W_i} \quad (7.18)$$

From a unit analysis, the moles of element i can be given by the expression below. The per total mass units cancels out both top and bottom of the equation.

$$x_i = \frac{\left(\frac{W_i}{M_i}\right)}{\sum_i \left(\frac{W_i}{M_i}\right)} \quad (7.19)$$

Substituting Equation (7.19) into Equation (7.18) and cancelling terms gives the final form of the expression for compound molar mass in terms of the weight fraction of elements and molar mass of the individual components.

$$M_{eff} = \left[\sum_i \left(\frac{W_i}{M_i} \right) \right]^{-1} \quad (7.3)$$

7.13 References

- [1] J.A.J. Robinson, A.T. Dinsdale, L.A. Chapman, P.N. Quested, J.A. Gisby, and K.C Mills. The Prediction of Thermophysical Properties of Steels and Slags. 2001.
- [2] D. Rosenthal. The Theory of Moving Sources of Heat and Its Application to Metal Treatments. *Transactions of the A.S.M.E.*, pages 849–866, 1946.
- [3] J.V. Sengers and M. Klein, editors. *The Technological Importance of Accurate Thermophysical Property Information*. American Society of Mechanical Engineers, National Bureau of Standards, 1979.
- [4] M.J. Peet, H.S. Hasan, and H.K.D.H. Bhadeshia. Prediction of Thermal Conductivity of Steel. *International Journal of Heat and Mass Transfer*, 54:2602–2608, 2011.
- [5] Z. Guo, N. Saunders, P. Miodownik, and J. Schille. Modelling Phase Transformations and Material Properties Critical to the Prediction of Distortion during Heat Treatment of Steels. *Int. J. Microstructure and Material Properties*, 4(2):187–195, 2009.
- [6] I.S. Cho, S.M. Yoo, V.M. Golod, K.D. Savyelyev, C.H. Lim, and J.K. Choi. Calculation of Thermophysical Properties of Iron Casting Alloys. *International Journal of Cast Metals Research*, 22(1–4):43–46, 2009.
- [7] J. Miettinen. Calculation of Solidification-Related Thermophysical Properties for Steels. *Metallurgical and Materials Transactions B*, 28B:281–297, 1997.

- [8] Alloy 4145 / 4145 MOD in bar, Castle Metals, 2015. <http://www.amcastle.com/stock/alloysteel/grade4145unsg41450alloybar.aspx>.
- [9] Alloy 4145 Modified API Spec. 7, Bohler Uddeholm, 2013. http://www.buau.com.au/media/4145H_2013.pdf.
- [10] AISI 4145 Alloy Steel, West Yorkshire Steel, 2015. <http://www.westyorkssteel.com/alloysteel/oilandgas/aisi4145/>.
- [11] A. Kamyabi-Gol. *Quantification of Phase Transformations using Calorimetry as an Alternative to Dilatometry*. PhD thesis, University of Alberta, 2015.
- [12] AISI 4145 Alloy Steel (UNS G41450), AZO Materials, 2015. <http://www.azom.com/article.aspx?ArticleID=6664>.
- [13] SAE-AISI 4145 SCM445, G41450 Cr-Mo Steel, MakeItFrom, 2015. <http://www.makeitfrom.com/material-properties/SAE-AISI-4145-SCM445-G41450-Cr-Mo-Steel/>.
- [14] SAE 4145 Chemical Composition, Mechanical Properties, and Heat Treatment, Jiangyou Longhai Steel, 2015. <http://www.steelgr.com/SteelGrades/CarbonSteel/sae4145.html>.
- [15] K.C. Mills, A.P. Day, and P.N. Queded. Details of METALS Model to Calculate the Thermophysical Properties of Alloys, 2002.
- [16] JAHM Software, I., Material Property Database (MPDB), 2003.
- [17] Y.S. Touloukian, R.W. Poewll, C.Y. Ho, and M.C. Nicolaou. *Therophysical Properties of Matter*, volume 3 of *The TPRC Data Series*. IFI/Plenum, 1973.
- [18] AISI 4140 (Oil-Hardening Cr-Mo Steel). ASM International, 1988.
- [19] AISI 4140 4140H, Engineering Properties of Steel. pages 113–116. ASM International, 1982.
- [20] AISI 4140, efunda, 2015. http://www.efunda.com/materials/alloys/alloy_steels/show_alloy.cfm?ID=aisi_4140&show_prop=elec&Page_Title=Alloy%20Steel%20aisi%204140.
- [21] Sommer. Material Data Sheet 4140, Application Institute for the Optimisation of Material, Process and Heat Treatment Applications, 2012.
- [22] AISI 4140 Steel, annealed at 815°C (1500°F) furnace cooled 11°C (20°F)/hour to 665°C (1230°F), air cooled, 25 mm (1 in.) round, MatWeb, 2015. <http://www.matweb.com/search/datasheet.aspx?matguid=7b75475aa1bc41618788f63c6500d36b&ckck=1>.

- [23] LSS 4140 and 4142HT Alloy Steels, Latrobe Specialty Steel Company, 2006. www.latrobesteel.com.
- [24] Evitherm, Material Property Database (MPDB), 2015. <http://ib.ptb.de/evitherm/evitherm.jsp?restart>.
- [25] 42CrMo4 Quality, Lucefin Group. http://www.lucefin.com/wp-content/files_mf/0242crmo472.pdf.
- [26] W.F. Gale and T.C. Totemeier, editors. *General Physical Properties*. Butterworth Heinemann, eighth edition, 2004.
- [27] J. Meija. Standard Atomic Weights. *Pure and Applied Chemistry*, 2013.
- [28] Y.S. Touloukian and E.H. Buyco. *Therophysical Properties of Matter*, volume 4 of *The TPRC Data Series*. Plenum Publishing Corp., 1971.
- [29] M. Niffenegger and K. Reichlin. The Proper Use of Thermal Expansion Coefficients in Finite Element Calculations. *Nuclear Engineering and Design*, 243:356–359, 2012.
- [30] ASM International. Thermal expansion. In *Thermal Properties of Metals*, chapter 2, pages 9–16. ASM International, 2002.
- [31] F.P. Incropera, D.P. Dewitt, T.L. Bergman, and A.S. Lavine. *Fundamentals of Heat and Mass Transfer*. John Wiley and Sons, Sixth edition, 2007.
- [32] Y.S. Touloukian, R.W. Poewll, C.Y. Ho, and M.C. Nicolaou. *Therophysical Properties of Matter*, volume 10 of *The TPRC Data Series*. IFI/Plenum, 1973.

Appendix B. Uncertainty Analysis

8.1 Introduction

This section outlines in detail the error propagation and uncertainty analysis related to the laser cladding experiments and associated calculations of clad bead geometries presented throughout the thesis. The techniques presented here are based upon mechanical engineering techniques for assessing and presenting experimental data outlined by Beckwith *et al.* in their book titled “Mechanical Measurements” [1]. Their approach outlines that the total uncertainty has a precision component (repeatability in many tests) and bias component (reported measuring device accuracy). These component uncertainties are combined in a root sum square operation to provide a total uncertainty for a given parameter. In mathematical form the total uncertainty ϵ can be described as follows:

$$\epsilon = \pm\sqrt{B^2 + P^2} \quad (8.20)$$

where ϵ is the total uncertainty, B is the bias uncertainty, and P is the precision uncertainty. Parameter subscripts are used to denote the specific parameter error and the units of uncertainty depend on the parameter under consideration. The definition of precision uncertainty is shown in Equation (8.21).

$$P = \pm t_{0,025,\nu} \frac{s_T}{\sqrt{n}} \quad (8.21)$$

where $t_{0,025,\nu}$ is the student's t-statistic for a two-tailed distribution (1), 95% confidence interval ($\alpha = 0.025$), and ν is the degrees of freedom (1). s_T is the standard deviation, and n is the number of samples (1). For calculated values based on a formula, an additional root sum square analysis is required to account for each parameter's contribution to the total uncertainty in the formula. Uncertainty analysis for formula values is accomplished by multiplying each parameter uncertainty by its formula derivative in the root sum square procedure, which is outlined in detail for each equation in the following subsections. The variables of interest in this uncertainty analysis can be subdivided into three groups: process parameters laser power Q , powder feed rate \dot{m}_p , and travel speed U ; measured aspects of the bead geometry and powders; and calculated values related to bead geometry. The procedures and all necessary values for calculating uncertainty for all parameters are summarized here.

The secondary objective of Appendix B is to provide all the as-measured values for variables and parameters, which often were not included in the published works comprising the body of the thesis. The entirety of this analysis rests on the 13 test experiments conducted as described in Chapters (2) and (4). Only single test beads at each parameter were run for this set of experiments, and only single measurements were taken for most relevant parameters, for which there is no possibility for meaningful statistical analysis. The limited data prevents evaluation of the precision uncertainty for a majority of this analysis, which is taken as 0 for all but the preheat temperature analysis. Where possible, a conservative bias uncertainty is used in an attempt to compensate, but this shortcoming in the analysis is acknowledged. Future testing will include both multiple trials and multiple measurements to more effectively evaluate the precision and therefore total uncertainties.

8.2 Uncertainty Analysis for Process Parameters

Included in this section are all the techniques used to quantify uncertainty in the laser power, travel speed, and travel speed ranges in this analysis of laser cladding. These parameters are displayed in several figures to outline trends in measured or calculated parameters with these process inputs. The quantified uncertainty in these variables is also incorporated in several calculations to determine uncertainty in model predictions.

8.2.1 Laser Power Uncertainty

Laser power was measured using a 10 kW Comet 10K-HD power probe described in the procedure sections of Chapters (2) and (4). The device, which is in essence a calibrated copper calorimeter, has a reported uncertainty from the manufacturer of 5% of the measured reading. An additional 0.5% is added by the manufacturer to account for the effects of the water quench between measurements that was necessary to cool down the device between tests in a practical time frame. Measurements were performed after each power level change in the experimental test matrix. Power was not measured for tests with powder feed rate and travel speed changes due to time and logistical constraints. The uncertainty and power levels for these tests is taken to be the same as the centre point of the matrix. The uncertainty in Q is summarized in Table (8.6). The total uncertainty for all experimental tests is shown in Table (8.7).

Table 8.6: Uncertainty analysis for measured laser power

Variable	Unit	Bias Uncertainty B	Precision Uncertainty P Equation (8.21)	Total Uncertainty ϵ Equation (8.20)	Notes for Bias Uncertainty
Q	(kW)	$0.055Q$	0	$0.055Q$	Manufacturer Reported Value

Table 8.7: Uncertainty analysis summary for measured laser power

Bead Number	Q (W)	$\pm\epsilon_Q$ (W)
1	4980	274
2	3090	219
3	3990	219
4	3990	219
5	3990	219
6	3990	219
7	4540	250
8	3530	194
9	3980	219
10	3980	219
11	3980	219
12	3980	219
13	3980	219

8.2.2 Powder Feed Rate Uncertainty

The powder feed rate is measured immediately prior to tests with a change in powder feed rate with a timed two minute powder flow test. The powder feed was turned on, allowed to stabilize for approximately 10 seconds, and then a beaker was placed under the stream. The tared weight of the beaker was measured directly, and a 1 minute average powder feed rate was calculated. The powder feed rate can be simply described as:

$$\dot{m}_p = \frac{m_p}{t} \quad (8.22)$$

where \dot{m}_p is the powder feed rate (g/min), m_p is the mass of the powder measured directly from the tared weight of the test beaker used to capture the powders (g), and t is the time of the powder test (s). The uncertainty in both parameters is summarized in Table (8.8). It is important to note that the timer was set as a countdown from 60 seconds therefore the uncertainty is related to reaction time of the individual holding the

beaker under the powder stream.

Table 8.8: Uncertainty analysis summary for the parameters of Equation (8.22)

Variable	Unit	Bias Uncertainty B	Precision Uncertainty P Equation (8.21)	Total Uncertainty ϵ Equation (8.20)	Notes for Bias Uncertainty
m_p	(g)	$0.0001m_p$	0	$0.0001m_p$	Scale Calibration Certificate
t	(s)	0.22	0	0.22	Reaction Time Analysis [2]

The uncertainty for Equation (8.22) is defined as follows:

$$\epsilon_{\dot{m}_p} = \pm \left\{ \left[\frac{\partial(\dot{m}_p)}{\partial(m_p)} \epsilon_{m_p} \right]^2 + \left[\frac{\partial(\dot{m}_p)}{\partial(t)} \epsilon_t \right]^2 \right\}^{1/2} \quad (8.23)$$

The formula for the partial derivatives of each term are summarized below in Equations (8.24) through (8.25).

$$\frac{\partial(\dot{m}_p)}{\partial(m_p)} = \frac{1}{t} \quad (8.24)$$

$$\frac{\partial(\dot{m}_p)}{\partial(t)} = -\frac{m_p}{t^2} \quad (8.25)$$

The powder feed rate tests having been performed prior to changes in the powder feed rate levels require only data for the 5 tests in the powder feed rate experimental block. All other tests are considered to have the same powder flow rate as the centre point of the experimental matrix. Table (8.9) presents the as-measured test values along with the final expression for the total uncertainty in the powder feed rate for the tests by combining Equations (8.23), (8.24), and (8.25) and the data from Table (8.8). The test time t was 2 min for all beads.

Table 8.9: Uncertainty analysis summary for Equation (8.22)

Bead Number	Target \dot{m}_p (g/min)	m_p (g)	Actual \dot{m}_p (g/min)	$\pm\epsilon_{\dot{m}_p}$ (g/min)
1	50	98.4	49.20	0.090
2	50	98.4	49.20	0.090
3	50	98.4	49.20	0.090
4	50	98.4	49.20	0.090
5	30	57.6	28.80	0.053
6	50	98.4	49.20	0.090
7	50	98.4	49.20	0.090
8	50	98.4	49.20	0.090
9	50	98.4	49.20	0.090
10	60	125.9	62.95	0.116
11	40	84.5	42.45	0.078
12	50	98.4	49.20	0.090
13	70	136.6	68.30	0.125

8.2.3 Travel Speed Uncertainty

Uncertainty in travel speed value are determined from the rotation axis records from the precision CNC equipment. The rotation is recorded in degrees per minute. Combining the rotation value with measured values of the substrate diameter, the travel speed can be calculated as:

$$U = \frac{a\pi D}{360} \quad (8.26)$$

where U is the travel speed (mm/s), a is the rotation speed of the a-axis of the CNC ($^\circ$ /s), and D is the measured substrate diameter (mm). The 360 value represents 360° per revolution in the formula. The measured values of D are summarized below in Table (8.10). The uncertainty in the a and D is summarized in Table (8.11).

Table 8.10: Measured 4145-MOD Steel Substrate Diameter D

Measure 1		Measure 2		Measure 3		Average		Standard Deviation	
(in)	(mm)	(in)	(mm)	(in)	(mm)	(in)	(mm)	(in)	(mm)
6.5098	165.35	6.5095	165.34	6.5094	165.34	6.5096	165.34	0.0002	0.0053

Table 8.11: Uncertainty analysis summary for the parameters of Equation (8.26)

Variable	Unit	Bias Uncertainty B	Precision Uncertainty P Equation (8.21)	Total Uncertainty ϵ Equation (8.20)	Notes for Uncertainty
a	(°/s)	0.0167	0	0.0167	Reported Uncertainty of 1°/min Bias Uncertainty from Resolution of OD Micrometer (0.0001 in)
D	(mm)	0.0025	0.0189	0.0191	

The uncertainty for Equation (8.26) is defined as follows:

$$\epsilon_U = \pm \left\{ \left[\frac{\partial(U)}{\partial(a)} \epsilon_a \right]^2 + \left[\frac{\partial(U)}{\partial(D)} \epsilon_D \right]^2 \right\}^{1/2} \quad (8.27)$$

The formula for the partial derivatives of each term are summarized below in Equations (8.28) through (8.29).

$$\frac{\partial(U)}{\partial(a)} = \frac{\pi D}{360} \quad (8.28)$$

$$\frac{\partial(U)}{\partial(D)} = \frac{a\pi}{360} \quad (8.29)$$

Table (8.12) presents the as-measured test values along with the final expression for the total uncertainty in the travel speed for the tests by combining Equations (8.27), (8.28), and (8.29) and the data from Tables (8.10) and (8.11).

Table 8.12: Uncertainty analysis summary for Equation (8.22)

Bead Number	Target U		a		Actual U		$\pm\epsilon_U$	
	(in/min)	(mm/s)	($^\circ$ /min)	($^\circ$ /s)	(mm/s)	(m/min)	(mm/s)	($\times 10^3$ m/min)
1	60	25.40	1058.3	17.64	25.45	1.527	0.0242	1.4536
2	60	25.40	1058.3	17.64	25.45	1.527	0.0242	1.4536
3	60	25.40	1058.3	17.64	25.45	1.527	0.0242	1.4536
4	45	19.05	793.7	13.23	19.09	1.145	0.0241	1.4489
5	60	25.40	1058.3	17.64	25.45	1.527	0.0242	1.4536
6	75	31.75	1322.9	22.05	31.81	1.909	0.0243	1.4597
7	60	25.40	1058.3	17.64	25.45	1.527	0.0242	1.4536
8	60	25.40	1058.3	17.64	25.45	1.527	0.0242	1.4536
9	30	12.70	529.2	8.82	12.73	0.764	0.0241	1.4456
10	60	25.40	1058.3	17.64	25.45	1.527	0.0242	1.4536
11	60	25.40	1058.3	17.64	25.45	1.527	0.0242	1.4536
12	90	38.10	1587.5	26.46	38.18	2.291	0.0244	1.4670
13	60	25.40	1058.3	17.64	25.45	1.527	0.0242	1.4536

8.3 Uncertainty Analysis for Measured Parameters

Included in this section are all the techniques used to quantify uncertainty in the mass fractions of carbide and metal powders in the powder feed, physical dimensions of the experimental clad beads, and relevant area regions of the cross sections. Many of these parameters were required as inputs to predict the bead geometry or serve as the direct comparison values to the models in this work.

8.3.1 Powder Feed Mass Fraction Uncertainty

The powder feed was a mixture of carbide and metal powders in a carefully controlled ratio. The mass fractions of these components in the feed was required for calculation of the proposed catchment efficiency equations of Chapter (2). Shown here is the procedure for the mass fraction of carbide in the powder feed $f_{m_{cp}}$. The same procedure was followed for the mass fraction of metal powders in the powder feed $f_{m_{mp}}$ using values of

m_m in place of m_c . Only the necessary data to calculate $f_{m_{m_p}}$ has been included here in Tables (8.13) and (8.14). The formula for $f_{m_{c_p}}$ is simply:

$$f_{m_{c_p}} = \frac{m_c}{m_t} \quad (8.30)$$

where $f_{m_{c_p}}$ is the mass fraction of carbide in the powder feed (kg), m_c is the mass of carbide in the powder feed (kg), and m_t is the total mass of the powder feed batch (kg). The uncertainty in these parameters is summarized in Table (8.13) along with m_m .

Table 8.13: Uncertainty analysis summary for the parameters of Equation (8.30)

Variable	Unit	Bias Uncertainty B	Precision Uncertainty P Equation (8.21)	Total Uncertainty ϵ Equation (8.20)	Notes for Bias Uncertainty
m_x	(kg)	$0.0001m_x$	0	$0.0001m_x$	Scale Calibration Certificate

The subscript “x” stands for interchangeable “c” for carbide, “m” for metal powders, and “t” for total.

The uncertainty for Equation (8.30) is defined as follows:

$$\epsilon_{f_{m_{c_p}}} = \pm \left\{ \left[\frac{\partial(f_{m_{c_p}})}{\partial(m_c)} \epsilon_{m_c} \right]^2 + \left[\frac{\partial(f_{m_{c_p}})}{\partial(m_t)} \epsilon_{m_t} \right]^2 \right\}^{1/2} \quad (8.31)$$

The formulae for the partial derivatives of each term are summarized below in Equations (8.24) and (8.25).

$$\frac{\partial(f_{m_{c_p}})}{\partial(m_c)} = \frac{1}{m_t} \quad (8.32)$$

$$\frac{\partial(f_{m_{c_p}})}{\partial(m_t)} = -\frac{m_c}{m_t^2} \quad (8.33)$$

Table (8.14) presents the as-measured test values, calculated final value, and the final expression for the total uncertainty in the mass fraction of carbide in the bead. The same powder batch was used for all test, and therefore only single values for the powder masses are required to represent all tests. The final values for total uncertainty combine Equations (8.31), (8.32), and (8.33) and the data from Table (8.13). Values for the parallel $f_{m_{mp}}$ analysis are also included.

Table 8.14: Uncertainty analysis summary for Equation (8.30)

m_c (kg)	m_m (kg)	m_t (kg)	$f_{m_{cp}}$ (%)	$\pm\epsilon_{f_{m_{cp}}}$ (%)	$f_{m_{mp}}$ (%)	$\pm\epsilon_{f_{m_{mp}}}$ (%)
52.578	31.412	83.990	62.60	0.0089	37.40	0.0052

8.3.2 Cross Section Area Measurement Uncertainties

The area of the cross section of the bead can be subdivided into a reinforcement area A_{b_R} , a dilution area A_{b_D} , and the total combined area A_{b_T} . These different areas are discussed in detail in Chapter (2), and schematically shown in Figure (2.1). These areas were measured directly in PhotoshopTM from panorama cross section images of the deposited beads, and a line connecting the clad toes was considered to subdivide the above and below surface areas. The procedure for calculating all areas is nearly identical, and so only A_{b_T} is shown here in detail. Values for calculating A_{b_R} are also included in the tables in this section for a parallel analysis (A_{b_D} did not appear in any required calculation and therefore was not included). The formula for A_{b_T} in terms of measured parameters is shown in Equation (8.34).

$$A_{b_T} = A_{b_{Tm}} \left(\frac{l_{sc}}{l_{sm}} \right)^2 \quad (8.34)$$

where A_{b_T} is the total cross sectional area of the deposited bead (mm^2), $A_{b_{T_m}}$ is the measured total cross sectional area of the deposited bead (pixels^2), l_{sc} is the calibrated length of the scale (μm), and l_{sm} is the measured length of the scale bar (pixels). The uncertainty in each parameter (including $A_{b_{R_m}}$) is shown in Table (8.15). A larger value for the uncertainty of l_{sm} is used to compensate for the larger overall effect of a few pixels on a measurements of hundreds of pixels compared to the hundreds of thousands of pixels of the area measurements.

Table 8.15: Uncertainty analysis summary for the parameters of Equation (8.34)

Variable	Unit	Bias Uncertainty B	Precision Uncertainty P Equation (8.21)	Total Uncertainty ϵ Equation (8.20)	Notes for Bias Uncertainty
$A_{b_{T_m}}$	(pixels^2)	$0.01A_{b_{T_m}}$	0	$0.01A_{b_{T_m}}$	Conservative Estimate
$A_{b_{R_m}}$	(pixels^2)	$0.01A_{b_{R_m}}$	0	$0.01A_{b_{R_m}}$	Conservative Estimate
l_{sc}	(μm)	10	0	10	Scale Resolution
l_{sm}	(pixels)	$0.05l_{sm}$	0	$0.05l_{sm}$	Conservative Estimate

The uncertainty for Equation (8.34) is defined as follows:

$$\epsilon_{A_{b_T}} = \pm \left\{ \left[\frac{\partial(A_{b_T})}{\partial(A_{b_{T_m}})} \epsilon_{A_{b_{T_m}}} \right]^2 + \left[\frac{\partial(A_{b_T})}{\partial(l_{sc})} \epsilon_{l_{sc}} \right]^2 + \left[\frac{\partial(A_{b_T})}{\partial(l_{sm})} \epsilon_{l_{sm}} \right]^2 \right\}^{1/2} \quad (8.35)$$

The formulae for the partial derivatives of each term are summarized below in Equations (8.36) through (8.38).

$$\frac{\partial(A_{b_T})}{\partial(A_{b_{T_m}})} = \left(\frac{l_{sc}}{l_{sm}}\right)^2 \quad (8.36)$$

$$\frac{\partial(A_{b_T})}{\partial(l_{sc})} = 2A_{b_{T_m}} \frac{l_{sc}}{l_{sm}^2} \quad (8.37)$$

$$\frac{\partial(A_{b_T})}{\partial(l_{sm})} = -2A_{b_{T_m}} \frac{l_{sc}^2}{l_{sm}^3} \quad (8.38)$$

Table (8.16) presents the as-measured test values along with the final expression for the total uncertainty in the total cross sectional area in the bead. Values of A_{b_T} , $A_{b_{T_m}}$, and l_{sm} for all 13 beads are presented along with values for $A_{b_{R_m}}$ and A_{b_R} . The value of l_{sc} was 500 μm for all tests. The final values for total uncertainty combine Equations (8.35), Equations (8.36) through (8.38) and the data from Table (8.15).

Table 8.16: Uncertainty analysis summary for Equation (8.34)

Bead Number	$A_{b_{T_m}}$ (pixels ²)	l_{sm} (pixels)	A_{b_T} (mm ²)	$\pm\epsilon_{A_{b_T}}$ (mm ²)	$A_{b_{R_m}}$ (pixels ²)	A_{b_R} (mm ²)	$\pm\epsilon_{A_{b_R}}$ (mm ²)
1	970284	358	1.893	0.205	845090	1.648	0.178
2	370339	358	0.722	0.078	350856	0.684	0.074
3	778094	358	1.518	0.164	716668	1.398	0.151
4	1164058	358	2.271	0.246	1079599	2.106	0.228
5	608713	358	1.187	0.128	435681	0.850	0.092
6	524547	358	1.023	0.111	489216	0.954	0.103
7	746200	358	1.456	0.157	707236	1.380	0.149
8	608568	358	1.187	0.128	575897	1.123	0.122
9	1838008	358	3.585	0.388	1753665	3.421	0.370
10	973731	358	1.899	0.205	916895	1.789	0.193
11	701946	358	1.369	0.148	596804	1.164	0.126
12	343101	358	0.669	0.072	331894	0.647	0.070
13	259944	182	1.962	0.212	248604	1.876	0.203

The volume fraction of carbide, $f_{v_{cb}}$, in the deposited bead is another important cross sectional measurement. This parameter is necessary to calculate catchment efficiencies (Chapter (2)), bead height (Chapter (4)), and effective material properties of the composite used for the fluid flow analysis in Chapter (5). The volume fraction of carbide formula is shown below:

$$f_{v_{cb}} = \frac{A_{bc}}{A_{b_{T_m}}} \quad (8.39)$$

where $f_{v_{cb}}$ is the carbide volume fraction in the deposited bead (1), and A_{bc} is the carbide area in the deposited bead (pixels²). The area fraction is representative of the volume fraction assuming uniform distribution of the carbide phase throughout the bead. Described in detail in Chapters (2) and (4), the carbide area is measured using a python script developed at the Canadian Centre fo Welding and Joining that distinguishes the phase difference based on contrast pixel by pixel. The measurement is output in pixels directly. The uncertainty in A_{bc} and $A_{b_{T_m}}$ is shown in Table (8.17).

Table 8.17: Uncertainty analysis summary for the parameters of Equation (8.39)

Variable	Unit	Bias Uncertainty B	Precision Uncertainty P Equation (8.21)	Total Uncertainty ϵ Equation (8.20)	Notes for Bias Uncertainty
A_{bc}	(pixels ²)	$0.05A_{bc}$	0	$0.05A_{bc}$	Conservative Estimate
$A_{b_{T_m}}$	(pixels ²)	$0.01A_{b_{T_m}}$	0	$0.01A_{b_{T_m}}$	Conservative Estimate

The uncertainty for Equation (8.39) is defined as follows:

$$\epsilon_{f_{v_{cb}}} = \pm \left\{ \left[\frac{\partial(f_{v_{cb}})}{\partial(A_{bc})} \epsilon_{A_{bc}} \right]^2 + \left[\frac{\partial(f_{v_{cb}})}{\partial(A_{b_T})} \epsilon_{A_{b_T}} \right]^2 \right\}^{1/2} \quad (8.40)$$

The formulae for the partial derivatives of each term are summarized below in Equa-

tions (8.41) and (8.42).

$$\frac{\partial(f_{v_{cb}})}{\partial(A_{bc})} = \frac{1}{A_{b_{T_m}}} \quad (8.41)$$

$$\frac{\partial(f_{v_{cb}})}{\partial(A_{b_{T_m}})} = -\frac{A_{bc}}{A_{b_{T_m}}^2} \quad (8.42)$$

Table (8.18) presents the as-measured test values along with the final value for the total uncertainty in $f_{v_{cb}}$. The final values for total uncertainty combine Equations (8.40), (8.41), and (8.42) and Table (8.17).

Table 8.18: Uncertainty analysis summary for Equation (8.39)

Bead Number	A_{bc} (pixels ²)	$A_{b_{T_m}}$ (pixels ²)	$f_{v_{cb}}$ (1)	$\pm\epsilon_{f_{v_{cb}}}$ (1)
1	326391.0	970284	0.3364	0.0171
2	111301.5	370339	0.3005	0.0153
3	221624.0	778094	0.2848	0.0145
4	341075.5	1164058	0.2930	0.0149
5	123413.0	608713	0.2027	0.0103
6	180570.0	524547	0.3442	0.0176
7	255873.0	746200	0.3429	0.0175
8	231491.5	608568	0.3804	0.0194
9	637902.0	1838008	0.3471	0.0177
10	354339.5	973731	0.3639	0.0186
11	254510.5	701946	0.3626	0.0185
12	128602.5	343101	0.3748	0.0191
13	100235.5	259944	0.3856	0.0197

8.3.3 Cross Section Measured Width and Height Uncertainty

Cross section measurements for bead width were calculated using the following equation:

$$2y_{m_{o,b}} = 2y_{meas} \frac{l_{sc}}{l_{sm}} \quad (8.43)$$

where y_{meas} is the measured bead width from PhotoshopTM (pixels). The convention $2y_{meas}$ is used to maintain consistency with the definition of width defined from the bead centreline to the clad toe such as for $y_{m_{o,b}}$. In reality, a single measurement is made that constitutes the $2y_{meas}$ value. As a single length dimension measurement h_m , the maximum height of the clad bead, can be calculated using Equation (8.43) substituting h_m for $2y_{m_{o,b}}$ and h_{meas} for $2y_{meas}$. Components of the uncertainty for $2y_{meas}$ and h_{meas} are summarized in Table (8.19).

Table 8.19: Uncertainty analysis summary for the parameters of Equation (8.43)

Variable	Unit	Bias Uncertainty B	Precision Uncertainty P Equation (8.21)	Total Uncertainty ϵ Equation (8.20)	Notes for Bias Uncertainty
$2y_{meas}$	(pixels)	$0.05(2y_{meas})$	0	$0.05(2y_{meas})$	Conservative Estimate
l_{sc}	(μm)	10	0	10	Scale Resolution
l_{sm}	(pixels)	$0.05l_{sm}$	0	$0.05l_{sm}$	Conservative Estimate
h_{meas}	(pixels)	$0.05h_{meas}$	0	$0.05h_{meas}$	Conservative Estimate

The uncertainty for Equation (8.43) is defined as follows:

$$\epsilon_{2y_{m_{o,b}}} = \pm \left\{ \left[\frac{\partial(2y_{m_{o,b}})}{\partial(2y_{meas})} \epsilon_{2y_{meas}} \right]^2 + \left[\frac{\partial(2y_{m_{o,b}})}{\partial(l_{sc})} \epsilon_{l_{sc}} \right]^2 + \left[\frac{\partial(2y_{m_{o,b}})}{\partial(l_{sm})} \epsilon_{l_{sm}} \right]^2 \right\}^{1/2} \quad (8.44)$$

The formula for the partial derivatives of each term are summarized below in Equ-

tions (8.45) through (8.47).

$$\frac{\partial(2y_{m_{o,b}})}{\partial(2y_{meas})} = \frac{l_{sc}}{l_{sm}} \quad (8.45)$$

$$\frac{\partial(2y_{m_{o,b}})}{\partial(l_{sc})} = \frac{2y_{meas}}{l_{sm}} \quad (8.46)$$

$$\frac{\partial(2y_{m_{o,b}})}{\partial(l_{sm})} = -\frac{2y_{meas}l_{sc}}{l_{sm}^2} \quad (8.47)$$

Table (8.20) summarizes the measured and converted values for $2y_{meas}$, and the total for uncertainty in bead width for all 13 experimental clad beads. The value for l_{sc} was 500 μm for all tests. The last column in Table (8.20) represents the total uncertainty in measured cross section width (y-axis error bars) in Figures (3.6) through (3.9) in Appendix 3.1. Data for h_{meas} , h_m , and ϵ_{h_m} is also presented for all beads. The uncertainty in h_m appears in Figure (4.16) in Chapter (4).

Table 8.20: Uncertainty analysis summary for Equation (8.43)

Bead Number	$2y_{meas}$ (pixels)	l_{sm} (pixels)	$2y_{m_{o,b}}$ (mm)	$\pm\epsilon_{2y_{m_{o,b}}}$ (mm)	h_{meas} (pixels)	h_m (mm)	$\pm\epsilon_{h_m}$ (mm)
1	2924	358	4.084	0.300	425	0.594	0.044
2	1456	358	2.034	0.149	353	0.493	0.036
3	2687	358	3.753	0.276	353	0.493	0.036
4	3031	358	4.233	0.311	512	0.710	0.052
5	3038	358	4.243	0.312	224.5	0.314	0.023
6	2427	358	3.390	0.249	299.5	0.418	0.031
7	2498	358	3.489	0.256	392	0.548	0.040
8	2379	358	3.323	0.244	350.5	0.490	0.036
9	3186	358	4.450	0.327	802	1.120	0.082
10	2688	358	3.754	0.276	497	0.694	0.051
11	2735	358	3.820	0.281	325	0.454	0.033
12	1751	358	2.446	0.180	282.5	0.395	0.029
13	1327	182	3.646	0.268	278	0.764	0.056

8.3.4 Stereo Photograph Measurement Uncertainty

Stereo photograph measurements for bead width were calculated using the following equation:

$$2y_{m_{o,b}} = \frac{A_{b_p} l_{sc}}{l_b l_{sm}} \quad (8.48)$$

where A_{b_p} is the measured projected bead area of the bead surface in the stereo photograph (pixels²). Curvature effects on the area measurement (projected area in the image) are considered negligible for the small relative length of bead measured on the 165 mm diameter cylindrical sample. l_b is the visible length of the bead measured centre to centre along the longitudinal axis of the bead (same direction as the substrate travel direction) (pixels). Measurements for both A_{b_p} and l_b are made in PhotoshopTM. The definitions of l_{sc} and l_{sm} remain the same, but the stereo photo values are different because the scale length and calibration were different for the macro scale photos compared to

the micrograph cross sections. The uncertainty in all four parameters in Equation (8.48) is summarized in Table (8.21).

Table 8.21: Uncertainty analysis summary for the parameters of Equation (8.48)

Variable	Unit	Bias Uncertainty B	Precision Uncertainty P Equation (8.21)	Total Uncertainty ϵ Equation (8.20)	Notes for Bias Uncertainty
A_{b_p}	(pixels ²)	$0.05A_{b_p}$	0	$0.05A_{b_p}$	Conservative Estimate
l_b	(pixels)	$0.01l_b$	0	$0.01l_b$	Conservative Estimate
l_{sc}	(mm)	1	0	1	Ruler Scale Resolution
l_{sm}	(pixels)	$0.01l_{sm}$	0	$0.01l_{sm}$	Conservative Estimate

The uncertainty for Equation (8.48) is defined as follows:

$$\epsilon_{2y_{m_o,b}} = \pm \left\{ \left[\frac{\partial(2y_{m_o,b})}{\partial(A_{b_p})} \epsilon_{A_{b_p}} \right]^2 + \left[\frac{\partial(2y_{m_o,b})}{\partial(l_b)} \epsilon_{l_b} \right]^2 + \left[\frac{\partial(2y_{m_o,b})}{\partial(l_{sc})} \epsilon_{l_{sc}} \right]^2 + \left[\frac{\partial(2y_{m_o,b})}{\partial(l_{sm})} \epsilon_{l_{sm}} \right]^2 \right\}^{1/2} \quad (8.49)$$

The formula for the partial derivatives of each term are summarized below in Equa-

tions (8.50) through (8.53).

$$\frac{\partial(2y_{m_{o,b}})}{\partial(2y_{meas})} = \frac{l_{sc}}{l_{sm}} \quad (8.50)$$

$$\frac{\partial(2y_{m_{o,b}})}{\partial(l_b)} = \frac{-A_{b_p}l_{sc}}{l_b^2l_{sm}} \quad (8.51)$$

$$\frac{\partial(2y_{m_{o,b}})}{\partial(l_{sc})} = \frac{A_{b_p}}{l_b l_{sm}} \quad (8.52)$$

$$\frac{\partial(2y_{m_{o,b}})}{\partial(l_{sm})} = \frac{-A_{b_p}l_{sc}}{l_b l_{sm}^2} \quad (8.53)$$

Table (8.22) summarizes the measured values for A_{b_p} , l_b , and the total for uncertainty calculated for all 13 experimental clad beads. The last column in Table (8.22) represents the total uncertainty in measured bead width (y-axis error bars) for stereo photo measurements in Figures (3.6) through (3.8) and Figure (3.10) in Appendix 3.1. Stereo width measurements and their uncertainty also appear in Figure (4.14) in Chapter (4).

Table 8.22: Uncertainty analysis summary for Equation (8.49)

Bead Number	A_{b_p} (pixels ²)	l_b (pixels)	l_{sc} (mm)	l_{sm} (pixels)	$\pm\epsilon_{2y_{m_{o,b}}}$ (mm)
1	387881	1160.53	18	1153.54	0.295
2	190273	1136.25	17	1472.98	0.152
3	348487	1145.28	17	1477.06	0.275
4	389408	1138.50	17	1484.54	0.307
5	385117	1131.62	17	1514.56	0.300
6	300588	1129.51	17	1493.83	0.238
7	343172	1161.00	17	1477.08	0.267
8	342023	1181.50	10	868.36	0.376
9	418800	1154.22	18	1571.52	0.316
10	349981	1148.00	17	1501.03	0.271
11	374002	1163.06	17	1496.56	0.287
12	253001	1174.69	18	1577.51	0.187
13	309441	1157.32	17	1483.19	0.241

8.4 Uncertainty Analysis for Material Properties

Uncertainty in the relevant material property values to this work has been determined for the 4145-MOD steel substrate. Material properties are taken from literature sources and ThermoCalcTM modelled values as an average across the temperature range of interest related to the HAZ or solidus temperature of the steel. The uncertainty in the material property values here is typically quantified as half the range of the property value across the appropriate temperature range.

The steel properties relevant to this work are thermal conductivity k_{eff} , heat capacity $c_{p_{eff}}$, density ρ_{eff} , and thermal diffusivity α_{eff} . Table (8.23) summarizes the temperature range of interest, data source, and uncertainty value for the aforementioned property values with the exception of thermal diffusivity, which is calculated using Equation (7.12). Heat capacity is also technically calculated from an enthalpy output as a function of temperature from ThermoCalcTM, but it is considered appropriate to quantify uncertainty

from the output calculated figure. This difference in procedure is due to the inability to quantify uncertainty in output enthalpy and temperature values from the software. For the maximum value determination in the range for $c_{p_{eff}}$, the heat capacity values located in the ferrite to austenite transformation were not included. Duplicate uncertainty values for the HAZ and melting isotherm values occur due to the maximum or minimum value of the range existing within the HAZ temperature range.

Table 8.23: Uncertainty analysis summary for 4145-MOD thermophysical properties

Material Property	Unit	Temperature Range (K)	Figure Number	Source Reference	Bias Uncert. B	Precision Uncert. P	Total Uncert. ϵ
$k_{eff,HAZ}$	(W/mK)	533-981	(7.1)	Mills [3]	5.33	0	5.33
$k_{eff,melt}$	(W/mK)	533-1692	(7.1)	Mills [3]	5.33	0	5.33
$c_{p_{eff},HAZ}$	(J/kgK)	533-981	(7.6)	ThermoCalc TM	201.1	0	201.1
$c_{p_{eff},melt}$	(J/kgK)	533-1692	(7.6)	ThermoCalc TM	201.1	0	201.1
$\rho_{eff,HAZ}$	(kg/m ³)	533-981	(7.9)	ThermoCalc TM	76.0	0	76.0
$\rho_{eff,melt}$	(kg/m ³)	533-1692	(7.9)	ThermoCalc TM	200.3	0	200.3

$$\alpha_{eff} = \frac{k_{eff}}{\rho_{eff}c_{p_{eff}}} \quad (7.12)$$

where α_{eff} is the effective thermal diffusivity (m²/s), k_{eff} is the effective thermal conductivity (W/mK), $c_{p_{eff}}$ is the effective heat capacity (J/kgK), and ρ_{eff} is the effective density (kg/m³). The “eff” notation is reserved for the 4145-MOD substrate for this analysis and can represent the HAZ or melting isotherm depending on the presence of the “HAZ” or “melt” subscripts. The uncertainty for Equation (7.12) is defined as follows:

$$\epsilon_{\alpha_{eff}} = \pm \left\{ \left[\frac{\partial(\alpha_{eff})}{\partial(k_{eff})} \epsilon_{k_{eff}} \right]^2 + \left[\frac{\partial(\alpha_{eff})}{\partial(c_{p_{eff}})} \epsilon_{c_{p_{eff}}} \right]^2 + \left[\frac{\partial(\alpha_{eff})}{\partial(\rho_{eff})} \epsilon_{\rho_{eff}} \right]^2 \right\}^{1/2} \quad (8.54)$$

The formula for the partial derivatives of each term are summarized below in Equations (8.55) through (8.57).

$$\frac{\partial(\alpha_{eff})}{\partial(k_{eff})} = \frac{1}{c_{p_{eff}} \rho_{eff}} \quad (8.55)$$

$$\frac{\partial(\alpha_{eff})}{\partial(c_{p_{eff}})} = \frac{k_{eff}}{c_{p_{eff}}^2 \rho_{eff}} \quad (8.56)$$

$$\frac{\partial(\alpha_{eff})}{\partial(\rho_{eff})} = \frac{k_{eff}}{c_{p_{eff}} \rho_{eff}^2} \quad (8.57)$$

$$(8.58)$$

Table (8.24) summarizes the effective values for k , c_p , ρ , and α for both the HAZ and melting temperature ranges as well as the total for uncertainties for thermal diffusivity $\alpha_{eff,HAZ}$ and $\alpha_{eff,melt}$.

Table 8.24: Uncertainty analysis summary for Equation (8.54)

Temperature Range (K)	k_{eff} (W/mK)	$c_{p_{eff}}$ (J/kgK)	ρ_{eff} (kg/m ³)	α_{eff} ($\times 10^6$ m ² /s)	$\epsilon_{\alpha_{eff}}$ ($\times 10^6$ m ² /s)
HAZ: 533-981	32.52	737.61	7689.4	5.734	1.825
Melt: 533-1692	30.15	743.97	7589.5	5.339	1.731

8.5 Uncertainty Analysis for Calculated Values

Summarized in this section are the formulae and values used to quantify uncertainty for all calculated model quantities in this thesis. The four sections presented here are: uncertainty in the Rosenthal width calculated in Appendix 3.1, the uncertainty in the

calculated carbide, metal powder, and overall catchment efficiency formulae presented in Chapter (2), the calculated bead height formula in Chapter (4), and finally the calculated reinforcement bead area predictions in Appendix 4.1. Uncertainty in optimized values taken from MATLABTM were considered to be 0; therefore, uncertainty for the calculated width for the Gaussian heat source and the predicted catchment efficiency in Chapter (4) were not quantified. Effective power uncertainty was also not quantified as it appears only in the width optimization.

8.5.1 Uncertainty Analysis for Calculated Bead Width

The calculated bead width formula in this analysis is for the advective dominant case ($T^* \ll 1$), whose formula is shown Equation (3.38) or with the substitutions for $\widehat{y_{m_0}}$ and $f_{y_{m_0}}$:

$$\widehat{2y_{m_0}}^+ = \frac{4\alpha}{U} \sqrt{\frac{2}{eT^*}} [1 + (C_1 T^*)^{C_3}]^{\frac{C_2}{C_3}} \quad (8.59)$$

where $\widehat{2y_{m_0}}^+$ is the total predicted width of the clad bead (mm), α is the thermal diffusivity (m^2/s), U is the travel speed (mm/s), T^* is the dimensionless temperature defined in Equation (3.11), and C_1 , C_2 , and C_3 are the correction factor constants for $f_{y_{m_0}}$ defined in Table (3.1). The dimensionless form of Equation (8.59) in terms of T^* has been kept to minimize the size of the derivative terms in this analysis through use of the chain rule. In this uncertainty analysis for calculated bead width, the following assumptions were made:

- No error in the literature value for thermal efficiency of a CO₂ laser on a steel substrate η .
- No error in the isotherm temperature values T , taken in this analysis as the equi-

librium solidus temperature of the 4145-MOD substrate.

With these assumptions, the parameters that contribute to the uncertainty in the calculated bead width were α_{eff} , k_{eff} , Q , U , T_0 . The uncertainty in Q has been previously quantified as 5.5% for all laser power tests. The measurements for preheat at the 0° , 90° , 180° , and 270° positions on the cylindrical steel sample (0° being directly beneath the beam) were completed using an HH11B Omega touch thermometer. These measurements are summarized in Table (8.25).

Table 8.25: Preheat measurement summary for the experimental cladding of Ni-WC on 4145-MOD steel

Bead Number	Temperature				Average Temperature		Standard Deviation	
	(F)				(F)	(K)	(F)	(K)
Bead 1	499	487	490	504	495	530	7.87	4.37
Bead 2	488	491	492	504	494	530	7.04	3.91
Bead 3	506	496	509	499	503	535	6.03	3.35
Bead 4	507	487	485	504	496	531	11.35	6.31
Bead 5	507	520	506	527	515	541	10.23	5.68
Bead 6	517	502	506	506	508	537	6.45	3.58
Bead 7	499	495	528	499	505	536	15.28	8.49
Bead 8	517	505	501	508	508	537	6.80	3.78
Bead 9	506	511	501	503	505	536	4.35	2.42
Bead 10	504	515	500	510	507	537	6.60	3.67
Bead 11	504	507	511	510	508	538	3.16	1.76
Bead 12	516	505	518	508	512	540	6.24	3.47
Bead 13	515	500	504	506	506	537	6.34	3.52

The reported uncertainty by the Omega for the touch thermocouple is shown in Equation (8.60). 8.60) is for Fahrenheit measurements.

$$B_T = 0.001T + 2 \quad (8.60)$$

where B_T is the bias uncertainty in temperature measurements (F) at temperature T, and T is any temperature reading between -76 F to 1999 F. The precision error in these measurements is calculated considering $n = 4, 3$ degrees of freedom, and a 95% confidence interval. The bias, precision, and total uncertainty are summarized below in Table (8.26).

Table 8.26: Uncertainty analysis summary for the parameters of Equation (8.59)

Bead Number	Bias Uncertainty B_{T_0} Equation (8.60) (K)	Precision Uncertainty P_{T_0} Equation (8.21) (K)	Total Uncertainty ϵ_{T_0} Equation (8.20) (K)
Bead 1	1.39	2.15	2.56
Bead 2	1.39	1.92	2.37
Bead 3	1.39	1.64	2.15
Bead 4	1.39	3.10	3.39
Bead 5	1.40	2.79	3.12
Bead 6	1.39	1.76	2.24
Bead 7	1.39	4.17	4.39
Bead 8	1.39	1.85	2.32
Bead 9	1.39	1.19	1.83
Bead 10	1.39	1.80	2.28
Bead 11	1.39	0.86	1.64
Bead 12	1.40	1.70	2.20
Bead 13	1.39	1.73	2.22

The uncertainty for Equation (8.59) is defined below in Equation (8.61).

$$\epsilon_{\widehat{2y_{m_0}^+}} = \pm \left\{ \left[\frac{\partial(\widehat{2y_{m_0}^+})}{\partial(Q)} \epsilon_Q \right]^2 + \left[\frac{\partial(\widehat{2y_{m_0}^+})}{\partial(T_0)} \epsilon_{T_0} \right]^2 + \left[\frac{\partial(\widehat{2y_{m_0}^+})}{\partial(U)} \epsilon_U \right]^2 + \left[\frac{\partial(\widehat{2y_{m_0}^+})}{\partial(\alpha_{eff})} \epsilon_{\alpha_{eff}} \right]^2 + \left[\frac{\partial(\widehat{2y_{m_0}^+})}{\partial(k_{eff})} \epsilon_{k_{eff}} \right]^2 \right\}^{1/2} \quad (8.61)$$

The formula for the partial derivatives of each term are summarized below in Equa-

tions (8.62) through (8.66).

$$\frac{\partial(\widehat{2y_{m_0}}^+)}{\partial(Q)} = \frac{4\alpha}{UQ} \left(\frac{2T^*}{e}\right)^{1/2} \left\{ [1 + (C_1T^*)^{C_3}]^{C_2/C_3} - C_2 [1 + (C_1T^*)^{C_3}]^{\frac{C_2}{C_3}-1} (C_1T^*)^{C_3-1} \right\} \quad (8.62)$$

$$\frac{\partial(\widehat{2y_{m_0}}^+)}{\partial(T_0)} = \frac{4\alpha_{eff}}{U(T-T_0)} \left(\frac{2T^*}{e}\right)^{1/2} \left\{ [1 + (C_1T^*)^{C_3}]^{C_2/C_3} - C_2 [1 + (C_1T^*)^{C_3}]^{\frac{C_2}{C_3}-1} (C_1T^*)^{C_3-1} \right\} \quad (8.63)$$

$$\frac{\partial(\widehat{2y_{m_0}}^+)}{\partial(U)} = \frac{4\alpha_{eff}}{U^2} \left(\frac{2T^*}{e}\right)^{1/2} \left\{ [1 + (C_1T^*)^{C_3}]^{C_2/C_3} - C_2 [1 + (C_1T^*)^{C_3}]^{\frac{C_2}{C_3}-1} (C_1T^*)^{C_3-1} \right\} \quad (8.64)$$

$$\frac{\partial(\widehat{2y_{m_0}}^+)}{\partial(T_0)} = \frac{-4}{U} \left(\frac{2T^*}{e}\right)^{1/2} \left\{ [1 + (C_1T^*)^{C_3}]^{C_2/C_3} - C_2 [1 + (C_1T^*)^{C_3}]^{\frac{C_2}{C_3}-1} (C_1T^*)^{C_3-1} \right\} \quad (8.65)$$

$$\frac{\partial(\widehat{2y_{m_0}}^+)}{\partial(T_0)} = \frac{-8\alpha_{eff}}{Uk_{eff}} \left(\frac{2T^*}{e}\right)^{1/2} \left\{ [1 + (C_1T^*)^{C_3}]^{C_2/C_3} - C_2 [1 + (C_1T^*)^{C_3}]^{\frac{C_2}{C_3}-1} (C_1T^*)^{C_3-1} \right\} \quad (8.66)$$

The values of α_{eff} , k_{eff} and T for Equations (8.62) through (8.66) were constant for all test beads, 5.399×10^{-6} m/s, 30.15 W/mK and 1692 K respectively. The values of C_1 , C_2 , and C_3 were $2/e$, -0.5 , and 0.865 respectively. Table (8.27) summarizes the measured values for Q , U , T^* , and finally the total uncertainty in the calculated width $\epsilon_{\widehat{2y_{m_0}}^+}$ for all 13 experimental clad beads. The calculation of $\epsilon_{\widehat{2y_{m_0}}^+}$ from Equation (8.61) requires ϵ_Q

from Table (8.7), ϵ_U from Table (8.12), $\epsilon_{k_{eff}}$ from Table (8.23), $\epsilon_{\alpha_{eff}}$ from Table (8.24), and ϵ_{T_0} from Table (8.26). The last column represents the x-axis error bars in Figures (3.9) and (3.10) in Appendix 3.1.

Table 8.27: Uncertainty analysis summary for Equation (8.59)

Bead Number	Q (W)	U (mm/s)	T^* (1)	$\widehat{2y_{m_0}^+}$ (mm)	$\pm \epsilon_{\widehat{2y_{m_0}^+}}$ (mm)
1	4980	25.40	0.0619	2.776	0.0164
2	3090	25.40	0.0999	2.776	0.0197
3	3990	25.40	0.0770	2.464	0.0180
4	3990	19.05	0.1030	2.798	0.0269
5	3990	25.40	0.0765	2.481	0.0178
6	3990	31.75	0.0615	2.231	0.0131
7	4540	25.40	0.0676	2.649	0.0170
8	3530	25.40	0.0868	2.311	0.0188
9	3980	12.70	0.1542	3.333	0.0471
10	3980	25.40	0.0770	2.462	0.0180
11	3980	25.40	0.0770	2.469	0.0179
12	3980	38.10	0.0512	2.050	0.0101
13	3980	25.40	0.0771	2.460	0.0180

8.5.2 Catchment Efficiency Calculation Uncertainty

Outlined in this section are the steps for determining carbide, metal powder, and overall catchment efficiency uncertainty presented in Chapter (2). The calculated values presented here are in essence “measured” values from the experimental cross sections that are calculated from direct measurements of the beads. Typically “calculated” quantities in this work refer to predicted values from a model and so the distinction is made here for catchment efficiency.

Carbide Catchment Efficiency Uncertainty

Carbide catchment can be inferred from measured parameters using the following equation:

$$\eta_{m_c} = \frac{U A_{b_T} \rho_c}{\dot{m}_p} \frac{f_{v_{c_b}}}{f_{m_{c_p}}} \quad (2.4)$$

where η_{m_c} is the carbide catchment efficiency (1) and ρ_c is the density of the carbides (kg/m^3). Uncertainty in ρ_c is shown in Table (8.28). Uncertainty in U has been summarized previously for all tests (Table (8.12)). The value of $\epsilon_{A_{b_T}}$ for all tests is shown in Table (8.16), $\epsilon_{\dot{m}_p}$ for the experiments is included in Table (8.9), $\epsilon_{f_{v_{c_b}}}$ is summarized in Table (8.18), and $\epsilon_{f_{m_{c_p}}}$ is shown in Table (8.14).

Table 8.28: Uncertainty analysis summary for the parameters of Equation (2.4)

Variable	Unit	Bias Uncertainty B	Precision Uncertainty P Equation (8.21)	Total Uncertainty ϵ Equation (8.20)	Notes for Bias Uncertainty
ρ_c	(kg/m^3)	82.5	0	82.5	Half the range of Figure (2.9)

The uncertainty for Equation (2.4) is defined as follows:

$$\epsilon_{\eta_{m_c}} = \pm \left\{ \left[\frac{\partial(\eta_{m_c})}{\partial(U)} \epsilon_U \right]^2 + \left[\frac{\partial(\eta_{m_c})}{\partial(A_{b_T})} \epsilon_{A_{b_T}} \right]^2 + \left[\frac{\partial(\eta_{m_c})}{\partial(\rho_c)} \epsilon_{\rho_c} \right]^2 + \left[\frac{\partial(\eta_{m_c})}{\partial(\dot{m}_p)} \epsilon_{\dot{m}_p} \right]^2 + \left[\frac{\partial(\eta_{m_c})}{\partial(f_{v_{c_b}})} \epsilon_{f_{v_{c_b}}} \right]^2 + \left[\frac{\partial(\eta_{m_c})}{\partial(f_{m_{c_p}})} \epsilon_{f_{m_{c_p}}} \right]^2 \right\}^{1/2} \quad (8.67)$$

The formulae for the partial derivatives of each term of Equation (8.67) are summa-

rized below in Equations (8.68) through (8.73).

$$\frac{\partial(\eta_{m_c})}{\partial(U)} = \frac{A_{b_T} \rho_c f_{v_{c_b}}}{\dot{m}_p f_{m_{c_p}}} \quad (8.68)$$

$$\frac{\partial(\eta_{m_c})}{\partial(A_{b_T})} = \frac{U \rho_c f_{v_{c_b}}}{\dot{m}_p f_{m_{c_p}}} \quad (8.69)$$

$$\frac{\partial(\eta_{m_c})}{\partial(\rho_c)} = \frac{U A_{b_T} f_{v_{c_b}}}{\dot{m}_p f_{m_{c_p}}} \quad (8.70)$$

$$\frac{\partial(\eta_{m_c})}{\partial(\dot{m}_p)} = -\frac{U A_{b_T} \rho_c f_{v_{c_b}}}{\dot{m}_p^2 f_{m_{c_p}}} \quad (8.71)$$

$$\frac{\partial(\eta_{m_c})}{\partial(f_{v_{c_b}})} = \frac{U A_{b_T} \rho_c}{\dot{m}_p f_{m_{c_p}}} \quad (8.72)$$

$$\frac{\partial(\eta_{m_c})}{\partial(f_{m_{c_p}})} = -\frac{U A_{b_T} \rho_c f_{v_{c_b}}}{\dot{m}_p f_{m_{c_p}}^2} \quad (8.73)$$

Table (8.29) summarizes the measured values for calculated carbide catchment efficiency. The values of ρ_c and $f_{m_{c_p}}$ were the same for all experiments (16896 kg/m³ and 0.6260 respectively). The uncertainty for carbide catchment efficiency was determined from Equation (8.67) and the respective partial derivatives from Equations (8.68) through (8.73). The uncertainty calculated here appears in Figure (2.5), (2.6), and (2.7) as the y-axis error bars for carbide catchment efficiency.

Table 8.29: Uncertainty analysis summary for Equation (2.4)

Bead Number	U (m/min)	A_{b_T} ($\times 10^{-6}$ m ²)	$f_{v_{cb}}$ (1)	\dot{m}_p (g/min)	η_{m_c} (1)	η_{m_c} (%)	$\pm\epsilon_{\eta_{m_c}}$ (1)	$\pm\epsilon_{\eta_{m_c}}$ (%)
1	1.527	1.893	0.3364	49.20	0.5333	53.333	0.06384	6.384
2	1.527	0.722	0.3005	49.20	0.1819	18.187	0.02177	2.177
3	1.527	1.518	0.2848	49.20	0.3621	36.214	0.04335	4.335
4	1.145	2.271	0.2930	49.20	0.4180	41.798	0.05003	5.003
5	1.527	1.187	0.2027	28.80	0.3445	34.450	0.04124	4.124
6	1.909	1.023	0.3442	49.20	0.3688	36.883	0.04415	4.415
7	1.527	1.456	0.3429	49.20	0.41811	41.810	0.05005	5.005
8	1.527	1.187	0.3804	49.20	0.3783	37.826	0.04528	4.528
9	0.764	3.585	0.3471	49.20	0.5212	52.122	0.06240	6.240
10	1.527	1.899	0.3639	62.95	0.4525	45.253	0.05417	5.417
11	1.527	1.369	0.3626	42.45	0.4843	48.429	0.05797	5.797
12	2.291	0.669	0.3748	49.20	0.3152	31.522	0.03773	3.773
13	1.527	1.962	0.3856	68.30	0.4565	45.651	0.05464	5.464

Metal Powder Catchment Efficiency Uncertainty

The formulae for calculating metal powder catchment is presented below in Equation (2.8).

$$\eta_{m_m} = \frac{U A_{b_R} \rho_m}{\dot{m}_p} \frac{1 - f_{v_{cb}}}{f_{m_{m_p}}} \quad (2.8)$$

where η_{m_m} is the metal powder catchment efficiency (1), and ρ_m is the density of the metal powders (kg/m³) Uncertainty in ρ_m is assumed to be 0 from the reported manufacturer. Uncertainty in U has been summarized previously for all tests (Table (8.12)). The value of $\epsilon_{A_{b_R}}$ for all tests is shown in Table (8.16), $\epsilon_{\dot{m}_p}$ for the experiments is included in Table (8.9), $\epsilon_{f_{v_{cb}}}$ is summarized in Table (8.18), and $\epsilon_{f_{m_{m_p}}}$ is shown in Table (8.14).

The uncertainty for Equation (2.8) is defined as follows:

$$\begin{aligned} \epsilon_{\eta_{m_m}} = \pm \left\{ \left[\frac{\partial(\eta_{m_m})}{\partial(U)} \epsilon_U \right]^2 + \left[\frac{\partial(\eta_{m_m})}{\partial(A_{b_R})} \epsilon_{A_{b_R}} \right]^2 + \left[\frac{\partial(\eta_{m_m})}{\partial(\rho_m)} \epsilon_{\rho_m} \right]^2 \right. \\ \left. + \left[\frac{\partial(\eta_{m_m})}{\partial(\dot{m}_p)} \epsilon_{\dot{m}_p} \right]^2 + \left[\frac{\partial(\eta_{m_m})}{\partial(f_{v_{c_b}})} \epsilon_{f_{v_{c_b}}} \right]^2 + \left[\frac{\partial(\eta_{m_m})}{\partial(f_{m_{m_p}})} \epsilon_{f_{m_{m_p}}} \right]^2 \right\}^{1/2} \end{aligned} \quad (8.74)$$

The formulae for the partial derivatives of each term of Equation (8.74) are summarized below in Equations (8.75) through (8.80).

$$\frac{\partial(\eta_{m_m})}{\partial(U)} = \frac{A_{b_R} \rho_m (1 - f_{v_{c_b}})}{\dot{m}_p f_{m_{m_p}}} \quad (8.75)$$

$$\frac{\partial(\eta_{m_m})}{\partial(A_{b_R})} = \frac{U \rho_m (1 - f_{v_{c_b}})}{\dot{m}_p f_{m_{m_p}}} \quad (8.76)$$

$$\frac{\partial(\eta_{m_m})}{\partial(\rho_m)} = \frac{U A_{b_R} \rho_m (1 - f_{v_{c_b}})}{\dot{m}_p f_{m_{m_p}}} \quad (8.77)$$

$$\frac{\partial(\eta_{m_m})}{\partial(\dot{m}_p)} = - \frac{U A_{b_R} \rho_m (1 - f_{v_{c_b}})}{\dot{m}_p^2 f_{m_{m_p}}} \quad (8.78)$$

$$\frac{\partial(\eta_{m_m})}{\partial(f_{v_{c_b}})} = \frac{U A_{b_R} \rho_m}{\dot{m}_p f_{m_{m_p}}} \quad (8.79)$$

$$\frac{\partial(\eta_{m_m})}{\partial(f_{m_{m_p}})} = - \frac{U A_{b_R} \rho_m (1 - f_{v_{c_b}})}{\dot{m}_p f_{m_{m_p}}^2} \quad (8.80)$$

Table (8.30) summarizes the measured values for metal powder catchment efficiency. The values of ρ_m and $f_{m_{m_p}}$ were the same for all experiments (8100 kg/m³ and 0.3740

respectively). Combining ϵ_U from Table (8.12), $\epsilon_{A_{bR}}$ from Table (8.16), $\epsilon_{f_{v_{cb}}}$ from Table (8.18), $\epsilon_{\dot{m}_p}$ from Table (8.9), and $\epsilon_{f_{m_{mp}}}$ from Table (8.14), the uncertainty for metal powder catchment efficiency was determined from Equation (8.74) and the respective partial derivatives from Equations (8.75) through (8.80). The uncertainty calculated here appears in Figure (2.5), (2.6), and (2.7) as the y-axis error bars for metal powder catchment efficiency.

Table 8.30: Uncertainty analysis summary for Equation (2.8)

Bead Number	U (m/min)	A_{bR} ($\times 10^{-6}$ m ²)	$f_{v_{cb}}$ (1)	\dot{m}_p (g/min)	η_{m_m} (1)	η_{m_m} (%)	$\pm \epsilon_{\eta_{m_m}}$ (1)	$\pm \epsilon_{\eta_{m_m}}$ (%)
1	1.527	1.649	0.3364	49.20	0.3727	37.274	0.08179	8.179
2	1.527	0.684	0.3005	49.20	0.1383	13.826	0.03552	3.552
3	1.527	1.398	0.2848	49.20	0.2677	26.765	0.07398	7.398
4	1.145	2.106	0.2930	49.20	0.3111	31.710	0.08274	8.274
5	1.527	0.850	0.2027	28.80	0.1979	19.786	0.08478	8.478
6	1.909	0.954	0.3442	49.20	0.2760	27.602	0.05860	5.860
7	1.527	1.380	0.3429	49.20	0.3180	31.798	0.06789	6.789
8	1.527	1.123	0.3804	49.20	0.2872	28.724	0.05269	5.296
9	3.585	3.421	0.3471	49.20	0.3991	39.905	0.08374	8.374
10	1.527	1.789	0.3639	62.95	0.3419	34.193	0.06697	6.697
11	1.527	1.164	0.3626	42.45	0.3304	33.040	0.06506	6.506
12	2.291	0.647	0.3748	49.20	0.2447	24.468	0.04588	4.588
13	1.527	1.876	0.3856	68.30	0.3503	35.034	0.06298	6.298

Overall Catchment Efficiency Uncertainty

The formulae for calculating overall powder catchment efficiency is presented below in Equation (2.10).

$$\eta_m = \frac{U}{\dot{m}_p} [A_{bT} f_{v_{cb}} \rho_c + A_{bR} (1 - f_{v_{cb}}) \rho_m] \quad (2.10)$$

where η_m is the overall catchment efficiency (1). The uncertainty for Equation (2.10)

is defined as follows:

$$\epsilon_{\eta_m} = \pm \left\{ \left[\frac{\partial(\eta_m)}{\partial(U)} \epsilon_U \right]^2 + \left[\frac{\partial(\eta_m)}{\partial(\dot{m}_p)} \epsilon_{\dot{m}_p} \right]^2 + \left[\frac{\partial(\eta_m)}{\partial(A_{b_T})} \epsilon_{A_{b_T}} \right]^2 + \left[\frac{\partial(\eta_m)}{\partial(f_{v_{cb}})} \epsilon_{f_{v_{cb}}} \right]^2 + \left[\frac{\partial(\eta_m)}{\partial(\rho_c)} \epsilon_{\rho_c} \right]^2 + \left[\frac{\partial(\eta_m)}{\partial(A_{b_R})} \epsilon_{A_{b_R}} \right]^2 + \left[\frac{\partial(\eta_m)}{\partial(\rho_m)} \epsilon_{\rho_m} \right]^2 \right\}^{1/2} \quad (8.81)$$

The formulae for the partial derivatives of each term of Equation (8.81) are summarized below in Equations (8.82) through (8.88).

$$\frac{\partial(\eta_m)}{\partial(U)} = \frac{1}{\dot{m}_p} [A_{b_T} f_{v_{cb}} \rho_c + A_{b_R} (1 - f_{v_{cb}}) \rho_m] \quad (8.82)$$

$$\frac{\partial(\eta_m)}{\partial(\dot{m}_p)} = -\frac{U}{\dot{m}_p^2} [A_{b_T} f_{v_{cb}} \rho_c + A_{b_R} (1 - f_{v_{cb}}) \rho_m] \quad (8.83)$$

$$\frac{\partial(\eta_m)}{\partial(A_{b_T})} = \frac{U f_{v_{cb}} \rho_c}{\dot{m}_p} \quad (8.84)$$

$$\frac{\partial(\eta_m)}{\partial(f_{v_{cb}})} = \frac{U}{\dot{m}_p} [A_{b_T} \rho_c + A_{b_R} \rho_m] \quad (8.85)$$

$$\frac{\partial(\eta_m)}{\partial(\rho_c)} = \frac{U A_{b_T} f_{v_{cb}}}{\dot{m}_p} \quad (8.86)$$

$$\frac{\partial(\eta_m)}{\partial(A_{b_R})} = \frac{U}{\dot{m}_p} [A_{b_T} \rho_c + A_{b_R} \rho_m] \quad (8.87)$$

$$\frac{\partial(\eta_m)}{\partial(\rho_m)} = \frac{U A_{b_T} f_{v_{cb}}}{\dot{m}_p} \quad (8.88)$$

Table (8.31) summarizes the measured values for overall catchment efficiency from Equation (8.81) and the respective partial derivatives from Equations (8.82) through (8.88). The uncertainty calculated here appears in Figure (2.5), (2.6), and (2.7) as the y-axis error bars for overall catchment efficiency.

Table 8.31: Uncertainty analysis summary for Equation (2.8)

Bead Number	U (m/min)	\dot{m}_p (g/min)	A_{bT} ($\times 10^{-6}$ m ²)	$f_{v_{cb}}$ (1)	A_{bR} ($\times 10^{-6}$ m ²)	η_m (1)	η_m (%)	$\pm\epsilon_{\eta_m}$ (1)	$\pm\epsilon_{\eta_m}$ (%)
1	1.527	49.20	1.893	0.3364	1.649	0.6089	60.888	0.04787	4.787
2	1.527	49.20	0.722	0.3005	0.684	0.2342	23.420	0.01821	1.821
3	1.527	49.20	1.518	0.2848	1.398	0.4780	47.804	0.03721	3.721
4	1.145	49.20	2.271	0.2930	2.106	0.5424	54.237	0.04220	4.220
5	1.527	28.80	1.187	0.2027	0.850	0.5066	50.665	0.03987	3.987
6	1.909	49.20	1.023	0.3442	0.954	0.4275	42.754	0.03347	3.347
7	1.527	49.20	1.456	0.3429	1.380	0.4896	48.963	0.03827	3.827
8	1.527	49.20	1.187	0.3804	1.123	0.4118	41.178	0.03256	3.256
9	3.585	49.20	3.585	0.3471	3.421	0.6071	60.707	0.04748	4.748
10	1.527	62.95	1.899	0.3639	1.789	0.5068	50.682	0.03987	3.987
11	1.527	42.45	1.369	0.3626	1.164	0.5204	52.040	0.04141	4.141
12	2.291	49.20	0.669	0.3748	0.647	0.3500	34.996	0.02754	2.754
13	1.527	68.30	1.962	0.3856	1.876	0.4945	49.454	0.03912	3.912

8.5.3 Height Model Prediction Uncertainty

The formulae for calculating bead height is presented below in Equation (4.19).

$$\widehat{h}_m = \frac{3\dot{m}_p}{8U [f_{v_{cb}}\rho_c + (1 - f_{v_{cb}})\rho_m]} \widehat{r}_p \quad (4.19)$$

where h_m is bead height (mm), and \widehat{r}_p is the optimized value of the powder cloud radius (mm). The uncertainty in the calculated value of \widehat{r}_p was taken to be 0 from the

optimization. The uncertainty for Equation (4.19) is defined as follows:

$$\epsilon_{h_m} = \pm \left\{ \left[\frac{\partial(h_m)}{\partial(\dot{m}_p)} \epsilon_{\dot{m}_p} \right]^2 + \left[\frac{\partial(h_m)}{\partial(U)} \epsilon_U \right]^2 + \left[\frac{\partial(h_m)}{\partial(f_{v_{cb}})} \epsilon_{f_{v_{cb}}} \right]^2 + \left[\frac{\partial(h_m)}{\partial(\rho_c)} \epsilon_{\rho_c} \right]^2 + \left[\frac{\partial(h_m)}{\partial(\rho_m)} \epsilon_{\rho_m} \right]^2 + \left[\frac{\partial(h_m)}{\partial(\hat{r}_p)} \epsilon_{\hat{r}_p} \right]^2 \right\}^{1/2} \quad (8.89)$$

The formulae for the partial derivatives of each term of Equation (8.89) are summarized below in Equations (8.90) through (8.95).

$$\frac{\partial(h_m)}{\partial(\dot{m}_p)} = \frac{3}{8U\hat{r}_p [f_{v_{cb}}\rho_c + (1 - f_{v_{cb}})\rho_m]} \quad (8.90)$$

$$\frac{\partial(h_m)}{\partial(U)} = -\frac{3}{8U^2\hat{r}_p [f_{v_{cb}}\rho_c + (1 - f_{v_{cb}})\rho_m]} \quad (8.91)$$

$$\frac{\partial(h_m)}{\partial(f_{v_{cb}})} = \frac{3\dot{m}_p}{8U\hat{r}_p [-f_{v_{cb}}^2\rho_c + f_{v_{cb}}^2\rho_m]} \quad (8.92)$$

$$\frac{\partial(h_m)}{\partial(\rho_c)} = -\frac{3\dot{m}_p}{8Uf_{v_{cb}}\rho_c^2\hat{r}_p} \quad (8.93)$$

$$\frac{\partial(h_m)}{\partial(\rho_m)} = -\frac{3\dot{m}_p}{(8U\rho_m^2 + f_{v_{cb}}\rho_m^2)\hat{r}_p} \quad (8.94)$$

$$\frac{\partial(h_m)}{\partial(\hat{r}_p)} = -\frac{3\dot{m}_p}{(8U [f_{v_{cb}}\rho_c + (1 - f_{v_{cb}})\rho_m] \hat{r}_p^2)} \quad (8.95)$$

Table (8.32) summarizes the measured values for overall catchment efficiency from Equation (8.89) and the respective partial derivatives from Equations (8.90) through

(8.95). The uncertainty calculated here appears in Figure (4.16) as the x-axis error bars for calculated height.

Table 8.32: Uncertainty analysis summary for Equation (4.19)

Bead Number	U (m/min)	\dot{m}_p (g/min)	$f_{v_{c_b}}$ (1)	h_m (mm)	$\pm\epsilon_{h_m}$ (mm)
1	0.0254	49.20	0.3364	0.6187	0.04190
2	0.0254	49.20	0.3005	0.6368	0.04690
3	0.0254	49.20	0.2848	0.6451	0.04949
4	0.0191	49.20	0.2930	0.8544	0.06415
5	0.0254	28.80	0.2027	0.4052	0.04070
6	0.0318	49.20	0.3442	0.4919	0.03276
7	0.0254	49.20	0.3429	0.6155	0.04111
8	0.0254	49.20	0.3804	0.5978	0.03706
9	0.0127	49.20	0.3471	1.2268	0.08122
10	0.0254	62.95	0.3639	0.7746	0.04956
11	0.0254	42.45	0.3626	0.5204	0.03339
12	0.0381	49.20	0.3748	0.4002	0.02507
13	0.0254	68.30	0.3856	0.8265	0.05075

8.5.4 Bead Reinforcement Area Uncertainty

In Appendix 4.1 formulae for the parabolic area estimate and circular area estimate for the cross sectional area of the deposited clad bead are presented. In this section, the uncertainty in both techniques is evaluated.

8.5.5 Parabolic Reinforcement Area Uncertainty

The reinforcement area of the bead can be calculated using Equation (4.18).

$$\widehat{A}_{b,r} = \frac{4}{3}y_{m,b}h_m \quad (4.17)$$

where $\widehat{A}_{b,r}$ is the calculated reinforcement area (mm^2). The uncertainty in $y_{m,b}$ is

tabulated for the stereo photograph measured width in Section 8.3.4; and the uncertainty in h_m is shown in Section 8.3.3. The uncertainty in Equation (4.17) can be represented as follows:

$$\epsilon_{\widehat{A_{b_R}}} = \pm \left\{ \left[\frac{\partial(\widehat{A_{b_R}})}{\partial(y_{m,b})} \epsilon_{y_{m,b}} \right]^2 + \left[\frac{\partial(\widehat{A_{b_R}})}{\partial(h_m)} \epsilon_{h_m} \right]^2 \right\}^{1/2} \quad (8.96)$$

The formulae for the partial derivatives of both terms of Equation (8.96) are summarized below.

$$\frac{\partial(\widehat{A_{b_R}})}{\partial(y_{m,b})} = \frac{4}{3} h_m \quad (8.97)$$

$$\frac{\partial(\widehat{A_{b_R}})}{\partial(h_m)} = \frac{4}{3} y_{m,b} \quad (8.98)$$

Table (8.33) summarizes the measured values for Equation (4.17). The uncertainty in measured width and height are tabulated in Tables (8.22) and (8.20) respectively. The uncertainty calculated here appears in Figure (4.17) as the x-axis error bars for calculated height for the parabolic reinforcement area prediction.

Table 8.33: Uncertainty analysis summary for Equation (4.17)

Bead Number	$y_{m,b}$ (mm)	h_m (mm)	\widehat{A}_{b_R} (mm ²)	$\pm \epsilon_{\widehat{A}_{b_R}}$ (mm ²)
1	1.936	0.594	1.532	0.2589
2	0.966	0.493	0.635	0.1101
3	1.751	0.493	1.151	0.1995
4	1.958	0.715	1.867	0.3236
5	1.910	0.314	0.798	0.1384
6	1.514	0.418	0.845	0.1464
7	1.701	0.547	1.242	0.2152
8	1.667	0.490	1.088	0.2579
9	2.078	1.120	3.103	0.5243
10	1.726	0.694	1.598	0.2769
11	1.826	0.454	1.105	0.1916
12	1.229	0.395	0.646	0.1092
13	1.532	0.764	1.560	0.2704

8.5.6 Circular Reinforcement Area Uncertainty

The formula for the circular segment reinforcement area proposed by Colaço is as follows:

$$\widehat{A}_{b,r} = y_{m,b} \sqrt{R^2 - y_{m,b}^2} + R^2 \arcsin\left(\frac{y_{m,b}}{R}\right) + 2y_{m,b}(h_m - R) \quad (4.21)$$

where $\widehat{A}_{b,r}$ is the calculated circular segment reinforcement approximation (mm²), and R is the radius of the circle that subtends the segment (mm). The uncertainty in $y_{m,b}$ is tabulated for the stereo photograph measured width in Section 8.3.4; and the uncertainty in h_m is shown in Section 8.3.3. The value of R is found using the MATLABTM solver *fzero* to solve the implicit expression above. The uncertainty in this optimized value was taken to be zero. The uncertainty in Equation (4.21) can be described as follows:

$$\epsilon_{\widehat{A}_{b_R}} = \pm \left\{ \left[\frac{\partial(\widehat{A}_{b_R})}{\partial(y_{m,b})} \epsilon_{y_{m,b}} \right]^2 + \left[\frac{\partial(\widehat{A}_{b_R})}{\partial(R)} \epsilon_R \right]^2 + \left[\frac{\partial(\widehat{A}_{b_R})}{\partial(h_m)} \epsilon_{h_m} \right]^2 \right\}^{1/2} \quad (8.99)$$

The formulae for the partial derivatives of each of the three terms term of Equation (8.99) are summarized below.

$$\frac{\partial(\widehat{A_{bR}})}{\partial(y_{m,b})} = (R^2 + y_{m,b}^2)^{1/2} - y_{m,b}^2(R^2 - y_{m,b}^2)^{-1/2} + R \left[1 - \left(\frac{y_{m,b}}{R} \right)^2 \right]^{-1/2} + 2(h_m - R) \quad (8.100)$$

$$\frac{\partial(\widehat{A_{bR}})}{\partial(R)} = y_{m,b}R(R^2 - y_{m,b}^2)^{-1/2} + 2R \arcsin \left(\frac{y_{m,b}}{R} \right) - y_{m,b} \left[1 - \left(\frac{y_{m,b}}{R} \right)^2 \right]^{-1/2} - 2y_{m,b} \quad (8.101)$$

$$\frac{\partial(\widehat{A_{bR}})}{\partial(h_m)} = 2y_{m,b} \quad (8.102)$$

Table (8.34) summarizes the measured values for Equation (4.17). The uncertainty in measured width and height are tabulated in Tables (8.22) and (8.20) respectively. The uncertainty calculated here appears in Figure (4.17) as the x-axis error bars for calculated height for the circular segment reinforcement area prediction.

Table 8.34: Uncertainty analysis summary for Equation (4.21)

Bead Number	$y_{m,b}$ (mm)	R (mm)	h_m (mm)	\widehat{A}_{bR} (mm ²)	$\pm \epsilon_{\widehat{A}_{bR}}$ (mm ²)
1	1.936	3.472	0.594	1.565	0.1689
2	0.966	1.198	0.493	0.669	0.0700
3	1.751	3.375	0.493	1.172	0.1269
4	1.958	3.023	0.715	1.911	0.2058
5	1.910	6.031	0.314	0.807	0.0880
6	1.514	2.939	0.418	0.856	0.0931
7	1.701	2.904	0.547	1.264	0.1369
8	1.667	3.083	0.490	1.107	0.1199
9	2.078	2.488	1.120	3.277	0.3421
10	1.726	2.505	0.694	1.652	0.1761
11	1.826	3.933	0.454	1.123	0.1219
12	1.229	2.132	0.395	0.663	0.0713
13	1.532	1.924	0.764	1.638	0.1720

8.6 References

- [1] T.G. Beckwith, R.D. Marangoni, and J.H. Leinhard V. *Mechanical Measurements*. Pearson Prentice Hall, 6 edition, 2007.
- [2] R.J. Kosinski. A Literature Review on Reaction Time, 2013.
- [3] K.C. Mills, A.P. Day, and P.N. Quedsted. Details of METALS Model to Calculate the Thermophysical Properties of Alloys, 2002.

Appendix C. MATLAB Code for Chapter 4

Included in this appendix are the code files used to output the optimized values of the beam distribution parameter $\hat{\sigma}$, temperature of the heat affected zone (HAZ) \widehat{T}_{HAZ} , and the geometries of the HAZ for the experimental conditions outlined in the Chapter 4. The code for the melting isotherm is identical to the HAZ using the appropriate input values for experimental measurements and material properties, and is not included here. The melting isotherm analysis consists of steps 1 and 2 only.

9.1 Step 1a. Determining the \hat{y}^* Solution Set for the Heat Affected Zone

```
1 function [ y_star_g ] = y_star_gauss(T_star, x_star, sigma_star)
2 %y_star_gauss solves for the y_star value from Eagar's equation for ...
   moving heat sources for inputs of T_star, x_star, and sigma_star ...
   that minimizes the difference between the calculated value of ...
   T_star (T_star_C) and the input value of T_star
3 %Notation for T_star is slightly different from Eagar's paper, T_star_C ...
   = theta/n where theta is Eagar's dimensionless temperature that we ...
   set to equal 1 and n is the dimensionless operating parameter
```

```

4
5 fy = @(t, y_star)((1./((2.*pi).^0.5)).*(t.^-0.5./(t + ...
    sigma_star.^2)).*exp(-(x_star.^2 + y_star.^2 + (2.*x_star.*t) + ...
    t.^2)./(2.*t + 2.*sigma_star.^2)));
6 %Place holder for function to be integrated to solve for T_star_C
7 %Equation is valid for the surface of the isotherm, (z_star = 0) or ...
    ("Zeta "=0, Eagar notation)
8
9 T_star_C = @(y_star)(integral(@(t)fy(t,y_star), 0, 50));
10 %Integral of fz to solve for T_star_C
11 %Integration limits set between 0 and 50 (dimensionless time), previous ...
    work by Ying has shown that steady state is reached after 20s
12
13 objfun = @(y_star)(T_star_C(y_star) - T_star);
14 %Objective function that is the difference between the input value of ...
    T_star and the calculated value of the integral for T_star_C
15
16 y_star_seed = 1/T_star;
17 %Starting point value for y_star for fzero optimization
18 %Value is Rosenthal's point heat source prediction for maximum width ...
    for slow moving heat sources (high T_star values)
19 %Future iterations to include use of blended function as prediction
20
21 y_star_g = fzero(@(y_star)objfun(y_star), y_star_seed);
22 %Optimization which attempts to find that value of y_star that forces ...
    the the objective function to equal 0 (T_star_C = T_star)
23
24 end

```

9.2 Step 1b. Determining the \hat{z}^* Solution Set for the Heat Affected Zone

```

1 function [ z_star_g ] = z_star_gauss(T_star, x_star, sigma_star)
2 %z_star_gauss solves for the z_star value from Eagar's equation for ...
   moving heat sources for inputs of T_star, x_star, and sigma_star ...
   that minimizes the difference between the calculated value of ...
   T_star (T_star_C) and the input value of T_star
3 %Notation for T_star is slightly different from Eagar's paper, T_star_C ...
   = theta/n where theta is Eagar's dimensionless temperature that we ...
   set to equal 1 and n is the dimensionless operating parameter
4
5 fz = @(t, z_star)((1./((2.*pi).^0.5)).*(t.^-0.5./(t + ...
   sigma_star.^2)).*exp((-x_star.^2 + (2.*x_star.*t) + t.^2)./(2.*t + ...
   2.*sigma_star.^2))-(z_star.^2./(2.*t))));
6 %Place holder for function to be integrated to solve for T_star_C
7 %Equation is valid along the centreline of the isotherm, (y_star = 0) ...
   or ("PSI"=0, Eagar notation)
8
9 T_star_C = @(z_star)(integral(@(t)fz(t,z_star), 0, 50));
10 %Integral of fz to solve for T_star_C
11 %Integration limits set between 0 and 50 (dimensionless time), previous ...
   work by Ying has shown that steady state is reached after 20s
12
13 objfun = @(z_star)(T_star_C(z_star) - T_star);
14 %Objective function that is the difference between the input value of ...
   T_star and the calculated value of the integral for T_star_C
15

```

```

16 z_star_seed = 0;
17 %Starting point value for z_star for fzero optimization
18
19 z_star_g = fzero(@(z_star)objfun(z_star), z_star_seed);
20 %Optimization which attempts to find that value of z_star that forces ...
    the the objective function to equal 0 (T_star_C = T_star)
21
22 end

```

9.3 Step 2a. Determination of Maximum $-\hat{y}^*$

```

1 function [ y_star_g ] = y_star_gauss(T_star, x_star, sigma_star)
2 %y_star_gauss solves for the y_star value from Eagar's equation for ...
    moving heat sources for inputs of T_star, x_star, and sigma_star ...
    that minimizes the difference between the calculated value of ...
    T_star (T_star_C) and the input value of T_star
3 %Notation for T_star is slightly different from Eagar's paper, T_star_C ...
    = theta/n where theta is Eagar's dimensionless temperature that we ...
    set to equal 1 and n is the dimensionless operating parameter
4
5 fy = @(t, y_star)((1./((2.*pi).^0.5)).*(t.^-0.5./(t + ...
    sigma_star.^2)).*exp(-(x_star.^2 + y_star.^2 + (2.*x_star.*t) + ...
    t.^2)./(2.*t + 2.*sigma_star.^2)));
6 %Place holder for function to be integrated to solve for T_star_C
7 %Equation is valid for the surface of the isotherm, (z_star = 0) or ...
    ("Zeta "=0, Eagar notation)
8
9 T_star_C = @(y_star)(integral(@(t)fy(t,y_star), 0, 50));
10 %Integral of fz to solve for T_star_C

```

```

11 %Integration limits set between 0 and 50 (dimensionless time), previous ...
    work by Ying has shown that steady state is reached after 20s
12
13 objfun = @(y_star)(T_star_C(y_star) - T_star);
14 %Objective function that is the difference between the input value of ...
    T_star and the calculated value of the integral for T_star_C
15
16 y_star_seed = 1/T_star;
17 %Starting point value for y_star for fzero optimization
18 %Value is Rosenthal's point heat source prediction for maximum width ...
    for slow moving heat sources (high T_star values)
19 %Future iterations to include use of blended function as prediction
20
21 y_star_g = fzero(@(y_star)objfun(y_star), y_star_seed);
22 %Optimization which attempts to find that value of y_star that forces ...
    the the objective function to equal 0 (T_star_C = T_star)
23
24 end

```

9.4 Step 2b. Determination of Maximum $-\hat{z}^*$

```

1 function [z_star_max, x_star_max] = zstarf_gauss(T_star, sigma_star)
2 %zstarf_gauss inputs values of T_star and sigma_star and finds the ...
    x_star (x solution for fminsearch) corresponding to the maximum ...
    z_star (fcn value of the objective function)
3
4 objfun = @(x_star)(z_star_gauss(T_star, x_star, sigma_star));
5 %Objective function that calls z_star_gauss function to find z_star for ...
    inputs of x_star, T_star, and sigma_star

```

```

6
7 x_star_seed = 0;
8 %Starting point for fminsearch optimization for x_star
9
10 options = optimset('TolX', 1e-6, 'Tolfun', 1e-6, 'MaxFunEvals', 5000);
11 %Options for fminsearch, tolerances and maximum number of function ...
    evaluations
12
13 [x_star_max, z_star_max] = fminsearch(@(x_star)objfun(x_star), ...
    x_star_seed, options);
14 %Optimization which finds the value of x_star that gives the minimum ...
    value (most negative value) of z_star, z_star is negative by ...
    definition with z_star=0 at the surface, -z_star measured into the ...
    solid
15 end

```

9.5 Step 3. Optimization for $\hat{\sigma}$ and \widehat{T}_{HAZ}

```

1 function [x, fval] = T-sigma-opt-V2(y_star_max_meas, z_star_max_meas, ...
    q, u, To, k, alpha, eta)
2 %T-sigma-opt-V2 inputs the experimental measured maximums, experimental ...
    parameters and outputs the values of sigma and T-HAZ that minimize ...
    the difference between the calculated ym and zm for the width and ...
    height of the clad
3
4 %x(1) = T
5 %x(2) = sigma
6
7 T_star = @(x) (x(1)-To).*(4*pi*k*alpha)./(eta.*q.*u);

```

```

8 sigma_star = @(x) (u.*x(2))./(2*alpha);
9 %Expressions for T_star and sigma_star are necessary to optimize x(1) ...
   and x(2) the dimensional values that are common to all tests (or ...
   assumed to be constant for all tests)
10
11 counter = length(y_star_max_meas);
12 %Variable to check the number of experimental measures from the y measure
13 %input
14
15 function [y_star_max] = y_fun(T_star, sigma_star)
16 y_star_max = zeros(counter,1);
17 for i=1:counter
18 y_star_max(i) = (y_starf_gauss(T_star(i), sigma_star(i)));
19 end
20 end
21 %Loop function that creates function handles to match measured values ...
   in the fminsearch algorithm
22
23 function [z_star_max] = z_fun(T_star, sigma_star)
24 z_star_max = zeros(counter,1);
25 for i=1:counter
26 z_star_max(i) = (z_starf_gauss(T_star(i), sigma_star(i)));
27 end
28 end
29 %Loop function that creates function handles to match measured values ...
   in the fminsearch algorithm
30
31 y_star_max = @(x) y_fun(T_star(x), sigma_star(x));
32 z_star_max = @(x) z_fun(T_star(x), sigma_star(x));
33 %Required representation of the function handle in terms of x, which ...
   simultaneously optimizes x1 and x2

```

```

34
35 objfun = @(x)sum(((log((y_star_max(x))./(y_star_max_meas))).^2)+...
36 ((log((z_star_max(x))./(z_star_max_meas))).^2));
37 %Objective function that minimizes the difference between the square of ...
    the log difference between the y_meas and y_calc and z_meas and ...
    z_calc simulataneously
38
39 T_seed = 981;%4145 MOD HAZ AC1
40 sigma_seed = 0.001;%Reasonable seed estimate for obj function equation
41
42 options = optimset('Display', 'iter','TolX', 1e-6, 'Tolfun', 1e-6, ...
    'MaxFunEvals', 5000);
43 %Options for fminsearch, tolerances and maximum number of function ...
    evaluations
44
45 [x, fval] = fminsearch(@(x)objfun(x), [T_seed, sigma_seed], options);
46 %Stores the values of x1 and x2 as well as the function values (error)
47 %Possible to see the contribution of each term to the total error/see ...
    if a single test biases the result
48
49 end

```

9.6 Output All Values of Interest to Excel

```

1 format long
2 %Inputs optimized values of T and sigma into all functions to calculate ...
    T_star, sigma_star, y_star_max, x_star_max_y, z_star_max, x_star_max_z
3
4 x(1) = 1.219141230409474*1000;%Optimized solution for T

```

```

5 x(2) = 0.000001615750988*1000;%Optimized solution for sigma
6
7 [y_star_max_meas,z_star_max_meas] = ...
    import_exp_dim_val('exp_dim_val.xlsx','Sheet1',3,15);
8 [q,u,To] = import_exp_param('exp_param.xlsx','Sheet1',3,15);
9 [k,rho,cp,alpha] = import_mat_props('mat_props.xlsx','Sheet1',3,3);
10 eta = 0.3; %Universal eta assumed - from literature Schneider1998
11 %All required inputs: experimental measurements, experimental ...
    parameters, and material properties
12
13 counter = length(y_star_max_meas);
14 %Variable to check the number of experimental measures from the y ...
    measure input
15
16 for i=1:counter
17 T_star_(i) = (x(1)-To(i))*(4*pi*k*alpha)/(eta*q(i)*u(i));
18 sigma_star_(i) = (u(i)*x(2))/(2*alpha);
19 [y_star_max_(i), x_star_max_y_(i)] = ystarf_gauss(T_star_(i), ...
    sigma_star_(i));
20 [z_star_max_(i), x_star_max_z_(i)] = zstarf_gauss(T_star_(i), ...
    sigma_star_(i));
21 y_error_(i) = ((log((y_star_max_(i))./(y_star_max_meas((i))))).^2);
22 z_error_(i) = ((log((z_star_max_(i))./(z_star_max_meas((i))))).^2);
23 end
24 %T_star for all experiments, x(1) is the same for all
25 %sigma_star for all experiments, x(2) is the same for all
26 %y_star_max, x_star_max_y for all experiments
27 %z_star_max, x_star_max_z for all experiments
28 %y_error component
29 %z_error component
30

```